



UNIVERSITY OF ILLINOIS  
URBANA

# AERONOMY REPORT NO. 78

## ENERGETIC PARTICLES AND IONIZATION IN THE NIGHTTIME MIDDLE AND LOW LATITUDE IONOSPHERE

by  
H. D. Voss  
L. G. Smith

November 1, 1977

Library of Congress ISSN 0568-0581

(NASA-CR-156943) ENERGETIC PARTICLES AND  
IONIZATION IN THE NIGHTTIME MIDDLE AND LOW  
LATITUDE IONOSPHERE (Illinois Univ.) 323 p  
HC A14/MF A01

CSCS 04A

N78-29665

Unclas

G3/46

27857

Supported by  
National Aeronautics and Space Administration  
Grant NGR 14-005-181

Aeronomy Laboratory  
Department of Electrical Engineering  
University of Illinois  
Urbana, Illinois

### CITATION POLICY

The material contained in this report is preliminary information circulated rapidly in the interest of prompt interchange of scientific information and may be later revised on publication in accepted aeronomic journals. It would therefore be appreciated if persons wishing to cite work contained herein would first contact the authors to ascertain if the relevant material is part of a paper published or in process.

A E R O N O M Y   R E P O R T

N O.   7 8

ENERGETIC PARTICLES AND IONIZATION  
IN THE NIGHTTIME MIDDLE AND LOW LATITUDE IONOSPHERE

by

H. D. Voss  
L. G. Smith

November 1, 1977

Supported by  
National Aeronautics and  
Space Administration  
Grant NGR 14-005-181

Aeronomy Laboratory  
Department of Electrical Engineering  
University of Illinois  
Urbana, Illinois

## ABSTRACT

Seven Nike Apache rockets, each equipped with an energetic particle spectrometer ( $12 < E < 80$  keV) and electron-density experiments, have been launched from Wallops Island, Virginia and Chilca, Peru, under varying geomagnetic conditions near midnight. At Wallops Island the energetic particle flux ( $E < 40$  keV) is found to be strongly dependent on  $K_p$ . The pitch-angle distribution is asymmetrical about a peak at  $90^\circ$  signifying a predominantly quasi-trapped flux and explaining the linear increase of count rate with altitude in the altitude region 120 to 200 km. The height-averaged ionization rates derived from the electron-density profiles are consistent with the rates calculated from the observed total particle flux for magnetic index  $K_p > 3$ . In the region 90 to 110 km it is found that the nighttime ionization is primarily a result of Ly- $\beta$  radiation from the geocorona and interplanetary hydrogen for even very disturbed conditions. Below 90 km during rather disturbed conditions energetic electrons can be a significant ionization source. Two energetic particle precipitation zones have been identified at midlatitudes. The Wallops Island precipitation zone is centered at  $L = 2.6$  and the Arecibo precipitation zone is centered at  $L = 1.4$ . A precipitation null exists at  $L = 1.8$  which is the situation for White Sands. The locations of maximum precipitation in the South Atlantic Magnetic Anomaly are found to be associated directly with the precipitation zones at  $L = 1.4$  and  $L = 2.6$ . At the equator the first rocket-borne detection of low altitude kilovolt protons is observed with count rates steadily increasing from 170 km altitude. The flux depends strongly on magnetic activity and is believed to be associated with a double charge exchange mechanism of neutral hydrogen with the ring current. Furthermore, it is found that at



kilovolt energies the theoretical calculations used to compute multiple scattering for electrons are largely in error. An experimental apparatus was developed to measure the scattering of a beam of electrons in air. These results were then used to obtain profiles of mirror-height spreading as a function of altitude.

# TABLE OF CONTENTS

ABSTRACT . . . . .	iii
TABLE OF CONTENTS . . . . .	v
LIST OF TABLES . . . . .	x
LIST OF FIGURES . . . . .	xi
1 INTRODUCTION . . . . .	1
1.1 <i>General Introduction</i> . . . . .	1
1.2 <i>Objectives of this Study</i> . . . . .	3
2. IONIZATION SOURCES IN THE NIGHTTIME E REGION . . . . .	7
2.1 <i>Electron Density in the Nighttime Midlatitude Ionosphere</i> . . .	7
2.2 <i>Evidence for an Ionization Source</i> . . . . .	12
2.2.1 <i>Recombination</i> . . . . .	12
2.2.2 <i>Transport</i> . . . . .	19
2.3 <i>Ionization Rates for the Nighttime E Region</i> . . . . .	20
2.3.1 <i>Ionization rates calculated from the continuity</i> <i>equation for the steady-state no-transport case</i> . . . .	20
2.3.2 <i>Ionization rates calculated from the intermediate</i> <i>layer</i> . . . . .	21
2.3.3 <i>Wind shear theory as an explanation of the</i> <i>intermediate layer</i> . . . . .	28
2.4 <i>Significance of Ultraviolet Ionization in the Nighttime</i> <i>Ionosphere</i> . . . . .	33
2.4.1 <i>Introduction</i> . . . . .	35
2.4.2 <i>Hydrogen Ly-<math>\alpha</math> emission</i> . . . . .	35
2.4.3 <i>Hydrogen Ly-<math>\beta</math> emission</i> . . . . .	37
2.4.4 <i>Helium I emission</i> . . . . .	39
2.4.5 <i>Helium II emission</i> . . . . .	39

2.4.6	<i>Ionization rates and electron densities produced by ultraviolet radiation at night.</i>	40
3	EXPERIMENTAL TECHNIQUE.	43
3 1	<i>Design and Calibration of a Rocket-borne Energetic Electron Spectrometer</i>	43
3 1 1	<i>Choice of detector</i>	43
3 1 2	<i>Electronic circuits.</i>	46
3 1.3	<i>Calibration</i>	49
3 2	<i>Determination of the Rocket Attitude from the Magnetometer Signal</i>	49
3 3	<i>The Flux Related to the Detector Count Rate</i>	58
3.3 1	<i>General considerations</i>	58
3 3 2	<i>Detector count rate</i>	64
3 3 3	<i>Shadowing by the payload</i>	68
4	DIRECT OBSERVATIONS OF ENERGETIC ELECTRONS.	71
4 1	<i>New Rocket Measurements at Midlatitudes</i>	71
4.1 1	<i>Nike Apache 14.439; 1 November 1972</i>	72
4.1 2	<i>Nike Apache 14.520, 18 April 1974</i>	78
4 1 3	<i>Nike Apaches 14 521 and 14.522, 29 June 1974</i>	88
4 2	<i>New Rocket Measurements at the Geomagnetic Equator</i>	91
4.3	<i>Satellite Observations.</i>	98
4.4	<i>Other Rocket Measurements</i>	107
4 5	<i>Summary of Observations</i>	111
4 5 1	<i>Geographic variations and precipitation zones</i>	111
4 5 2	<i>Variation of count rate with altitude</i>	113
4.5 3	<i>Magnetic activity and particle precipitation</i>	115
5	INDIRECT EVIDENCE OF ENERGETIC ELECTRON PRECIPITATION	120

5 1	<i>Midlatitude 391.4 nm Emission</i>	120
5 2	<i>Ionization Rate Variations with Kp</i>	125
5.3	<i>VL F Doppler Shifts and Field Intensity Variations</i>	125
5.4	<i>The Critical Frequency, <math>f_{XEn}</math>, of the nighttime Intermediate Layer</i>	126
5.5	<i>Kp Variations and electron Temperature</i>	127
5.6	<i>Bremsstrahlung X-rays as a Global Precipitation Snapshot</i>	129
6	<b>PARTICLE INJECTION AND DIFFUSION</b>	131
6 1	<i>The Magnetosphere</i>	131
6.2	<i>Radiation Belts</i>	135
6 3	<i>Particle Precipitation Excited by Wave-particle Interactions</i>	136
6.4	<i>Plasmaspheric Hiss Exciting the Wallops Island and Arecibo Precipitation Zones</i>	140
6 5	<i>Longitude Variations of Particle Precipitation and the Cause of the South Atlantic Magnetic Anomaly Precipitation</i>	144
7.	<b>MODELING THE PARTICLE SOURCE FUNCTION</b>	152
7.1	<i>The Variation of Count Rate with Altitude</i>	152
7.2	<i>The Pitch-angle Distribution</i>	160
7.2.1	<i>Observation of pitch-angle distributions</i>	161
7 2 2	<i>Change of pitch angle with altitude for a dipole field</i>	164
7.3	<i>Computer Simulation of the Count-rate Profile</i>	167
7 4	<i>Equatorial Proton Precipitation</i>	172
7.5	<i>Comparison Between Near Simultaneous Satellite and Rocket Measurements</i>	176
7.6	<i>Global Precipitation Patterns at Night</i>	183

7.7	<i>The Relative Importance of Energetic Electrons and Protons.</i>	188
8	INTERACTION OF ENERGETIC ELECTRONS WITH THE ATMOSPHERE	191
8.1	<i>Electron Scattering Cross Sections</i>	192
8.1.1	<i>Elastic collisions</i>	192
8.1.2	<i>Inelastic collisions</i>	196
8.1.3	<i>Combined elastic and inelastic scattering.</i>	198
8.2	<i>Energy Loss by Particle Precipitation, Ionization, Excitation and Heating</i>	199
8.2.1	<i>Introduction</i>	199
8.2.2	<i>Electron energy loss rate in air</i>	200
8.3	<i>Basic Multiple Scattering Formulas.</i>	204
8.4	<i>Experimental Study of Electron Scattering in Air.</i>	207
8.4.1	<i>Experimental arrangement</i>	208
8.4.2	<i>Experimental results of electron scattering</i>	211
8.4.3	<i>Observations of electron energy loss in air.</i>	216
8.5	<i>Scattering Influence on the Pitch-angle Distribution.</i>	216
9	CALCULATION OF IONIZATION RATES FOR ENERGETIC PARTICLES	225
9.1	<i>Atmospheric Ionization by Electrons</i>	225
9.1.1	<i>Empirical methods.</i>	225
9.1.2	<i>Monte Carlo simulation</i>	226
9.1.3	<i>Boltzmann equation methods</i>	229
9.2	<i>Ionization Rate for a Quasi-trapped Distribution of Energetic Electrons</i>	231
9.2.1	<i>Energy considerations</i>	231
9.2.2	<i>Pitch-angle distribution</i>	234
9.3	<i>Energy Loss and Ionization by Quasi-trapped Energetic Electrons</i>	235

9.3.1	<i>Approximate calculation . . . . .</i>	235
9 3.2	<i>Calculation of ionization rate for individual electrons . . . . .</i>	237
9.4	<i>Numerical Studies of Ionization by Quasi-trapped Energetic Electrons . . . . .</i>	243
9.5	<i>Average Ionization Rates Computed from Rocket-borne Particle Measurements . . . . .</i>	256
9 5.1	<i>Ionization rates obtained from the incident energy flux . . . . .</i>	256
9 5 2	<i>Detailed calculations of energy flux . . . . .</i>	259
9.5.3	<i>Calculations of ionization rates . . . . .</i>	262
9.5.4	<i>Comparison with ionization rates due to UV . . . . .</i>	265
10.	<i>CONCLUSION . . . . .</i>	269
10 1	<i>Summary . . . . .</i>	269
10.2	<i>Conclusions . . . . .</i>	271
10.3	<i>Suggestions for Future Work . . . . .</i>	273
REFERENCES	<i>. . . . .</i>	275

## LIST OF TABLES

Table		Page
2 1	Recombination Rate Calculations . . . . .	15
4 1	Nighttime Middle and Low Latitude Rocket Experiments .	108
4 2	Magnetic Index Comparisons . . . . .	117
9 1	Average Ionization Rates (120-200 km). . . . .	266

## LIST OF FIGURES

Figure		Page
1 1	Profile 1 is representative of the daytime electron density ( $10^5 \text{ cm}^{-3}$ ). Towards night this electron density rapidly decays to a lower nighttime equilibrium level of about $10^3 \text{ cm}^{-3}$ (Profile 2). The nighttime density profile shows much variability and structure . . . . .	2
2.1	Three electron-density profiles representative of Kp values of 3+ (Profile 1), 5+ (Profile 2) and 8 (Profile 3) . . . .	8
2.2	Electron-density profiles from the probes on rockets launched from Wallops Island on 22 February 1976 [ <i>Smith</i> , 1970]. The profiles are each displaced by one decade. The electron-density scales for the first and last profiles are given. The part of the profiles below 90 km should be regarded as indicating the structure, rather than as absolute values . . .	10
2 3	The nighttime electron-density profile in the <i>E</i> region shows much variability before midnight due to the tidal wind system as shown by these two sounding rocket measurements. The profiles are separated in time by 140 min . . . . .	11
2.4	Effective recombination coefficients deduced by <i>Smith et al.</i> [1974] for Kp = 3 (Profile 1), and <i>Cladis et al.</i> [1973] (Profile 2) . . . . .	16
2.5	Decay of ionization in the nighttime <i>E</i> region for three initial values of electron density (infinity, $1 \times 10^5$ , $1 \times 10^4 \text{ cm}^{-3}$ ) and three values of ionization rate (0, $3 \times 10^{-1}$ , $3 \times 10^{-3} \text{ cm}^{-3} \text{ s}^{-1}$ ) . . . . .	17



Figure		Page
2.6	Ionization rate computed from the electron-density profile of Nike Apache 14 520 assuming no transport . . . .	22
2.7	Compilation of electron-density profile measurements taken near midnight at Wallops Island, Virginia, under various geomagnetic conditions [Geller <i>et al.</i> , 1975] . . . .	23
2.8	A comprehensive series of electron-density profiles at Arecibo were made by Shen <i>et al.</i> [1976] on three consecutive nights Nike Apache 14.520 was launched during the night of 18-19 April, 1974 from Wallops Island . . . .	25
2.9	The ionization rates calculated from the intermediate layer electron-density profile show a strong correlation with Kp (0.94 correlation coefficient) The particle energy flux shows a similar variation with Kp . . . .	27
2.10	Simulations of the intermediate layer with the vertical ion drift given by $w = 20 \sin[\pi(150-z)/30] \text{ m s}^{-1}$ for altitude $z$ in km, with the recombination coefficient $1.9 \times 10^{-7} \text{ cm}^3 \text{ s}^{-1}$ , for production rates of (1) 0.4, (2) 4.0, (3) 40, (4) 400 and (5) 4000 $\text{cm}^{-3} \text{ s}^{-1}$ The thin line is the solution neglecting diffusion the thick line is the complete solution with a diffusion coefficient of $2 \times 10^8 \text{ cm}^2 \text{ s}^{-1}$ . . . .	31
2.11	Calculated intermediate layer for ionization rates deduced from Kp given by equation (2.12) . . . .	32
2.12	Sensitivity of the continuity equation (2.14) to vertical ion wind variations in amplitude . . . .	34
2.13	The hydrogen Lyman-alpha emission from the earth's geocorona as photographed from the moon during the Apollo 16 mission (upper	

## Figure

## Page

	figure) Subsequent analysis of these profiles has shown agreement with the geocorona models of <i>Meyer and Mange</i> [1973] (lower figure) [ <i>Carruthers et al.</i> , 1976] . . . . .	36
2 14	Profile 1 is the electron density calculated by <i>Strobel et al.</i> [1974] for a model of the nighttime ultraviolet radiation. The experimental measurements at Wallops Island made by Nike Apache 14.520 (Profile 2; $K_p = 5+$ ) and 14.439 (Profile 3; $K_p = 8$ ) show that the electron density can be more than an order of magnitude greater than the ultraviolet model predicts . . . . .	42
3 1	Sensitive energy range for various rocket-borne particle detection schemes. The energy comparison is made for electrons in the top half and for protons in the lower half . . . . .	44
3.2	Three types of solid-state particle detectors are represented showing their respective geometry and electric field strengths. For totally depleted detectors, the depletion region depth is equal to the detector length $L$ . . . . .	47
3.3	The upper figure shows the particle detector basic amplification system. The preamplifier uses double integration and double differentiation stages to minimize noise. The lower figure illustrates the total system operation. An energetic particle produces a small charge within the detector, whereupon it is amplified and pulse-height discriminated. Each pulse within the discriminator range triggers a digital 4-bit counter and is then converted into analog form for transmission by the telemetry system . . . . .	48

Figure		Page
3.4	The arrangement of the energetic electron spectrometer in the payload of a Nike Apache rocket. The upper deck contains the detector, preamplifier and high voltage supply complementing the lower deck counting electronics and low voltage power supplies. Both decks are interfaced through pin connectors to the main wiring channel shown on the extreme left . . .	50
3.5	The upper diagram shows the angular patterns of the energetic particle detector. The beamwidth of $60^\circ$ represents a collimator system and the beamwidth of $82^\circ$ represents the effect of scattering for $E > 50$ keV. The lower figure is a pulse-height analyzer spectrum for 20, 40, and 60 keV electrons .	51
3.6	The coordinate system used to describe the magnetometer signal in terms of the magnetic field, $\vec{B}_0$ and spin axis of the rocket . . . .	53
3.7	The variation of pitch angle normal to the detector with rocket azimuth for different angles, $\delta$ , between the magnetic field and rocket spin axis. Note that the detector passes through $90^\circ$ pitch angle twice each revolution .	55
3.8	A sketch of the magnetometer signal representing equation (3.6). The figure is adapted from <i>Cladis et al.</i> [1961] . . .	57
3.9	Three models are shown representing the particle flux $F(E, \alpha, d)$ along a field line making various approximations as described in the text .	59
3.10	Pitch as a ratio with gyroradius at the mirror point plotted against altitude above the mirror point .	63

Figure		Page
3.11	Looking down the magnetic field line at the detector as shown, it is found that only particles with gyrocenters inside of the shaded area are able to reach the detector sensitive area. An approximation to the complex geometry is shown in (b). For collimators the effective projected area is significantly reduced as shown in (c) and (d) . . . . .	65
3.12	The shadowing of the particle sensor by the rocket body may cause significant modulation and reduction in the measured particle flux. Illustrated is a charged particle with gyro-radius, $R$ , which would intersect the detector at the number 3 position if no collision with the rocket body occurred .	69
4.1	Nike Apache 14 439 count rate observed on a disturbed night at Wallops Island using a Geiger counter sensitive to electrons ( $> 70$ keV). Also shown is the magnetometer precession envelope . . . . .	73
4.2	Nike Apache 14.439 count rate versus altitude on a disturbed night at Wallops Island using a Geiger counter sensitive to electrons ( $> 70$ keV) . . . . .	75
4.3	Small-scale modulation of the electron-density profile by energetic electron burst. The arrows indicate peaks . . .	77
4.4	EES count rates versus time for Nike Apache 14.520. Both upgoing and downgoing count rates are shown for energy channels of 12, 25, 48, 36 and 80 keV . . . . .	79
4 5	EES counting rate versus altitude for Nike Apache 14 520 launched 18 April 1974. The three low energy channels are shown corresponding to threshold energies of 12, 25 and 36 keV.	

Figure		Page
	The data are averaged over one second . .	82
4 6	Least-squares fit to particle flux versus altitude for 25 keV energetic electrons recorded by the EES experiment on Nike Apache 14.520 . . . .	84
4 7	Azimuthal variations of the count rate observed on Nike Apache 14 520 for the 25 and 36 keV channels at an altitude of 150 km . . . .	85
4 8	Log-log second-order least-squares fit of count rate versus energy for 10-km intervals above 100 km The spectrum is approximately a power law . . . .	87
4 9	EES counting rate versus altitude for Nike Apache 14.521 launched 29 June 1974 The profiles shown correspond to threshold energies of >13, >16.5, >32, and >57 keV One-second average of data except for the highest energy channel which is a five-second average .	89
4 10	Log-log plot of count rate versus energy for 10-km intervals above 100 km for Nike Apache 14.521 The spectrum is approximately power law . .	90
4 11	Detector geometry and collimator used on rockets 14.524 and 14 525 Dimensions are given in inches . .	93
4 12	Count rate versus altitude at Chilca, Peru during geomagnetically quiet conditions . . . .	94
4 13	Count rate versus altitude profile at Chilca, Peru during geomagnetically disturbed conditions	95
4 14	Histogram of 160 counts as a function of rocket azimuth for >17 keV electrons (or >40 keV protons) This histogram includes	

Figure		Page
	all counts above an altitude of 180 km . . . . .	97
4.15	Electron flux measurements by satellites illustrate the rapid cutoff at $L = 2.0$ for the trapped and dumped flux. The dumped flux and auroral frequency decrease monotonically from the auroral region while at $L \approx 2.6$ there is an increase in the trapped flux . . . . .	100
4.16	Regions of high omnidirectional electron flux measured by <i>Seward</i> [1973] using a polar orbiting satellite (240-410 km altitude). These data clearly show two zones of midlatitude precipitation. Also shown on this map are $L$ shells at 100 km corresponding to these zones ( $L = 2.6$ and $L = 1.4$ ). Various rocket launch sites are indicated . . . . .	101
4 17	Midlatitude satellite observations ( $\approx 800$ km altitude) made by <i>Larsen et al.</i> [1976b] for $K_p = 1$ (16 December 1971) and $K_p = 3$ (19 December 1971). The locations of Wallops Island (WI) and White Sands (WS) are indicated. The cutoff at $L = 2.0$ and the maximum in the quasi-trapped flux (HEES detector) near Wallops Island are evident. For moderately disturbed conditions the particle flux increases with largest increases in the precipitated flux (REES detector) and in the slot region with particular increases in the trapped flux . . . . .	105
4.18	Particle data by <i>Cladis et al.</i> [1961] was obtained for electron with $E > 50$ keV from a Javelin sounding rocket launched from Wallops Island which covered $L$ shells between 2.5 and 1.9. Also illustrated are the iso-count rates indicated by these data The flux at a given altitude decreases with decreasing	

Figure		Page
	latitude . . . . .	109
4 19	This figure, adapted from <i>Seward</i> [1973], shows the omnidirectional flux of energetic electrons for $E > 100$ keV. Added to this figure are the B-L coordinates of Chilca, Natal, Arecibo and Volograd for altitudes of 150, 300, and 500 km. The Arecibo and Wallops Island precipitation zones are clearly evident . . . . .	112
4 20	Count rate profiles for quasi-trapped electrons observed by rockets launched in the Arecibo precipitation zone. Identification is given in Table 4.1 according to the launch date . . . . .	114
4.21	The particle flux at 150 km is shown versus magnetic activity index $K_p$ for different energies at Wallops Island. Before the plasmasphere crossing (cross hatched area) and for $E > 50$ keV the flux does not change much with $K_p$ . For lower energies the electron flux depends strongly on $K_p$ . Also shown is the ionization rate (from Figure 2.8) . . . . .	119
5 1	This figure illustrates the complex process involved with particle precipitation. In addition to direct observations many indirect techniques may be used to investigate the energy flux and aeronomc effects of charged particles. Energetic particles are ejected from the sun with kinetic energies of a few hundred electron volts and travel as a solar wind to the earth's magnetosphere. Many mechanisms are associated with transport, acceleration, and precipitation of these particles. A complex series of atmospheric reactions may occur such as emission of radiation, ionization composition changes, changes	

Figure		Page
	of temperature and generation of winds . . . . .	121
5.2	Various measurements of midlatitude 391.4 nm radiation are consistent with the concept of an Arecibo zone and a Wallops Island zone of particle precipitation. Identification of the measurements is given in the text . . . . .	123
5.3	Variation of the peak electron density of the intermediate layer with magnetic activity. These measurements were taken from the electron-density profiles of Figures 2.1 and 2.7. Times are EST . . . . .	128
6.1	Representation of the earth's dipole field interconnecting with the interplanetary magnetic field and being modified by the solar wind. Figures are from <i>Ratcliffe</i> [1972] . . . . .	132
6.2	Illustration of 500 Hz whistler-mode propagation and the resulting electron pitch-angle diffusion [ <i>Lyons et al.</i> , 1972]. Waves are thought to be generated near the plasma-pause as shown on the left-hand side. The right-hand side shows the resonant interactions that occur between the low frequency waves and the radiation belt electrons. Landau resonances occur near the mirror points with higher order resonances occurring towards higher latitudes . . . . .	139
6.3	The radial diffusion of trapped particles of lower $L$ values following the magnetic storm of 17 December 1971 is shown in satellite data analyzed by <i>Lyons and Williams</i> [1975b] . . . . .	141
6.4	A possible explanation for the Arecibo precipitation zone ( $L = 1.4$ ) is the marked increase of low frequency hiss at $L = 1.4$ as shown in these data from <i>Tsurutani et al.</i> [1975].	



Figure		Page
	The rapid cutoff of low frequency hiss at $L = 2$ and minimum at $L = 1.8$ are in keeping with the precipitation null at White Sands .	143
6.5	The longitudinal variation of the $B$ field at 100 km for $L = 2.5$ and $L = 1.4$ in the northern and southern hemispheres . At Wallops Island the mirror height is about 300 km lower in the southern hemisphere than in the northern hemisphere . The dashed arrows indicate the longitude of maximum precipitation . .	145
6.6	Longitudinal variation of precipitated electron flux deduced by <i>Torr et al.</i> [1975] . The relative magnitudes for the different $L$ shells are inconsistent with data from rockets and satellites	147
6.7	Scatter plots for trapped and precipitated particles are shown for $L = 2.2$ and $L = 2.6$ from <i>Armstrong</i> [1965] . Lines are drawn through the median points every 0.2 gauss	148
6.8	Satellite observations of the South Atlantic anomaly are consistent with the maximum precipitation in the Arecibo zone ( $L = 1.4$ ). Contours 1, 2, 3 and 4 are given by <i>Gunzburg et al.</i> [1962], <i>Vernov et al.</i> [1967], <i>Seward</i> [1973], and <i>Gledhill and Daves</i> [1976], respectively. The points A and B correspond to the dashed arrows of Figure 6.5	150
7.1	Shown is the effective pitch-angle distribution at 200 km (solid line) for a count-rate profile which increases linearly with altitude . The dashed line indicates the isotropic component of the flux	155

Figure		Page
7 2	Satellite data [Allan, 1974] on 26 May 1967 shows that at Wallops Island ( $L = 2.6$ ) the density at 150 km can change significantly during a magnetic storm. This density increase causes the count-rate intercept to move to a higher altitude . . . . .	159
7 3	The pitch-angle distribution at midlatitudes peaks near $90^\circ$ . Curve 1 is from Tuohy and Harnes [1973], curve 2 from Cladis et al. [1960] and curve 3 is a theoretical profile by Spjeldvik [1976]. Curve 4 from Figure 7.1 is the pitch-angle distribution deduced from the linear count-rate profile .	161
7 4	Calculations by Cladis et al. [1976] show how a quasi-trapped distribution of electrons is scattered for different wave-particle amplitudes. The ascending particles show the effect of energy loss and scattering . . . . .	163
7.5	During times of high magnetic activity the isotropic component of the flux is very variable and can increase substantially as shown in these satellite data from Imhof et al. [1976]. Nike Apache 14.439 was launched at nearly the same time that these distributions were observed . . . . .	165
7 6	Geometry used to convert a pitch-angle distribution from one altitude to another . . . . .	166
7.7	The pitch-angle distribution derived from equation (7 3) for different altitudes . . . . .	168
7.8	Computer simulation of the count-rate profiles for a quasi-trapped distribution of particles in the atmosphere with initial energy of 3 keV. The upper figure shows the downward flux, the	

Figure		Page
	lower left figure shows the upward flux and the lower right figure shows the combined upward and downward flux .	170
7 9	Same as Figure 7 8 but for an initial energy of 11 keV	171
7 10	The total composite count-rate profile for several energy spectrums (see Figure 9 9) The nearly linear increase of the count rate with altitude in this model is similar to the experimental observations discussed in Section 4 1	173
7 11	Rocket and satellite measurements of protons at the equator 1 is the rocket data from Nike Apache 14 525, 2 is from <i>Butenko et al</i> [1975], 3 is from <i>Moritz</i> [1973], and 4 is from <i>Mzera and Blake</i> [1973] . . . .	177
7.12	Satellite data [ <i>Imhof et al</i> , 1976] taken during the same night that Nike Apache 14.439 was launched (0503 UT)	179
7 13	Satellite data [ <i>Imhof et al.</i> , 1976] for different energies taken nearly simultaneously with the launch of Nike Apache 14 439 .	180
7 14	Various energy spectrums measured with satellite particle detectors [ <i>Imhof et al.</i> , 1976] during the night of the launch of Nike Apache 14 439 . . . .	182
7 15	Satellite data taken at nearly the same time as the launch of Nike Apache 14 520 [ <i>Reagan</i> , personal communication]	184
7 16	Global precipitation map based on rocket and satellite observations Shown are the auroral zones, the equatorial proton zone and the midlatitude zones at $L = 2.6$ and $L = 1.4$ The enhancement in the vicinity of the South Atlantic anomaly is also indicated .	185

Figure		Page
8.1	Plot of the correction factor, $q(\theta)$ , to be applied to the Rutherford formula to allow for screening by the electron cloud . . . . .	194
8.2	Comparison of differential scattering cross-section, given by equations (8.1), (8.5) and (8.8), for 10 and 50 keV electrons . . . . .	197
8.3	The energy loss rate for electrons in air computed by three methods corresponding to equations (8.21), (8.23), and (8.24) . . . . .	203
8.4	Block diagram of the experimental apparatus used to measure the scattering of electrons in air . . . . .	209
8.5	The beam transport section with the T mount and steering magnet is shown in the upper photograph and the vacuum chamber, rotating platform and solid-state detectors are shown in the lower photograph . . . . .	210
8.6	The angular spreading of the electron beam may be seen by looking through the side window of the test chamber at a phosphor plate. Chamber pressures are 0, 0.37, 0.7, 1, 2, and 5 mm of mercury for the increasing diameters in the photographs shown. The ellipsoidal shape is due to the off-axis viewing angle . . . . .	212
8.7	Experimental results for 30 keV electrons scattering in air at different pressures . . . . .	213
8.8	Experimental results for 50 keV electrons scattering in air at different pressures . . . . .	214

Figure		Page
8.9	Comparison between calculated and experimental spreading of an electron beam in air. The method commonly used for approximation can be seen to differ significantly from the experimental results . . .	215
8 10	The upper figure is the pulse-height distribution for 50 keV electrons at essentially zero chamber pressure. The lower figure shows the slight displacement ( $\approx 1$ keV) of the profile to the left when the pressure is increased to 6 torr. The full width at half maximum for the distribution is 5 keV.	217
8 11	Plot of equation (8.34) which illustrates that most of the collision of an energetic particle with the atmospheric constituents occurs near the mirroring altitude. The effect of scattering is not included . . .	219
8.12	The reduction of mirror altitude caused by a change in pitch angle at the mirror altitude. The reduction is least sensitive for small changes in pitch angle near the mirroring point . . . .	221
8.13	The change in pitch angle from $\alpha_1$ to $\alpha_2$ associated with a collision process having a scattering angle $\theta$ . $\vec{v}_1$ and $\vec{v}_2$ are the initial and final velocities.	222
8.14	The spreading in mirror-height distributions due to atmospheric collisions for 30 and 50 keV electrons which, in the absence of collisions, would mirror at altitudes of 120, 130 , . . . , 200 km . . . .	224
9 1	Comparison by <i>Wedde</i> [1970] of the Monte Carlo method and the empirical method of <i>Rees</i> [1963]. For the isotropic distribu-	

Figure		Page
	tions chosen these two methods are in good agreement. The Rees original and the Monte Carlo (1) are for an isotropic distribution between 0 and 80 deg pitch angle and the Rees corrected and Monte Carlo (2) are for an isotropic distribution between 0 and 90 deg pitch angle . . . . .	227
9.2	The upper figure shows the integral method for determining the average ionization rate from the net incident energy The lower figure gives a model pitch-angle distribution for the net flux calculations . . . . .	232
9.3	An approximate calculation of the variation of ionization rate with altitude for a mirroring distribution of particles. For this case $H = 20$ km, $z_0 = 120$ km and an exponential atmosphere is assumed . . . . .	236
9.4	The <i>CIRA</i> [1972] model used for ionization calculations. The assumed value of exospheric temperature is 1000 K . . . . .	238
9.5	Energy loss curves for electrons ( $E_0 = 1, 2, 5, 10$ , and 20 keV) in a uniform magnetic field (1 e , no mirroring) for initial pitch angles of 0, 60, and 80 deg . . . . .	239
9.6	Energy loss curves for energetic electrons mirroring at altitudes of 130, 140, 150, 160, and 170 km with initial energies of 5, 7, 10, 20, and 50 keV. Atmospheric scattering is not included in these results . . . . .	241
9 7	Ionization formed in each altitude increment of 1 km by 10 keV keV electrons with mirror heights at 10-km intervals Note that all the ionization occurs near the mirroring height. Electrons with a mirror height of 120 km are absorbed, all	

Figure		Page
	others escape . . . . .	244
9 8	Block diagram of the program used to compute the ionization rate and count rates as a function of altitude for a mirroring distribution of electrons with different energy spectrums .	246
9.9	Power law energy spectrums for $\alpha = 1, 2$ and 3 and an experimental spectrum used in the count rate and ionization calculations . . . . .	247
9.10	The figure on the left shows a series of profiles ( $1 < E < 10$ keV) of the ionization produced using equation (9 17) for the incident flux. The figure at the right is normalized so that a total of 1 keV of energy is deposited below 250 km for each energy . . . . .	249
9 11	The figure at the left shows a series of profiles which are normalized such that the energy absorbed is equal to the incident energy of the particles The figure on the right is the total ionization for the various spectrums of Figure 9 9 in the energy interval $1 < E < 10$ keV .	250
9 12	These figures are the same as Figure 9.10 but for the energy range $12 < E < 22$ keV, in intervals of 2 keV	251
9.13	These figures are the same as Figure 9 10 but for the energy range $30 < E < 100$ keV, in intervals of 10 keV	252
9 14	These figures show the total ionization rates for the energy intervals of $12 < E < 25$ keV and $25 < E < 100$ keV for the various spectrums shown in Figure 9 9 where $\alpha$ is the exponent of a power law spectrum and $E$ represents an experimental spectrum .	253

Figure		Page
9 15	Ionization rate calculations for an isotropic distribution of particles. The range of pitch angles is 0 to $89^\circ$ . The upper two figures are similar to Figure 9 10 and the lower two figures to Figure 9 11 except for the energy range $12 < E < 22$ keV . . . . .	254
9 16	The ionization rate profiles are shown for energetic electrons having energies between 1 and 100 keV, having a linearly increasing count-rate profile, and for the energy spectrums of Figure 9.9 . . . . .	
9.17	For a square-root mirror-height distribution of energetic electrons the energy absorbed versus the incident energy is compared in this figure for different initial energies. The energies are computed for 5000 electrons incident on the atmosphere . . . . .	264
9.18	The ionization rate computed for energetic electrons for $K_p = 1, 3, 5,$ and $8$ . Also shown are the UV ionization rate calculations of <i>Ogawa and Tohmatsu</i> [1967] (large dashed line) and <i>Strobel et al.</i> [1974] (small dashed lines). For $K_p \geq 3$ the ionization rate in the region 120 to 200 km at Wallops Island is predominantly due to energetic electrons. T and ET stand for terrestrial and extraterrestrial sources of UV . . . . .	267



## 1. INTRODUCTION

### 1.1 General Introduction

During the daytime the upper atmosphere is partially ionized by intense solar radiation producing an electron density of the order of  $10^5 \text{ cm}^{-3}$  at altitudes between 100 to 200 km (Profile 1 in Figure 1.1). The daytime electron-density profile at a given solar zenith angle remains nearly constant from day to day except for occasional sporadic-*E* layers ( $\approx 2$  km thick) which are found to exist in the altitude region 90 to 110 km (e.g., in Figure 1.1 a sporadic-*E* layer is seen at 100 km in profile 1 and at 106 km in profile 2).

After sunset the electron density decays rapidly to a nighttime density of the order of  $10^3 \text{ cm}^{-3}$  (Profile 2 in Figure 1.1). The nighttime electron densities show much temporal variability and complex altitude structure. Intense sporadic-*E* layers are occasionally observed at night.

Also evident on many of the nighttime electron-density profiles in the region 120 to 200 km is the presence of a broad layer of electron density between the *E* and *F* regions, known as the intermediate layer. This layer is usually many tens of kilometers in vertical extent and is observed to descend during the night. The existence of this layer provides a fortuitous opportunity to deduce the average ionization rate from the electron-density profile without detailed knowledge of the diffusion and transport mechanisms.

The explanation of the electron density being maintained at relatively high levels at night in the absence of direct solar radiation has been unresolved for many years. Various possibilities which have been suggested include, a slow nighttime recombination rate, transport processes, extraterrestrial radiation, geocoronal radiation (i.e., scattered solar radiation) and energetic particles precipitated from the radiation belts.

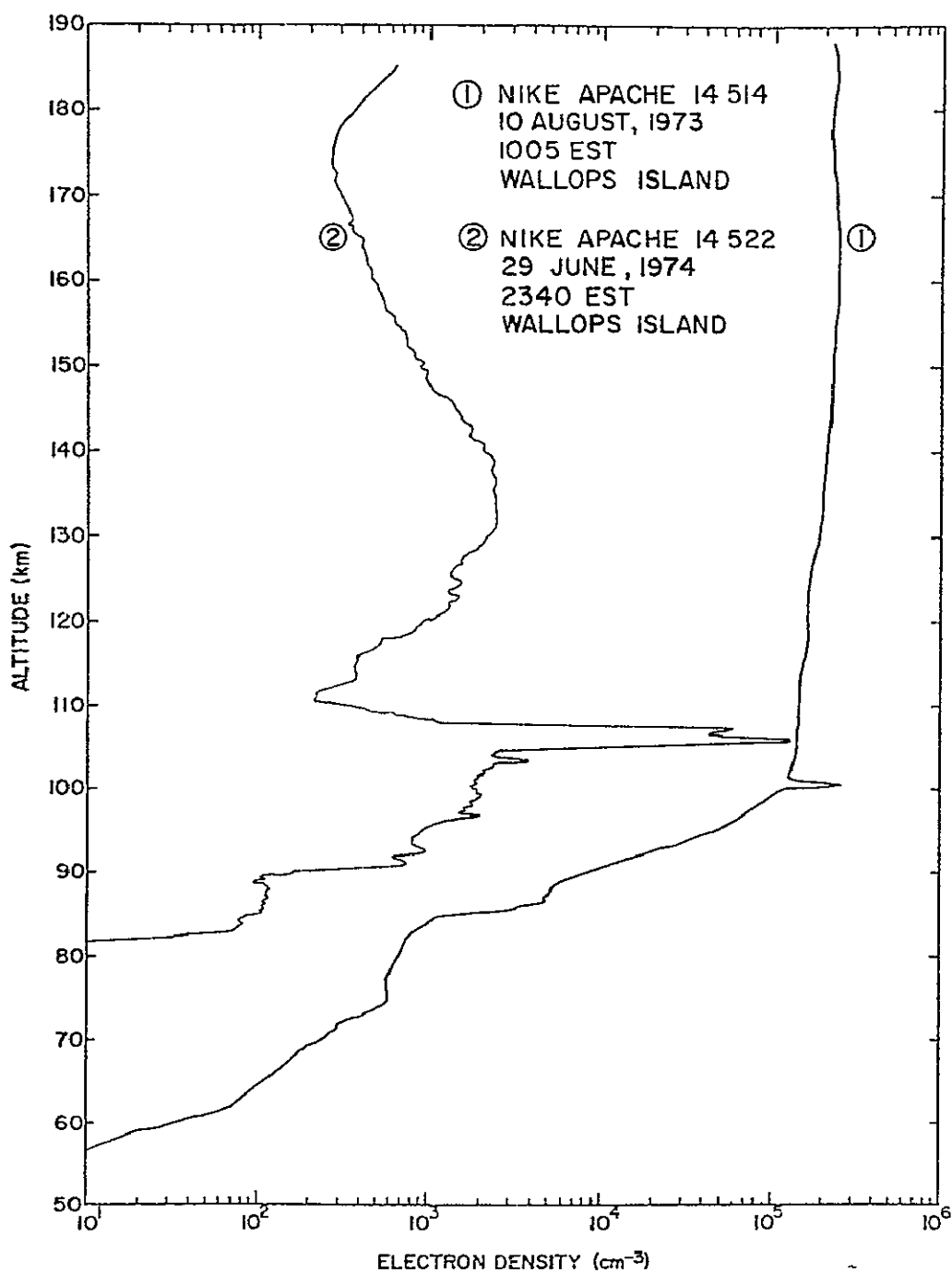


Figure 1 1 Profile 1 is representative of the daytime electron density ( $10^5 \text{ cm}^{-3}$ ). Towards night this electron density rapidly decays to a lower nighttime equilibrium level of about  $10^3 \text{ cm}^{-3}$  (Profile 2). The nighttime density profile shows much variability and structure.

The precipitation of energetic particles at middle and low latitudes has only recently been investigated. The characteristics of particle precipitation and ionization at midlatitudes is considerably different from that in the auroral region. Techniques used previously to calculate particle ionization rates in the auroral region are not applicable at lower latitudes. At midlatitudes the majority of particles are quasi-trapped (pitch angles near  $90^\circ$ ), this is not the case in the auroral zone.

Particle ionization at middle and low latitudes is a localized effect and will be shown to maximize in specific zones. A particle precipitation model is developed which includes the effects of geographic location, altitude variations, and magnetic activity. The influence of atmospheric scattering and energy loss processes are studied to yield energetic particle ionization rates.

A comparison between the various ionization sources is made to determine the significance of each for different temporal, spatial and magnetic conditions. It is shown that energetic electrons can be the primary source of ionization in the region 120 to 200 km in specific midlatitude precipitation zones.

## 1.2 *Objectives of this Study*

The main objectives of this investigation are to determine the relative importance of various nighttime ionization sources and in particular to investigate the ionization by energetic particles at middle and low latitudes.

Chapter 2 begins with a study of the characteristics of the nighttime electron density and a review of possible mechanisms which can sustain these densities. The analysis then shows that an ionization source is required and that the intensity of this source in various midlatitude

locations can vary by a factor of 100 with magnetic activity. The formation of the intermediate layer by the action of tidal winds is discussed and related calculations are used to deduce the ionization rates and ion vertical drift velocities. Finally, a critical review is given of nighttime ultraviolet radiation sources. These are shown to be the principal ionization sources in various geographic locations and altitude regions.

The previous methods of obtaining an incident flux from a detector count-rate profile using the concept of a geometrical factor are shown to lead to serious errors for a quasi-trapped distribution of particles.

In Chapter 3 a method is described for converting the count-rate profile to an incident flux for a quasi-trapped distribution of particles. Also discussed is an energetic electron spectrometer which was built to measure the particle flux, spectrum, and relative directional properties.

The experiment has been successfully operated on seven sounding rockets launched at Wallops Island, Virginia, and Chilca, Peru. The measurements are reported in Chapter 4. The count rates are observed to increase rapidly in intensity above 120 km altitude in a linear fashion. The increasing count rates at midlatitudes are interpreted to be the effect of quasi-trapped electrons in the radiation belts which are scattering and mirroring in the region above 120 km. The equatorial observations are interpreted as due to protons. An analysis and comparison of other rocket and satellite measurements is made to establish the spatial and temporal characteristics of energetic particle precipitation on a global scale.

In Chapter 5 a number of indirect techniques are used to further define the morphological characteristics of particle precipitation in certain mid-latitude regions (e.g., 391.4 nm emission, X-rays, Kp dependence, etc.).

In Chapter 6 a general discussion is given of the global characteristics

of particle precipitation in terms of a large-scale model of the magnetosphere. The primary questions addressed in this chapter are the source mechanism of midlatitude particles (injection and radial diffusion), the explanation for mirror height lowering and pitch-angle scattering, the existence of two midlatitude precipitation zones and the cause of the longitudinal variation and localized maximums of precipitation in the region of the South Atlantic anomaly.

Based on the experimental and theoretical analysis of the previous chapters a unified model of particle precipitation is developed in Chapter 7. A computer program is used to simulate the effects of mirroring and energy loss of a quasi-trapped distribution of particles. Additionally, the first rocket measurements of the equatorial proton belt are discussed and analyzed. A world map of precipitation patterns is developed.

Chapter 8 concerns the loss of energy and scattering of charged particles in the earth's atmosphere. It is shown here that various theoretical and semi-empirical methods which have been used in the past for calculating cross sections, energy loss, and multiple scattering are inconsistent with each other. Because of the difficulties an experimental apparatus was developed using an electron accelerator to measure scattering typical of atmospheric conditions, for use in subsequent calculations.

In Chapter 9 various methods are used to calculate the ionization rate of energetic particles for a quasi-trapped distribution of electrons. A method based on energy considerations is used to calculate an average ionization rate and these rates are found to be consistent with more elaborate calculations and with the ionization rates independently derived from the electron-density profile.

The principal conclusion of this study is that ionization by energetic

electrons in certain midlatitude precipitation zones and in the altitude region 120-200 km is more important than ionization by ultraviolet radiation even during periods of rather low magnetic activity. The identification and characteristics of the midlatitude precipitation zones and the equatorial proton zone are established.

## 2 IONIZATION SOURCES IN THE NIGHTTIME *E* REGION

This chapter will review the salient characteristics of the electron-density profile in the region 120 to 200 km and the associated mechanisms required for maintaining the nighttime *E*-region ionization and structure. For such analysis proper consideration must be given to transport, production, recombination and diffusion. First, representative electron-density profiles will be discussed to illustrate the variation with respect to time, altitude and magnetic activity. It will then be shown that the region between 120 to 200 km requires a nighttime ionization source. Next, the dynamics and average ionization rates observed in the region 120 to 200 km will be investigated. Finally, an evaluation will be made of the nighttime ionization produced by ultraviolet radiation from the geocorona and also of extraterrestrial origin. These ionization measurements will be compared to the average ionization rates calculated from the intermediate layer.

### 2.1 *Electron Density in the Nighttime Midlatitude Ionosphere*

Rocket-borne Langmuir probes have been used to obtain a number of high resolution nighttime electron-density profiles. Three profiles are shown in Figure 2.1 for data taken at Wallops Island near midnight. Profiles labeled 1, 2 and 3 are for  $K_p$  values of 3+, 5+ and 8, respectively. The intermediate layer extends from 120 to 180 km and is most clearly evident on the night of lowest  $K_p$ . The intermediate layer becomes less pronounced at the higher  $K_p$  and essentially disappears at the highest value of  $K_p$ .

At high values of  $K_p$  the electron-density profile develops many small-scale irregularities. No complete explanation exists for this behavior, however, the very sporadic and intense particle precipitation observed on this night (Section 4.2.1) can possibly produce fluctuating ionization (columns) as the rocket proceeds horizontally and vertically in its trajectory. The

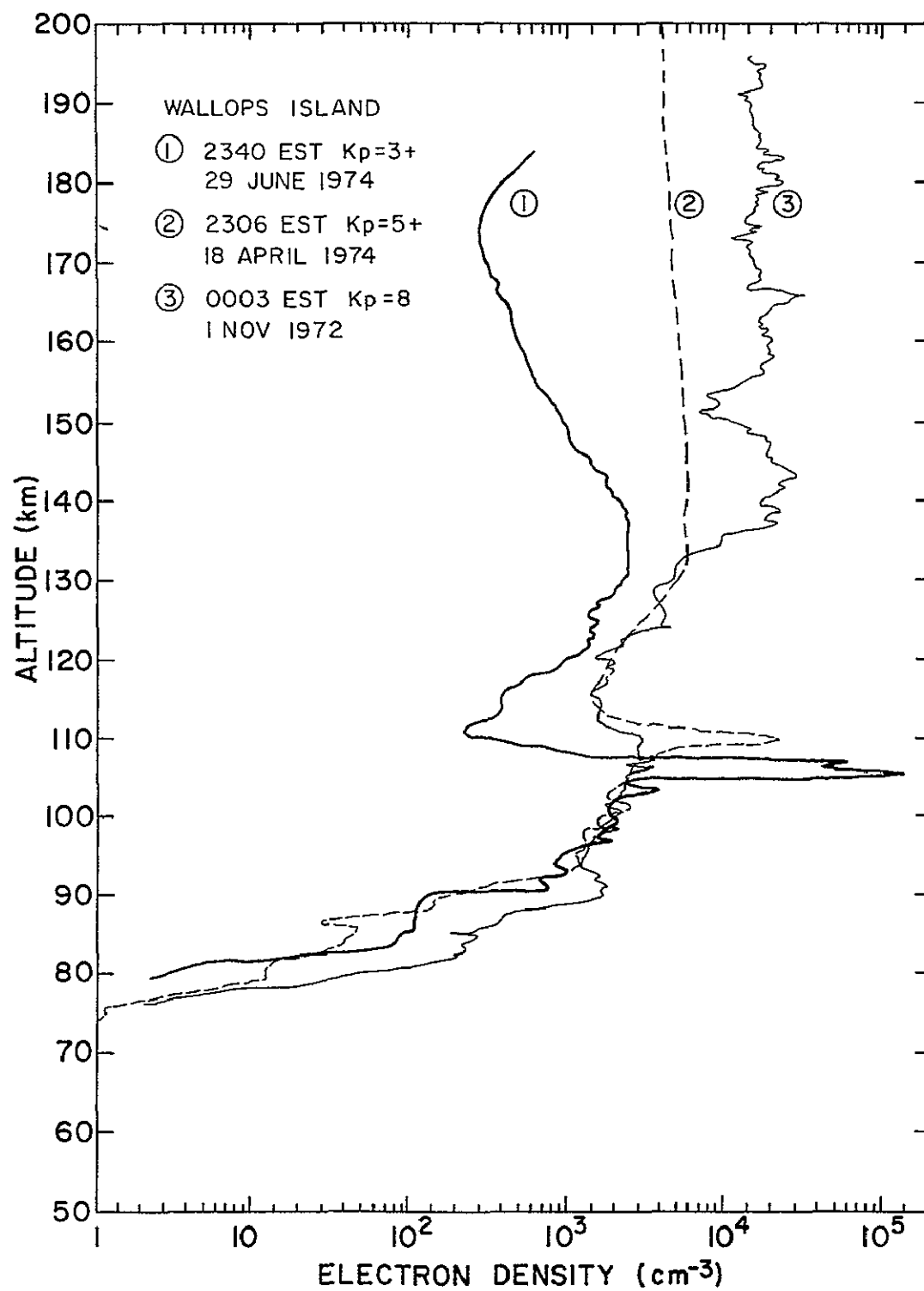


Figure 2 1 Three electron-density profiles representative of Kp values of 3+ (Profile 1), 5+ (Profile 2) and 8 (Profile 3)



irregular structure is also observed in the auroral region. Very smooth profiles of electron density and particle precipitation are always observed on lower Kp nights.

Nearly constant average electron density ( $10^3 \text{ cm}^{-3}$ ) is evident in the lower E region (90-105 km). Profiles 1 and 2 contain sporadic-E layers at 106 and 110 km, respectively. The D-region electron density is enhanced during the Kp = 8 night.

The temporal behavior of the electron-density profile during the night for Kp = 3+ is shown in Figure 2.2 [Smith, 1970] for five electron-density profiles obtained with a rocket-borne Langmuir probe and propagation instrument. The objective of this experiment was to follow the development of the ionospheric layers from midnight to sunrise.

The layer is observed to descend through the night at about 7 km per hour and progressively becomes more peaked with time after 0130 EST. The intermediate layer is now known to be the result of electron redistribution by the tidal winds of the (2,4) mode of the solar semidiurnal tide.

Figure 2.3 illustrates the dynamic nature of the nighttime upper E region before midnight as seen in data of Nike Apaches 14.521 and 14.522 launched at Wallops Island during the ALADDIN Project. In a period of 140 minutes the electron-density profile changed from a valley at 135 km to an intermediate layer maximum. Similar observations have been reported by Wakar [1967] at Boulder, Colorado and Shen *et al.* [1976] at Arecibo. The time of observation is critical when comparing nighttime electron-density profiles such that the dynamic transport forces are similar.

The intermediate layer is discussed by Fujitaka [1974], Fujitaka and Tohmatsu [1973] and Geller *et al.* [1975]. The valley seen in profile 1 of Figure 2.3 is caused by a divergent wind system which is gradually overcome

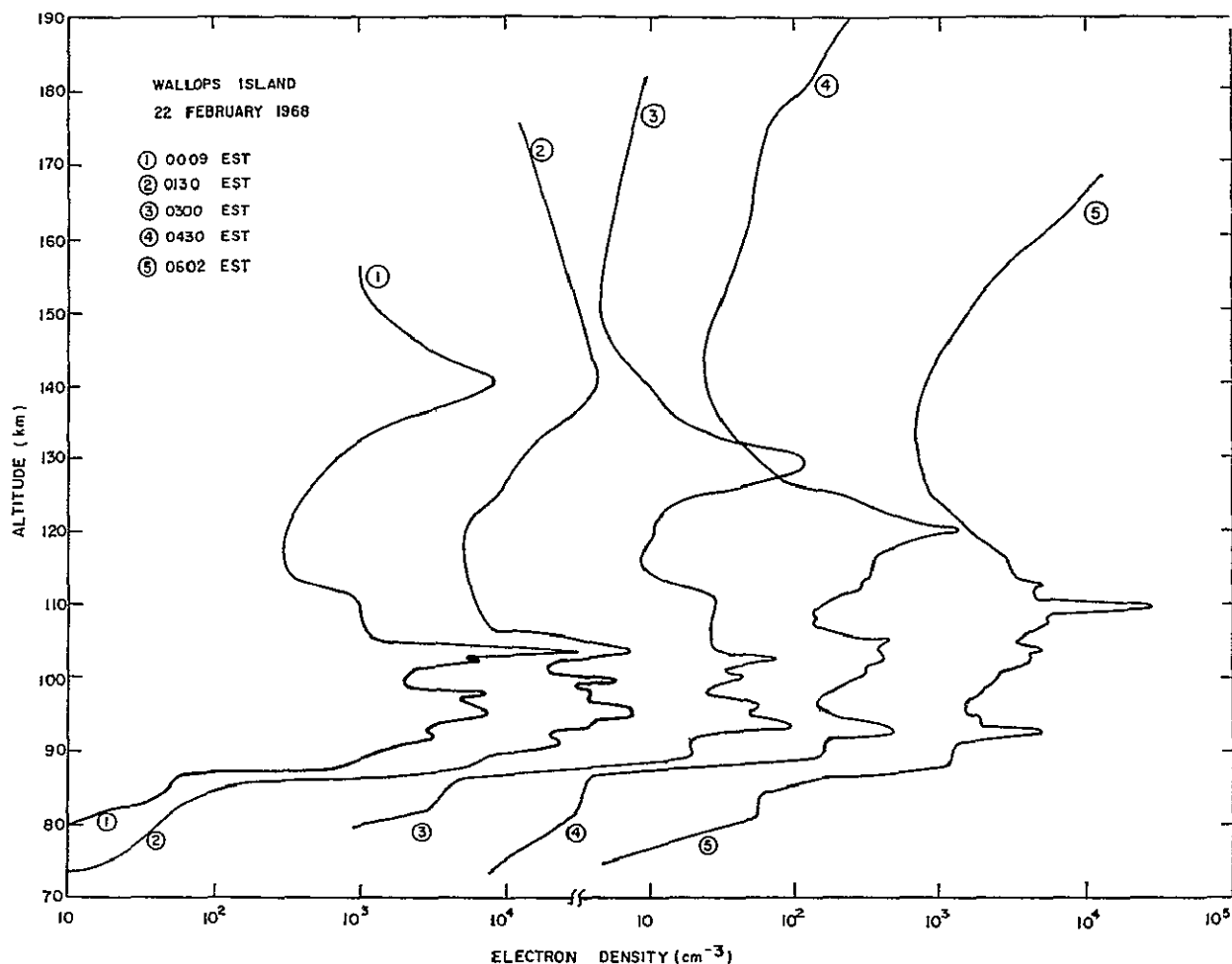


Figure 2.2 Electron-density profiles from the probes on rockets launched from Wallops Island on 22 February 1968 [Smith, 1970]. The profiles are each displaced by one decade. The electron-density scales for the first and last profiles are given. The part of the profiles below 90 km should be regarded as indicating the structure, rather than as absolute values.

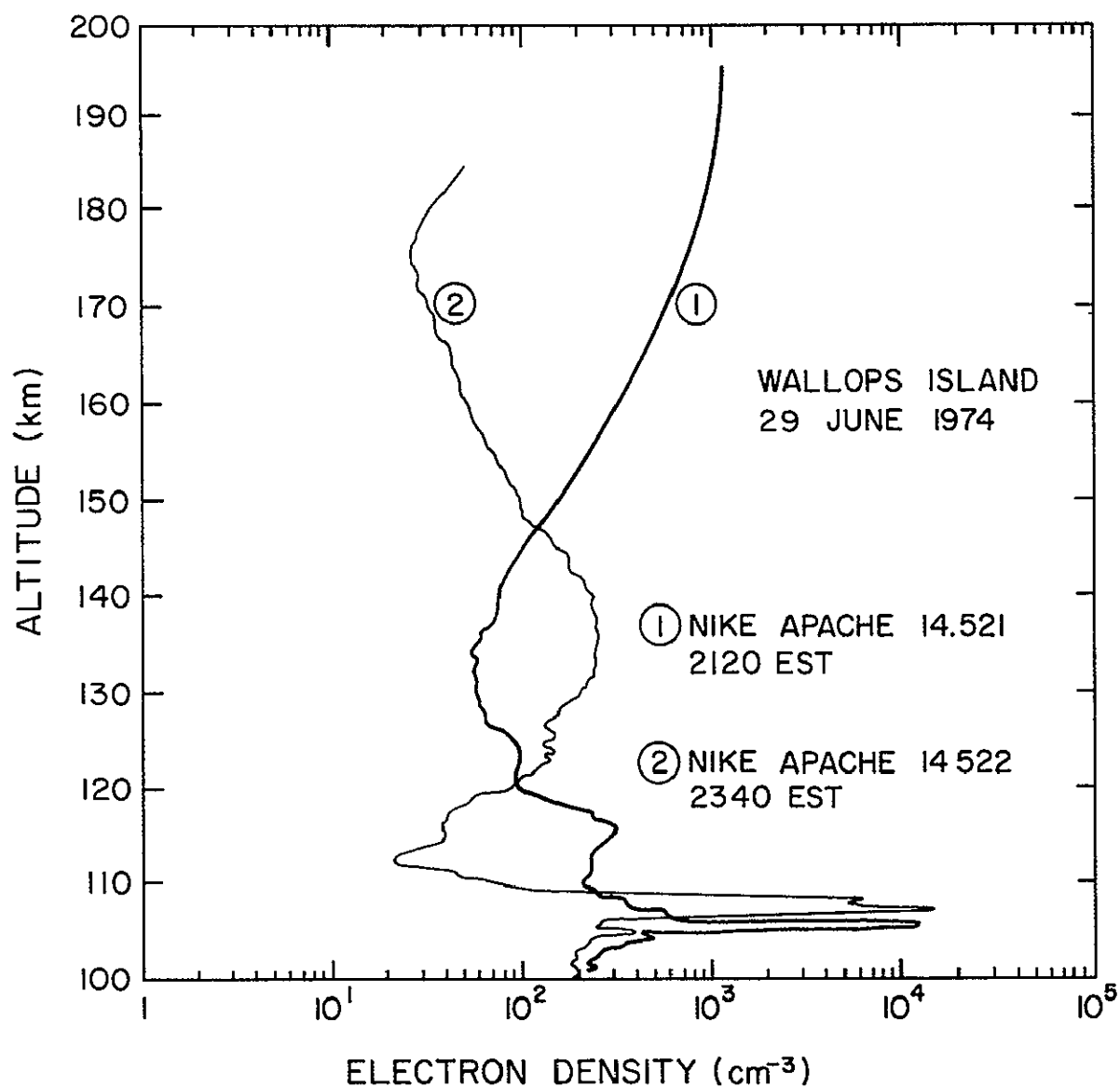


Figure 2 3 The nighttime electron-density profile in the *E* region shows much variability before midnight due to the tidal wind system as shown by these two sounding rocket measurements. The profiles are separated in time by 140 min.

by a convergent wind system which builds up ionization and produces the intermediate layer. This descending divergent (2200 hr) and convergent (0100 hr) wind system is associated with the descending solar semidiurnal tidal wind of the (2,4) mode.

A further relevant characteristic of the nighttime electron-density profile (120 to 200 km) is the strong correlation of magnetic activity with the density maximum. This is seen in data from rocket launches (Section 5.4). *Wakar* [1967] has found a similar dependence on magnetic activity at Boulder, Colorado using an ionosonde to measure the critical frequency of the intermediate layer. He has also studied the latitude variation of the critical frequency at 24 stations and has found that the critical frequency drops abruptly (4.5 to 2 MHz) at 50° geomagnetic latitude with highest critical frequencies in the auroral region.

## 2.2 Evidence for an Ionization Source

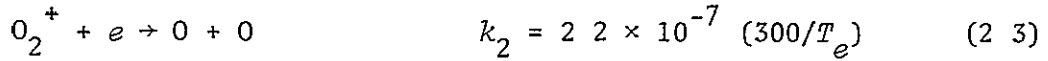
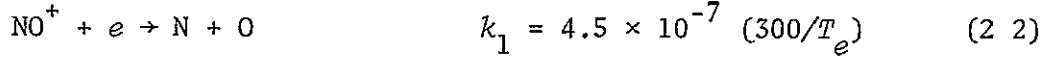
Various attempts have been made to explain the nighttime E-region ionosphere in terms of chemical and transport processes. In these explanations the nighttime electron density is simply a decaying remnant of the daytime ionosphere. The critical evaluation of these models and others are the subject of this section.

**2.2.1 Recombination** In order to model the influence of production, loss, transport and diffusion in the nighttime ionosphere in the altitude range 120 to 200 km it is necessary to use a continuity equation. The basic continuity equation assuming horizontal stratification is

$$\frac{dn_e}{dt} = q - L - \frac{dn_e w}{dz} + \frac{d}{dz} \left( D \frac{dn_e}{dz} \right) \quad (2.1)$$

where  $dn_e/dt$  is the time rate of change of electron density,  $q$  is the ionization production rate,  $L$  is the loss rate,  $w$  is the vertical ion drift velocity and  $D$  is the diffusion coefficient.

The loss rate of electrons at night in the region 120 to 200 km is governed primarily by dissociative recombination of  $\text{NO}^+$  and  $\text{O}_2^+$ . From data by *Brondi* [1969] the reaction rates are



In the absence of production, transport and diffusion, but including these two loss processes the continuity equation can be written

$$-\frac{dn_e}{dt} = k_1 [\text{NO}^+] n_e + k_2 [\text{O}_2^+] n_e = n_e^2 \left[ k_1 \frac{[\text{NO}^+]}{n_e} + k_2 \frac{[\text{O}_2^+]}{n_e} \right] = \alpha_{\text{eff}} n_e^2 \quad (2.4)$$

where  $n_e$  is the electron density and  $\alpha_{\text{eff}}$  is the effective recombination coefficient. The recombination coefficient is defined in this manner because the ratio  $[\text{NO}^+]/n_e$  and  $[\text{O}_2^+]/n_e$  changes slowly with altitude. The effective recombination coefficient is therefore given as

$$\alpha_{\text{eff}} = \sum_{i=1}^m \frac{[M_i]}{n_e} k_i = \frac{1}{n_e} \left[ k_1 [\text{NO}^+] + k_2 [\text{O}_2^+] \right] \quad (2.5)$$

where  $n_e = [\text{NO}^+] + [\text{O}_2^+]$  from charge neutrality,  $m$  is the number of ion species,  $M_i$ , involved in dissociative recombination and  $k_i$  is the  $i$ th reaction rate constant. At night in this region the concentration of  $\text{NO}^+$  is an order of magnitude greater than  $\text{O}_2^+$  [*Goldberg et al.*, 1974].

*Smith et al.* [1974] have deduced an effective recombination coefficient as a function of altitude and magnetic index,  $K_p$ . Using electron temperature data from *Evans* [1973] at an altitude of 200 km a least squares fit was made with respect to magnetic index giving

$$T_e = 112K_p + 588 \quad (2.6)$$

with a correlation coefficient of 0.90. These data were taken during the nighttime (2100-0300 EST) at Millstone Hill on eight occasions in 1966 and 1967 with a range of Kp values from 1 to 5. Following Evans the electron temperature at 120 km is assumed to be 355°K. A linear interpolation for altitude between 120 and 200 km gives

$$T_e(z) = (z - 120)(1.4 Kp + 2.9) + 355 \quad (2.7)$$

The effective recombination coefficient may now be easily obtained by substitution of the electron temperature variation into the experimental data for the dissociative recombination of  $\text{NO}^+$  given by *Biondi* [1969], equation (2.2). Table 2.1 gives the calculated values of  $T_e$  and  $\alpha_{\text{NO}^+}$  for Kp value of 0 and 8 and at altitudes of 120, 150, and 180 km. Recombination rate altitude profiles are shown in Figure 2.4 by *Cladis et al.* [1973] and *Smith et al.* [1974].

The competing effect of recombination loss and sources of ionization is illustrated in Figure 2.5 for several initial values of electron density and several ionization rates.

These are solutions of the equation

$$\frac{dn_e}{dt} = q - \alpha n_e^2$$

which, for  $q = 0$ , is

$$n_e = (\alpha t + n_{e0}^{-1})^{-1}$$

and for finite values of  $q$ , is

$$n_e = (q/\alpha)^{1/2} \left[ \frac{(q/\alpha)^{1/2} \{\exp[2(\alpha q)^{1/2} t] - 1\} + n_o \{\exp[2(\alpha q)^{1/2} t] + 1\}}{(q/\alpha)^{1/2} \{\exp[2(\alpha q)^{1/2} t] + 1\} + n_o \{\exp[2(\alpha q)^{1/2} t] - 1\}} \right] \quad (2.8)$$

In these equations,  $n_e$  is the electron density,  $n_{e0}$  is the initial value of

Table 2.1  
Recombination Rate Calculations

Altitude (km)	Magnetic index (Kp)	T <sub>e</sub> (°K)	$\alpha_{\text{eff}}(\text{cm}^3 \text{ sec}^{-1})$
120	0	355	$3.8 \times 10^{-7}$
	8	355	$3.8 \times 10^{-7}$
150	0	442	$3.05 \times 10^{-7}$
	8	778	$1.73 \times 10^{-7}$
180	0	530	$2.55 \times 10^{-7}$
	8	1201	$1.12 \times 10^{-7}$

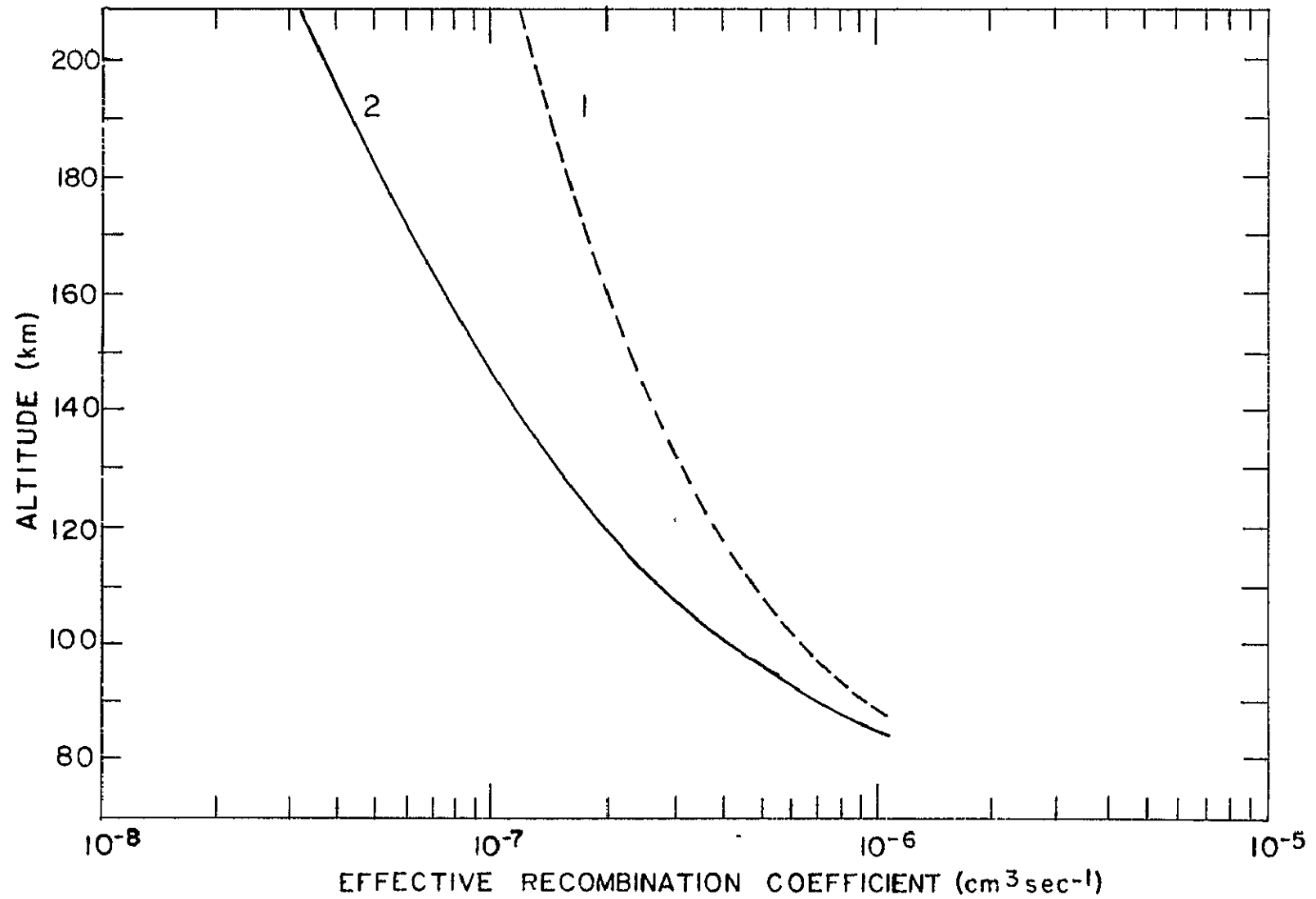


Figure 2 4 Effective recombination coefficients deduced by *Smith et al.* [1974] for  $K_p = 3$  (Profile 1), and *Cladis et al* [1973] (Profile 2)



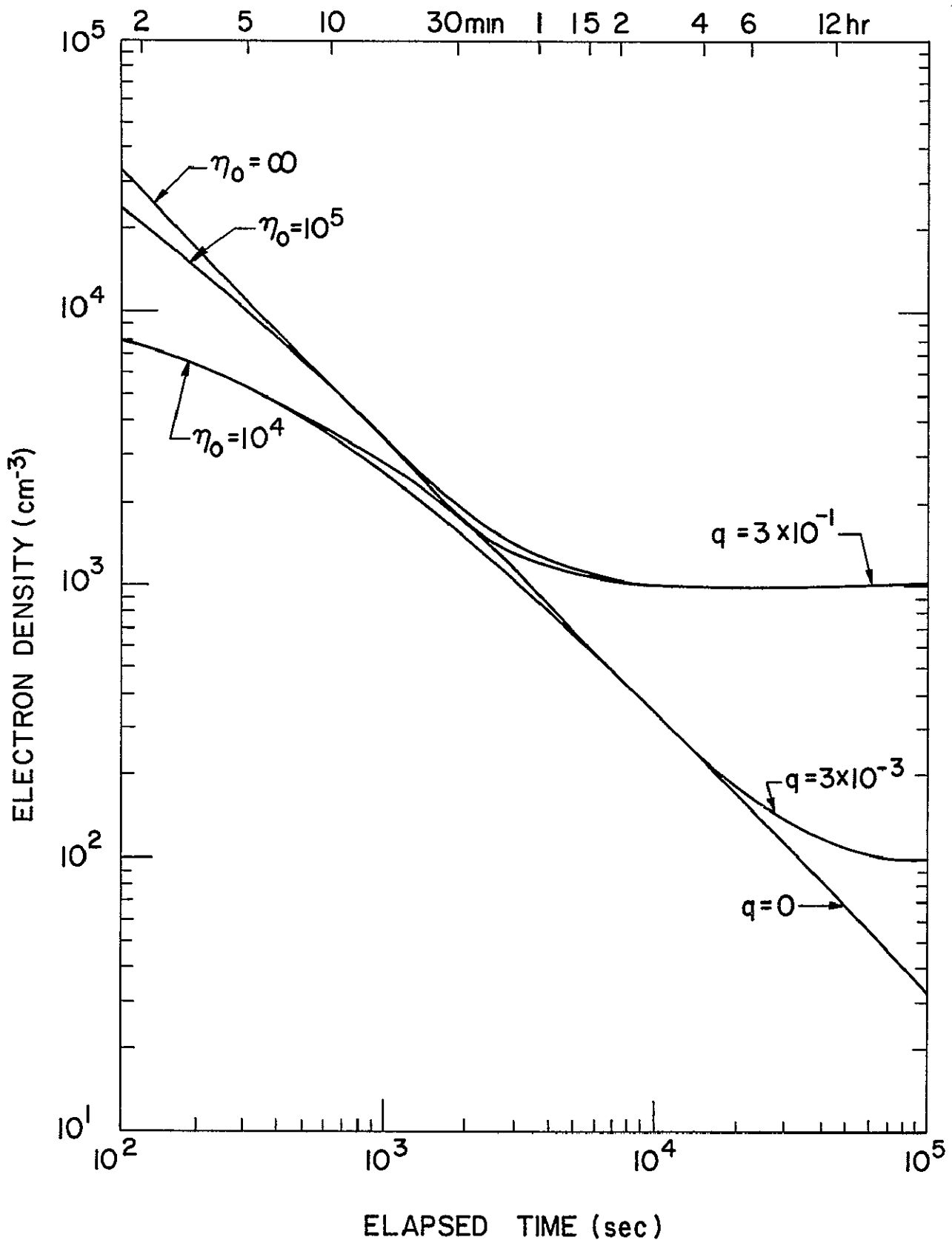


Figure 2 5 Decay of ionization in the nighttime  $E$  region for three initial values of electron density (infinity,  $1 \times 10^5$ ,  $1 \times 10^4 \text{ cm}^{-3}$ ) and three values of ionization rate ( $0$ ,  $3 \times 10^{-1}$ ,  $3 \times 10^{-3} \text{ cm}^{-3} \text{ sec}^{-1}$ )

electron density,  $t$  is elapsed time,  $q$  the ionization rate and  $\alpha$  the recombination rate. As the elapsed time increases the electron density asymptotically approaches the value  $(q/\alpha)^{1/2}$ . The recombination coefficient is taken to be  $3 \times 10^{-7} \text{ cm}^3 \text{ sec}^{-1}$ . The initial values of electron density are  $1 \times 10^4$ ,  $1 \times 10^5 \text{ cm}^{-3}$  and infinity. One hour later, in the absence of any large source of ionization, the electron density has decayed to  $900 \text{ cm}^{-3}$ , irrespective of the initial value, but determined by the value of this recombination coefficient. The curves are drawn for values of the ionization rate of 0,  $3 \times 10^{-3}$  and  $3 \times 10^{-1} \text{ cm}^3 \text{ sec}^{-1}$ . At four hours elapsed time an ionization rate greater than  $3 \times 10^{-3} \text{ cm}^3 \text{ sec}^{-1}$  produces significant deviation from the line representing  $q = 0$ . Thus, in the absence of transport, a source of ionization is required to explain the nighttime electron-density profile. This conclusion was pointed out by *Ferguson et al.* [1965] and *Donahue* [1966].

Furthermore, if smaller recombination rates are assumed ( $\alpha_{\text{eff}} < 10^{-8} \text{ cm}^3 \text{ s}^{-1}$ ) there would be an inconsistency with too high electron density during the daytime. *Holmes et al.* [1965] has assumed that the rate constants of equations (2.2) and (2.3) are increasing functions of electron temperature and thus the lower temperatures of the nighttime ionosphere would give slower recombination rates. However, *Biondi* [1969] shows that the opposite is true and the rate constant is a decreasing function of electron temperature (equations 2.2 and 2.3).

Another explanation of the nighttime electron density is that the recombination coefficient is much smaller than  $10^{-7} \text{ cm}^3 \text{ s}^{-1}$  due to the presence of metallic ions such as  $\text{Fe}^+$ ,  $\text{Si}^+$ ,  $\text{Ca}^+$ ,  $\text{Mg}^+$  and  $\text{Na}^+$  from meteors. The coefficient is believed to be no greater than  $10^{-12} \text{ cm}^3 \text{ s}^{-1}$ . *Narcisi and Bailey* [1965] and *Young et al.* [1967] have shown that below 120 km long-lived metallic ions are present and must be properly incorporated

into the recombination term. At altitudes above 120 km the observational evidence that metal ions, when present, have very small concentrations. *Miller and Smith* [1976] have discussed the importance of metal ions in sporadic-*E* layers.

In summary, the examination of the effective recombination coefficient shows that it is too large (i.e.,  $\sim 10^{-7} \text{ cm}^3 \text{ s}^{-1}$ ) to explain the existence of the observed nighttime electron density in the absence of a source of ionization. Before the production term is considered in Section 2.3, it must be further established that the *E*-region ionization is not simply a transport of *F*-region ionization to lower altitudes.

**2.2.2 Transport.** The vertical ion drifts between 90 and 135 km are of the order of a few tens of meters per second while *F*-region drifts are rarely above  $80 \text{ m s}^{-1}$  [*Behnke*, 1970, *Behnke and Harper*, 1973, *Harper et al.*, 1975, *Salah et al.*, 1975, *Shen et al.*, 1976]. *Shen et al.* [1976] conclude that, to maintain the nighttime upper *E* region by transport alone, the downward flux would require ion drift velocities on the order of  $200 \text{ m s}^{-1}$  which are much higher than the daytime and nighttime measurements. It is further concluded by *Shen et al.* [1976] that vertical transport could supply no more than 10-20% of the required ionization. *Geller et al.* [1975] have shown that for the special case of the intermediate layer the vertical transport is indeed small due to the low density in the valley region above and below the layer. Detailed analysis of the intermediate layer is given in Section 2.3.

In addition to the evidence of a rapid decay rate and positive electron-density variation with Kp the presence of  $\text{N}_2^+$  at night requires a nighttime ionization source [Donahue, 1966]. *Ferguson et al.* [1965], *Nicolet* [1965] and *Donahue* [1966] point out that a source of  $\text{O}_2^+$  must also be present at

night since  $O_2^+$  undergoes rapid charge exchange with N and NO to give additional  $NO^+$

These considerations imply the need for an ionization source and are well supported by the observations of nighttime UV from the geocorona and extraterrestrial origin plus evidence of ionization by energetic particles. The next section will be concerned with the determination of the magnitude of this source and the variation of the source with altitude and magnetic activity followed by an analysis of the ultraviolet and corpuscular ionization source. As will be shown, the UV radiation is the most significant ionization source at  $E$ -region altitudes of 95 to 110 km but may be enhanced at times by precipitating fluxes of energetic electrons. This upper  $E$ -region corpuscular source is operative in distinct midlatitude zones approximating  $L$ -shell values greater than 2.2 and to a lesser extent a precipitation zone at  $L = 1.4$  (Section 7.6). The energetic particle source will be investigated in Chapter 6.

### 2.3 Ionization Rates for the Nighttime $E$ Region

Ionization rates may be deduced from the electron-density profile by use of the continuity equation, using appropriate recombination and transport models. These ionization rates may then be compared with various ultraviolet and energetic particle ionization models to ascertain their relative importance. First, a case with no transport will be studied. This is a good approximation for high ionization conditions. A more complete model will then be developed invoking transport to determine an average ionization rate for the upper  $E$  region.

#### 2.3.1 Ionization rates calculated from the continuity equation for the steady-state no-transport case

For conditions of high ionization (i.e., high electron density) the effects of transport are minimized due to the rapid

recombination rate. A basic understanding of the ionization profile may simply be obtained from the continuity equation for the steady-state case as

$$q(z) = L(z) = \alpha_{\text{eff}}(z) n_e(z)^2 \quad (2.9)$$

where  $\alpha_{\text{eff}}$  is the effective recombination coefficient of *Smith et al.* [1974], shown in Figure 2.4, and  $n_e(z)$  is an experimentally-observed electron-density profile. Profile 2 of Figure 2.1 is used in this analysis to compute the ionization rate shown in Figure 2.6. A conclusion inferred from this and other ionization rate profiles is that the ionization source varies slowly with altitude in the region 120-200 km. It will be shown in Section 9.4 that this is consistent with a corpuscular source.

2.3.2 *Ionization rates calculated from the intermediate layer.* The intermediate layer is observed near midnight in the altitude region 120-180 km and provides a fortuitous opportunity to deduce an average ionization rate from the electron-density profile which is independent of detailed knowledge of the diffusion and transport mechanisms. A study of the relevant mechanics of the intermediate layer will be given first followed by a discussion and analysis of the calculated ionization rates.

Examples of the intermediate layer which have been used in this analysis are shown in Figures 2.1 and 2.7. For values of Kp less than 4 at Wallops Island the intermediate layer is a typical feature of the nighttime upper E region and is formed as a result of the action of the neutral winds [Smith et al., 1974]. For Kp values greater than five the intense ionization rate dominates over the weaker redistribution force resulting in a more uniform electron-density profile. The primary reason for this is the decrease in lifetime of the ions as the electron density increases.

*Shen et al.* [1976] have obtained a number of informative electron-

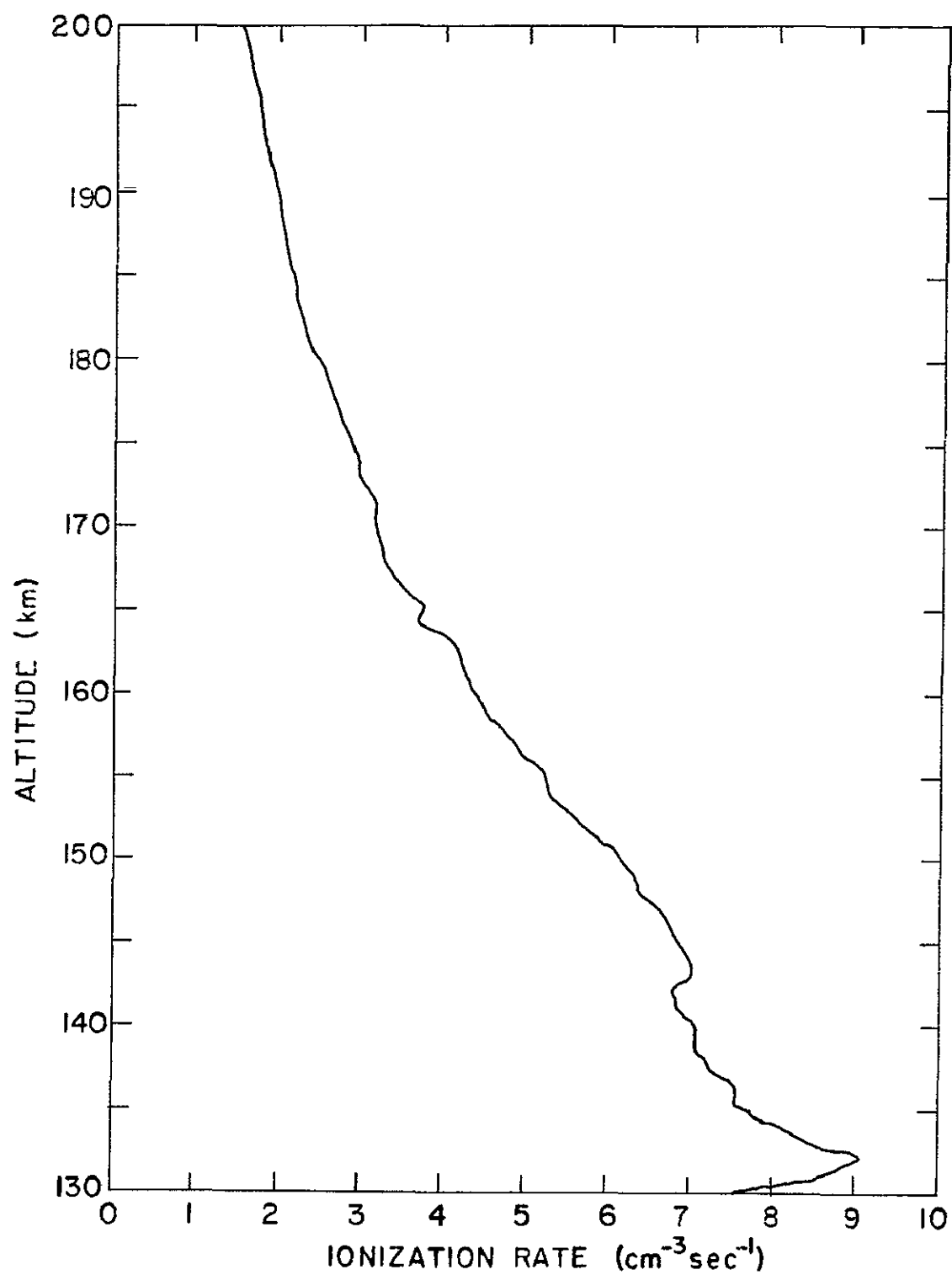


Figure 2 6 Ionization rate computed from the electron-density profile of Nike Apache 14 520 assuming no transport

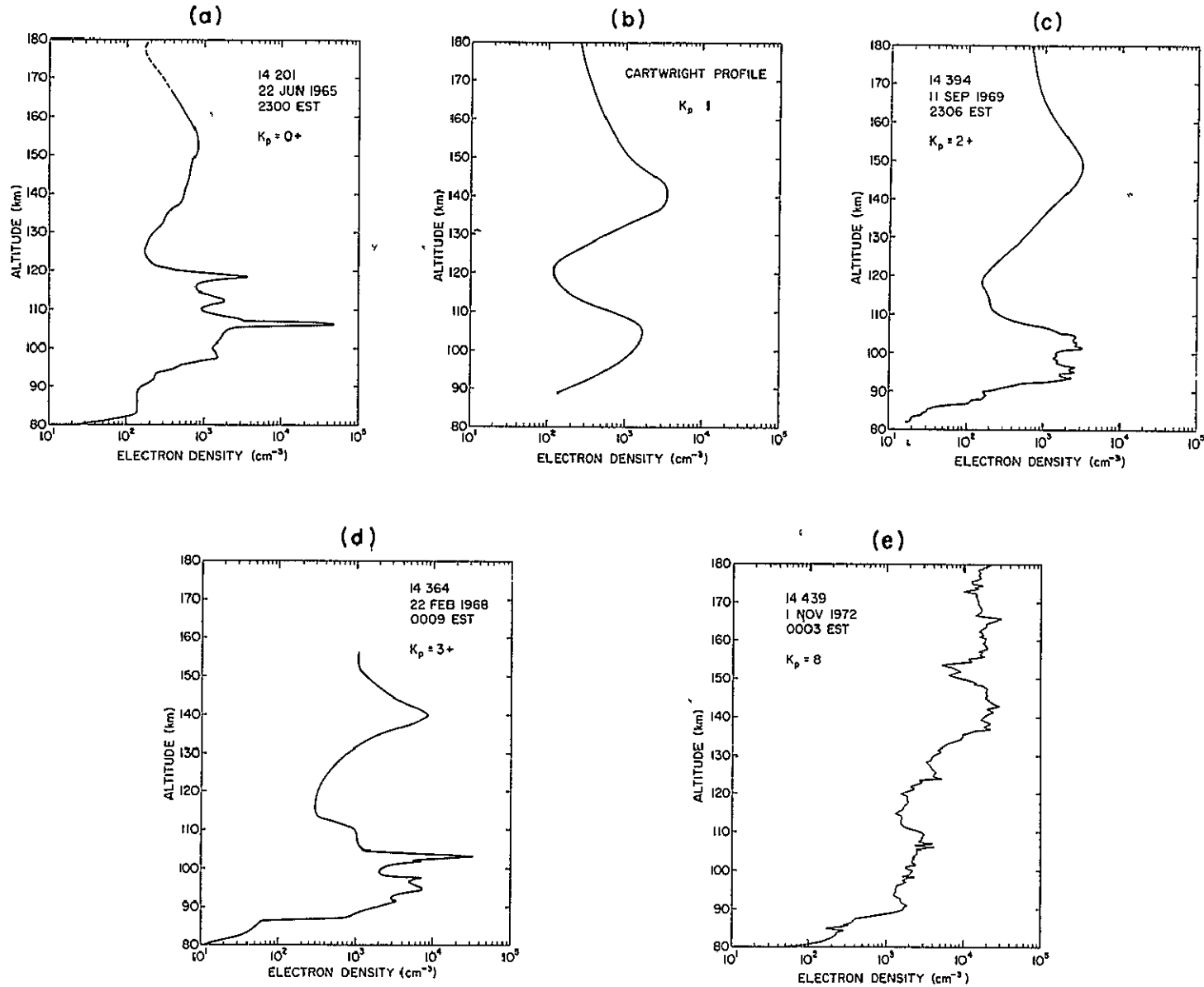


Figure 2.7 Compilation of electron-density profile measurements taken near midnight at Wallops Island, Virginia, under various geomagnetic conditions [Geller *et al.*, 1975]

ORIGINAL PAGE IS  
OF POOR QUALITY

density profiles of the intermediate layer at Arecibo, Puerto Rico, using the incoherent scatter facility. Figure 2.8 shows three sequences of nighttime electron-density profiles over Arecibo taken on 16-19 April 1974. Furthermore, the night of 18-19 April the electron density is quite spread out and similar to that observed at Wallops Island. Also the electron density for this night is enhanced by more than an order of magnitude over the lower Kp night of 16-17 April. In general, on these and other nights studied the higher densities and patchy density profiles of the valley region appear to correlate with the higher values of Kp index. The conclusion made by *Shen et al.* [1976] after analysis of these profiles is that there is an energetic particle ionization source at night. These findings are in agreement with the hypothesis of an Arecibo ( $L = 1.4$ ) precipitation zone as developed in later chapters.

From the intermediate layer the average ionization rate may be accurately obtained. For this case transport into or out of the layer is minimized since the valleys above and below the electron-density layer are much too low to support large fluxes. Furthermore, diffusion into or out of the region is suppressed because the gradient of electron density in the valley region is zero. The persistence of this "trapped" layer of electron density throughout the night provides an accurate method for calculating the ionization rate using the steady-state continuity equation. Setting  $dn_e/dt = 0$  in equation (2.1) and integrating over the altitude limits  $z_1$  and  $z_2$  gives

$$\int_{z_1}^{z_2} (q - \alpha_{\text{eff}} n_e^2) dz - n_e w \Big|_{z_1}^{z_2} + D \frac{dn_e}{dz} \Big|_{z_1}^{z_2} = 0 \quad (2.10)$$

where  $D$  is the ambipolar diffusion coefficient and  $w$  is the vertical ion wind velocity which is converging the ionization towards the wind shear



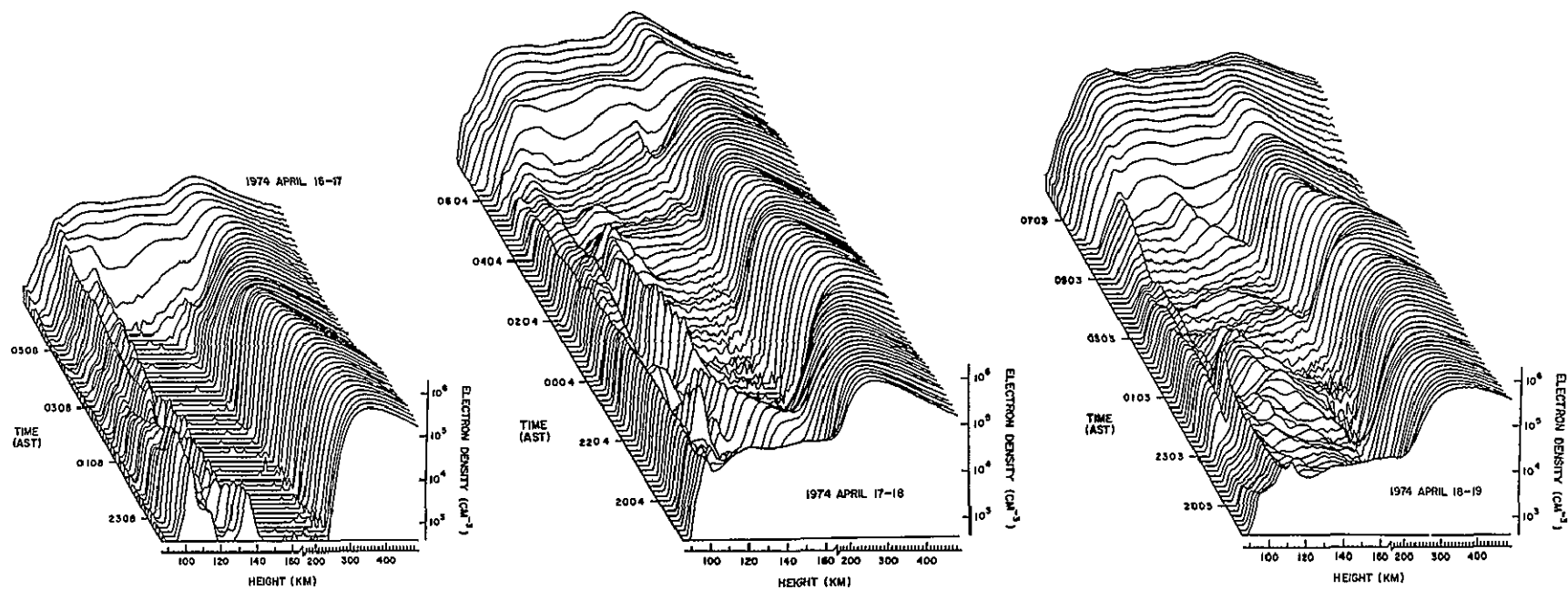


Figure 2.8 A comprehensive series of electron-density profiles at Arecibo were made by *Shen et al.* [1976] on three consecutive nights. Nike Apache 14.520 was launched during the night of 18-19 April 1974 from Wallops Island.

ORIGINAL PAGE IS  
OF POOR QUALITY

[Smith et al., 1974]

Now, if  $z_1$  and  $z_2$  are taken to be the nodes of the electron-density profile, then  $dn_e/dz$  and  $w = 0$  at  $z_1$  and  $z_2$  requiring the square brackets in equation (2.10) to be zero. Therefore,

$$\bar{q} = \frac{1}{z_2 - z_1} \int_{z_1}^{z_2} q dz = \frac{1}{z_2 - z_1} \int_{z_1}^{z_2} \alpha_{\text{eff}} n_e^2 dz \quad (2.11)$$

The integration limits are met at both lower and upper valleys and at the peak of the layer. Thus the average ionization rate may be computed for 1) the layer below the peak, 2) the layer above the peak and 3) the whole layer. Thus, the height-integrated ionization rate in the layer may be obtained without assuming any model for the vertical ion drift velocity. The proper choice of limits of integration has enabled the vertical ion drift (whether caused by neutral winds and/or electric fields) and diffusion to be averaged out — they have not been neglected.

Applying this procedure to the seven electron-density profiles obtained at Wallops Island for the nighttime upper  $E$  region (Figures 2.1 and 2.7) an average ionization rate,  $\bar{q}$ , is obtained for the upper, lower and whole part of each layer [Smith and Voss, 1976]. These ionization rates are plotted in Figure 2.9 versus magnetic index,  $K_p$ . The similarity of the ionization rates over the upper and lower portions of the layer suggest that the production is nearly uniform over this region. The ionization rates are also strongly correlated with magnetic activity and have a least-squares fit given by the experimental relationship.

$$q = 0.12 \exp (0.70 K_p) \quad (2.12)$$

The correlation coefficient for the seven observations is 0.94. Interestingly,

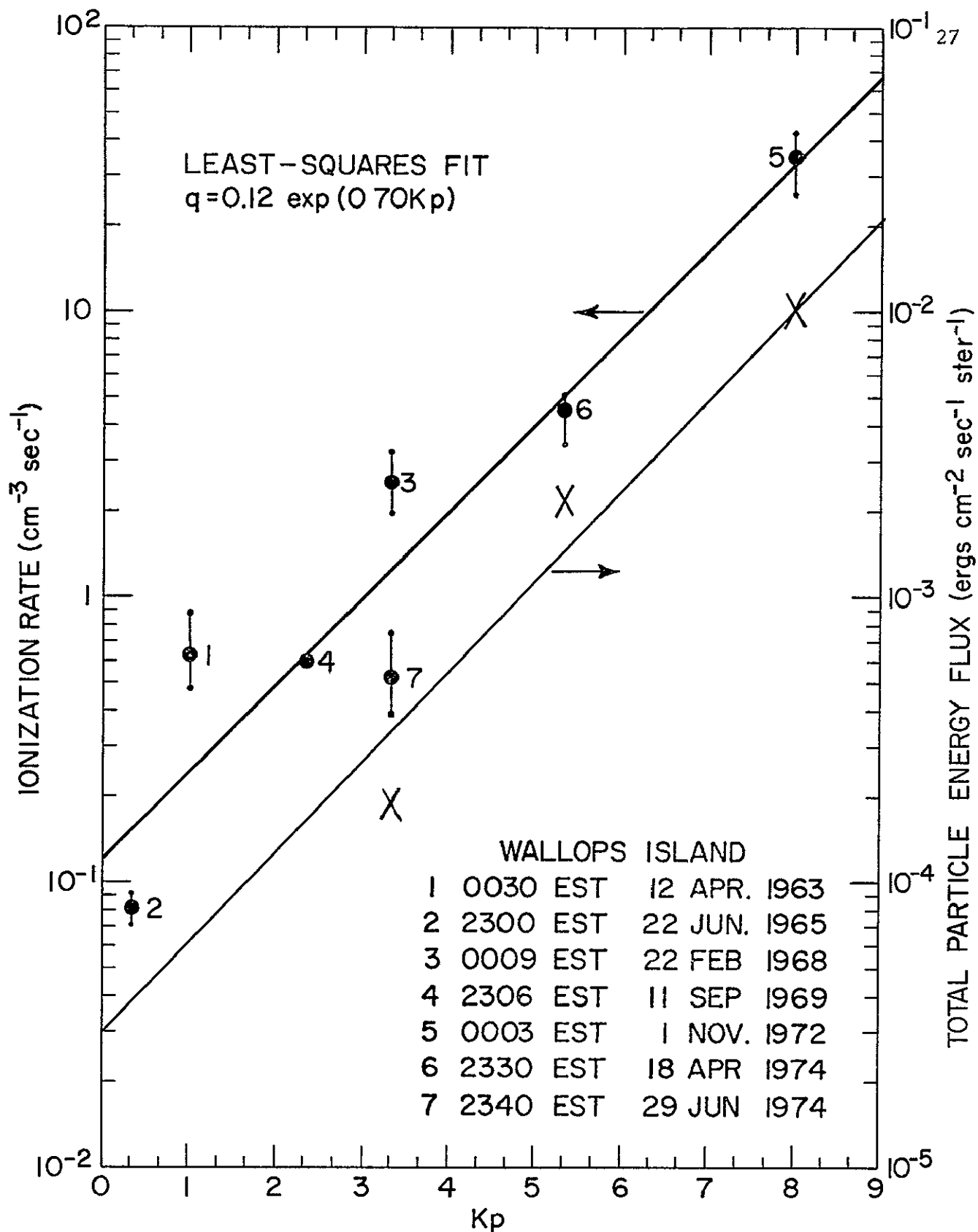


Figure 2.9 The ionization rates calculated from the intermediate layer electron-density profile show a strong correlation with Kp (0.94 correlation coefficient). The particle energy flux shows a similar variation with Kp.

the data indicate that the lower profile ionization rate,  $q_L$ , is always larger for Kp values less than 3 while the upper is always greater for Kp greater than 3. This reversal suggests that the particle spectrum and pitch-angle distribution for a corpuscular ionization model is such as to ionize more of the upper portions of the layer as Kp increases. The greater ionization rate observed at low Kp for the lower profile is expected since the maximum ionization rate for Ly- $\beta$  occurs in the lower E region. As will be shown later the particle spectrum measured is found to be softer for the higher Kp night and is in agreement with the higher ionization rates observed in the upper portion of the intermediate layer.

Also shown in the figure is the particle energy flux observed at Wallops Island for launches labeled 4, 6 and 7. For these three cases (which will be discussed in detail later) the particle flux is observed to increase proportionally with the ionization rate and this suggests that energetic particles are the dominant ionization mechanism for Kp values greater than at least 3.

### 2.3.3 *Wind shear theory as an explanation of the intermediate layer.*

The intermediate layer is now known to be caused by convergence of ionization due to the action of neutral winds forcing positive ions across the earth's magnetic field [Fujitaka et al., 1971, Constantinides and Bedinger, 1971, Smith et al., 1974 and Geller et al., 1975]. Briefly, the predominant horizontal winds associated with global tidal motions flow in opposite directions at different altitudes and times causing a shear in the vicinity of the wind reversal (1 e, 150 km near midnight). Now, the motion of ionization is subject not only to the force of the wind but also to the magnetic field giving rise to a  $\vec{v} \times \vec{B}$  force. It is this vertical ion force which is capable of bringing ionization towards the wind shear location.

*MacLeod* [1966] has derived the vertical ion drift velocity,  $\vec{v}_+$ , from the basic equation of motion as

$$\vec{v}_+ = \frac{1}{1+\rho_+} \left[ \rho_+^2 \vec{u} + \rho_+ \vec{u} \times \vec{\Gamma} + (\vec{u} \cdot \vec{\Gamma}) \vec{\Gamma} \right] \quad (2.13)$$

where  $\rho_+$  is the ratio of collision frequency to gyrofrequency given by  $\rho_+ = m_+ v_{n+} / (eB_0)$  and  $e$  and  $m_+$  are the charge and mass of the ions,  $\vec{u}$  is the neutral gas stream velocity,  $v_{n+}$  is the ion-neutral collision frequency and  $\vec{\Gamma}$  is a unit vector in the direction of the magnetic field  $\vec{B}$

To understand further the role of winds on the electron-density profile the time independent continuity equation (2.1) was solved both with and without the diffusion term. The time dependent term  $\partial n_e / \partial t$  is small since observations suggest the layer remains in an approximately steady-state condition throughout the night. Letting  $w$  represent the vertical ion drift velocity, equation (2.1) becomes

$$\frac{\partial}{\partial z} (w n_e) = q - \alpha_{\text{eff}} n_e^2 + \frac{\partial}{\partial z} D \frac{\partial n_e}{\partial z} \quad (2.14)$$

For the case of interest the ion wind system is observed to be convergent towards the intermediate layer peak. To ascertain the behavior of equation (2.14) a sinusoidal wind approximation is made. The actual winds measured, in fact, are in quite good agreement with this approximation [*Fujitaka et al.*, 1971 and *Geller et al.*, 1974]. The ion wind system, representative of the intermediate  $E$  layer, is taken to be

$$w = 20 \sin[\pi(150-z)/30] \quad (2.15)$$

where the amplitude is taken as  $20 \text{ m s}^{-1}$  with the layer peak at 150 km and upper and lower valleys at 120 and 180 km, respectively

*Voss and Smith* [1974] describe the computer solution of the continuity

equation (2.14) in detail for the cases of  $D = 0$  and  $D \neq 0$ . For the case of  $D = 0$  a precision predictor-corrector Euler-Romberg method was used for analysis due to the numerical sensitivity of this equation towards instability. Additionally, a complicated analytic series solution was derived for the  $D = 0$  case. The no-diffusion continuity equation may be transformed as the Riccati equation. Using various substitutions, a second order linear differential equation is obtained. Transformation again results in a form applicable to the WKB method of solution.

To solve the variable diffusion continuity equation, a Runge-Kutta method was applied with 0.2 km steps. Furthermore, since the initial conditions cannot be specified at one point, as required by this iterative scheme, a convergence procedure is required. The two known boundary conditions of the second order equation are zero slope (zero flux) at the peak and valleys of the profile. Thus, by starting at the peak of the profile and assuming a typical electron density ( $10^{11}$  cm<sup>-3</sup>, a value between the  $D = 0$  value and the photoequilibrium value) a convergence towards the actual initial point will occur, if one monitors the final slope of the valley and corrects accordingly.

Solutions with and without diffusion are shown in Figure 2.10 for five values of  $q$ . The thick profiles represent a value of  $D$  of  $2 \times 10^8$  cm<sup>2</sup> s<sup>-1</sup> and the thin profiles for  $D = 0$ . The results clearly indicate that diffusion is significant for low production rates. These results illustrate that the modeled nighttime intermediate layer is in close agreement with observations of Figure 2.6.

Profile 1 ( $q = 0.4$  cm<sup>-3</sup> s<sup>-1</sup>) gives results quite similar to the intermediate layer at midnight under rather quiet geomagnetic conditions. As the ionization rate increases according to Figure 2.9 the peak broadens and becomes less pronounced. Figure 2.11 illustrates the intermediate layer

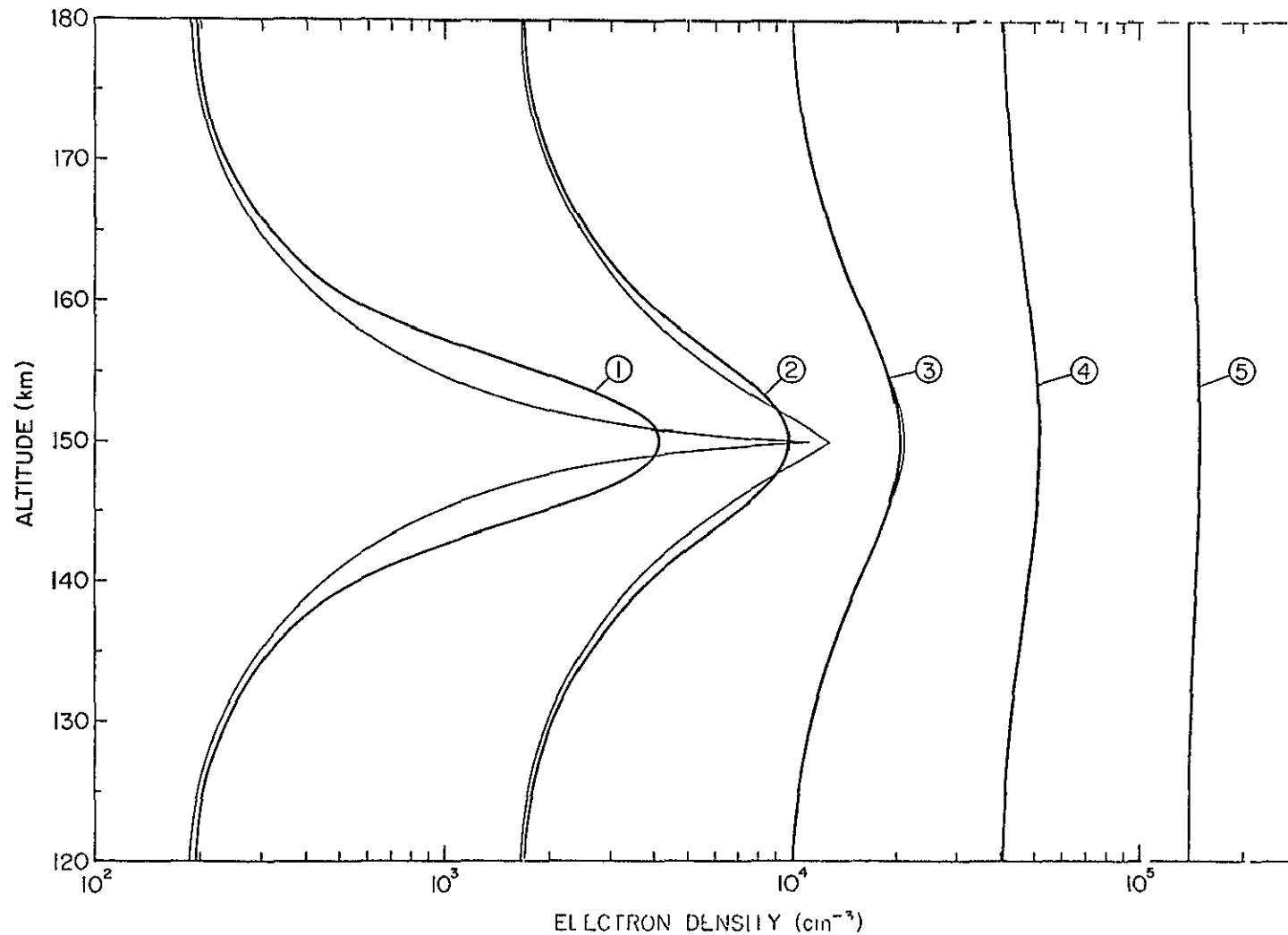


Figure 2.10 Simulations of the intermediate layer with the vertical ion drift given by  $w = 20 \sin[\pi(150-z)/30] \text{ m s}^{-1}$  for altitude  $z$  in km, with the recombination coefficient  $1.9 \times 10^{-7} \text{ cm}^3 \text{ s}^{-1}$ , for production rates of (1) 0.4, (2) 4.0, (3) 40, (4) 400 and (5) 4000  $\text{cm}^{-3} \text{ s}^{-1}$ . The thin line is the solution neglecting diffusion the thick line is the complete solution with a diffusion coefficient of  $2 \times 10^8 \text{ cm}^2 \text{ s}^{-1}$ .

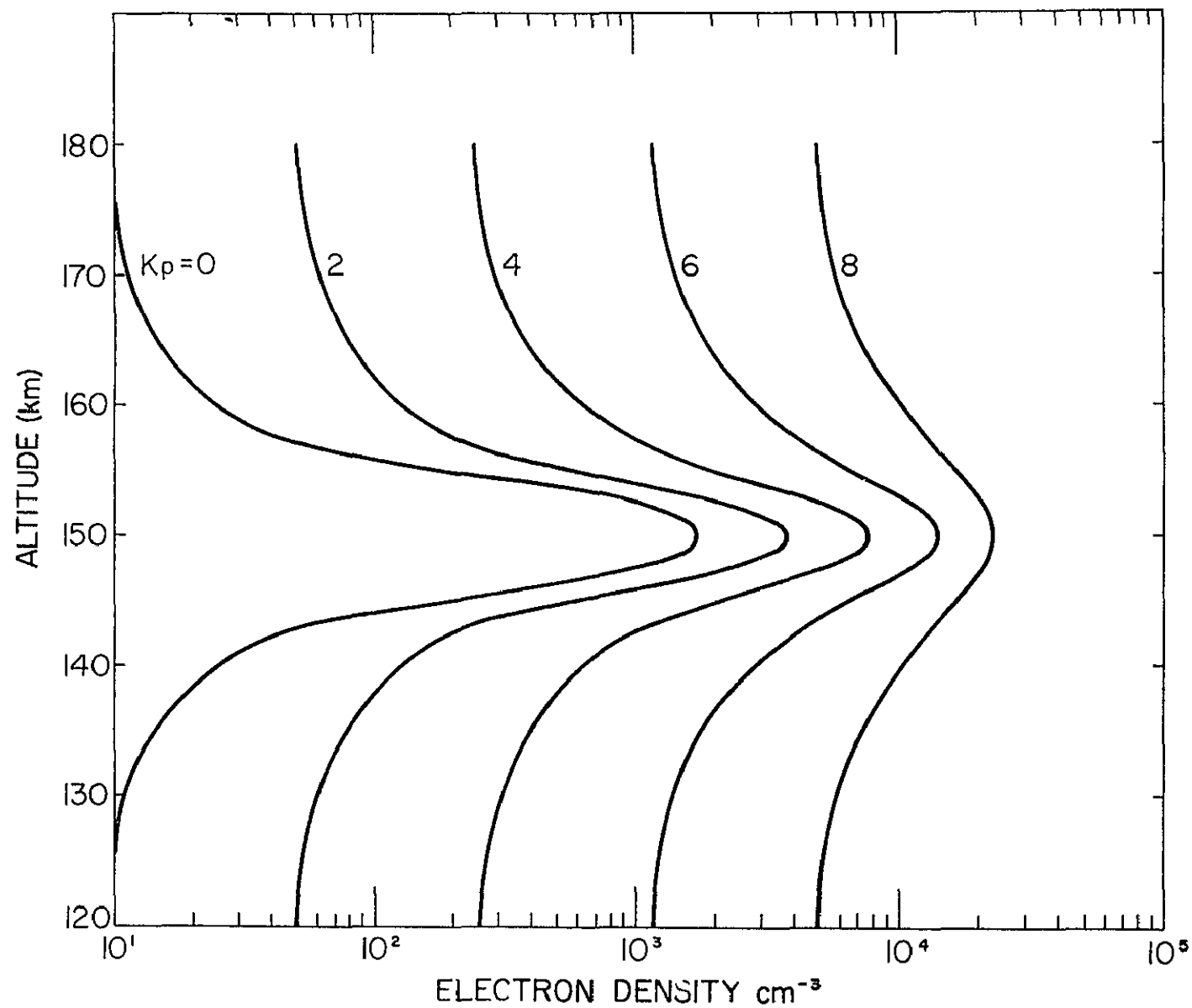


Figure 2 11 Calculated intermediate layer for ionization rates deduced from Kp given by equation (2 12)



dependence on Kp

The sensitivity of these calculations to variations in amplitude of the vertical ion wind are illustrated in Figure 2.12. The computations are carried out for values of amplitude,  $A$ , of 0, 10, 20 and 50  $\text{m s}^{-1}$ . Much ionization redistribution is observed to occur at relatively low values of the ionization drift velocity. However, this redistribution does not affect the electron-density profile in a proportional manner. For example, doubling  $A$  from 10 to 20  $\text{m s}^{-1}$  increases the peak value of electron density from 5100 to 7500  $\text{cm}^{-3}$  (and increase of about 50%), while increasing  $A$  from 20 to 50 gives an increase of only 20%.

The electron-density profiles of the intermediate  $E$ -region layer may be used to deduce information of ion winds and therefore neutral winds. For this purpose the continuity equation is employed, using the ionization rates calculated in e.g., Figure 2.9 for the upper and lower part of the layer. Equation (2.14) may be solved for  $w(z)$  when given the electron-density profile of the intermediate layer

$$w(z) = \frac{1}{n_e(z)} \int_{z_1}^{z_2} (q - \alpha_{\text{eff}} n_e^2) dz + D \left( \frac{dn}{dz} \right)_z \quad (2.16)$$

where  $z_1$  is the altitude where  $w = dn_e/dz = 0$ . The wind profiles calculated in this manner are discussed by Geller *et al.* [1974].

#### 2.4 Significance of Ultraviolet Ionization in the Nighttime Ionosphere

Ultraviolet radiation at night from the geocorona and extraterrestrial origin can excite and ionize the atmospheric constituents in the region above 80 km. The purpose of this section is to investigate the significance of this radiation as an ionization source and to understand its variation with altitude, solar zenith angle, and magnetic activity. Various UV ionization

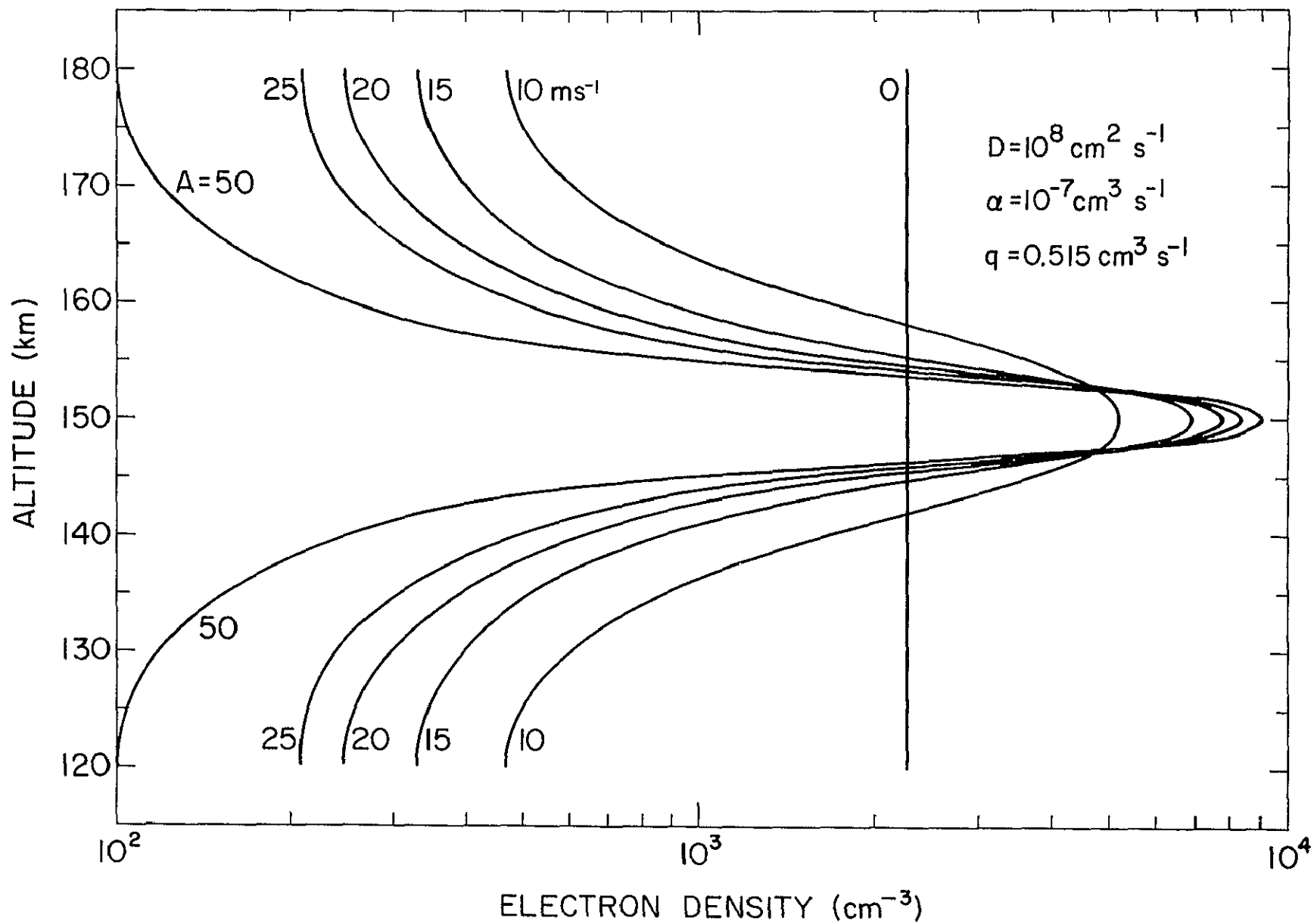


Figure 2.12 Sensitivity of the continuity equation (2.14) to vertical ion wind variations in amplitude

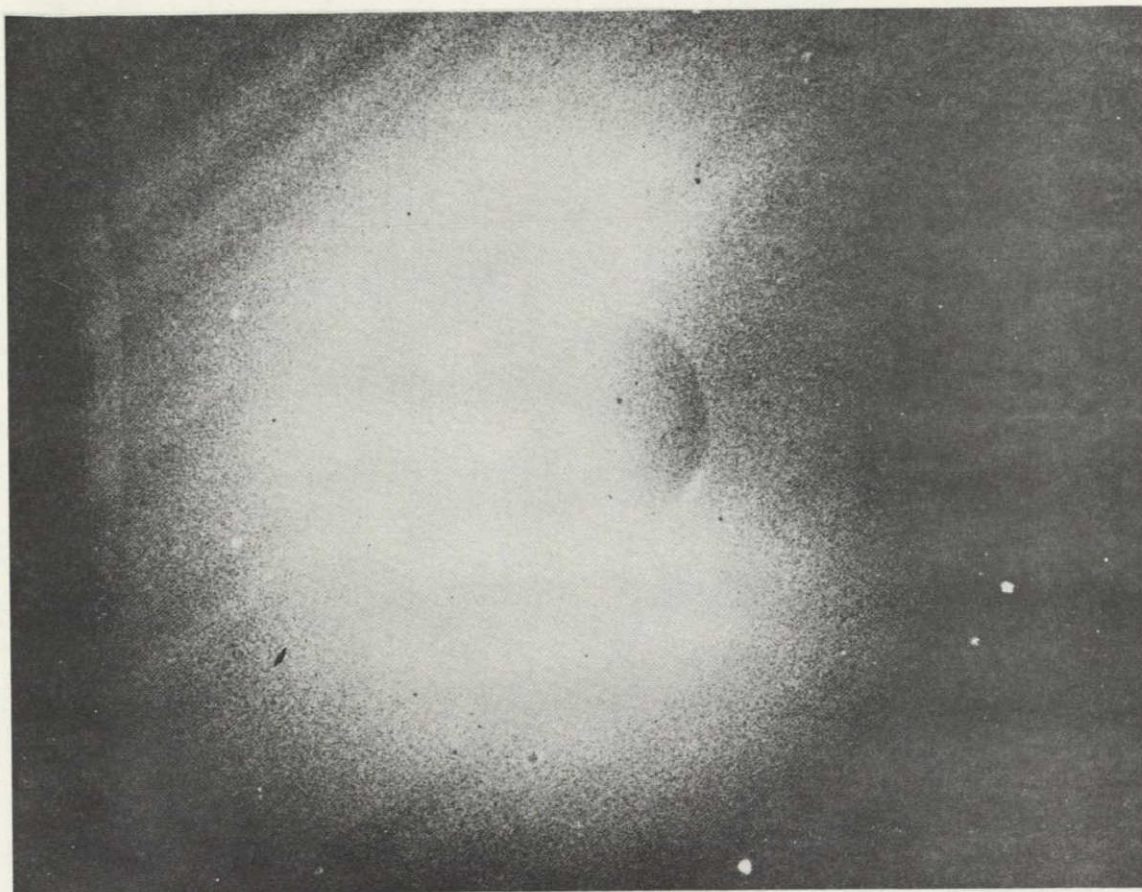
models will be reviewed and compared to ascertain whether they are able to maintain the observed nighttime electron density.

2.4.1 *Introduction.* Hydrogen and helium atoms comprise the outermost regions of the earth's atmosphere because of their low atomic weight. Typical scale heights for these constituents are approximately 100 to 300 km and therefore the hydrogen and helium extend out to a few earth radii in significant quantities. Because of these great distances, the solar ultraviolet emissions in the main absorption bands of H and He are able to reradiate (resonance scattering) into the nighttime ionosphere. This vast extension of hydrogen and helium above the earth with its ability to scatter solar radiation is called the geocorona.

2.4.2 *Hydrogen Ly- $\alpha$  emission.* Carruthers *et al.* [1976] have obtained the first global measurement of the hydrogen Ly- $\alpha$  emission from the geocorona (Figure 2.13a) by use of a special UV camera positioned on the moon during the Apollo 16 mission. These photographs have been analyzed by Carruthers *et al.* [1976] in detail and verify to the first order the geocorona models developed by Meier and Mange [1970, 1973]. A comparison with this model is illustrated in Figure 2.13(b). The experimental isodensity contours (15 second exposure) are given in units of kilorayleighs. The modeled contours have intensities from the outermost to the innermost contour of 2.1, 4.69, 8.59, 13.6, 19.0 and 22.7 kR, respectively, for a solar Ly- $\alpha$  flux of  $4 \times 10^{11}$  photons  $\text{cm}^{-2} \text{s}^{-1} \text{\AA}^{-1}$  at the center of the line. The optical depth of the geocorona is estimated to be 2.7.

At large earth distances of approximately  $8 R_e$  (not shown) the isodensity contours give clear evidence of a geotail effect due to solar Ly- $\alpha$  radiation pressure. Near the earth in the night sector the measured intensities are greater than the modeled values and suggest a buildup of hydrogen in relation





ORIGINAL PAGE IS  
OF POOR QUALITY

Figure 2.13 The hydrogen Lyman-alpha emission from the earth's geocorona as photographed from the moon during the Apollo 16 mission (upper figure). Subsequent analysis of these profiles has shown agreement with the geocorona models of *Meier and Mange* [1973] (lower figure) [*Carruthers et al.*, 1976].

to the spherically symmetric models. The full diurnal variation of the hydrogen density is approximately 2 to 2.5.

Theoretical models of the geocorona [Meier and Mange, 1973] are used by Strobel *et al.* [1974] to obtain Ly- $\alpha$ , Ly- $\beta$ , He I and He II flux variations with altitude for different solar zenith angles. The Ly- $\alpha$  model of Meier and Mange [1973] is referenced to OSO 4 satellite observations which give a subsolar and antisolar absolute brightness of 35 kR and 1 kR, respectively, for zenith observations made at 650 km.

Average Ly- $\alpha$  intensities compiled by Ogawa and Tohmatsu [1966] for a number of experimental observations give an intensity of 1.9 kR. Weller and Carruthers [1972] have observed a nighttime intensity of 1.6 kR at Wallops Island. These measurements suggest that in addition to geocorona Ly- $\alpha$  scattered from interplanetary hydrogen. Typical emission rates of 200 to 600 R are estimated by Thomas and Krassa [1971].

Although the total Ly- $\alpha$  flux is the largest of the nighttime ultraviolet emission, its ionization and absorption cross section are the smallest ( $2 \times 10^{-18} \text{ cm}^2$ ) and consequently is not appreciably attenuated above 120 km altitude. Furthermore because Ly- $\alpha$  ionizes only NO the maximum absorption takes place below 120 km where NO is greatest. The ionization rates for Ly- $\alpha$  are consequently very small in the region 120 to 200 km as will be shown later.

Weller *et al.* [1971] and Meier and Mange [1973] have discussed the temporal variations of the Ly- $\alpha$  flux from the geocorona due to magnetic activity and thermospheric temperatures. From their study it is inferred that the Ly- $\alpha$  flux changes by a factor of 4 at most.

2.4.3 *Hydrogen Ly- $\beta$  emission.* Ly- $\beta$  (102.6 nm) intensities were first estimated from hydrogen nightglow radiation (656.3 nm) and from Ly- $\alpha$ .

emissions (121.6 nm) by *Ogawa and Tohmatsu* [1966]. This analysis was based on the comparison of the spontaneous transition probabilities of the hydrogen atom between different states. Using this method the median intensity of Ly- $\beta$  is approximately 10 R, a good approximation to later experimental observations.

*Young et al.* [1971] using an Aerobee rocket launched from White Sands at 2330 MST ( $\chi = 131^\circ$ ) measured a Ly- $\beta$  intensity (90 to 108 nm) of 10 R at 200 km altitude. The Ly- $\beta$  radiation was reduced by only 1 R over the region 120 to 200 km with primary absorption in the altitude region 90 to 110 km. This is expected since Ly- $\beta$  predominately ionized molecular oxygen which has a cross section of absorption and ionization which is very small ( $1.52$  and  $0.97 \times 10^{-18} \text{ cm}^2$ , respectively) relative to the helium emissions.

Additional measurements of Ly- $\beta$  show that the midlatitude intensities may vary by a factor of 5 [*Swider*, 1972 and *Weller and Carruthers*, 1972]. It is also believed that approximately half of the Ly- $\beta$  radiation is of extraterrestrial origin [*Gough*, 1975] and therefore would remain nearly constant in time. The similar temporal variations for Ly- $\beta$  and Ly- $\alpha$  are expected since both originate from hydrogen emission. Because the change in Ly- $\beta$  flux is less than a factor of 5 with changes in magnetic activity and thermospheric temperatures the ionization rate remains nearly constant. The ionization rates calculated by *Ogawa and Tohmatsu* [1966] and *Strobel et al.* [1974] show that maximum ionization by Ly- $\beta$  ( $2 \text{ cm}^{-3} \text{ s}^{-1}$ ) occurs in the altitude region 90 to 110 km. Referring to the electron-density profiles in Figure 2.1, it is apparent that the density in this region is not a function of Kp. Simultaneous measurements of particles in this region (Section 4.1) show that the flux is very small and therefore it is concluded

that Ly- $\alpha$  and Ly- $\beta$  are the principal contributors to nighttime ionization between 90 to 110 km

At altitudes greater than 120 km the ionization rates produced by Ly- $\beta$  and Ly- $\alpha$  are very small ( $<0.1 \text{ cm}^{-3} \text{ s}^{-1}$ ) and are consequently a negligible ionization source compared to the helium emissions and energetic particle ionization.

2 4.4 *Helium I emission.* Meier and Weller [1972] have measured the neutral helium emission line at 58.4 nm and have made model calculations for this emission from the geocorona. The disagreement of the model calculations (1R) to the much larger measured fluxes (1 to 10 R) in the antisolar direction has led Meier and Weller to conclude that an extra-terrestrial source must be present such as interplanetary helium. Weller and Carruthers [1972] have not detected intensities greater than about 5 R for 58.4 nm emission from a rocket launched at Wallops Island at 0300UT on 25 November 1970.

When present, the He I emission is a most important ionization source in the altitude region 120 to 200 km since this wavelength is able to ionize  $\text{N}_2$ ,  $\text{O}_2$  and O (cross section of  $23.1 \times 10^{-18}$ ,  $22.7 \times 10^{-18}$  and  $10.1 \times 10^{-18} \text{ cm}^2$ , respectively). Typical emission rates are believed to vary between 1 and 10 R depending upon the time of year.

2 4.5 *Helium II emission.* The 30.4 nm emission from the ionized helium atom is an important ionization source in the region 120 to 200 km. Since the helium ion is charged, the ions are restricted to the closed electric field lines of the earth's plasmasphere. This added complication suggests that geographic location is an important parameter. The sharp cut-off of  $\text{He}^+$  ions between  $L$  values of 3 and 5 (plasmopause) marks a decrease in 30.4 nm intensity. During periods of magnetic storms the

plasmopause moves inward and so it would be expected that the 30.4 nm intensity from the plasmasphere would be negatively correlated with Kp. On the other hand 30.4 nm radiation may increase with Kp somewhat due to increases of  $\text{He}^+$  in the solar wind. These effects are believed to change the 30.4 nm flux by less than a factor of 5

*Meier and Weller* [1972] have reviewed the observations of 30.4 nm radiation and have found typical emission rates of less than 10 R at 200 km. *Young et al.* [1971] find a zenith intensity above 210 km at a solar zenith angle of  $134^\circ$  of 4 R. This value is adopted by *Strobel et al.* [1974] in their ionization rate calculations

2.4.6 *Ionization rates and electron densities produced by ultraviolet radiation at night.* Detailed calculations of the nighttime ultraviolet production rate and ion chemistry have been developed by *Strobel et al.* [1974]. These calculations are based on the geocorona models of *Meier and Mange* [1973] and experimental data. It is shown that in the region 90 to 110 km the ionization rates by ultraviolet emissions (principally Ly- $\beta$  and Ly- $\alpha$ ) are at a maximum with ionization rates of about  $2 \text{ cm}^{-3} \text{ s}^{-1}$  at 120 km with lower ionization rates at higher altitudes. Profiles of calculated ionization rates for UV by *Strobel et al.* [1974] and *Ogawa and Tohmatsu* [1966] are compared with energetic electron ionization in Figure 9.18

From these data it is concluded that in the region 90 to 110 km the nighttime ultraviolet ionization is at a maximum and hence dominates as the ionization source since particle ionization is at a minimum. This is in good agreement with the electron-density profile of Figure 2.1 which shows a very constant density over a large range of Kp values. Furthermore, this constancy suggests that the Ly- $\alpha$  and Ly- $\beta$  fluxes are not functions of magnetic activity.

Further support for ultraviolet ionization in this region (90 to 110 km)



is the large concentration of  $O_2^+$  ions observed (Ly- $\beta$  principally ionizes  $O_2$ ). Detailed analysis of the  $O_2^+$  to  $NO^+$  ion ratios are discussed by *Nesterov* [1974] and *Chasovitin and Nesterov* [1976]

In the region 120 to 200 km large fluxes of energetic electrons are detected and are correlated with large electron density increases and increased magnetic activity. In Chapter 9 it is shown that the observed electron fluxes do, in fact, produce the ionization rates necessary in this region

In Figure 2 14 a comparison of the electron-density profile predicted by ultraviolet ionization sources [*Strobel et al.*, 1974; profile 1] is compared with two experimental observations of electron densities measured by Nike Apaches 14 520 (profile 2,  $K_p = 5+$ ) and 14.439 (profile 3,  $K_p = 8$ ). Clearly for moderately disturbed magnetic conditions the observed electron densities are much higher than the ultraviolet model prediction and thus requires an ionization source which is approximately 200 times greater than the UV source for  $K_p = 8$ . The ultraviolet model predictions are in good agreement with observations below 120 km and for very quiet geomagnetic conditions in the region 120 to 200 km at Wallops Island

In summary, the intensities of the nighttime ultraviolet radiation from the geocorona and extraterrestrial origin have been well established. These intensities are not significantly correlated with magnetic activity but may vary by a factor of five at midlatitudes. It is shown that the ultraviolet intensities are able to reproduce the electron densities in the region 90 to 110 km but are inadequate to account for the variability of the region 120 to 200 km. Some other ionization source must be invoked to maintain the large electron densities observed in this region.

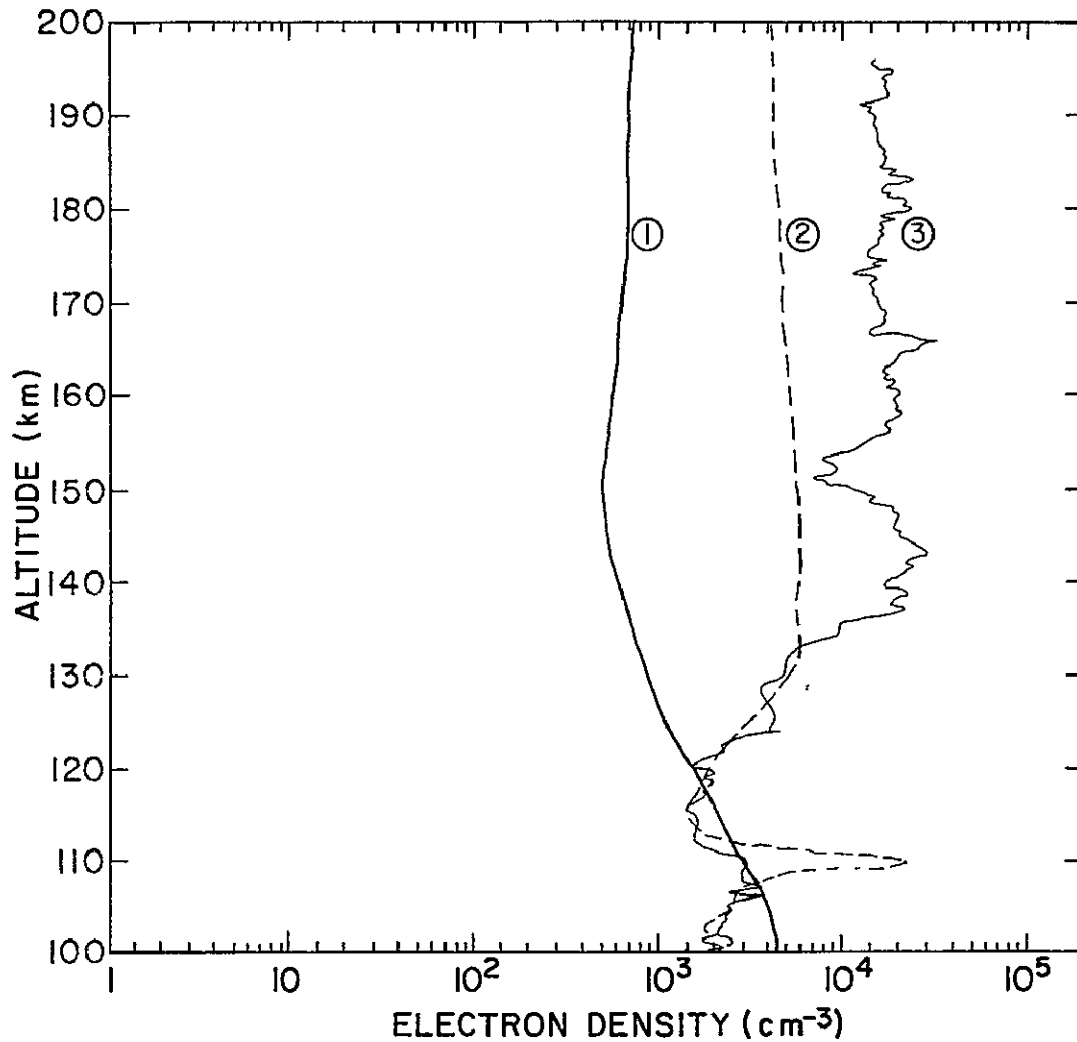


Figure 2.14 Profile 1 is the electron density calculated by *Strobel et al.* [1974] for a model of the nighttime ultraviolet radiation. The experimental measurements at Wallops Island made by Nike Apache 14 520 (Profile 2, Kp = 5+) and 14 439 (Profile 3, Kp = 8) show that the electron densities can be more than an order of magnitude greater than the ultraviolet model predicts

### 3. EXPERIMENTAL TECHNIQUE

This chapter describes the instrumentation used in the measurement of the flux, spectrum and pitch-angle distribution of energetic electrons in the ionosphere. The energetic electron spectrometer and its calibration have been described in detail previously [Voss and Smith, 1974]. After a description of the instrument the main part of the chapter is concerned with the conversion of the measured count rate to a flux, as a function of energy and pitch angle. Some emphasis is given to the problem of measurement from a spinning rocket, with its associated precessional motion, and the finite dimension of the payload compared with the radius of gyration of the electrons. It is shown that the simple concept of a geometrical factor, commonly used in the evaluation of particle fluxes, leads to erroneous results under some conditions.

#### 3.1 *Design and Calibration of a Rocket-borne Energetic Electron Spectrometer*

3.1.1 *Choice of detector.* The energy range capabilities for various detection schemes are compared in Figure 3.1. The channel multiplier is the most attractive instrument for electrons of low energy. However complications related to the implementation of the channel multiplier in rockets are 1) the gain is pressure sensitive due to the ionization of the neutral residual gas; 2) the need to vacuum seal the tube to prevent outgassing; 3) the presence of high voltages required for operation; 4) the "ram effect" with the neutral atmosphere [Hoffman et al., 1974], 5) the possibility of UV contamination, 6) the small geometrical factors, and 7) the saturation that begins at  $10^5$  pps because of field distortions and space charge effects. Scintillator particle detectors, on the other hand, are quite suitable for rocket use, the main drawback being the poor energy resolution.

# PARTICLE DETECTOR ENERGY COMPARISON

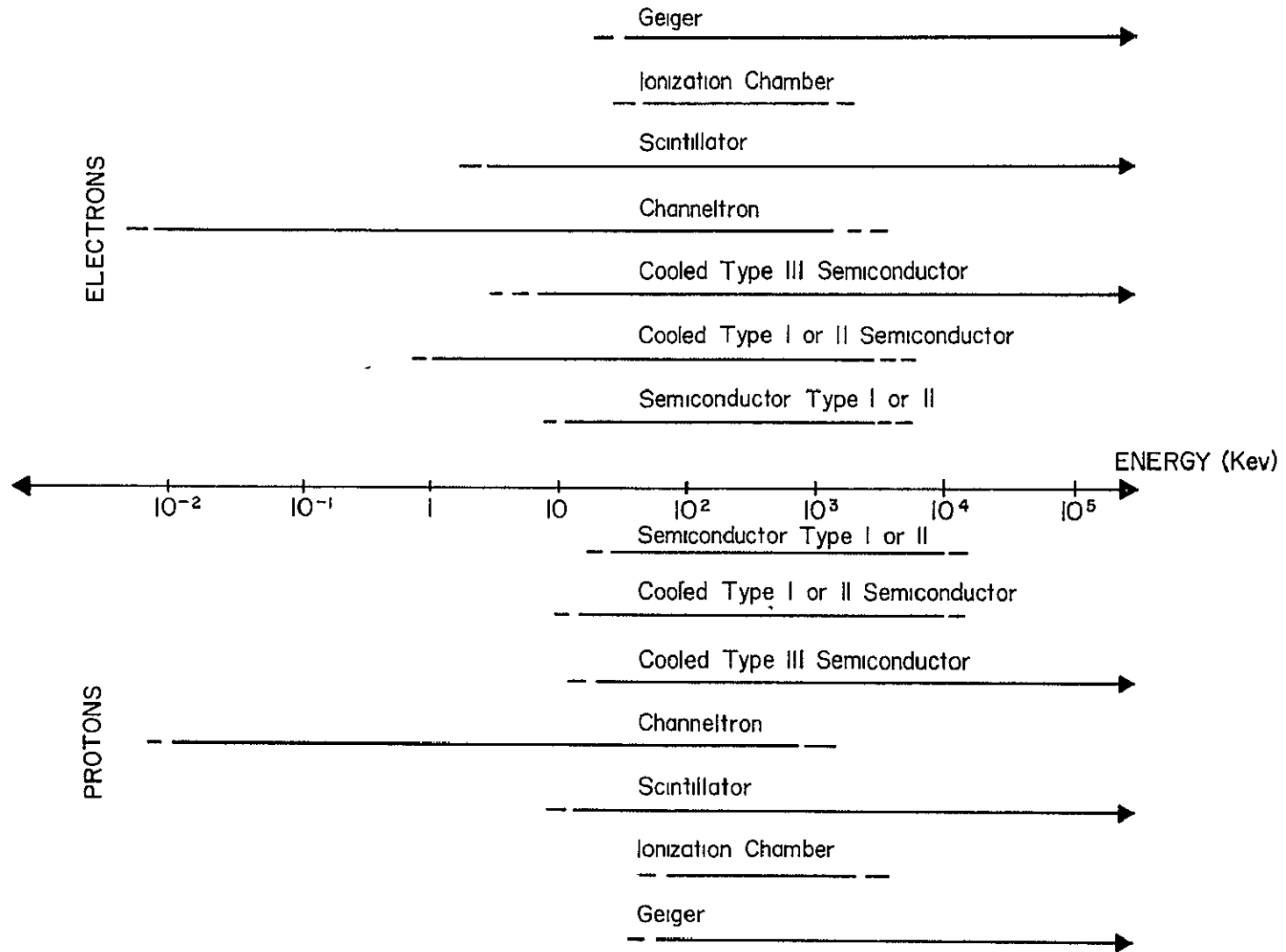


Figure 3.1 Sensitive energy range for various rocket-borne particle detection schemes. The energy comparison is made for electrons in the top half and for protons in the lower half.

Gaseous detectors may be classified into three modes of operation: ionization, proportional, and Geiger. These detectors are well suited to rocket-borne experiments. The main deficiencies associated with gaseous detectors are 1) sensitivity with respect to where the ionization track takes place within the gas, 2) gas purity, 3) relatively high low energy thresholds; 4) associated deadtimes due to slow ion mobilities, and 5) high voltage requirements.

The particle detector experiment which will be described in this section is based on a solid-state surface barrier detection system. The principal advantages of this technique are summarized as follows

- (a) better statistics and resolution result since many more charge carriers are released for a particular incident energetic particle, e g , an ionization event requires 35 eV, typically, for a gas and 3.5 eV for silicon per ionization
- (b) insensitivity to UV or low energy X rays since operated in a non-avalanche mode
- (c) very short deadtimes of the order of a few nanoseconds. The collected charge is independent of the location of the ionization event
- (d) the detectors are rugged, compact, easily mounted and use low voltages

The primary disadvantages are the relatively weak signals requiring extremely sensitive electronics, and a 10 keV low energy threshold (although this can be lowered to 1 keV with cooling and with a smaller detector area)

Energetically charged particles propagating within a solid lose their kinetic energy through lattice interactions. These interactions may be thought of as similar to ionization of a gas in a Geiger counter except that

the gas is in a condensed form, a solid. These energetic electrons supply energy to the lattice electrons and lift them from the valence band into the essentially empty conduction band. Using a reverse-biased p-n junction the electric field within the depletion region is such that the excited electron-hole pairs created by ionization are swept out of the depletion region and yield a current pulse proportional to the incident energetic particle energy for subsequent amplification. Various types of solid-state detectors are shown in Figure 3.2. Two qualifications placed on the diode are that it must be fabricated such that the depletion region extends over a range somewhat larger than the incident particle decay path (if energy spectrum information is desired) and that the energy lost in the thin surface layer (dead zone) adjacent to the depletion region be optimized to its smallest reasonable value.

3.1 2 *Electronic circuits.* A complete block diagram of the detection and amplifying circuits is represented in Figure 3.3(a). The Norton equivalent circuit is substituted for the detector where  $Z_N$  is primarily capacitive. The current introduced into the preamplifier from an energetic particle is integrated in the first stage by applying capacitive feedback (i.e., it is a charge amplifier). The resulting charge pulse is shaped (to minimize noise) and amplified in succeeding stages. The preamplifier uses a double differentiation and double integration pulse shaping network with a low-noise high-input-impedance field-effect transistor in the first stage. Postamplification is used for final pulse-height discrimination.

Figure 3.3(b) illustrates the technique used for resolving the energy spectrum. The system is straightforward and uses six series-connected voltage comparators as a pulse height circuit. Each signal is then shaped and accumu-

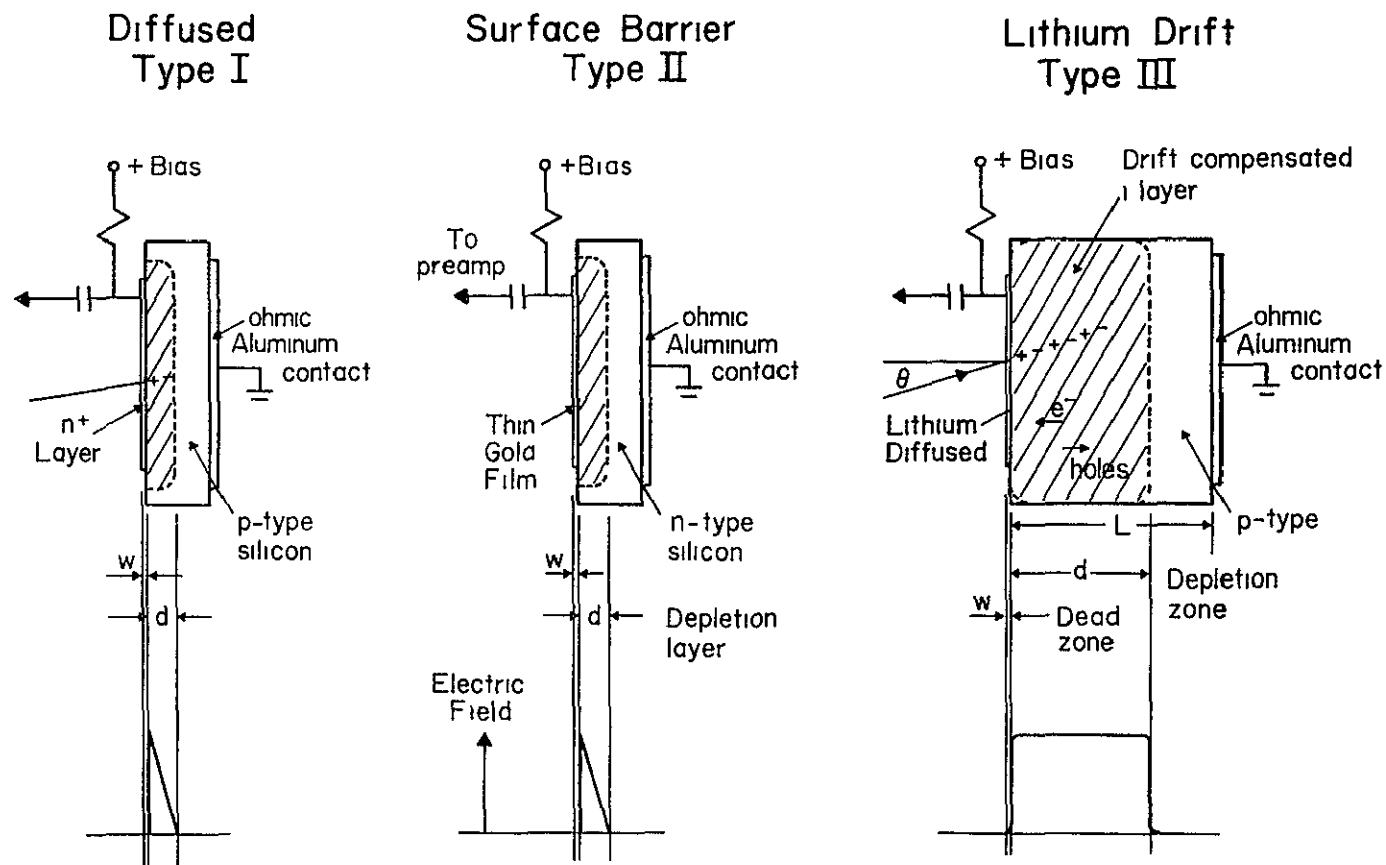


Figure 3.2 Three types of solid-state particle detectors are represented showing their respective geometry and electric field strengths. For totally depleted detectors, the depletion region depth is equal to the total detector length  $L$ .

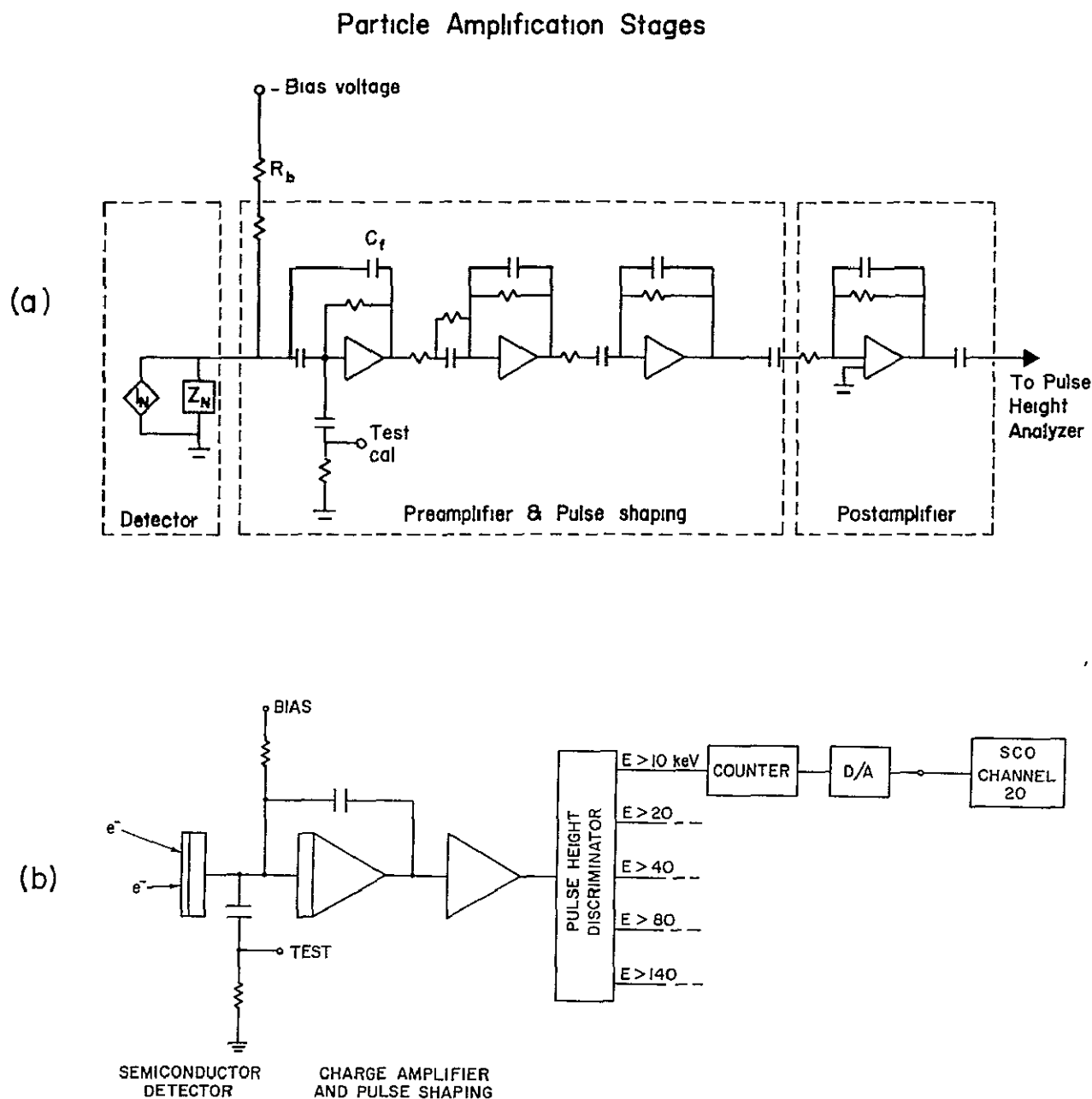


Figure 3 3 The upper figure shows the particle detector basic amplification system. The preamplifier uses double integration and double differentiation stages to minimize noise. The lower figure illustrates the total system operation. An energetic particle produces a small charge within the detector, whereupon it is amplified and pulse-height discriminated. Each pulse within the discriminator range triggers a digital 4-bit counter and is then converted into analog form for transmission by the telemetry system.



lated in a self-resetting 16-count 4-bit binary counter. This information is then converted to analog form for interface with telemetry VCO.

Figure 3.4 shows the arrangement of the energetic electron spectrometer in the payload of a Nike Apache rocket. The upper deck contains the detector, preamplifier and high voltage supply; the lower deck contains the counting electronics and low voltage power supplies. Both decks are interfaced through pin connectors to the main wiring channel shown on the extreme left.

**3.1.3 Calibration.** The calibration procedure involves consideration of the detector sensitivity to various kinds of energetic particles with respect to the incident energy and direction at which the particles impinge on the semiconductor. Various techniques were used and compared. They include use of: 1) conversion electron radioactive sources; 2) theoretical calculations; and 3) use of an electron and proton accelerator at the GSFC. The angular properties of the detector (without collimator) are shown in Figure 3.5(a). The measured beamwidth is in close agreement with the calculated value ( $64^\circ$ ) for particles with energies less than 25 keV but gradually broadens (due to scattering from the walls) to  $82^\circ$  at 60 keV and remains at  $82^\circ$  for higher energies. The pulse height was found to be extremely linear with energy determined by several techniques. Shown in Figure 3.5(b) is a pulse-height spectrum using the accelerator for energies of 20, 40, and 60 keV electrons. The pulse at the left is due to noise buildup. The noise HWHM (half width at half maximum) is approximately 5 keV. Further details on the calibration procedures are discussed by *Voss and Smith* [1974].

### 3.2 Determination of the Rocket Attitude from the Magnetometer Signal

To properly interpret the time variations of the count rate profiles, a model must be developed which gives the angle between the earth's magnetic field and the particle detector at all times in the flight as the rocket spins and

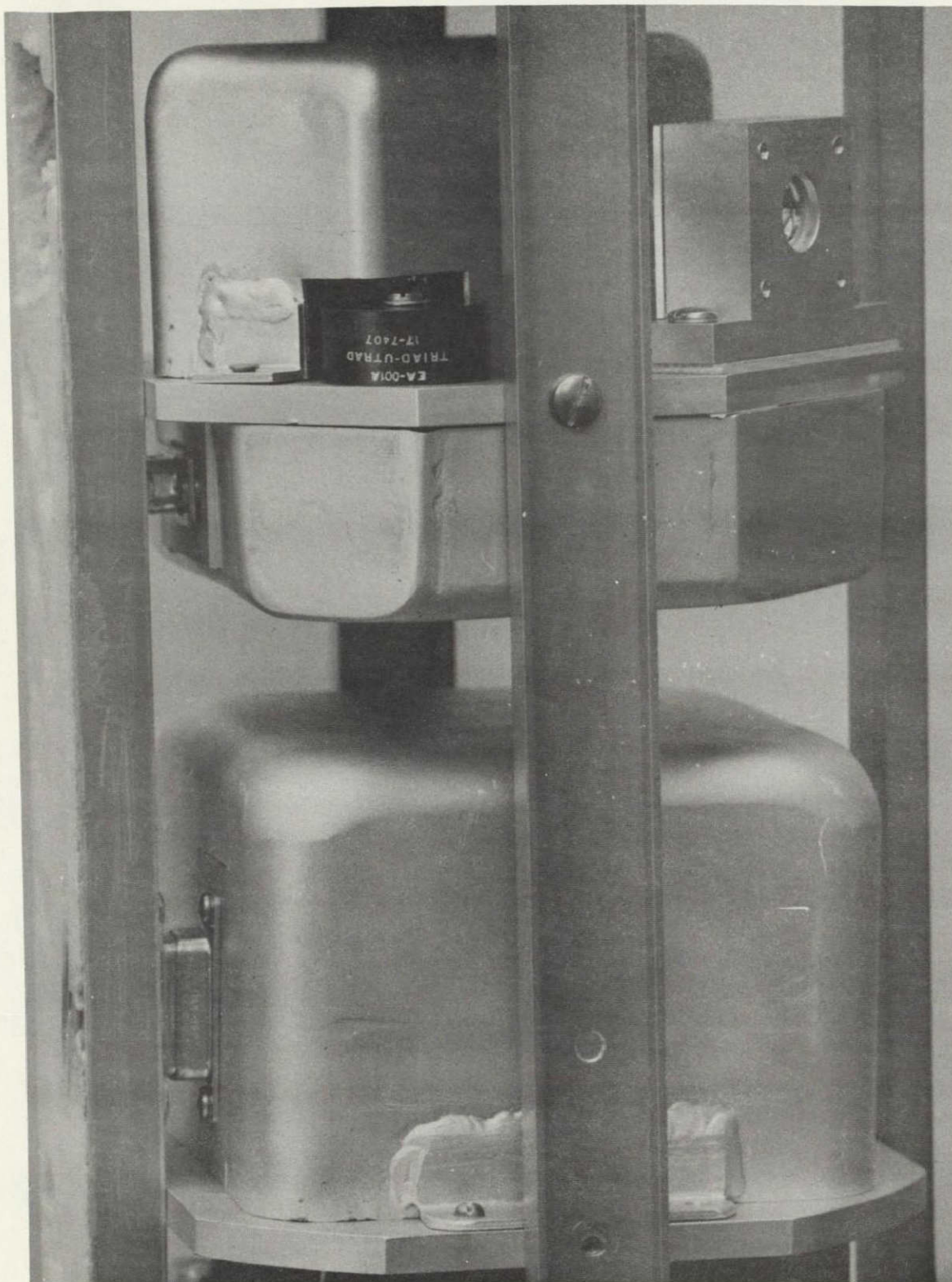


Figure 3.4 The arrangement of the energetic electron spectrometer in the payload of a Nike Apache rocket. The upper deck contains the detector, preamplifier and high voltage supply complementing the lower deck counting electronics and low voltage power supplies. Both decks are interfaced through pin connectors to the main wiring channel shown on the extreme left.

ORIGINAL PAGE IS  
OF POOR QUALITY



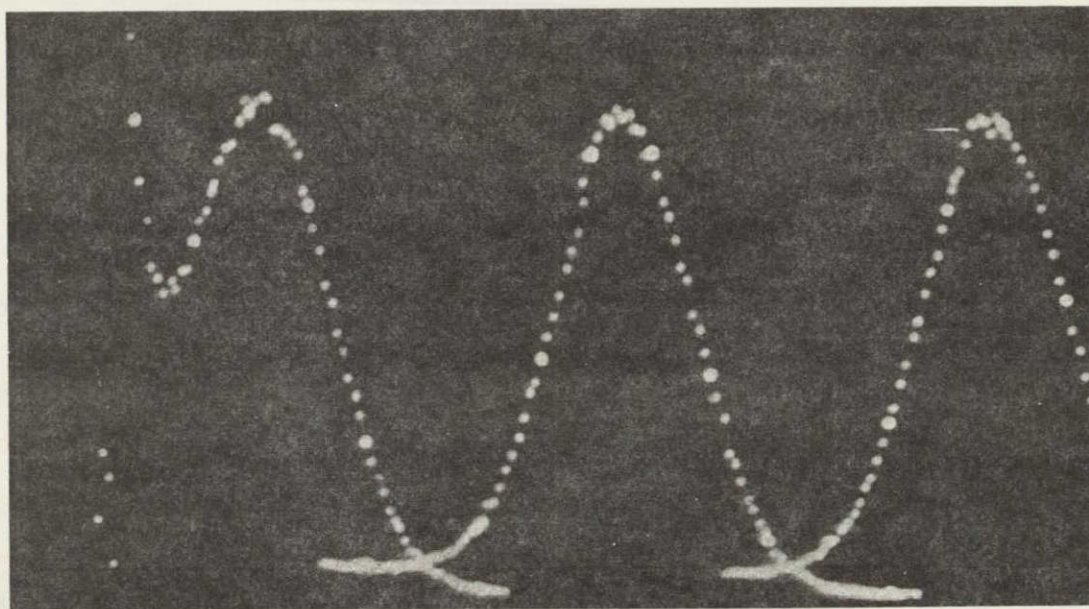
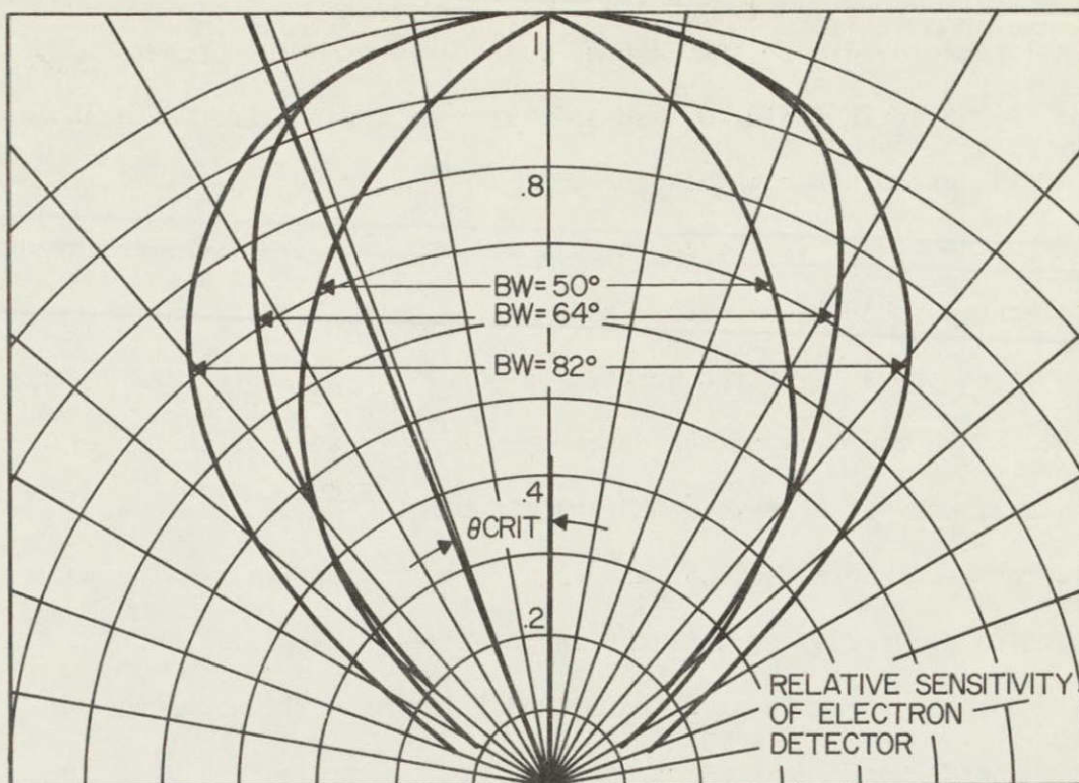


Figure 3.5 The upper diagram shows the angular patterns of the energetic particle detector. The beamwidth of  $60^\circ$  represents a collimator system and the beamwidth of  $82^\circ$  represents the effect of scattering for  $E > 50$  keV. The lower figure is a pulse-height analyzer spectrum for 20, 40, and 60 keV electrons.

precesses. The coordinate system used to describe the magnetometer signal in terms of the magnetic field,  $\vec{B}_0$  and spin axis of the rocket,  $\vec{S}$ , is shown in Figure 3.6(a) assuming that the detector is mounted perpendicular to the rocket axis. Here the origin of the coordinate system  $x, y, z$  is referenced to the center of the mass of the rocket with  $z$  in the direction of constant angular momentum (i.e. the axis of the precession cone) and  $\vec{B}_0$  positioned in the  $x, z$  plane.  $\vec{D}$  is the axis of the detector and  $\vec{x}'$  represents the intersection of the plane perpendicular to  $\vec{S}$  and the  $x, y$  plane. Derivatives  $d\psi/dt$  and  $d\phi/dt$  represent the precessional and spin rate, respectively. The precession half angle is denoted by  $\theta$ ,  $\gamma$  is the angle between the  $z$ -axis and  $\vec{B}_0$ ,  $\delta$  the angle between the spin axis and  $\vec{B}_0$  and  $\beta$  is the angle between  $\vec{B}_0$  and  $\vec{D}$ . The magnetometer signal is proportional to the projection of  $\vec{B}_0$  on the detector axis,  $\vec{D}$ , which is

$$B = B_0 \cos\beta \quad (3.1)$$

where  $\cos\beta$  is to be found as a function of  $\theta$ ,  $\psi$ ,  $\phi$ , and  $\gamma$ ;  $\psi$  and  $\phi$  are functions of time.

Before the complete geometry is solved, a useful result may be obtained by letting  $\theta = 0$ . This case (Figure 3.6c) is equivalent to the condition  $d\psi/dt \ll d\phi/dt$  and therefore the spin axis is taken to be in the  $z$  direction. The angle  $\delta$  is a function of the precession time. Using the definition of the vector dot product and letting  $\phi$  designate the angle between the  $x$  axis and  $\vec{D}$  then

$$\vec{B} \cdot \vec{D} = BD \cos\beta = B_x D_x = BD \sin\delta \cos\phi$$

which reduces to

$$\cos\beta = \sin\delta \cos\phi \quad (3.2)$$

where  $\delta$  is a function of the precession time and  $\phi$  is the spin rate  $\omega_s t$ .

ORIGINAL PAGE IS  
OF POOR QUALITY

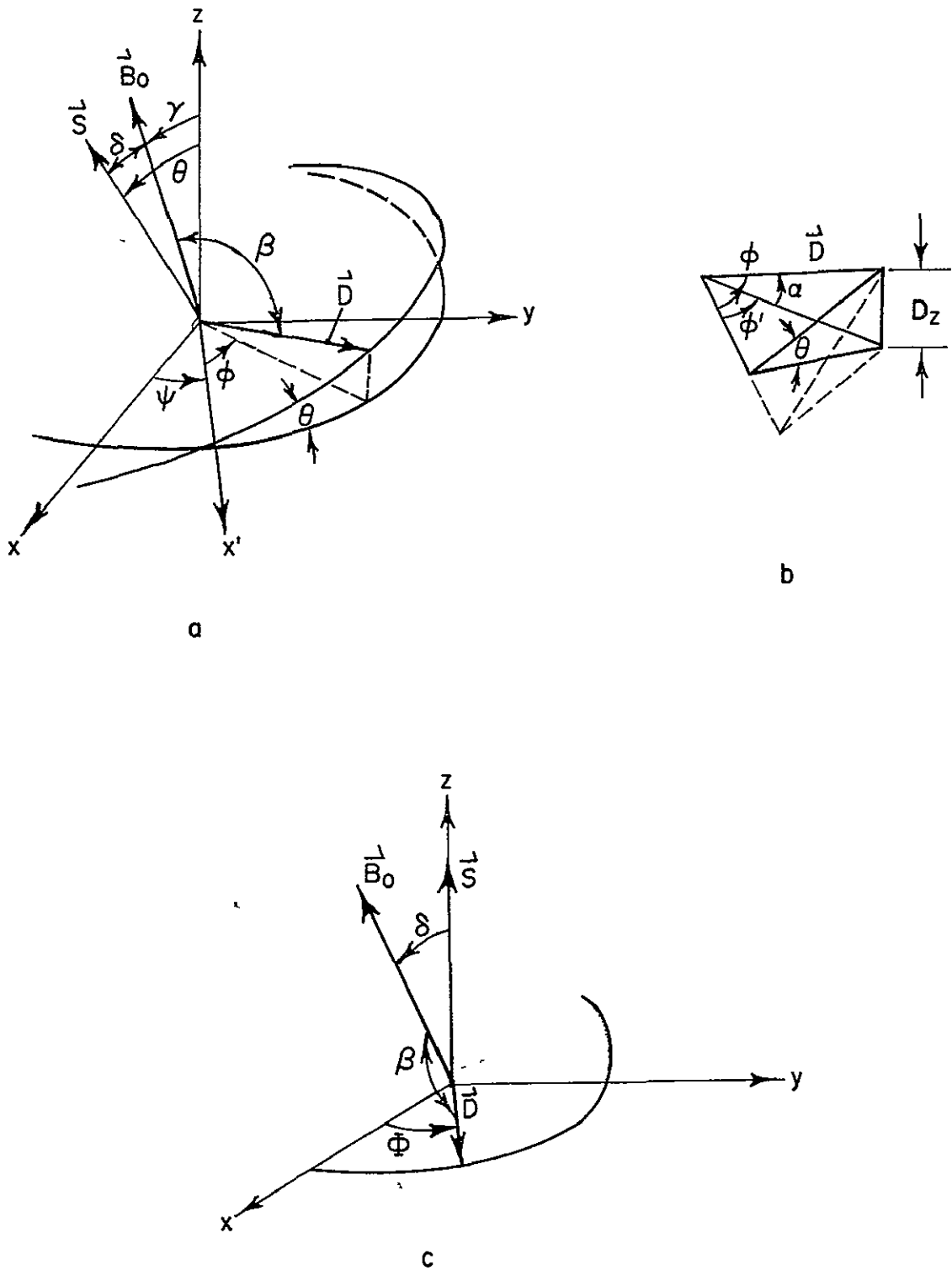


Figure 3.6 The coordinate system used to describe the magnetometer signal in terms of the magnetic field,  $\vec{B}_0$  and spin axis of the rocket,  $\vec{S}$ .



The cosine of the angle between the detector and the magnetic field (i.e., the pitch angle) is equal to the product of the sine of the angle between the magnetic field and spin axis and the cosine of the rocket azimuthal angle. A plot of this function is given in Figure 3.7. Note that the detector axis passes through the  $90^\circ$  pitch-angle position twice during each revolution.

The angle  $\delta$  may be found in terms of  $\theta$ ,  $\gamma$  and  $t$  by taking the dot product of  $\vec{S}$  and  $\vec{B}_O$  where  $\vec{S}$  is given by

$$\vec{S} = S \sin\theta \cos\omega_p t \hat{i} + S \sin\theta \sin\omega_p t \hat{j} + S \cos\theta \hat{k}$$

yielding

$$\vec{S} \cdot \vec{B}_O = S B_O \cos\delta = B_x S_x + B_z S_z$$

Substitution of the vector components and rearranging gives

$$\cos\delta = \sin\gamma \sin\theta \cos\omega_p t + \cos\gamma \cos\theta \quad (3.3)$$

Equations (3.2) and (3.3) can now be used to determine the variation of  $\beta$  with time by setting  $\phi = \delta_s t$ .

A general analysis of the detector motion can be derived utilizing the complete geometry presented in Figure 3.6. Taking the dot product of  $\vec{B}_O$  and  $\vec{D}$  yields

$$\vec{B}_O \cdot \vec{D} = B_O D \cos\beta = B_O D_x \sin\gamma + B_O D_z \cos\gamma \quad (3.4)$$

To determine the components  $D_x$  and  $D_z$  in terms of  $\phi$ ,  $\psi$  and  $\theta$  use is made of the angles defined in Figure 3.6(b) From the geometry

$$D_x = D \cos\alpha \cos(\psi + \phi')$$

$$D_z = D \sin\alpha$$

$$\sin\alpha = \sin\phi \sin\theta$$

$$\cos\phi' = \frac{\cos\phi}{\cos\alpha}$$

Making these substitutions in equation (3.4) and rearranging gives

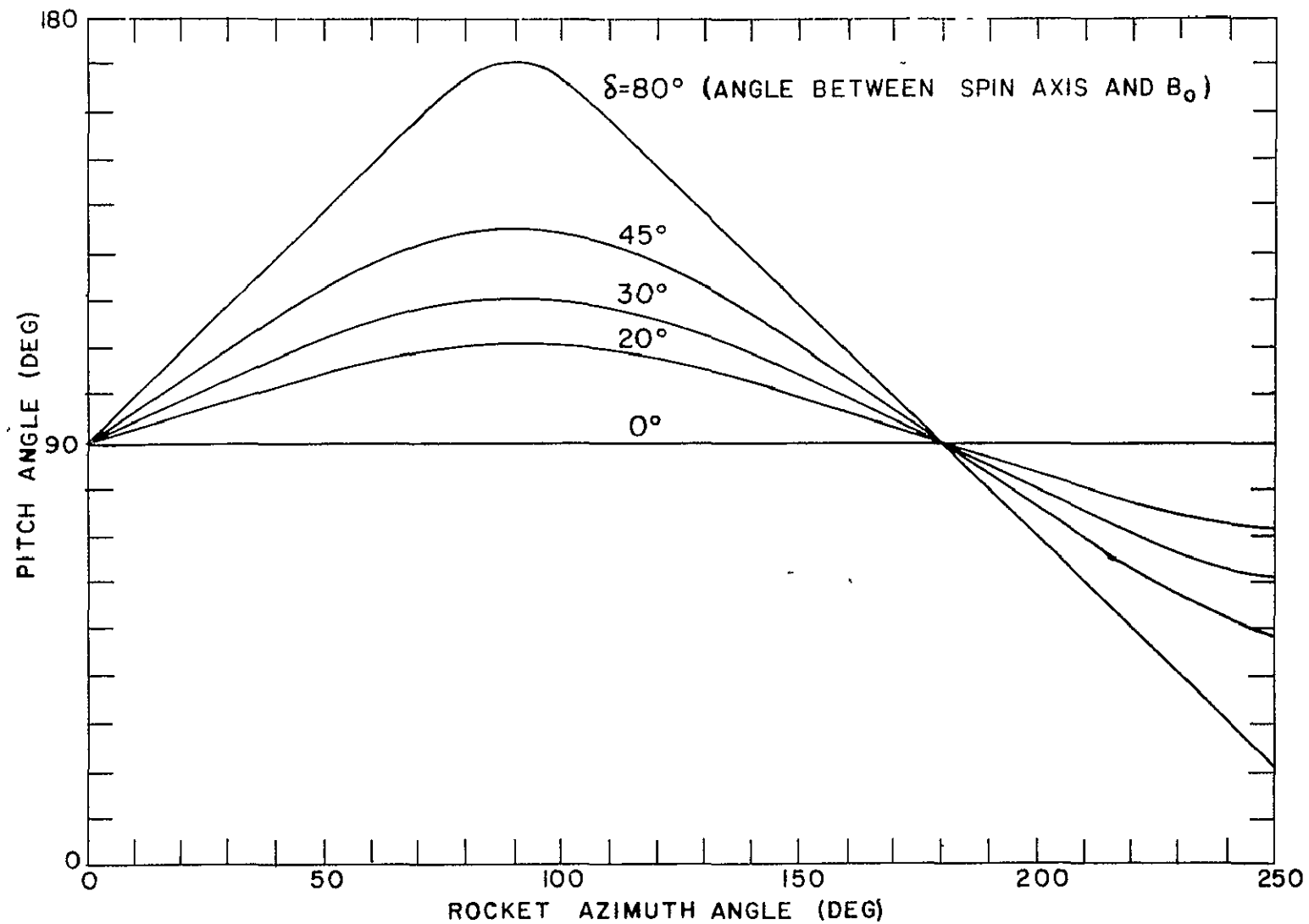


Figure 3 7 The variation of pitch angle normal to the detector with rocket azimuth for different angles,  $\delta$ , between the magnetic field and rocket spin axis. Note that the detector passes through 90° pitch angle twice each revolution.

$$\cos\beta = \sin\gamma(\cos\psi \cos\phi - \sin\psi \cos\theta \sin\phi) + \cos\gamma \sin\theta \sin\phi \quad (3.5)$$

For a detector set at an angle  $\eta$  with respect to the rocket spin axis equation (3.5) may be generalized to

$$\begin{aligned} \cos\beta = \sin\gamma \sin\eta(\cos\psi \cos\phi - \cos\theta \sin\psi \sin\phi) + \sin\gamma \cos\eta \sin\theta \sin\psi \\ + \cos\gamma \sin\eta \sin\theta \sin\phi + \cos\gamma \cos\eta \cos\theta \end{aligned} \quad (3.6)$$

A sketch of the magnetometer signal representing equation (3.6) is illustrated in Figure 3.8.

The angle  $\gamma$  may be determined from the ratio of the maximum to the minimum of the magnetometer signal over the precessional envelope. The minimum of the precessional signal occurs when  $\psi = 90^\circ$  and this reduces equation (3.5) to

$$B_{\min} = B_o \cos\beta = B_o \sin\phi[\cos\gamma \sin\theta - \cos\theta \sin\gamma]$$

The maximum of the precessional signal occurs when  $\psi = 270^\circ$  and

$$B_{\max} = B_o \sin\phi[\cos\gamma \sin\theta + \cos\theta \sin\gamma]$$

The ratio of  $B_{\max}$  to  $B_{\min}$  denoted by  $R$  is

$$\frac{B_{\min}}{B_{\max}} \equiv R = \frac{\cos\gamma \sin\theta - \cos\theta \sin\gamma}{\cos\gamma \sin\theta + \cos\theta \sin\gamma} \quad (3.7)$$

and solving equation (3.7) for  $\gamma$  yields

$$\tan\gamma = \frac{1 - R}{1 + R} \tan\theta \quad (3.8)$$

For example, if  $\theta = 17^\circ$  and  $R = 0.6$ , the angle,  $\gamma$ , between the center of the precession cone and  $\vec{B}$  is  $4.5^\circ$ . For a magnetometer which is not mounted perpendicular to the spin axis of the rocket ( $\eta \neq 90^\circ$ ) the angles  $\theta$ ,  $\gamma$  and  $\eta$  may be derived from the magnetometer signal.



ORIGINAL PAGE IS  
OF POOR QUALITY

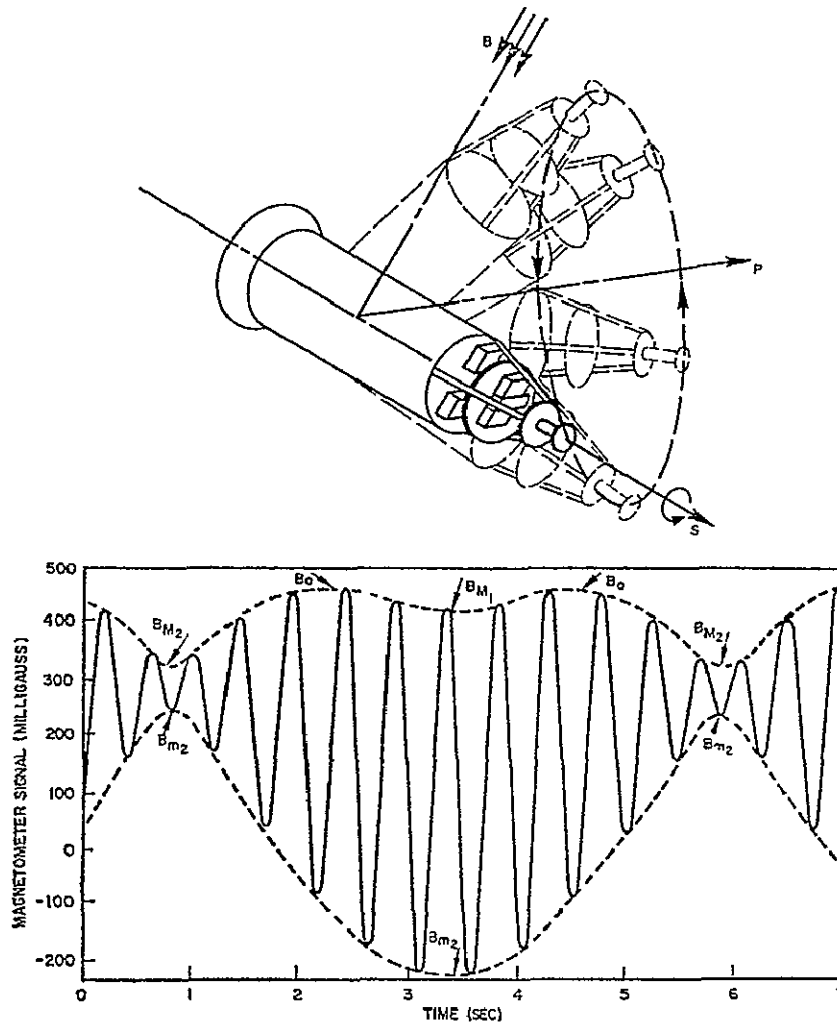


Figure 3.8 A sketch of the magnetometer signal representing equation (3.6).  
The figure is adapted from *Cladis et al.* [1961].

### 3.3 The Flux Related to the Detector Count Rate

3.3.1 *General considerations.* To interpret the count-rate profile, attention must be given to the energy and angular sensitivity of the detector. Moreover, for spiraling particles the count-rate profile is additionally affected by the pitch angle of the particles and by their gyroradius. These latter effects are often ignored but may contribute significantly to the derived flux,  $F(E, \alpha, d)$  particularly for pitch-angle distributions near  $90^\circ$  and for energies less than 5 keV.

To formulate the count rate function in terms of the significant variables, reference is made to the three models in Figure 3.9. Model 1 (Figure 3.9(a)) is to be used when the curvature in the magnetic field is important, i.e.,  $F(E, \alpha, d)$  is to be derived from a measurement made significantly far from  $d$  such that the  $B$  field curves. Here  $F(E, \alpha, d)$  is the unknown flux at some altitude  $d$  above the earth. The detector is at an altitude  $a$  and distance  $r$  from the dipole center.

Model 2 (Figure 3.9b) assumes that the magnetic field lines are straight but tilted at the dip angle  $\xi$  and that the rocket constant angular momentum vector,  $\vec{M}$ , makes an angle  $\gamma$  with the magnetic field. Model 3 (Figure 3.9(c)) assumes that the rocket constant angular momentum vector (center of precession cone) and magnetic field are parallel. Dimensions  $h$  and  $w$  refer to the effective height and width of the detector in the plane perpendicular to  $\vec{B}_0$ . Furthermore, it is found advantageous to reference the pitch angle in terms of its equivalent mirroring altitude located at an altitude  $z_m$  or a distance  $Z_m$  from the dipole center.

Before an analysis of the count rate is made, a short discussion will be given of the magnetic field of the earth. The dipole approximation is

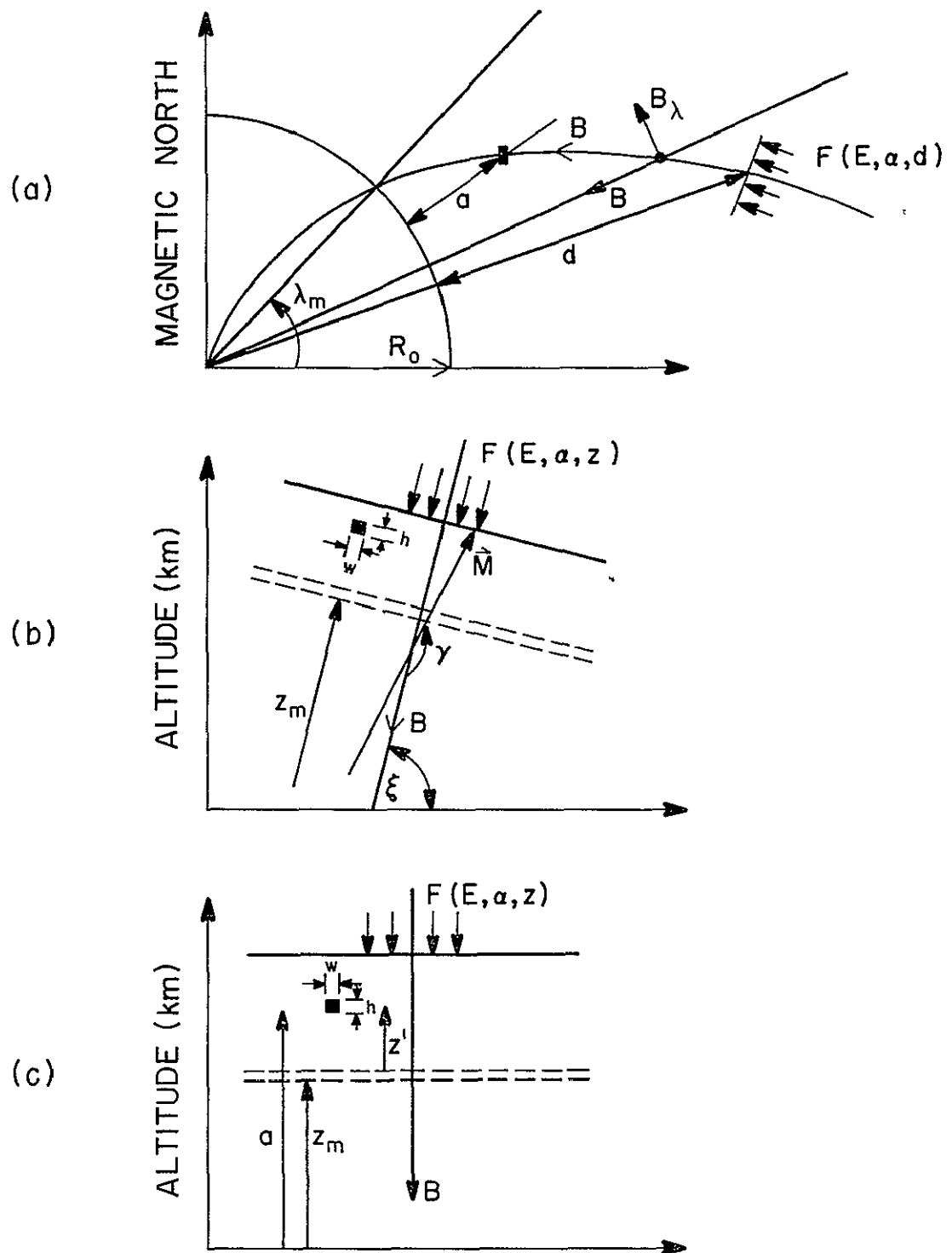


Figure 3.9 Three models are shown representing the particle flux  $F(E, \alpha, d)$  along a field line making various approximations as described in the text

accurate to within 10% near the surface of the earth if the dipole center is taken to be displaced 100 km toward the western Pacific from the center of the earth. The further distant one goes from the earth the dipole approximation becomes more accurate since the higher order multiple expansion terms fall off radially faster than the dipole term [Fan *et al.*, 1961].

The dipole field variation with geomagnetic latitude  $\lambda$  and radial distance  $r$  is given by

$$B(r, \lambda) = \frac{M}{r^3} \left( 1 + 3 \sin^2 \lambda \right)^{1/2} \quad (3.9)$$

where  $M$  is the earth's dipole moment ( $8.06 \times 10^{22}$  A-m<sup>2</sup>). The polar components of the field are

$$\begin{aligned} B_r &= -\frac{2M}{r^3} \sin \lambda \\ B_\lambda &= \frac{M}{r^3} \cos \lambda \end{aligned} \quad (3.10)$$

It follows that the equation of a field line is given by

$$r = r_o \cos^2 \lambda \quad (3.11)$$

where  $r_o$  is the radial distance of the field line at the equator.

The angle of the field line with the vertical at some altitude,  $\alpha$ , may be found from equations (3.9), (3.10) and (3.11) as

$$\sec \theta = \frac{ds}{dr} = -\frac{B}{B_r} = \frac{1}{2} \left( \frac{1 + 3 \sin^2 \lambda}{\sin^2 \lambda} \right)^{1/2} = \frac{1}{2} \left( \frac{4 - 3(r/r_o)}{1 - (r/r_o)} \right)^{1/2} \quad (3.12)$$

where

$$r/r_o = (1 + a/R_o) \cos^2 \lambda_m$$

and  $\lambda_m$  is the geomagnetic latitude of the place where the field line reaches the earth's surface. The angle  $90^\circ - \theta$  is called the magnetic dip angle. Figure

3.9(b) illustrates the model used when  $\theta$  remains approximately constant over the region of interest.

For a particle which mirrors at an altitude  $z_m$  in a dipole field the path length,  $s$ , swept out by the gyrating particle as it recedes from  $z_m$  may be deduced as follows.

Utilizing the first adiabatic invariant, the pitch angle  $\alpha$  for a particle which mirrors at field intensity  $B_m$  is related to the magnetic field,  $B$ , at a certain height by

$$\cos^2 \alpha = 1 - \frac{B}{B_m} \quad (3.13)$$

Also from the geometry of the velocity vector

$$\frac{ds}{dz} = \frac{v}{v_z} = \frac{1}{\cos \alpha} \quad (3.14)$$

Equation (3.14) shows that the path length of a mirroring particle is independent of the particle energy. This occurs because, as the gyroradius increases with energy, the pitch of the helix increases correspondingly. Integration of 3.14 for a dipole field from  $z_m$  to  $Z$  yields a rather complex expression for  $s$

$$s = \int_{z_m}^Z \left( 1 - \frac{z_m^3}{Z^3} \right)^{1/2} dz \quad (3.15)$$

where  $z_m = R_o + z_m$ ,  $Z = R_o + z$  and  $R_o$  is the earth radius.

This expression for the path length can be significantly simplified by making the reasonable approximation that the magnetic field strength near  $z_m$  decreases linearly with increasing altitude as

$$B = B_m \left( 1 - \frac{z}{R_o} \right) \quad (3.17)$$

where  $z$  is the altitude above the mirroring altitude  $z_m$ . Now substitution of this linear variation of  $B$  in equation (3.13) and integrating equation (3.14) from zero to  $z$  gives

$$s = 2 \sqrt{\frac{R_o z}{3}} \approx 91.1 \sqrt{z} \quad (3.18)$$

where  $z$  and  $s$  are expressed in kilometers. Therefore, the actual distance traveled by a mirroring particle in the first kilometer above its mirror point is 91 km.

If over one gyration of the helix the magnetic field is assumed constant, the path length  $\Delta s$  is

$$\Delta s = R \sqrt{4\pi^2 + \cot^2 \alpha} \quad (3.19)$$

where  $R$  is the gyroradius and  $\alpha$  is the pitch angle. Now by differentiating equation (3.18) and eliminating  $\Delta s$  from equation (3.19) and solving for  $\Delta z$  which is also the pitch,  $P$ , of the helix, one obtains

$$\Delta z \equiv P = R \left\{ \frac{3(\alpha - z_m)}{R_o} \left[ 4\pi^2 - 1 + \left( \frac{R_o + \alpha}{R_o + z_m} \right)^3 \right] \right\}^{\frac{1}{2}} \approx 2\pi R \left( \frac{3(\alpha - z_m)}{R_o} \right)^{\frac{1}{2}} \quad (3.20)$$

A plot of  $P$  versus  $\alpha$  is shown in Figure 3.10. For pitch angles near  $90^\circ$  the path length  $\Delta s$  can be approximated by  $2\pi R_m$  and equation (3.20) reduces to

$$P = 2\pi R_m \sqrt{\frac{3}{R_o} (\alpha - z_m)} \quad (3.21)$$

where  $R_m$  is the gyroradius at the mirror point (in the absence of collisions). Equations (3.20) and (3.21) give identical results over the range of values plotted in Figure 3.10.

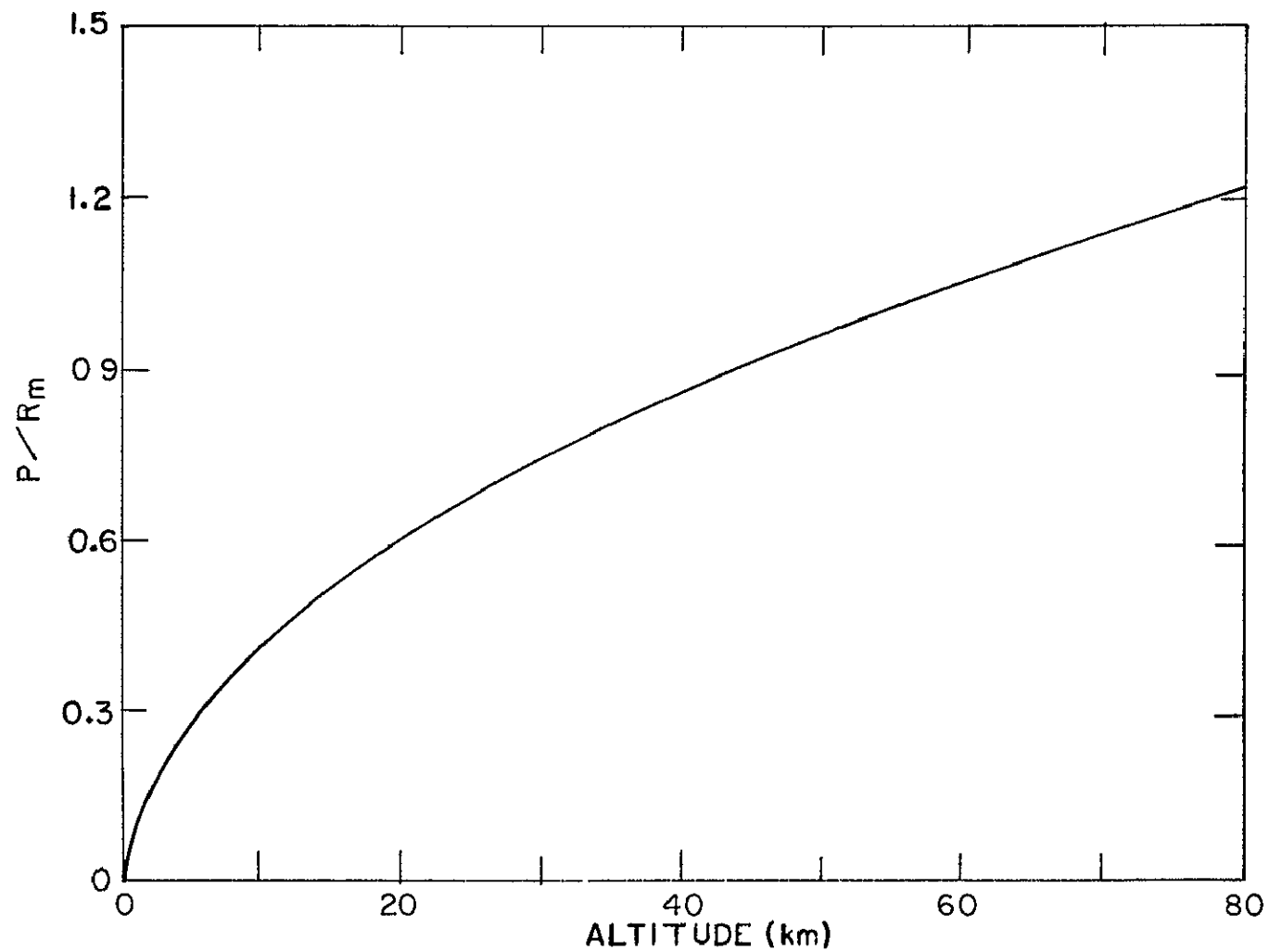


Figure 3.10 Pitch as a ratio with gyroradius at the mirror point plotted against altitude above the mirror point.

3.3.2 *Detector count rate.* To relate the measured count rate to the incident flux,  $F(E, \alpha, z)$  passing through the plane perpendicular to  $\vec{B}_0$ , proper attention must be made of the effective area, weighting functions and probabilities of particle-detector collisions. To facilitate an understanding in the essentials use is first made of Model 3 shown in Figure 3.9(c)

For this case, assuming no significant scattering or energy loss over the regions of interest, the count rate is simply the sum of all the incremental energy and angular intervals times their weighted transparency. The count rate for the  $i$ th channel may be expressed as

$$C_i = \int_0^\infty \int_{-R_0}^{\alpha} F(E, z_m, d) h_i(E) g[(\alpha - \alpha_0(t))] \frac{h}{P(z_m, \alpha, E)} A(E) dz_m dE \quad (3.22)$$

where  $F(z_m, E, d)$  is the incident flux at some reference altitude  $d$  (Figure 3.9),  $h_i(E)$  is the energy weighting function of the detector for the  $i$ th energy channel,  $g[\alpha - \alpha_0(t)] = g(\theta)$  is the angular pattern of the detector (Figure 3.5a) where  $\alpha$  is expressed as an equivalent mirror height,  $z_m$ , and  $\alpha_0(t)$  is the pitch angle of particles entering along the axis of the detector and is also expressed in terms of  $z_m$ ;  $h/P(z_m, \alpha, E)$  is the probability that a particle with pitch angle  $z_m$  will intercept the detector, where  $h$  is the effective height of the detector and  $P(z_m, \alpha, E)$  is the pitch of the particle given by equation (3.20); and  $A(E)$  is the area factor for the detector as defined below

The area factor is referenced to the plane perpendicular to  $\vec{B}_0$  defined by  $F(E, \alpha, d)$  as illustrated by the shaded region in Figure 3.11(a). Since magnetospheric particles execute circular motion in this view, only those particles which have guiding centers within the shaded region are able to impinge on the



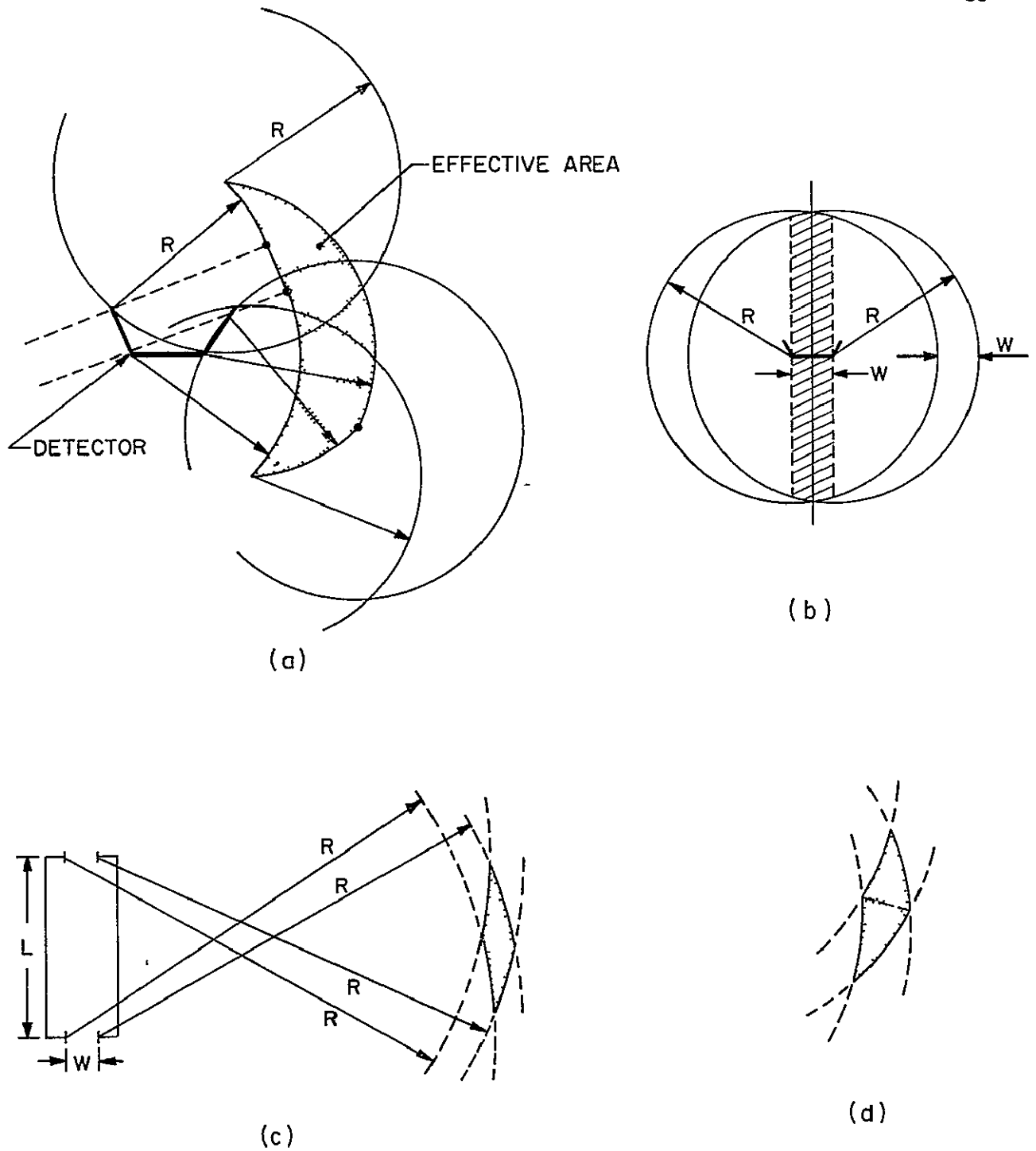


Figure 3.11 Looking down the magnetic field line at the detector as shown, it is found that only particles with gyrocenters inside of the shaded area are able to reach the detector sensitive area. An approximation to this complex geometry is shown in (b). For collimators the effective projected area is significantly reduced as shown in (c) and (d)

detector for any particular energy  $E$ . In this view the detector has a width,  $w$ , and a collimator dimension as drawn.

To the first approximation (Figure 3.11(b)) the shaded area of two offset circles approximates the shaded area of Figure 3.11(a) for a gyro-radius  $\gg w$ , and for a large collimator opening. Integration of this area gives

$$A_p = 2wR \quad (3.23)$$

Figure 3.11(c) illustrates the case for a detector when the collimator field of view is small and the gyroradius is much greater than the detector width,  $w$ . For this case the four limit points are calculated and the area is accurately approximated as that of two indentical triangles. Again by making the approximation as shown in Figure 3.11(d) the projected area is easily calculated. By writing the equation of the two circles which intersect the upper most point,  $A$ , and solving for the  $y$  value the area becomes

$$A_p = 2 \frac{w^2}{l} R \quad (3.24)$$

where  $l$  is the length of the collimator. In both equations (3.23) and (3.24) the projected area is proportional to  $w$  and  $R$  and varies with a square root dependence on energy.

Substitution into the count rate equation (3.22) of equations (3.20), (3.23), (3.5) and the first adiabatic invariant yields

$$C_z(t) = \int_0^\infty \int_{-R_0}^\alpha F(E, z_m, d) h_z(E) g[\alpha(z_m, E) - \alpha_0(t)] \frac{2w\hbar}{k(z_m, \alpha)} dz_m dE \quad (3.25)$$

where

$$\alpha(z_m) = \sin^{-1} \left( \frac{z_m}{R_o + \alpha} \right)^{3/2}$$

$$\cos \alpha_o(t) = \sin \gamma (\cos \omega_p t \cos \omega_s t - \sin \omega_p t \cos \theta \sin \omega_s t) + \cos \gamma \sin \theta \sin \omega_s t$$

$$k^2(z_m, \alpha) = \frac{3(\alpha - z_m)}{R_o} \left[ 4\pi^2 - 1 + \left( \frac{R_o + \alpha}{R_o + z_m} \right)^3 \right] \approx \frac{12\pi^2(\alpha - z_m)}{R_o}$$

Now assuming that the weighting functions  $h$  and  $g$  are square step passbands with limits of  $E_H$ ,  $E_L$  and  $\pm \theta_{\max}$  and that the flux,  $F$ , is expressible as the product  $I_o J(E) f(\alpha)$  then equation (3.25) may be reduced to

$$C_z(\alpha, t) = 2A_d \int_{E_L}^{E_H} J(E) \int_{Z_1}^{Z_2} \frac{f(z_m)}{k(z_m, \alpha)} dz_m dE \quad (3.26)$$

where

$A_d$  is the area of the detector ( $=wh$ )

$$Z_1 = (R_o + \alpha) \sin^{2/3} [\alpha_o(t) - \theta_{\max}]$$

$$Z_2 = (R_o + \alpha) \sin^{2/3} [\alpha_o(t) + \theta_{\max}]$$

The energy spectrum  $J(E)$  in many cases may be approximated by a power law,  $I_o E^{-x}$ , or by an exponential  $I_o e^{-E/E_o}$ . For a power law energy spectrum equation (3.26) simplified to

$$C_z(\alpha, t) = \frac{2A_d I_o}{1-x} \left( E_H^{1-x} - E_L^{1-x} \right) \int_{Z_1}^{Z_2} \frac{f(z_m)}{k(z_m, \alpha)} dz_m \quad (3.27)$$

Equation (3.27) is an integral equation and may be solved numerically for specified variations of the count rate with time and altitude. Upon analysis the angular dependence of the incident flux may be determined (see Section 3.5). For the special case when  $\alpha = 1$  in a power law spectrum equation (3.27) transforms to a logarithmic dependence on the ratio of the energy thresholds.

**3.3.3 Shadowing by the payload.** The shadowing of the particle sensor by the rocket body may cause a significant modulation and reduction in the measured particle flux. This effect is most pronounced for trapped particles which have peaked intensities near  $\alpha = 90^\circ$ . These quasi-trapped particles are typical for midlatitude observations. From Figure 3.10 or equation (3.20) the magnitude of the pitch can be comparable to the dimension of the rocket and consequently capable of scattering under proper vehicle orientation. Figure 3.12 illustrates this shadowing effect in the plane perpendicular to  $\vec{B}_0$  and the side view plane. As the rocket spins the shadowing effect similarly changes and is greatest in the positions number 1 and 3 (in the plane of  $\vec{B}_0$  and  $\vec{S}$ ) and smallest in the positions 2 and 4. The count rate will consequently be modulated at twice the spin rate of the rocket.

To obtain a typical correction factor, equation (3.27) may be used to represent the shadowing by assuming that the upper limit of the integral varies with time and energy. This is so since particles which mirror in the vicinity of the rocket will be most affected. Now assuming that the incident pitch-angle distribution,  $f(z_m)$ , is given by a square root dependence (equation 7.2) and that the pitch is given by equation (3.21) then

$$C(t) = \frac{A d_o I_o}{\pi} \sqrt{\frac{R_o}{3}} \int_{E_L}^{E_H} E^{-\alpha} \int_{z_o}^{\alpha \delta(t, E) \frac{\sqrt{z_m - z_o}}{\sqrt{\alpha - z_m}}} dz_m dE \quad (3.28)$$

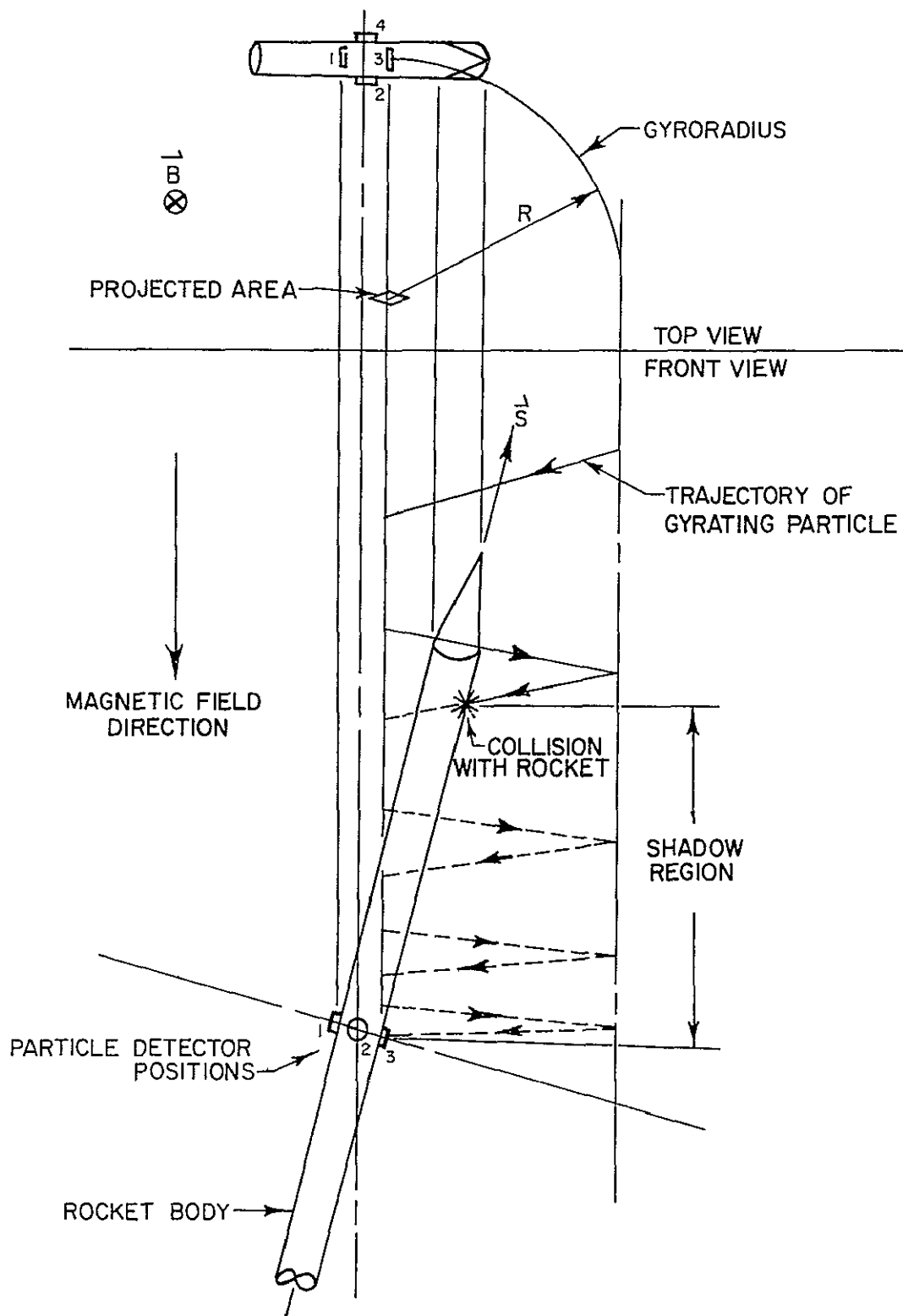


Figure 3.12 The shadowing of the particle sensor by the rocket body may cause significant modulation and reduction in the measured particle flux. Illustrated is a charged particle with gyro-radius,  $R$ , which would intersect the detector at the number 3 position if no collision with the rocket body occurred

where  $\delta(t, E)$  is the shadowing distance and, utilizing equation (3.21), may be defined as

$$\delta(t, E) = \frac{2 m_e}{6\pi q^2 B^2} \frac{d_m^2}{E} \cos 2\omega_s t \quad (3.29)$$

where  $d_m$  is the maximum shielding length of the rocket. Integration of equation (3.28) yields

$$C = \frac{A d_o}{\pi} \sqrt{\frac{R_o}{3}} I_o(\alpha - z_o) \left[ \cos^{-1} \sqrt{\frac{\delta}{\alpha - z_o}} - \frac{\sqrt{\delta(\alpha - z_o - \delta)}}{\alpha - z_o} \right] \quad (3.30)$$

For  $\delta = 2$  km and  $\alpha - z_o = 50$  km the ratios of the bracketed expression to the case when  $\delta$  is zero is

$$R = \frac{1.17}{1.57} = 0.75 \quad (3.31)$$

The count rate varies in this case by 25% for  $\alpha - z_o = 50$  km. A more rigorous analysis can be made by substitution of equation (3.29) into equation (3.28) and integrating over energy giving

$$C = \frac{A d_o}{2\pi^2} \frac{m_e}{q^2 B^2} \left( \frac{R_o}{3} \right)^{3/2} \frac{d_m^2}{x} \left( E_L^{-x} - E_H^{-x} \right) \cos 2\omega_s t \quad (3.32)$$

In summary the shadowing effect varies at twice the spin rate and may alter the count rate by 25% or more depending on the pitch-angle distribution energy spectrum, and rocket orientation with respect to the field line.

6-2

#### 4 DIRECT OBSERVATIONS OF ENERGETIC ELECTRONS

The most direct measurements of energetic charged particles interacting with the atmosphere can be made with properly designed rocket- or satellite-borne particle spectrometers. This type of experiment is capable of providing excellent height resolution in the energy spectrum and pitch-angle distribution. Although many rocket measurements have been made at high latitudes, relatively few have been concerned with middle and low latitude observations. In fact, much of the previous middle and low latitude data has been obtained fortuitously from the results of high background particle counts on rocket-borne X-ray experiments.

In this chapter new rocket measurements obtained at Wallops Island (representing a midlatitude location) and at Chilca, Peru (at the geomagnetic equator) are presented. These are then combined with satellite and other rocket observations to obtain a picture of energetic electron precipitation at middle and low latitudes, particularly with respect to variations with geographic location, altitude and magnetic activity.

##### 4.1 *New Rocket Measurements at Midlatitudes*

In the present investigation four particle experiments have been flown on rockets launched from Wallops Island (38°N, 75°W, geomagnetic latitude 49°N,  $L = 2.56$ ). The first payload on Nike Apache 14 439, launch time 0003 EST, 1 November 1972, was equipped with a Geiger counter sensitive to electrons with energy greater than 70 keV and to X-rays between 2 to 8 Å [Smith et al., 1974]. The high particle count rate observed on this flight warranted further investigation and this, in part, initiated the decision to design and construct an advanced solid-state

particle spectrometer (see Chapter 3). The four subsequent flights at midlatitudes and the two equatorial flights were each equipped with the energetic-electron spectrometer (EES), nose-tip electrode Langmuir probe [Smith, 1969] and a radio-wave-propagation experiment [Mechtly and Smith, 1970].

4.1.1 *Nike Apache 14.439, 1 November 1972.* The Geiger counter flown on Nike Apache 14.439 used a beryllium window of area  $0.203 \text{ cm}^2$  and thickness  $5.1 \times 10^{-3} \text{ cm}$ . The geometric factor is  $0.303 \text{ cm}^2 \text{ ster}$ . The counter was oriented perpendicular to the spin axis of the rocket and thereby was most sensitive to particles with pitch angles near  $90^\circ$ .

The count rate measured during the flight is shown in Figure 4.1. The uncertainty in the count rate is indicated by error bars at representative points. In other (daytime) flights with identical counters the background count rate, due to cosmic rays, has been found to be about  $10 \text{ s}^{-1}$  at altitudes greater than 40 km. This background has been subtracted for the data shown in the figure. The count rate reaches a maximum value of  $478 \pm 11 \text{ s}^{-1}$ , which gives a flux ( $< 70 \text{ keV}$ ), assumed isotropic, of  $1577 \pm 36 \text{ cm}^{-2} \text{ s}^{-1} \text{ ster}^{-1}$ . The average flux for times greater than 108 s from launch (altitudes  $> 135 \text{ km}$ ) is  $167 \text{ s}^{-1}$  or  $551 \text{ cm}^{-2} \text{ s}^{-1} \text{ ster}^{-1}$ .

A particularly interesting feature of the count-rate profile is that the rate increases significantly at altitudes above 135 km. Since 70 keV electrons penetrate down to 100 km before appreciable absorption, the increased count rate with altitude may be due to. 1) a temporal build-up, 2) a pitch-angle distribution maximized around  $90^\circ$  such that the majority of particles are backscattering or magnetically reflecting, and 3) atmospheric scattering and diffusion away from the detector field of view



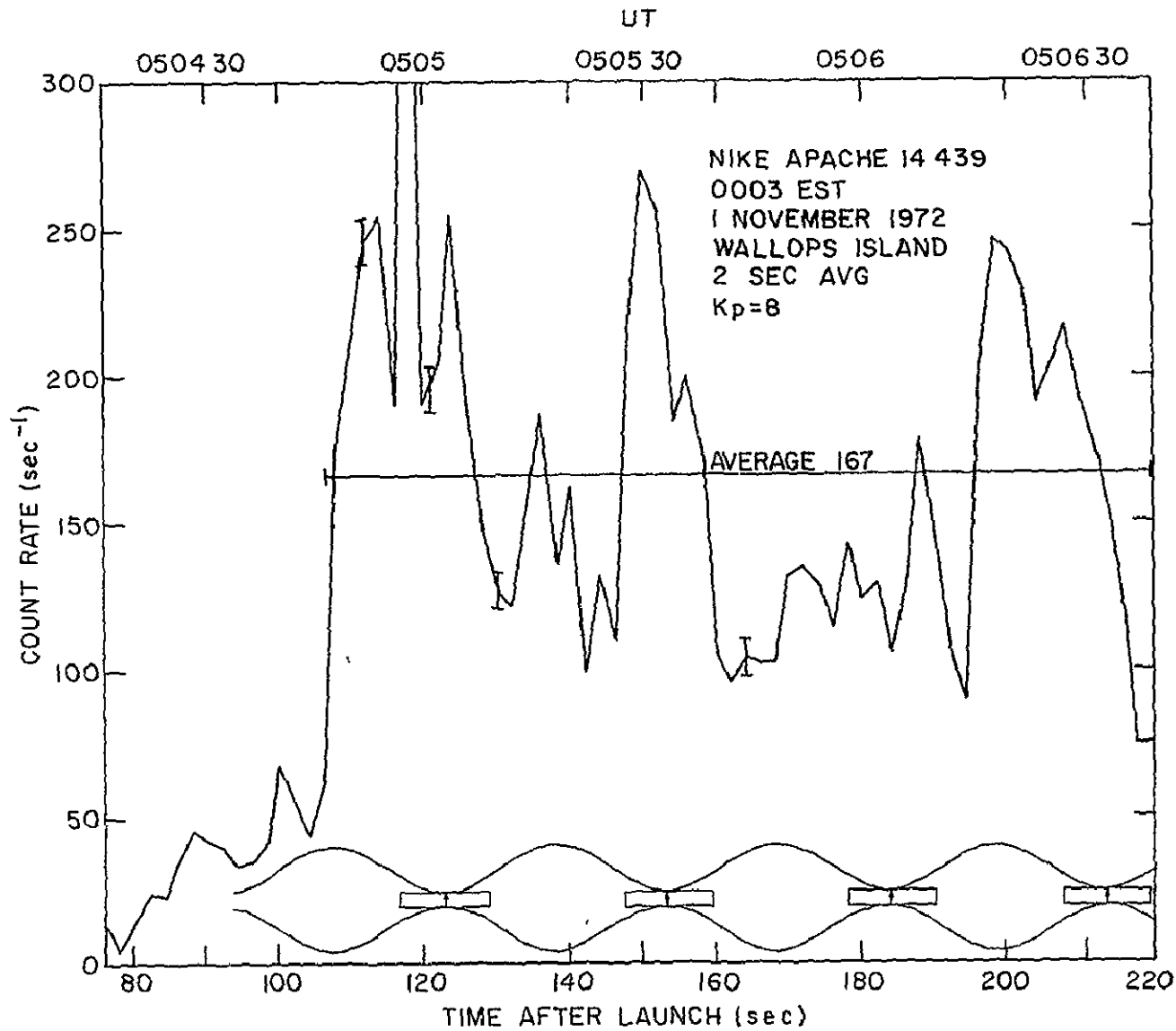


Figure 4 1 Nike Apache 14 439 count rate observed on a disturbed night at Wallops Island using a Geiger counter sensitive to electrons ( $> 70$  keV). Also shown is the magnetometer precession envelope

The temporal variations exhibited in the profile are similar to those observed at auroral latitudes. This variability is expected since the Kp for this period was very disturbed at 8. Furthermore, satellite data show that Wallops Island was at that time at the edge of the plasmapause. The most pronounced temporal variation occurs at 114 seconds at which time the flux increases from  $190 \text{ s}^{-1}$  to  $478 \text{ s}^{-1}$  and back to  $190 \text{ s}^{-1}$  in an interval of two seconds. This is a factor of 2.5 in flux.

Also shown in Figure 4.1 is the envelope of the magnetometer signal which is related to the precessional motion of the rocket. The included angle ( $\theta$ ) of the precession cone is  $17.1^\circ$  and the angle ( $\gamma$ ) between the axis of the precession cone and the magnetic field is given by equation (3.8) where  $B_{\text{max}} = 1.45$  and  $B_{\text{min}} = 0.4$ , yielding  $\gamma = 10^\circ$ . When the envelope is narrowest, the rocket is closest to the magnetic field direction and hence samples the energetic electrons predominantly around  $90^\circ$  pitch angle (Figure 3.7). The primary maxima of the count rate correlate fairly well with the minima of the envelope, except at 200 sec which may be attributed to a large temporal injection similar to that at 188 seconds. Subsequent flights have all shown a stronger correlation with the precession and spin period and with lower energies.

The rapid increase in the count rate at 135 km (see Figure 4.2) is unexpected (unless totally a temporal change) since 70 keV electrons are not absorbed until approximately 100 km altitude. This apparent anomaly may be explained if the majority of the particles are initially near  $90^\circ$  in pitch angle i.e., quasi-trapped. When the particles reach the atmospheric depth of 135 km, the exponential atmosphere scatters and more evenly distributes the particles over all pitch angles. The

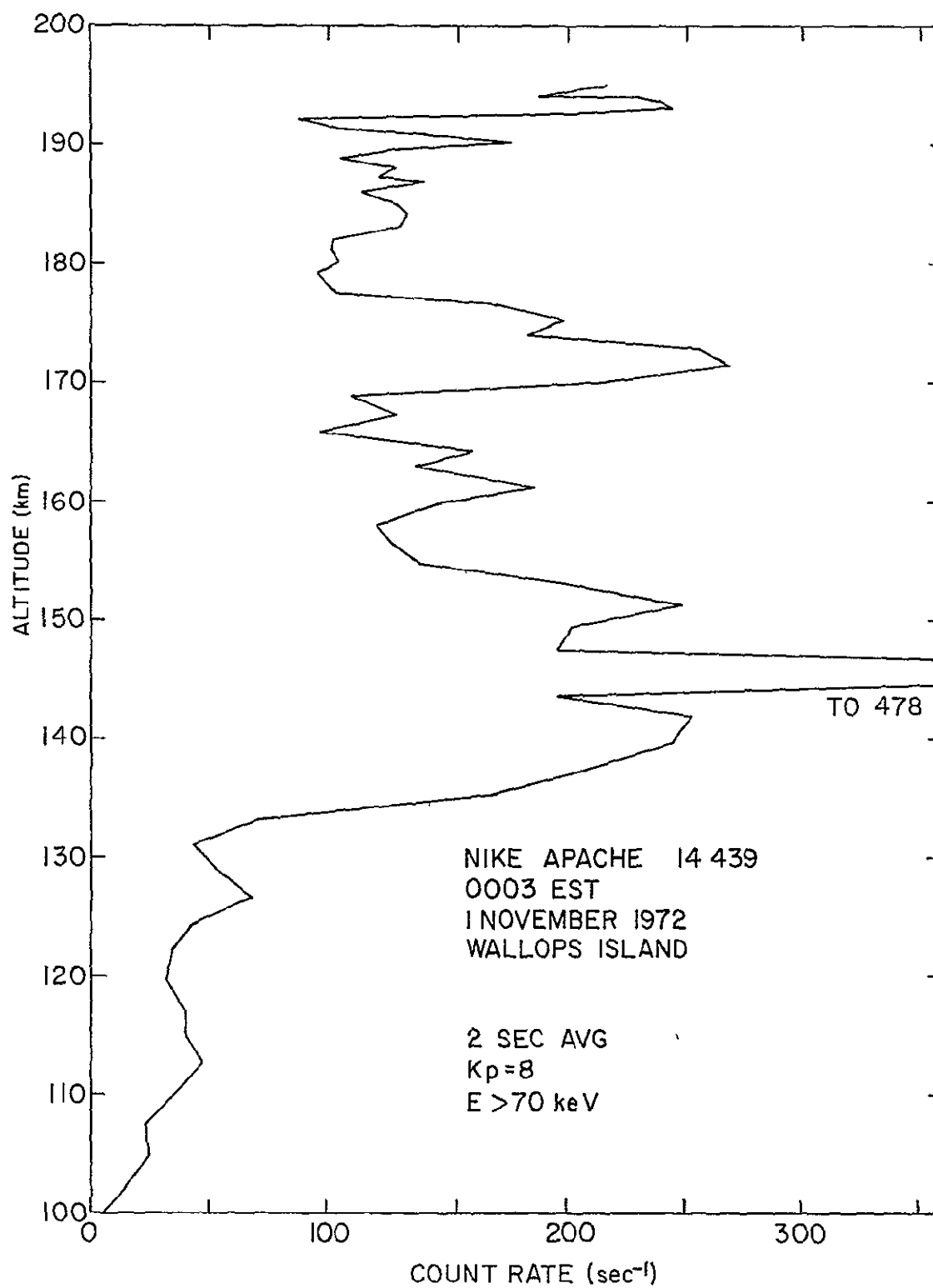


Figure 4 2 Nike Apache 14 439 count rate versus altitude on a disturbed night at Wallops Island using a Geiger counter sensitive to electrons ( $> 70$  keV)

detector samples primarily around  $90^\circ$  and therefore records a lower flux in the detector field of view because of the strong diffusion toward isotropy. This same cutoff at approximately 135 km is observed on all midlatitude flights, thereby eliminating the time variation hypothesis. A quantitative analysis of this scattering effect will be given later (in Chapter 8).

The electron density profile observed for this very disturbed magnetic condition exhibits strong small-scale fluctuations as seen in Figure 2.1. This phenomena is unlike all other midlatitude electron-density profiles which are observed to be relatively smooth, however, similar fluctuations have been observed in the auroral regions. Detailed explanations of this phenomenon should be further investigated and may be associated with 1) large scale source fluctuations in time and space which in part may excite instabilities, 2) electric fields or other mechanisms which may excite instabilities, and 3) a turbulent transport phenomenon.

Figure 4.3 is a plot of the electron density and count rate as a function of time for the altitude range 130 to 140 km. Although the 70 keV particle flux does not contribute significantly to the ionization at these altitudes, the flux is representative of the temporal changes of the lower portions of the energy spectrum. In Figure 4.3 the electron-density profile indicates small enhancements modulated on a more slowly varying background. As indicated by the arrows there seems to be fairly good agreement between the flux build-up (solid arrow) and the delayed (1 sec) electron-density enhancement (dashed arrow). Further analysis of the electron-density profile shows similar behavior. *Pfister* [1967] has shown the same effect in the auroral region.

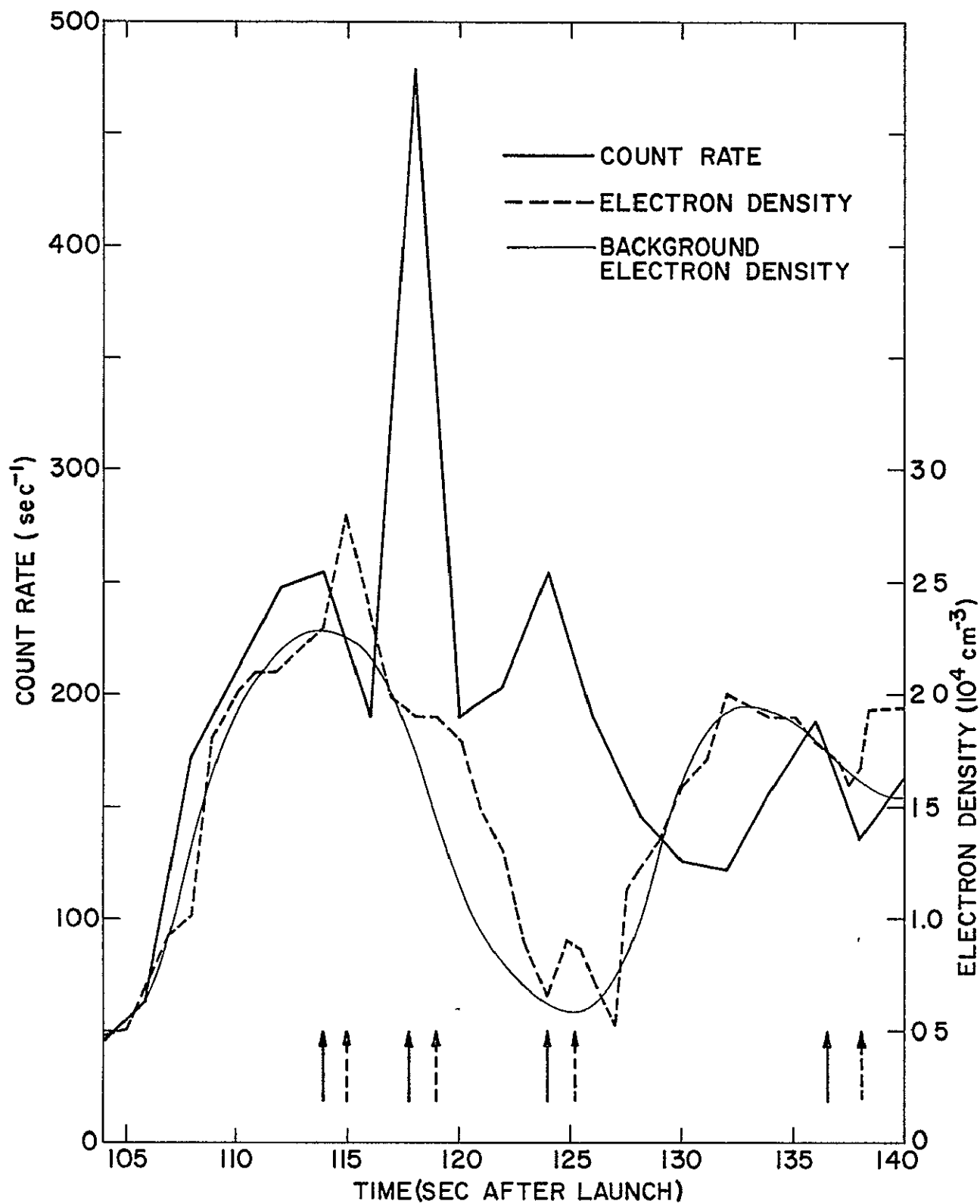


Figure 4.3 Small-scale modulation of the electron-density profile by energetic electron burst. The arrows indicate peaks.

A large particle impulse would be expected to yield rapidly a small increase in the electron density. The subsequent decay of the electron density, however, would be expected to be slow if only recombination is invoked ( $\tau \approx 10$  min for  $N \approx 10^4 \text{ cm}^{-3}$ ). The fact that the electron density decreases rapidly may be due to 1) a localized enhancement in ionization through which the rocket passes (the rocket velocity is about  $1 \text{ km s}^{-1}$ ), 2) a diffusion or turbulent mixing of the plasma, and 3) a plasma instability which may break up a localized enhancement.

The downleg portion of the electron density and the count-rate profiles (not shown) both have significantly smaller and less frequent fluctuations. This is consistent with the idea that the particle source excites the instabilities.

4.1.2 *Nike Apache 14.520; 18 April 1974.* The first flight utilizing the energetic electron spectrometer was Nike Apache 14.520, launched at 2330 EST on 18 April 1974 from Wallops Island, Virginia. The solid-state detector had a sensitive area of  $50 \text{ mm}^2$ , a field of view of  $64^\circ$  and was mounted with its axis perpendicular to the spin axis of the rocket. The magnetic conditions were moderately disturbed with the  $K_p = 5+$ . Figure 4.4 shows the count rate versus time for energies of 12, 25, 36, 48 and 80 keV. Each profile uses counts measured in one-second intervals.

Particularly noticeable on these profiles is the modulation associated with precessional motion of the rocket. The arrows indicate the times when the rocket is closest to the magnetic field direction and thereby sampling around  $90^\circ$ . Also, it can be seen that at the lowest altitudes the modulation peaks become more pronounced for higher energies.

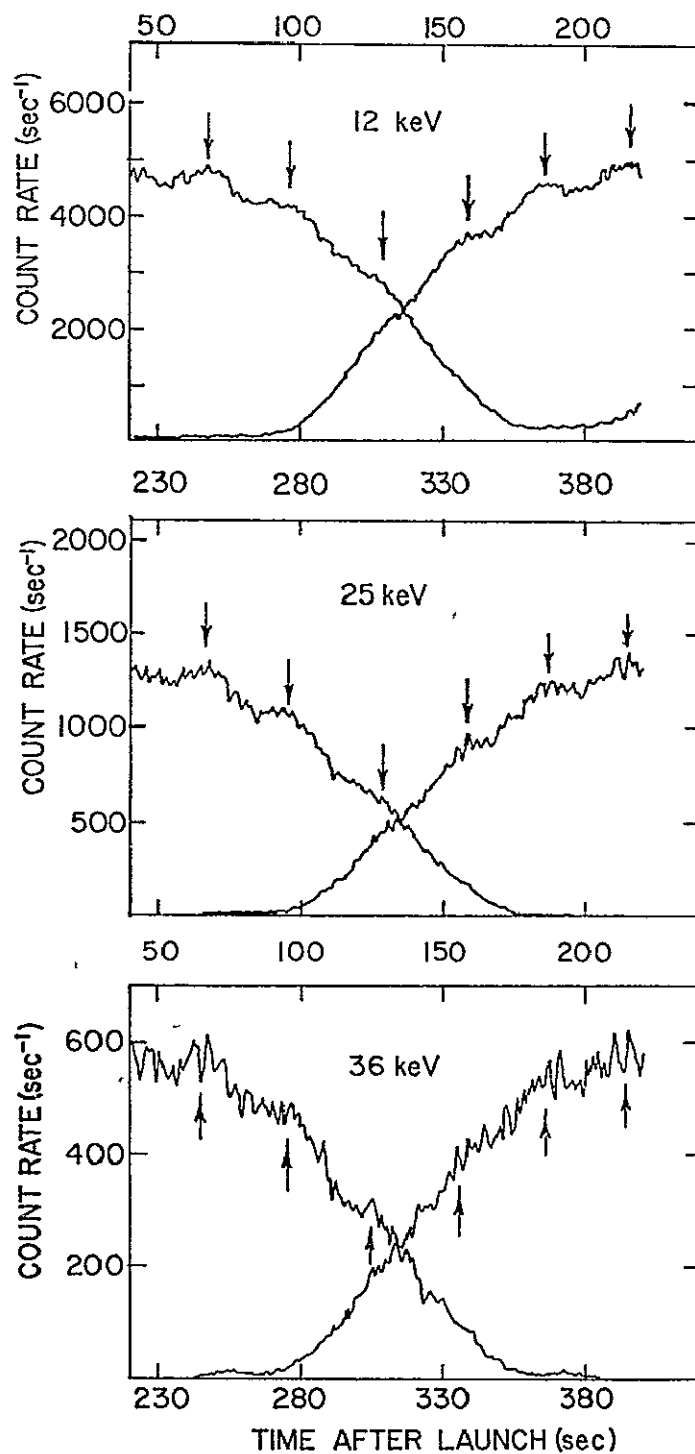


Figure 4 4 EES count rates versus time for Nike Apache 14 520 Both upgoing and downgoing count rates are shown for energy channels of 12, 25, 48, 36, and 80 keV

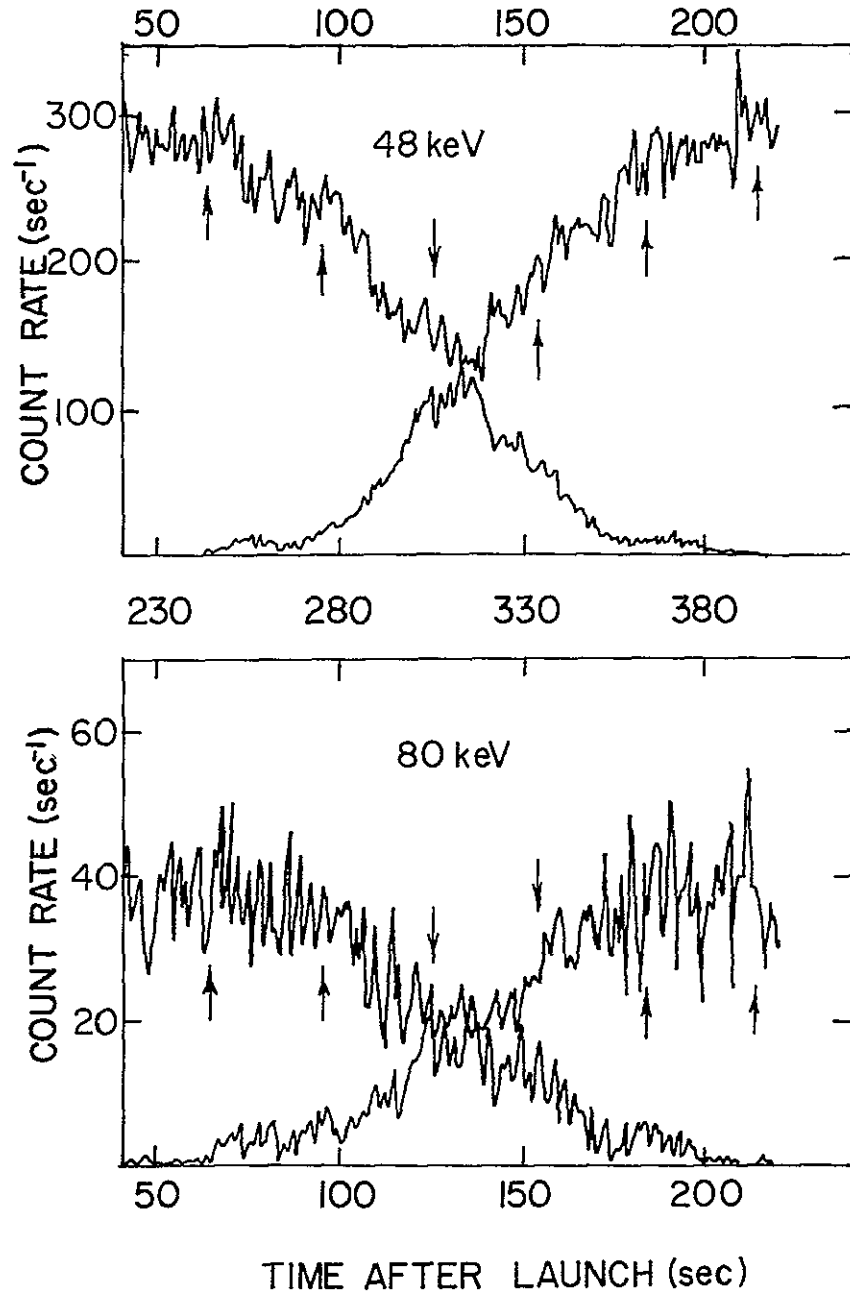


Figure 4 4 cont



These observations can be interpreted to show that the pitch-angle distribution of these quasi-trapped particles is peaked near  $90^\circ$ . The ratio of the modulation amplitude to the total count rate at apogee is approximately the same for energies from 10 keV to 80 keV indicating that the pitch angle-distribution remains similar over these energies. Also, because the ratio at apogee is the same for all energies, the conclusion can be drawn that the modulation is not due to high energy particles ( $E > 100$  keV) with  $90^\circ$  pitch angles superimposed on a uniform low energy count rate

For particles with the smallest energy (12 keV) the modulation becomes very small at 150 km. This is attributed to scattering of the quasi-trapped distribution such that the particles which are incident with a distribution peaked at  $90^\circ$  became more isotropic. The approximate altitudes at which scattering becomes important for particles with energies of 12, 25, 36, 48 and 80 keV can be derived from the modulation peaks and are found to be 150, 135, 120, 105 and 90 km, respectively

Comparison of the 80 keV channel of Nike Apache 14.520 ( $K_p = 5+$ ) (Figure 4.4) with the 70 keV channel of Nike Apache 14.439 ( $K_p = 8$ ) (Figure 4.1) reveals that the temporal variations are considerably less for the lower  $K_p$ . The average flux at 80 keV is  $27 \text{ cm}^{-2} \text{ s}^{-1} \text{ ster}^{-1}$ , for an assumed isotropic distribution, compared with the higher flux of  $551 \text{ cm}^{-2} \text{ s}^{-1} \text{ ster}^{-1}$  of 14.439. Later flights confirm that the flux and its time fluctuations are strong functions of magnetic activity at midlatitudes.

The count rates measured on the three lowest energy channels are plotted against altitude in Figure 4.5. The data have again been averaged over one-second intervals. The most striking feature of these

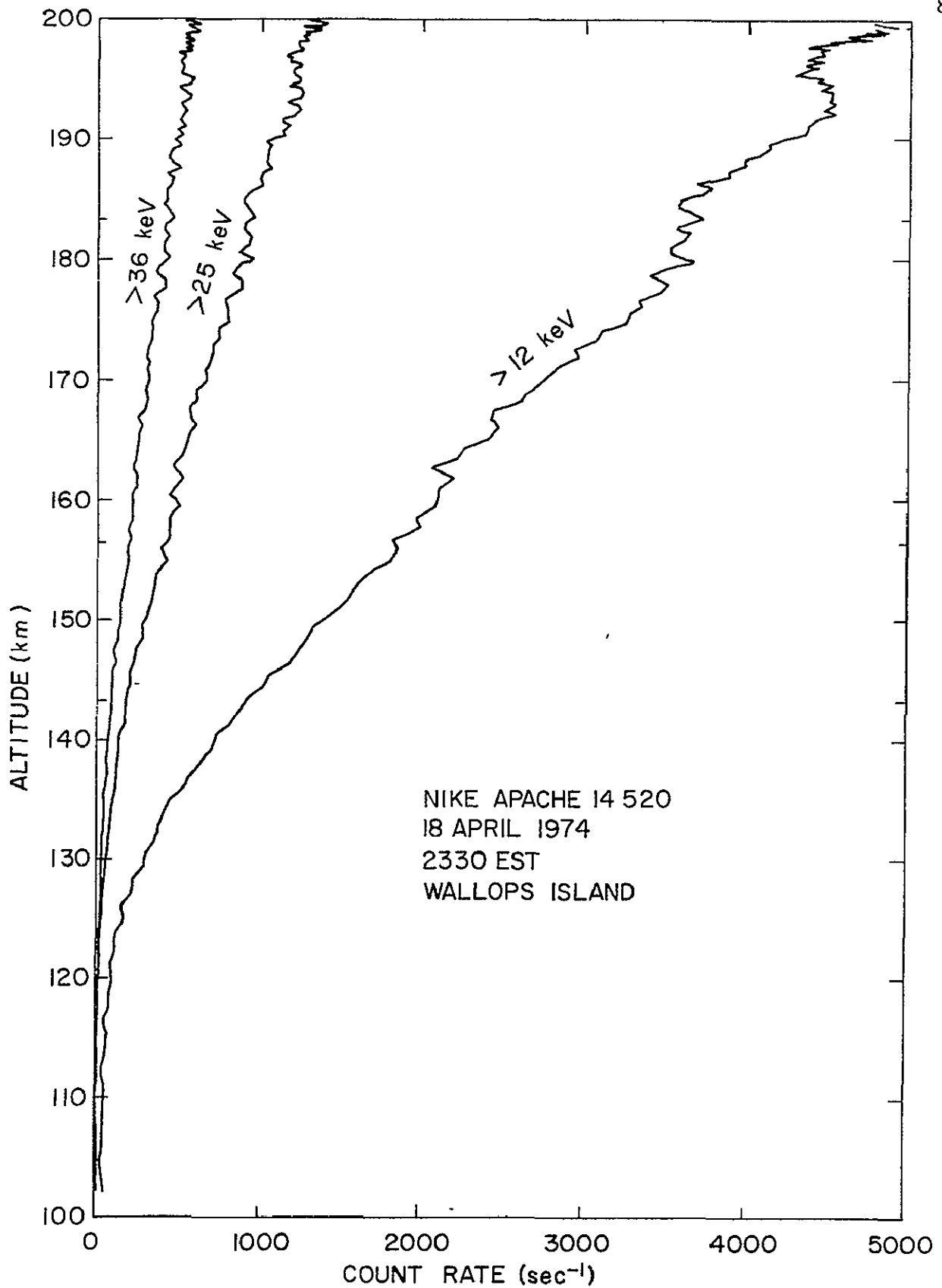


Figure 4 5 EES counting rate versus altitude for Nike Apache 14.520 launched 18 April 1974. The three low energy channels are shown corresponding to threshold energies of 12, 25, and 36 keV. The data are averaged over one second

data is the linear increase in the count rate between 140 km and 200 km on all channels. In this altitude range the measured particles lose only a few percent of their initial energy, therefore an explanation other than loss of energy is required to explain this linear attenuation with altitude. As already deduced from the precessional modulation the measured particles have a pitch-angle distribution centered about  $90^\circ$  and hence are near their mirroring altitudes. Above 150 km scattering is negligible and the increasing count rate is due to the distribution of mirror altitudes of the quasi-trapped particles. Below 150 km scattering becomes important, at these lower altitudes the count rate is observed to decrease because 1) backscattering occurs, and 2) the pitch-angle distribution is broadened and fewer particles remain within the detector field of view. A working model and computer simulation of these qualitative arguments will be given in Chapter 7.

Figure 4.6 shows a linear least-squares-fit for channel 2 (25 keV) as a function of altitude. The correlation coefficient is 0.99. The equation of this line has a slope of 0.0476 and an altitude axis intercept of 137.3 km.

A histogram plot of the count rate variation with detector azimuth (deduced from the magnetometer signal) is shown in Figure 4.7 for the 25 and 36 keV channels at an altitude of 150 km. Also shown is the geomagnetic azimuth. From Figure 3.7 the detector passes through ninety-degree pitch angle twice each revolution and hence for a symmetrical and peaked distribution about  $90^\circ$  one would expect an azimuthal variation at twice the spin rate. However, Figure 4.7 illustrates that the pitch-angle distribution is asymmetric since the azimuthal variation is at the spin frequency. It will be shown later that this variation can be

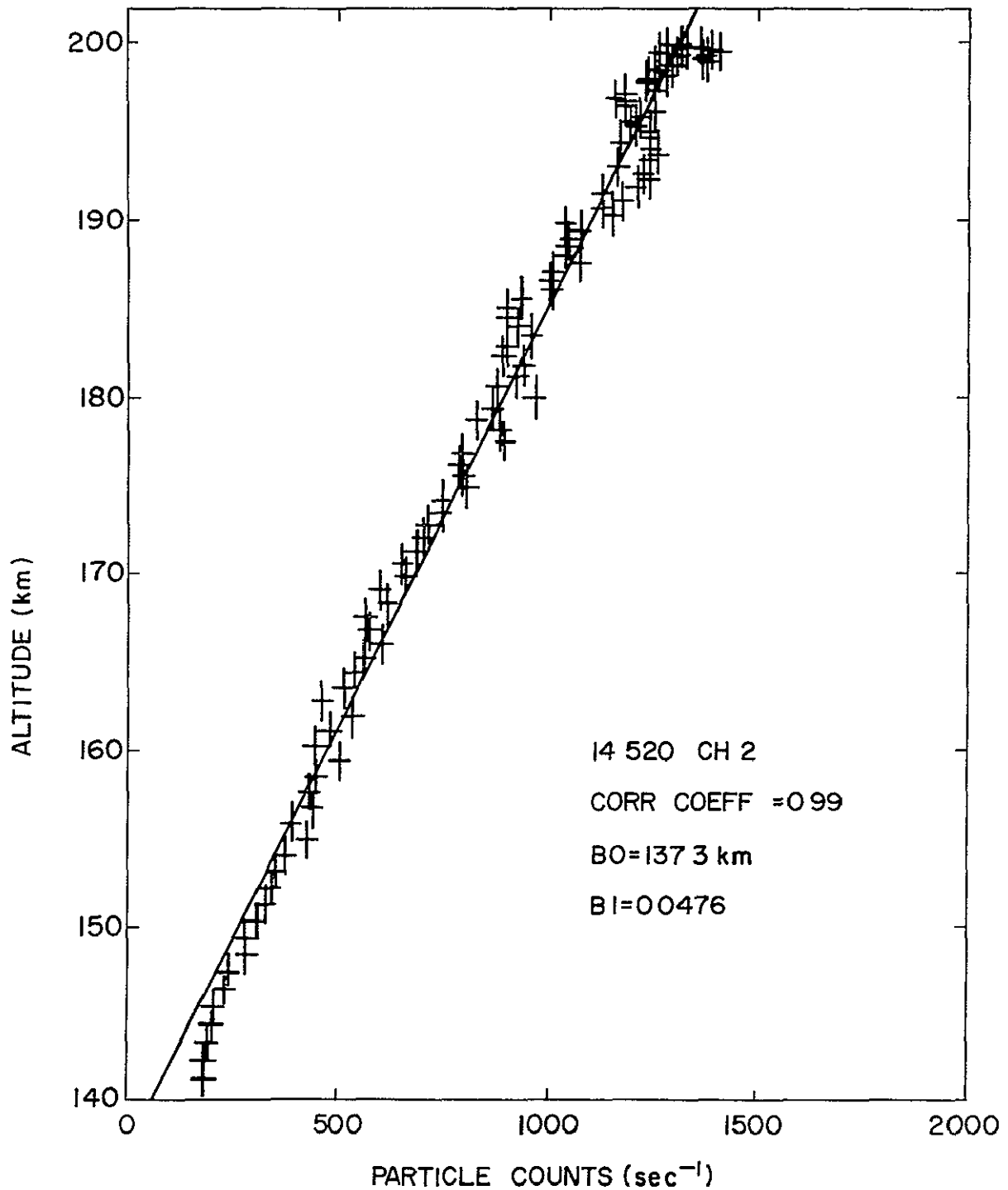


Figure 4 6 Least-squares fit to particle flux versus altitude for 25 keV energetic electrons recorded by the EES experiment on Nike Apache 14.520

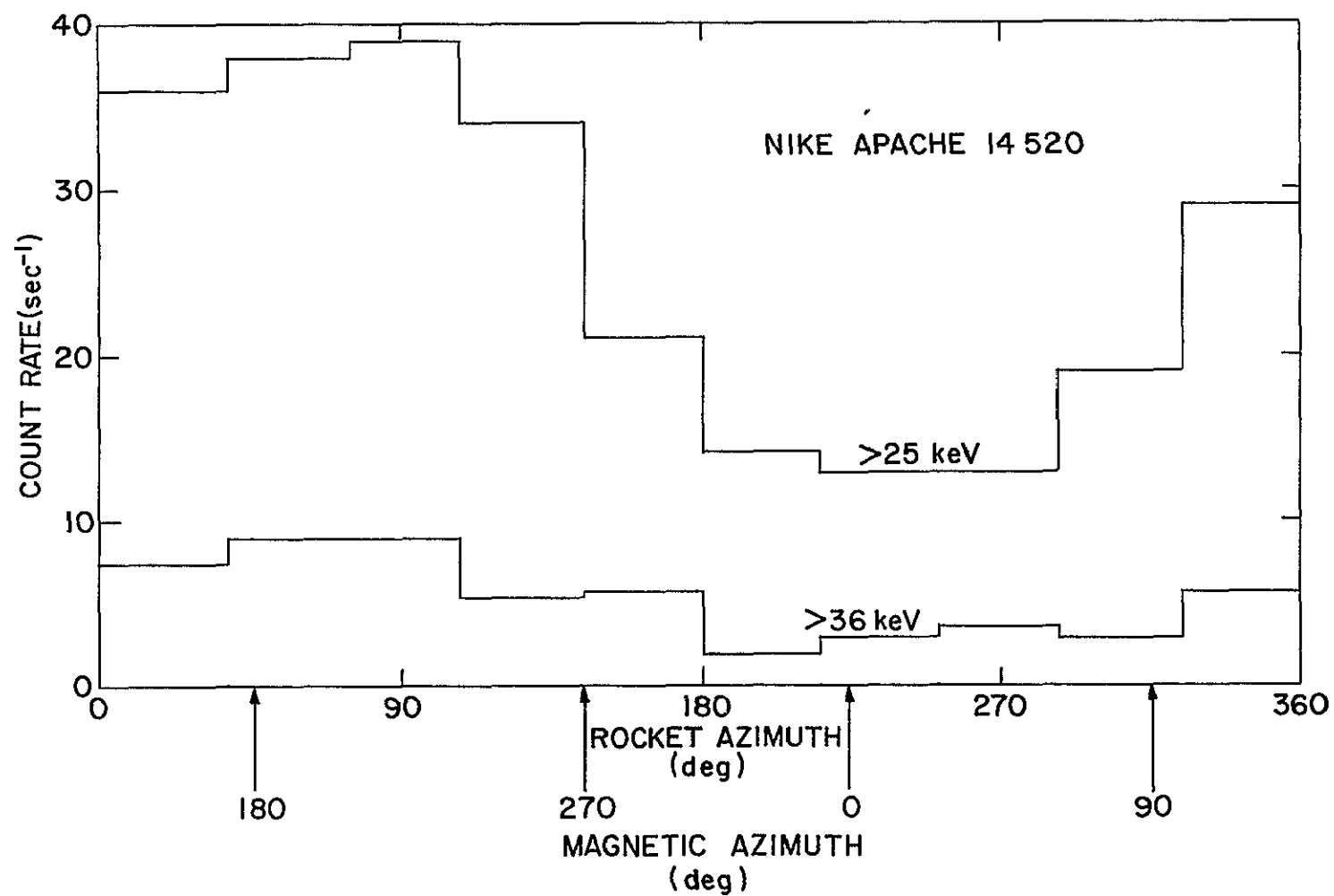


Figure 4.7 Azimuthal variations of the count rate observed on Nike Apache 14 520 for the 25 and 36 keV channels at an altitude of 150 km.

explained in terms of. 1) an isotropic component in addition to the quasi-trapped flux; 2) preferential scattering towards lower pitch angles giving an asymmetrical peak about  $90^\circ$ , and 3) the detector geometry.

The azimuthal variation is maximized in the scattering region of 135 km

The integrated energy spectrum above 12 keV fits a power law function as shown in Figure 4.8. Also shown is the second-order least-squares fit for every 10 km interval from 100 to 200 km. The integrated energy spectrum,

$$J_I(>E) = J_0 E^{-y} \quad (4.1)$$

is the integral flux of particles with energies greater than  $E$ . The differential flux,  $J_D$ , may be derived from the integral flux,  $J_I$ , for a power law variation as

$$J_D = J_I \frac{y}{E} \quad (4.2)$$

where  $y$  is the exponent on the integral power spectrum.

The energy spectrum between 135 and 200 km is closely approximated by a power law variation with, an exponent,  $y = 2.25$ . Below 135 km the low energy ( $E = 10$  to  $20$  keV) portion of the spectrum does not decrease as rapidly as the central portion resulting in a concave-upwards curve. This relative increase of flux at low energies is related to the ionization process creating secondary ionization. The central portion ( $E = 20$  to  $40$  keV) of the energy scale shows rapidly decreasing flux from 140 to 110 km indicating scattering to pitch angles outside the detector field of view in addition to the influence of magnetic mirroring of particles. Below 110 km the flux is expected to be nearly isotropic.

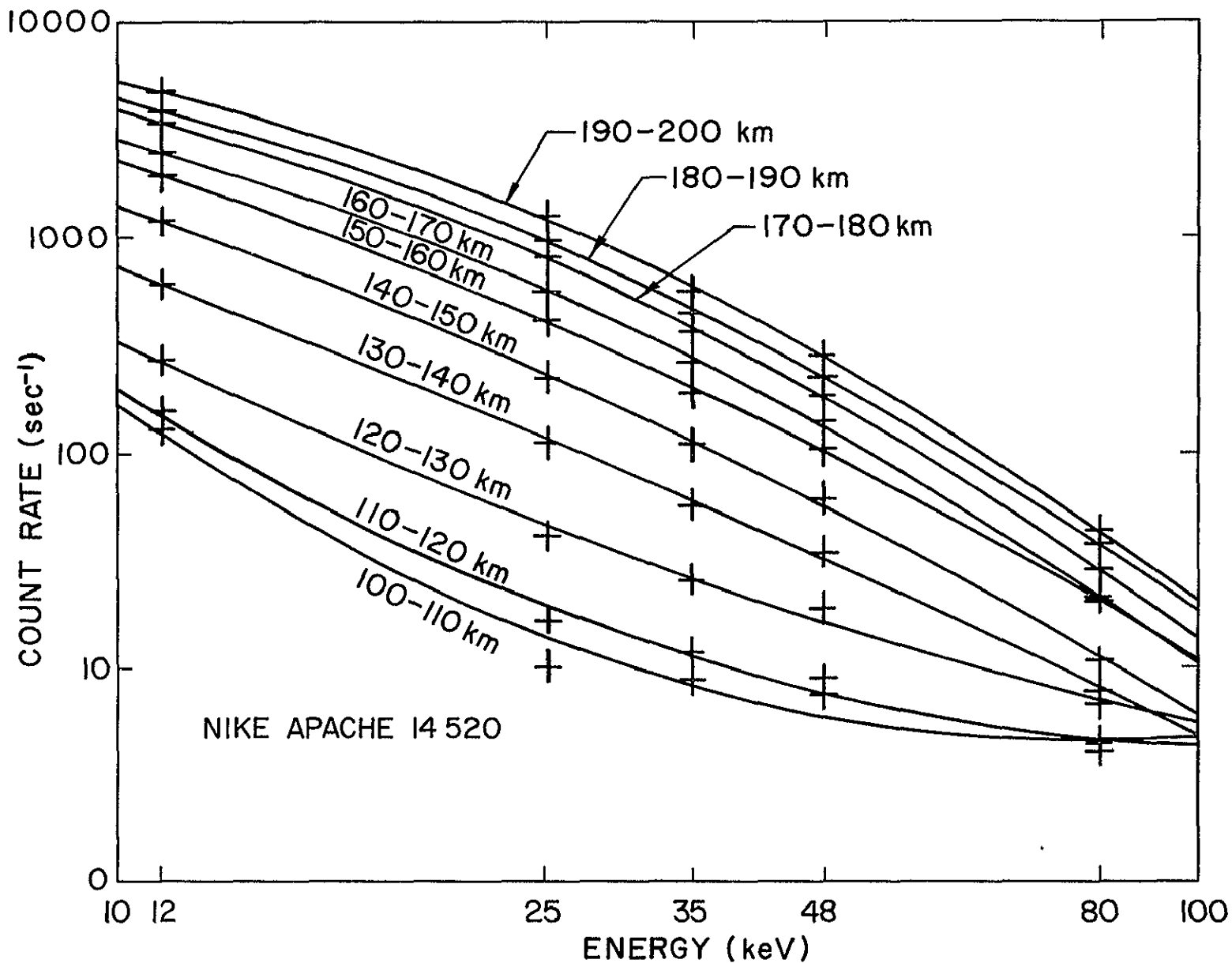


Figure 4.8 Log-log second-order least-squares fit of count rate versus energy for 10-km intervals above 100 km. The spectrum is approximately a power law.

4 1 3 *Nike Apaches 14.521 and 14.522; 29 June 1974.* The next two midlatitude flights, Nike Apaches 14.521 and 14.522, were launched from Wallops Island at 2120 and 2340 EST, respectively, on 29 June 1974 during the ALADDIN 74 program. The value of Kp was 3+ for both launch times. Both payloads were equipped, as before, with energetic electron spectrometer, Langmuir probe, propagation experiment and magnetometer. The energy thresholds calibrated for the EES are 13, 16.5, 32 and 57 keV for 14.521 and 12, 15, 24 and 44 keV for 14.522. The detector noise half width at half maximum (HWHM) is 5 keV for both detectors.

The count-rate profile versus altitude for 14.521 is shown in Figure 4.9. Channels corresponding to 13, 16.5, and 32 keV are averaged over one-second intervals and channel 57 is averaged over five-second intervals. Again these profiles exhibit precessional modulation and a linear increase with altitude. The differences in the count-rate profile between this night (Kp = 3+) and the night of 18 April 1974 (Kp = 5+) are 1) a significant reduction in the absolute flux, 2) a harder energy spectrum, and 3) a lowering of the altitude intercept to 100 km.

Figure 4.10 gives the energy spectrum for each 10 km interval between 100 and 200 km for 14.521. For a power-law representation of the energy spectrum the exponent is 1.25 which may be compared with the value 2.25 observed on the night with Kp = 5+. Further comparison between flights 14.520 and 14.521 indicate that the low energy flux is about an order of magnitude greater on the night with the higher value of Kp while the high energy flux is not significantly different (corresponding to their differing spectrums). Again the spectrum becomes softer at altitudes below 135 km for energies greater than



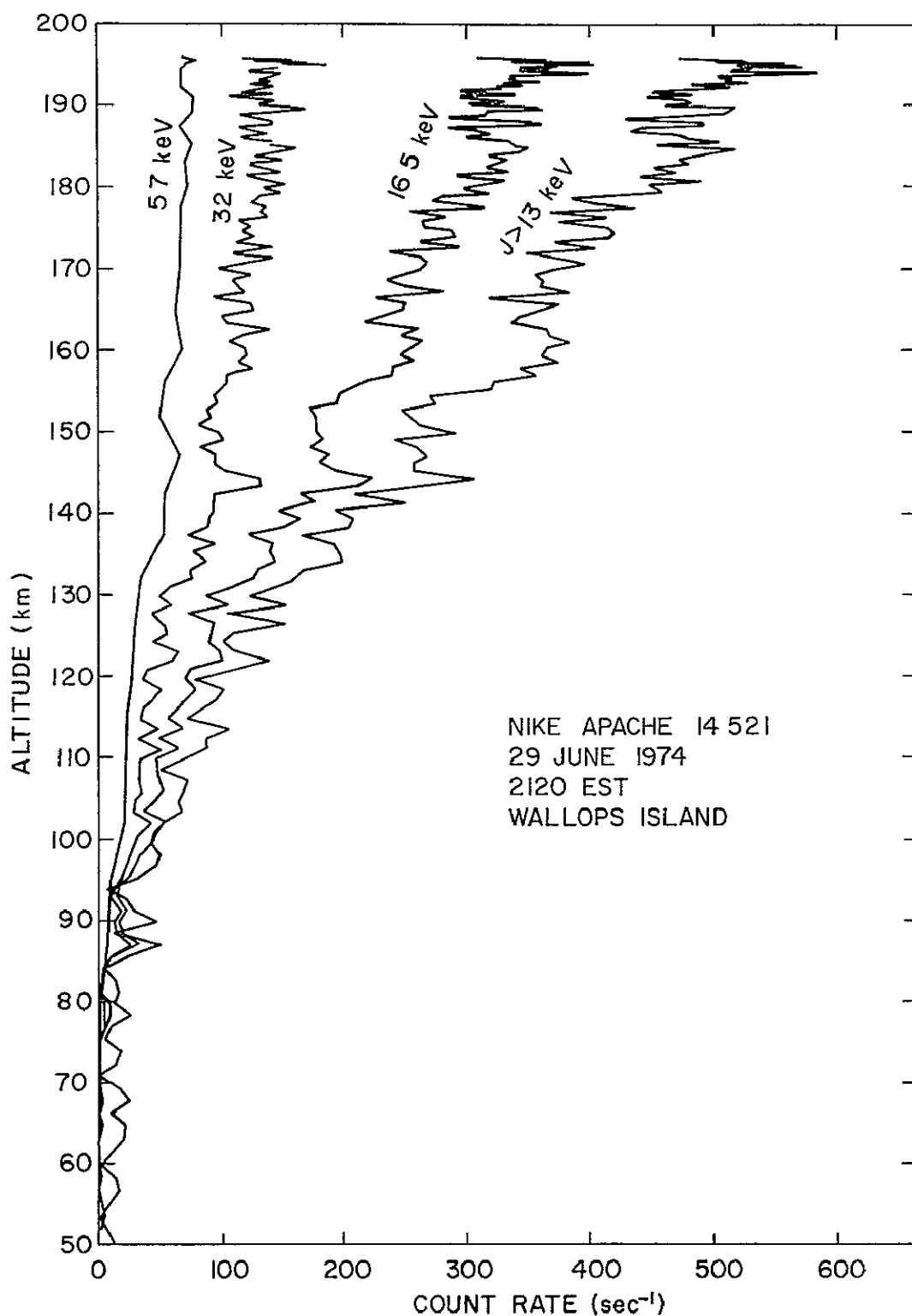


Figure 4 9 EES counting rate versus altitude for Nike Apache 14 521 launched 29 June 1974. The profiles shown correspond to threshold energies of >13, >16.5, >32 and >57 keV. One-second average of data except for the highest energy channel which is a five-second average.

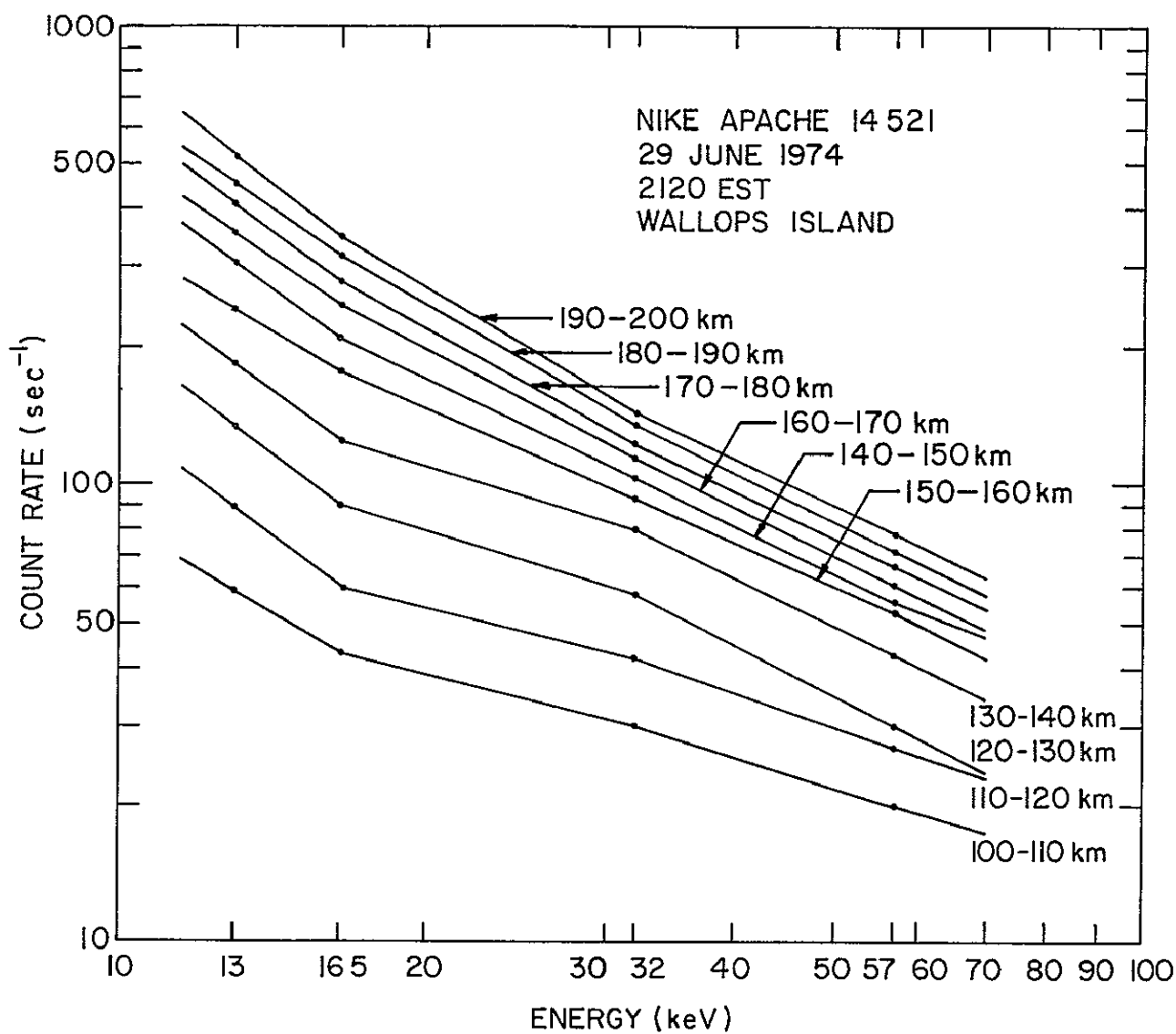


Figure 4.10 Log-log plot of count rate versus energy for 10-km intervals above 100 km for Nike Apache 14.521. The spectrum is approximately power law.

16 keV and remains peaked at lower energies

The lowering of the altitude intercept to 105 km for the night with  $K_p = 3+$  as compared to the 130 km observed for the night with  $K_p = 5+$  indicates that the altitude at which scattering becomes important is a function of  $K_p$ . It will be shown later that the general shape of the count-rate profile is dependent on the interaction of the energetic electrons with the atmosphere. For nights of low  $K_p$  the heating of the atmosphere is low, the neutral temperature is low and thus the integrated density and subsequent scattering is reduced. The energetic particles can therefore shift their quasi-trapped characteristics to lower altitudes, for example, from 130 to 105 km. Quantitative analysis of the effect is left to Section 7.1.

Nike Apache 14.522 was launched two hours and twenty minutes after Nike Apache 14 521. A partial failure in the payload telemetry transmitter resulted in noisy data which prevented use of the standard computer reduction programs. However, hand analysis of the chart records up to 160 km indicates that the count rates are identical with those measured on the preceding flight.

#### 4.2 *New Rocket Measurements at the Geomagnetic Equator*

Energetic particles have been observed at relatively low altitudes at the magnetic equator. The equatorial energetic electrons must rely on a strong radial diffusion mechanism at low altitudes to transport particles perpendicular to the magnetic field. On the other hand, *Mizera and Blake* [1973], *Moritz* [1972] and *Hovestadt et al.* [1972] conclude they are observing protons. The proton source has been explained as a two-step charge-exchange reaction from the ring current reservoir [*Mizera and Blake*, 1973].

The role of energetic particles in the nighttime equatorial ionosphere has been investigated in two rocket flights. Nike Apache rockets 14 524 and 14 525 were launched from Chilca, Peru ( $12.5^{\circ}\text{S}$ ,  $76^{\circ}\text{W}$ , magnetic dip =  $-07^{\circ}$ ) on nights representative of relatively quiet and disturbed conditions, respectively. The first (14.524) was launched on 29 May 1975 at 2336 LST ( $K_p = 2+$ ) and the second (14.525) was launched on 2 June 1975 at 0011 LST ( $K_p = 5$ ). The Peru location lies to the west of the South Atlantic anomaly and therefore eastward moving electrons would be expected to dip low into the atmosphere at this longitude.

Both rockets were equipped with the EES but modified with a collimator to give better pitch-angle information. Figure 4.11 shows this modification to the standard detector mount. The geometrical factor is  $0.05 \text{ cm}^{-2} \text{ ster}^{-1}$ . At the equator the magnetic field is horizontal so that a side-mounted detector on a rocket spinning about a vertical axis will sweep through the complete range of pitch angles. Rocket 14.524 has energy gates for electrons of 12, 21, 31 and 50 keV (with corresponding energies for protons of 35, 44, 54 and 73 keV) and rocket 14.525 has energy gates of 13, 17, 27 and 41 keV for electrons (36, 40, 50, 64 keV for protons).

The count rate versus altitude profiles measured on Nike Apaches 14.524 and 14 525 are shown in Figures 4.12 and 4.13, respectively. The rates are averaged over 5-second intervals. The flux recorded on the night with  $K_p = 5$  is about a factor of six greater than the flux on the night with  $K_p = 2+$ . The count rate is altitude dependent. Below 170 km the count rate is very small, above 170 km the count rate steadily increases with altitude. Due to the low count rate on 14 524 there are large statistical fluctuations.

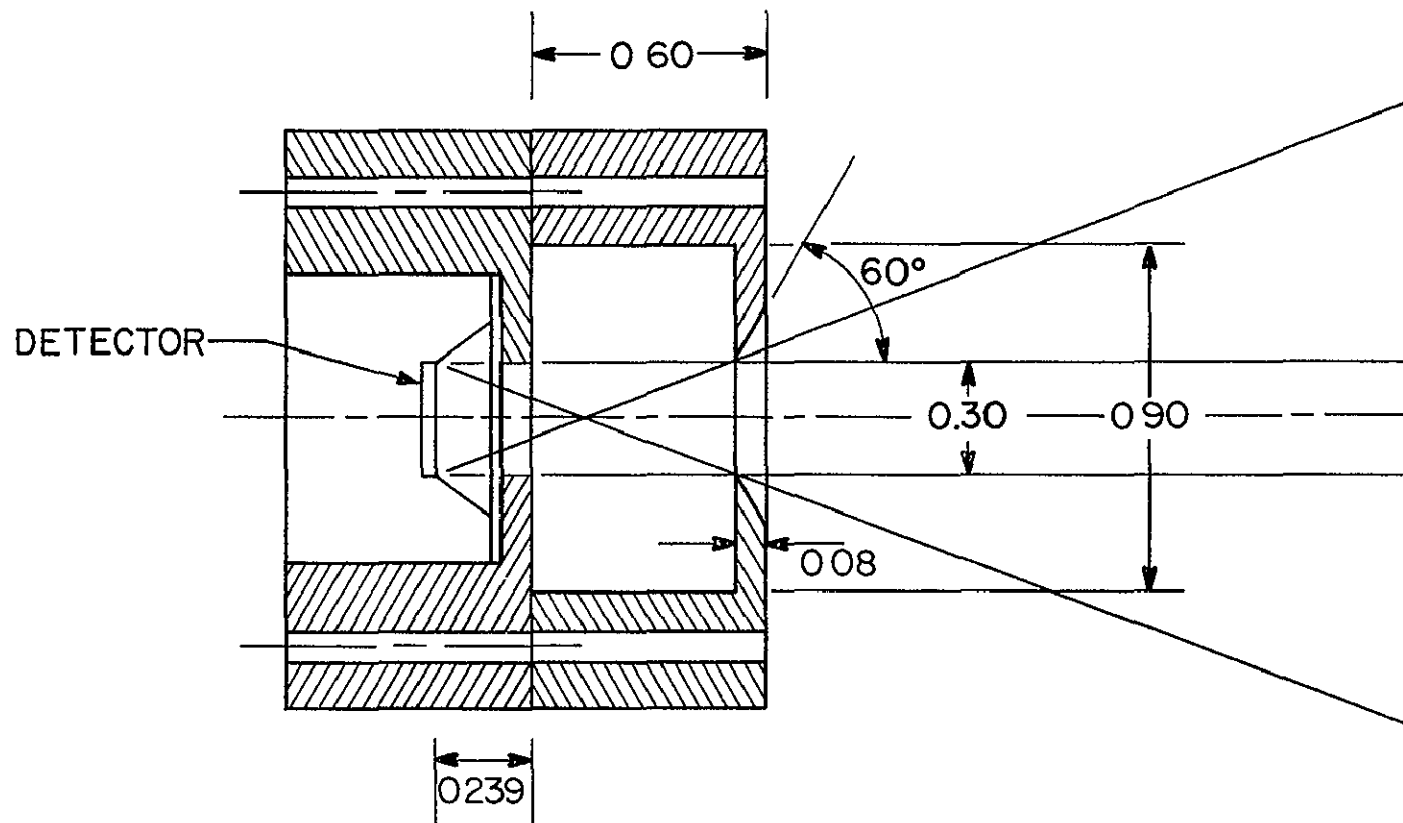


Figure 4 11 Detector geometry and collimator used on rockets 14 524 and 14 525 Dimensions are given in inches

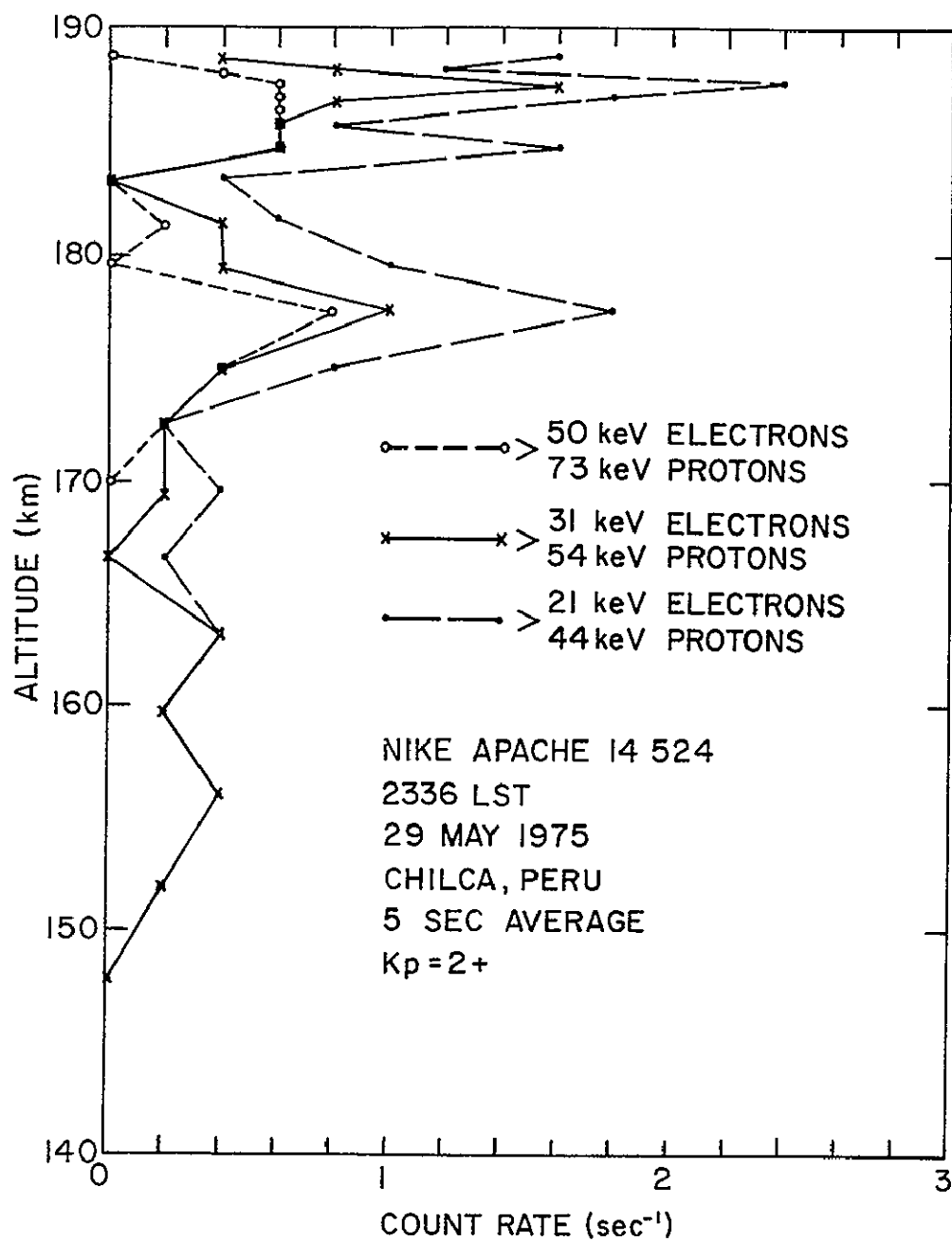


Figure 4.12 Count rate versus altitude at Chilca, Peru during geomagnetically quiet conditions.

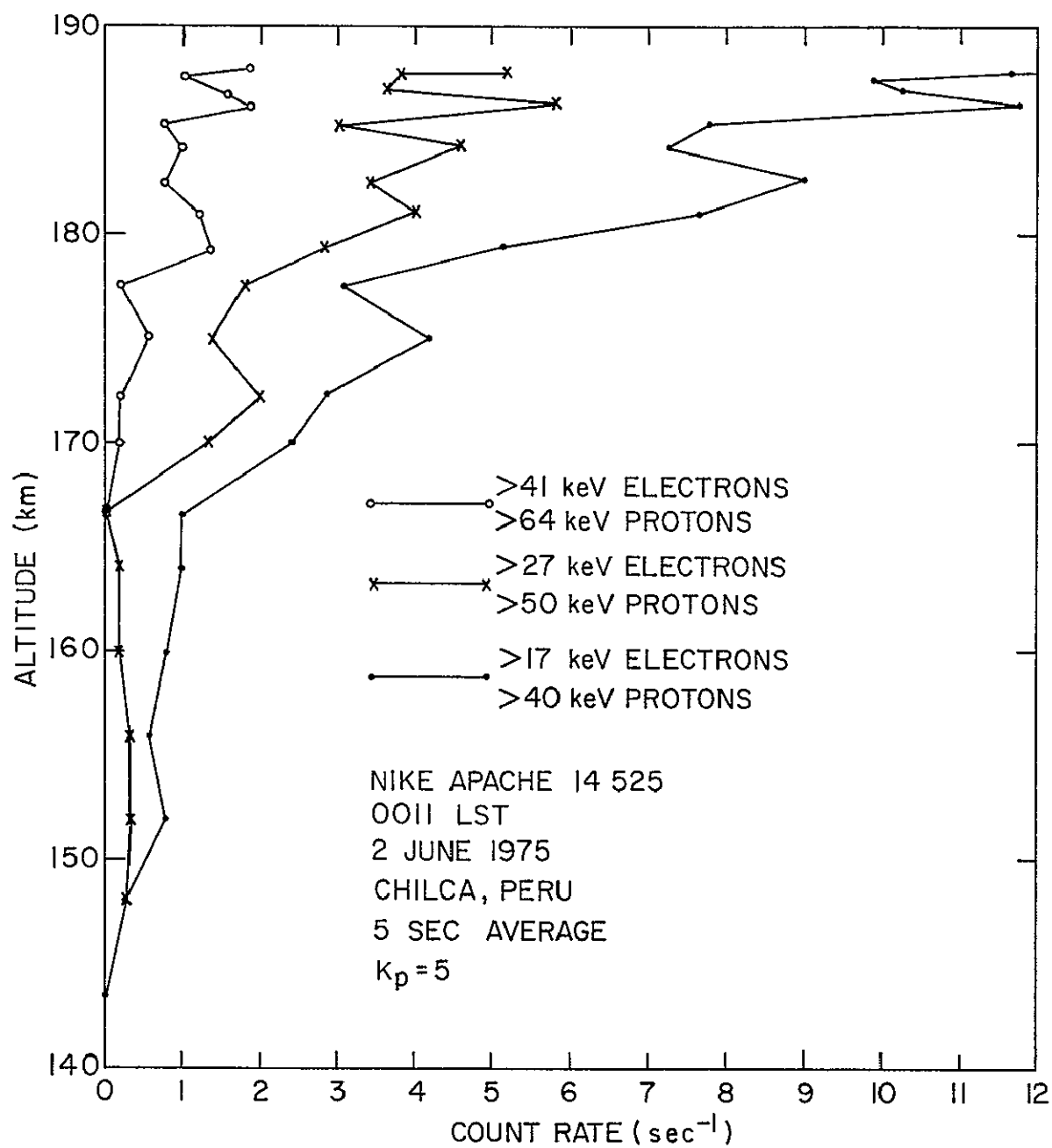


Figure 4 13 Count rate versus altitude profile at Chilca, Peru during geomagnetically disturbed conditions

The energy spectrum on 14 525 may be approximated by a power-law variation with an exponent of 2.2. This value is independent of the identification of the energetic particles as electrons or protons and is nearly identical with the spectrum obtained at Wallops Island for the same value of Kp (Nike Apache 14.520)

The spectrum exponent for protons in the ring current is about 1.8 over this energy range (derived from data by *Mizera and Blake*, 1973) Satellite data from *Moritz* [1972] shows that the low altitude equatorial flux varies directly with ring current flux and magnetic activity. This nearly simultaneous variation of flux with magnetic activity is verified by our rocket flights and therefore the source of the charged particles must invoke a rapid injection mechanism. The two-step charge-exchange process postulated for transporting ring current protons to low altitudes meets most of these criteria.

An interesting feature of the data is the sharp pitch-angle distribution of the particles. Figure 4.14 shows a histogram of 160 counts as a function of rocket azimuth for >17 keV electrons (or >40 keV protons). The magnetometer signal is also shown and is aligned with the detector axis. The histogram shows two peaks which are displaced by 180°, the first maximum (at 62°) is about one half the magnitude of the second (at 212°).

The maxima occur at a pitch angle of 90° and indicate a quasi-trapped flux. The smaller maximum occurs for particles impinging on the detector from the geomagnetic west (guiding center beneath the rocket, for electrons) while the large maximum occurs for particles impinging upon the detector from the east (guiding center above the rocket, for electrons). This observation is similar to the asymmetry recorded by *Heikkila* [1971]



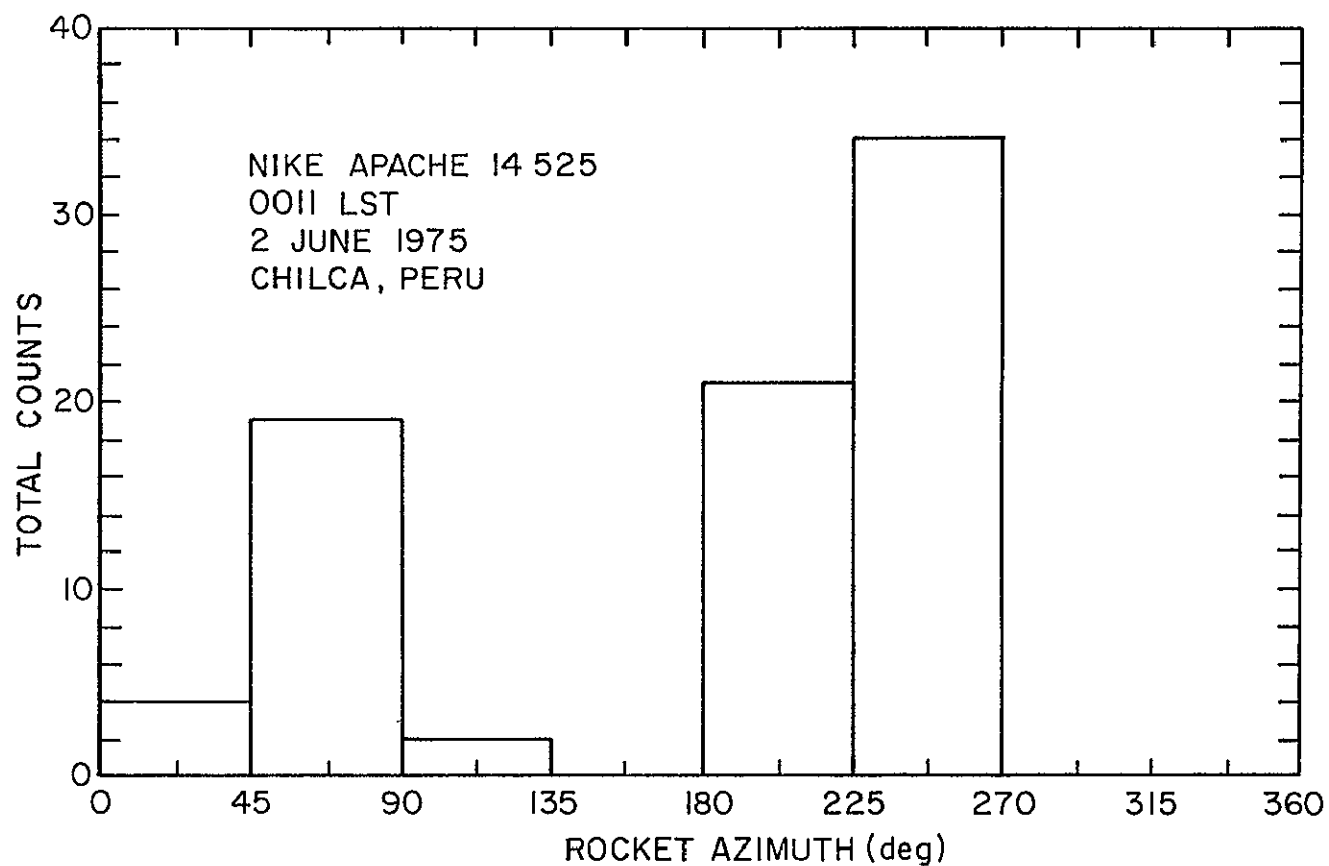


Figure 4 14 Histogram of 160 counts as a function of rocket azimuth for >17 keV electrons (or >40 keV protons) This histogram includes all counts above an altitude of 180 km

on the Isis I satellite

The asymmetry in the histogram cannot be explained by rocket shadowing (Section 3 3.3). For 40 keV protons the gyroradius is 540 m and for 17 keV electrons the gyroradius is 8 m. Consequently, the east-west effect [Hess, 1968] is inadequate as an explanation.

Furthermore, contamination by X-rays can be eliminated since the count rates increase dramatically with altitude above 170 km and X-rays ( $E > 12$  keV) are not absorbed above 80 km. Additionally, the count rate on the night with  $K_p = 2+$  indicates that extraterrestrial and other sources contribute less than one count per second.

Discussion of these equatorial results is deferred to Section 7 4. It will be concluded that the equatorial flux is caused by protons originating in the ring current.

#### 4 3 *Satellite Observations*

The interpretation of the large dynamic variations of the trapped radiation and the phenomenology of particle precipitation requires consideration of a variety of experimental observations. The morphological characteristics of midlatitude particle precipitation are at present only being investigated on a global scale. The purpose of this section is to assimilate the many observations made by rocket and satellite experiments sensitive to energetic particles and to sort this information out to appropriate regions of latitude, longitude,  $K_p$ , time and altitude. From this and other material a particle model can be developed.

Historically, the first indication that energetic electrons are precipitated into midlatitudes was obtained by Sputnik 3 during a 1 min pass on 15 May 1958 [Krassovsky *et al.*, 1962]. However, the first comprehensive satellite study involving latitudinal variations (over North America) was

obtained by Explorer 12 and Injun 1 [O'Brien, 1962, 1963]. Figure 4.15 illustrates these averaged results on an  $L$ -plot representation. The variations of electron flux are strongly dependent on magnetic activity and vary by an order of magnitude. This representation is useful in understanding and predicting the expected flux during low and moderately disturbed conditions. The slot region at  $L \approx 3.5$  is evident in the trapped flux distribution and a sharp cutoff at  $L = 2.0$  is seen for both the trapped and precipitated electrons. The flux ratios are in agreement with recent measurements. The precipitated flux is defined to be the flux at 1000 km which will mirror below 100 km altitude ( $\alpha < 55^\circ$ ).

Other relevant conclusions made by O'Brien in this analysis are:

- 1) that if there were no continuous source supplying an  $L$  shell, the observed magnitude of the precipitated flux would empty the outer zone of electrons in a few hours,
- 2) the lifetimes of electrons are independent of  $L$  values for  $2 \lesssim L \lesssim 10$ , and
- 3) the higher loss rate in the auroral region may be a consequence of the cornucopia effect of the enlargement of the geomagnetic tubes of force.

In short, O'Brien advanced the concept that the outer radiation belt is not a "leaky bucket" which drizzles precipitated particles from a vast reservoir but rather a "splash catcher" which absorbs some of the freshly injected (accelerated and precipitated) particles. Due to magnetic field inhomogeneities (mainly the South Atlantic anomaly), wave-particle interactions and radiation belt source mechanisms, the geographic distribution of middle and low latitude particles is not simply explained.

Figures 4.16(a) and (b) show the first global maps of particle precipitation [Seward, 1973]. These measurements were made with a polar orbiting satellite on 18 and 19 September 1961 ( $K_p = 1$ ) between altitudes of 410 km ( $32^\circ\text{S}$ ) and 240 ( $32^\circ\text{N}$ ). The detector [Seward and Kornblum, 1963] consisted

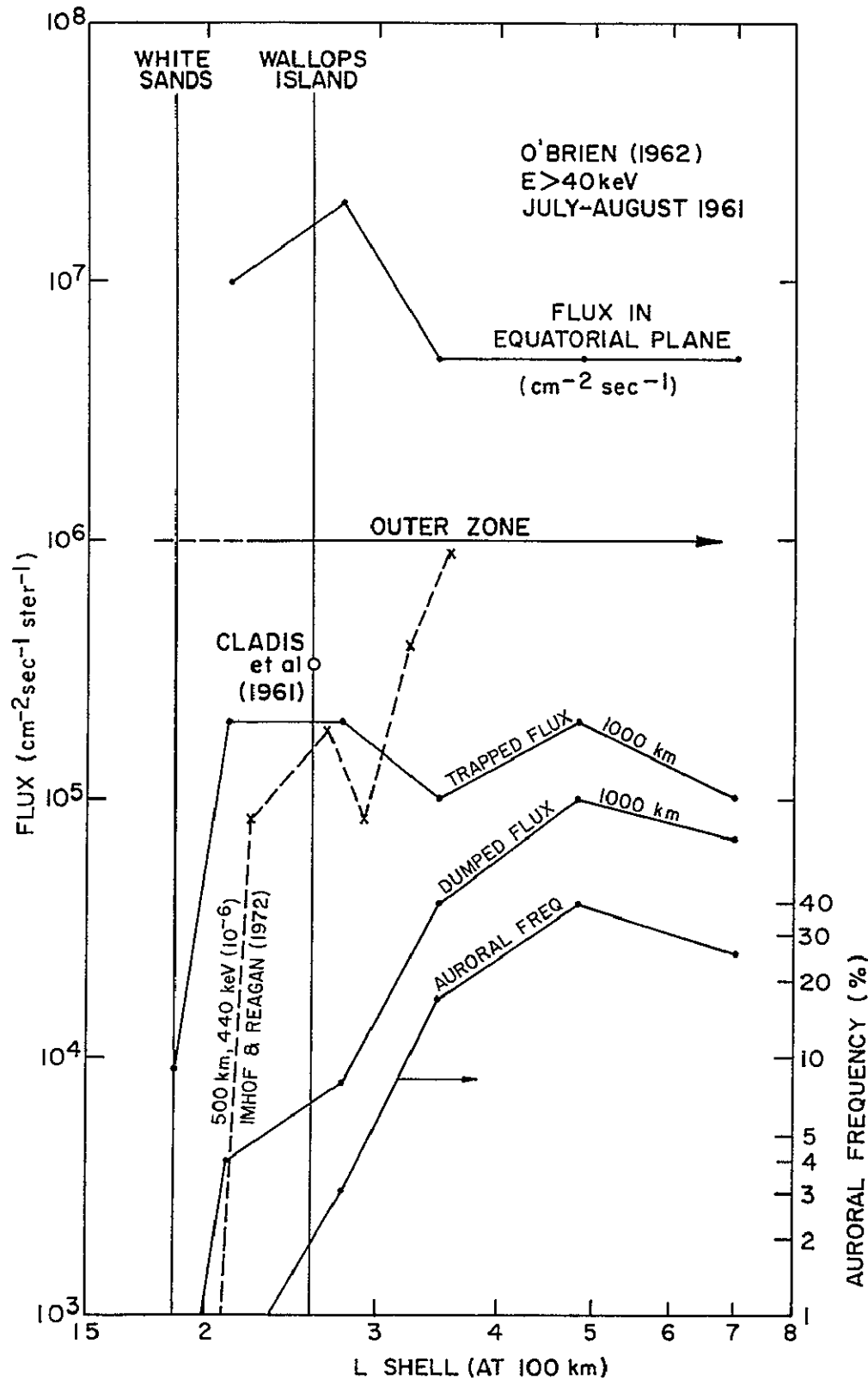


Figure 4 15 Electron flux measurements by satellites illustrate the rapid cutoff at  $L = 2.0$  for the trapped and dumped flux. The dumped flux and auroral frequency decrease monotonically from the auroral region while at  $L \approx 2.6$  there is an increase in the trapped flux

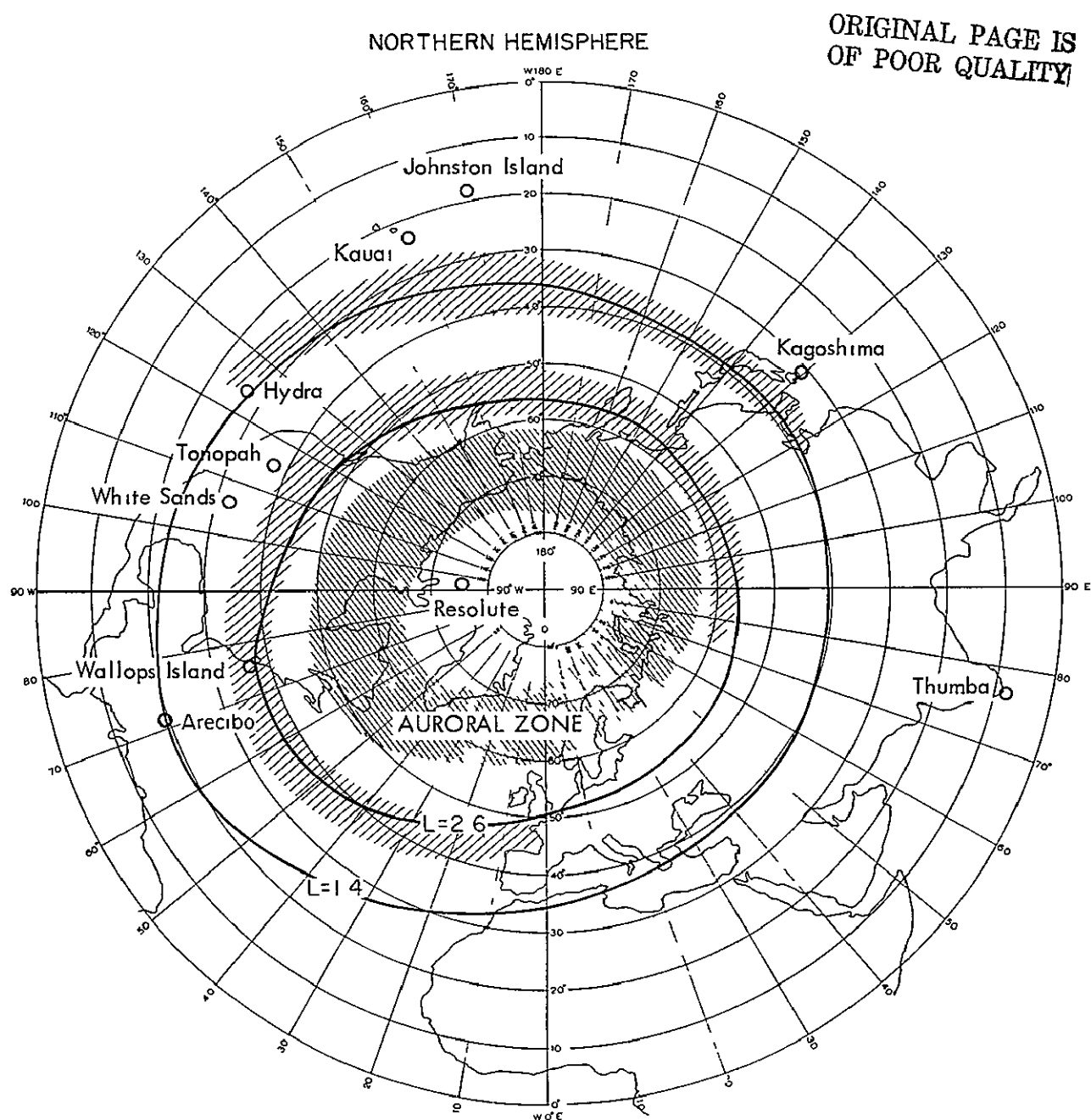


Figure 4 16 Regions of high omnidirectional electron flux measured by Seward [1973] using a polar orbiting satellite (240-410 km altitude) These data clearly show two zones of midlatitude precipitation Also shown on this map are  $L$  shells at 100 km corresponding to these zones ( $L = 2.6$  and  $L = 1.4$ ) Various rocket launch sites are indicated

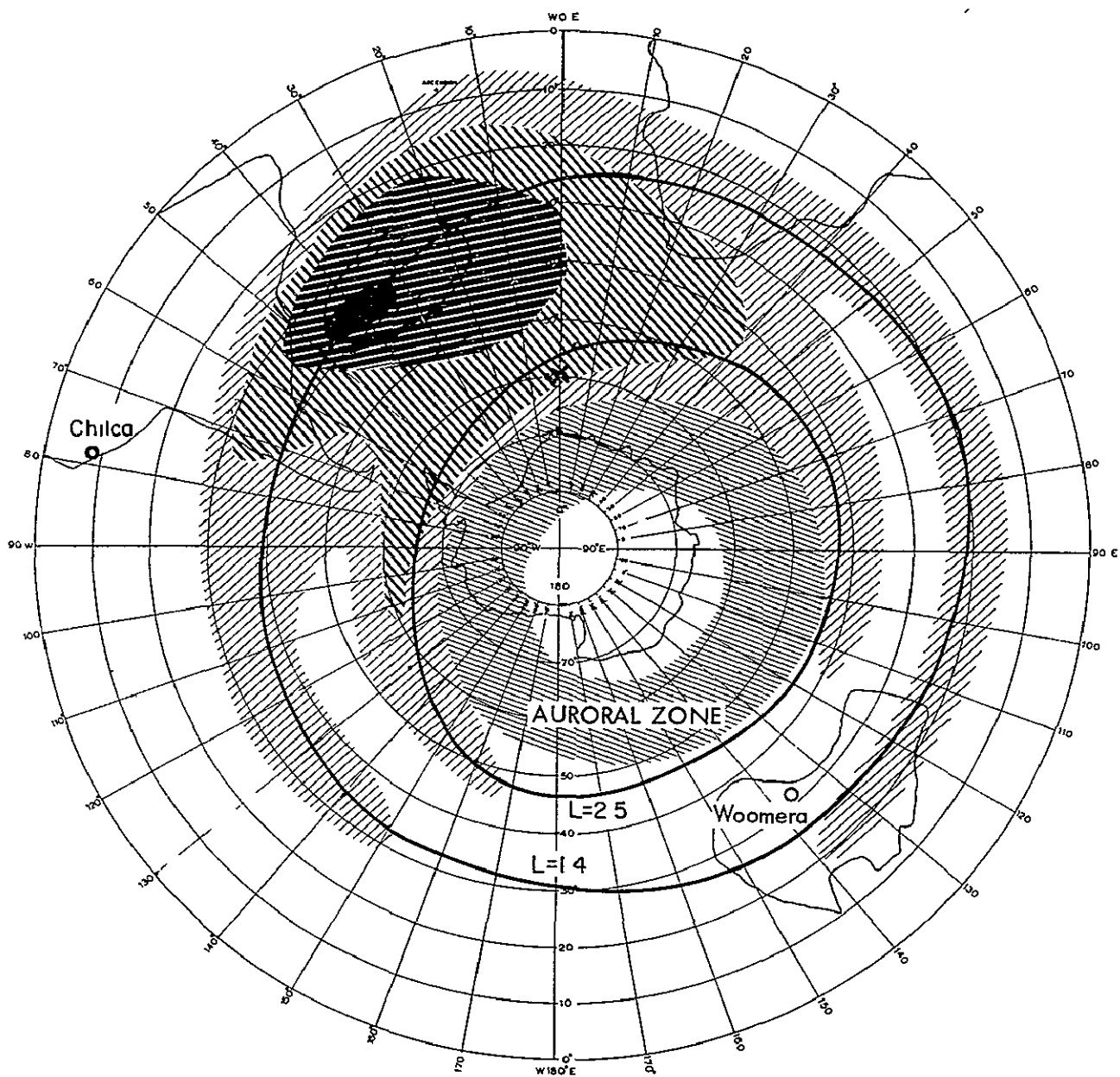


Figure 4 16 Continued

ORIGINAL PAGE IS  
OF POOR QUALITY

of a cesium iodide scintillator (area  $5 \text{ cm}^2$ ) covered by  $5 \times 10^{-3} \text{ cm}$  of beryllium and sensitive to electrons with energy greater than 100 keV. The field-of-view was 1 ster and the total omnidirectional flux was measured. Also shown in the figure are the launch sites from which various rocket particle experiments have been launched and are reported on elsewhere in this section.

The South Atlantic anomaly shows up clearly in the map of the Southern Hemisphere. The low magnetic field values reduce the mirroring heights of the drifting energetic particles (windshield-wiper effect) as they proceed around the earth. The north and south auroral ovals also are evident and are characterized by intense particle precipitation.

A most interesting feature, however, is the ring-like bands of midlatitude energetic particles. The fact that energetic electrons (which drift eastward) are found in abundance to the east and west of the anomaly suggests that other scattering mechanisms are important in addition to the steady-state magnetic field lowering of the mirror heights. The quasi-stationary concentric bands of midlatitude flux can be explained in terms of wave-particle interactions in the magnetosphere which are now known to be the primary driving force which lowers the mirror points of electrons to atmospheric levels. This will be discussed in detail in Chapter 7.

Our observations at Wallops Island of energetic particles are consistent with these general satellite observations. Similarly, measurements made by *Morse and Rice* [1976] at White Sands reveal an extremely low nighttime flux below 121 km. As evident in Figure 4.16 the longitude and latitude are of paramount importance when discussing particle precipitation.

Another valuable and representative series of midlatitude satellite observations has been reported on by *Larsen et al.* [1976]. These measurements

are shown in Figure 4 17 for passes on 16 and 19 December 1971. Various geophysical stations in North America are also shown on this plot since the measurements are believed representative of the Wallops Island precipitation band observed by Seward (Figure 4 16). The measurements by *Larsen et al.* [1976] were made in the low altitude (nominally 800 km) polar orbiting satellite 1971-089A. Electron spectrometers [*Reagan et al.*, 1973] measured the quasi-trapped flux ( $\alpha = 90^\circ$ , HEES detector) and loss cone flux ( $\alpha = 25^\circ$ , REES detector). The collimated acceptance cone for both of these detectors is  $\pm 27^\circ$ , the geometric factor is  $1.6 \text{ cm}^{-2} \text{ ster}$  and the energy span (256 channels) is from 130 keV to 2.8 MeV.

Features of the 16 December 1971 profile ( $K_p = 1$ ) shown in Figure 4 17(a) are 1) the sharp cutoff at  $L = 2.0$  of the trapped flux, 2) the slot valley at  $L = 3.5$  of the trapped flux, 3) the midlatitude maximum at Wallops Island of the trapped flux, and 4) the negligible loss-cone flux for  $L$  values below the slot region. Similar results have been found for higher energies by *Paulikas et al.* [1966] and *Williams and Kohl* [1965].

From Figure 4 17(a) at 800 km altitude over Wallops Island and with low magnetic activity, the trapped flux is  $2.5 \times 10^4 \text{ electrons cm}^{-2} \text{ s}^{-1} \text{ ster}^{-1}$ . The implications of this relatively high measured flux as a source of ionization in the upper  $E$  region will be considered later.

For moderately disturbed conditions (19 December 1971,  $K_p = 3$ ) as shown in Figure 4 17(b) the loss-cone flux increases and varies significantly with latitude. The slot region fills up, however the sharp cutoff at  $L = 2.0$  remains. It will be shown later that the explanation of these phenomena is the resonant interactions of LF waves with energetic particles.

*Torr et al.* [1976] used Atmospheric Explorer-C (AE-C) to obtain global



ORIGINAL PAGE IS  
OF POOR QUALITY

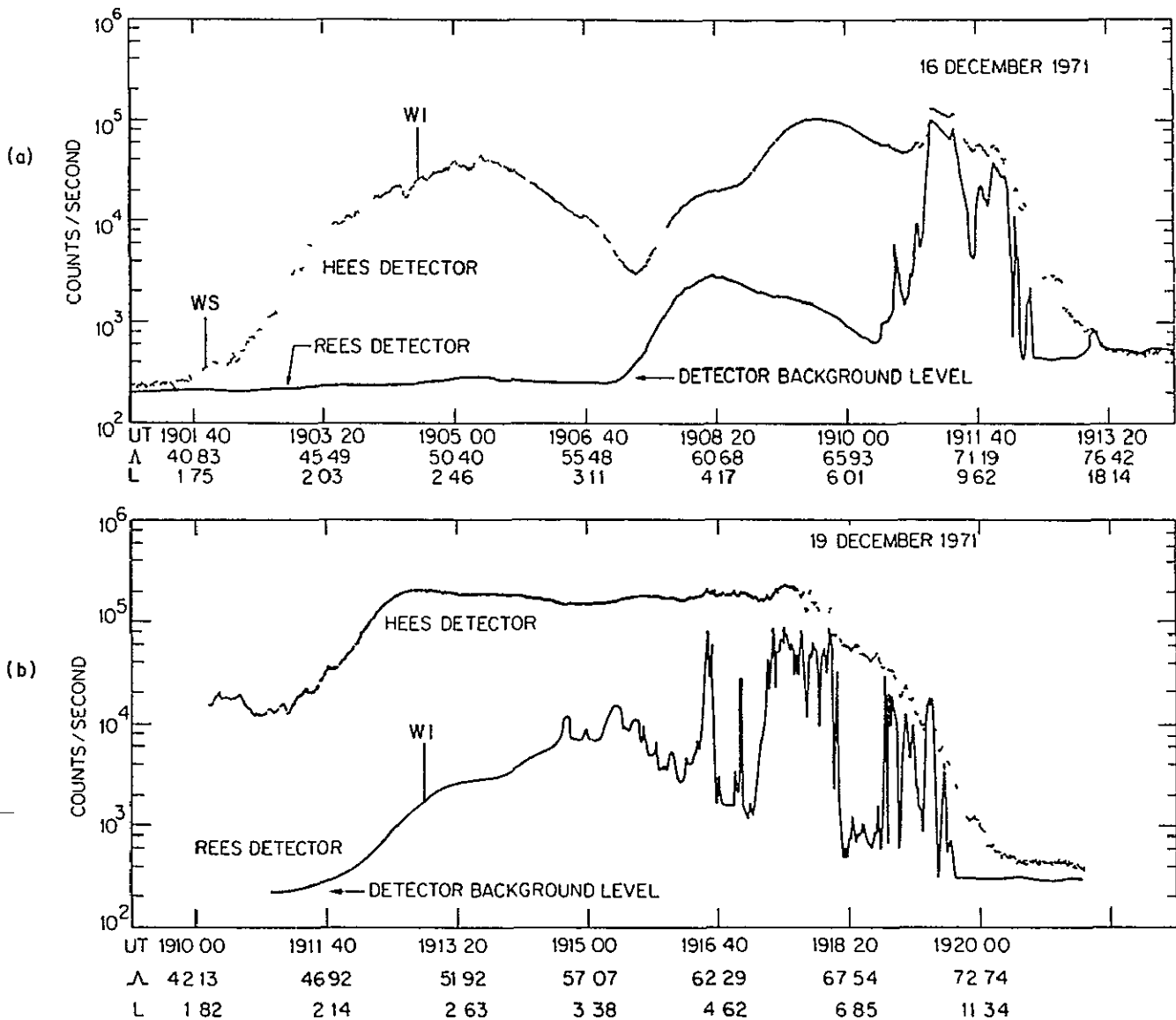


Figure 4.17 Midlatitude satellite observations ( $\approx 800$  km altitude) made by *Larsen et al.* [1976b] for  $K_p = 1$  (16 December 1971) and  $K_p = 3$  (19 December 1971). The locations of Wallops Island (WI) and White Sands (WS) are indicated. The cutoff at  $L = 2.0$  and the maximum in the quasi-trapped flux (HEES detector) near Wallops Island are evident. For moderately disturbed conditions the particle flux increases with largest increases in the precipitated flux (REES detector) and in the slot region with particular increases in the trapped flux.

characteristics of 0.2 to 26 keV energetic electrons at low altitudes (250-300 km). The channeltron detectors were insensitive and not well suited for midlatitude fluxes ( $10^3$ - $10^4$  cm<sup>-2</sup> s<sup>-1</sup> ster<sup>-1</sup> keV<sup>-1</sup>). It was necessary to accumulate counts for 500 to 1000 seconds at midlatitudes. Additionally, no information is given on the range of pitch angles measured and on the longitudinal variations of the count rates. It is presumed that they were looking at precipitating particles. Since numerous midlatitude particles ( $L > 2$ ) are quasi-trapped, it is important to measure the flux near  $\alpha = 90^\circ$  at these low altitudes and to translate this flux to scattering processes and ionization rates. In spite of these difficulties it seems that the measured, but small, isotropic component of the flux is about  $2 \times 10^{-4}$  ergs cm<sup>-2</sup> s<sup>-1</sup> and this flux remains unchanged throughout the middle and low latitudes but may vary by an order of magnitude under disturbed geomagnetic conditions. Using a detector looking at pitch angles between  $70^\circ$ - $90^\circ$ , it is believed that these flux measurements would have been increased by a factor of ten or more. Other satellite observations of midlatitude precipitation include *Imhof* [1968], *Paulikas et al.* [1966], *West and Buck* [1976] and *Lyons and Williams* [1975]. These are consistent with the observations already discussed.

In summary, the satellite observations indicate that at low altitudes in the midlatitudes there exist energetic electrons. The intensity increases with increasing magnetic activity and the majority of electrons are observed to be quasi-trapped with pitch angles near  $90^\circ$ . In midlatitudes there appears to be a sharp cutoff of precipitation at  $L = 2$  and another precipitation band at  $L \approx 1.4$ . The fact that energetic electrons are observed on both sides of the South Atlantic Anomaly suggests that a precipitation mechanism exists other than mirror height lowering due to the decreasing

magnetic field. The following sections will support these observations and interpretations.

#### 4.4 *Other Rocket Measurements*

Many rocket-borne experiments sensitive to energetic particle fluxes have been launched at middle and low latitudes. In some of these the measurements take the form of enhanced background counts on celestial X-ray experiments, UV detectors and ion mass spectrometers. The following is a review of the principal features of these particle measurements.

Table 4.1 is a compilation of the rocket-borne observations made in the nocturnal ionosphere at middle and low latitudes. The measurements indicate that the flux can vary by a factor of more than 1000 depending on the magnetic activity, geomagnetic location and look-angle of the detector. Some of these variations may be attributed to differences in instrumentation. However, the flux measurements made at a fixed location using the same instrument (e g , in Table 4.1 observations by Smith and Voss, Gough and Collin, and Seward and Hill) illustrate the strong dynamic variations of magnetic activity alone. The energy fluxes designated by asterisks are estimates based on a power-law spectrum. A brief review and analysis of some of these experiments is given below.

*Cladis et al.* [1961] and *Walt et al.* [1960] report one of the first (July 1959) and most important rocket-borne measurements of energetic electrons at midlatitudes. Utilizing a four-stage Javelin sounding rocket, a particle spectrometer sensitive to electrons in the energy range  $50 \text{ keV} < E < 1 \text{ MeV}$  was flown to an altitude of 1045 km from Wallops Island and covered  $L$  shells between 2.5 and 1.9. The  $K_p$  index was 3. Figure 4.18 shows the trajectory and count rates of the trapped flux. Also shown are

Table 4.1

## Nighttime middle and low latitude rocket experiments

Name	Location	L value	Altitude km	Energy <sup>#</sup> keV	Flux cm <sup>-2</sup> sec <sup>-1</sup> ster <sup>-1</sup>	Flux ergs cm <sup>-2</sup> sec <sup>-1</sup> ster <sup>-1</sup>	kp	$\chi^*$	UT	Date
Voss and Smith <sup>T</sup>	Chilca, Peru	1 0	200	E > 50	240		moderate		0511	6/2/75
Voss and Smith <sup>T</sup>	Chilca, Peru	1 0	200	E > 44	30		low		0436	5/30/75
Hill et al [1970]	Johnston Island	1 07	300	E > 3 5	800	3 5×10 <sup>-6</sup>	moderate			11/6/68
Seward et al [1973]	Johnston Island	1 07	500	E > 44	30		high			9/24/70
Hill et al [1970]	Kauai	1 16	160	E > 3 5	200		low	126°	0641	5/15/68
Hill et al [1970]	Kauai	1 16	160	E > 3 5	500	2 5×10 <sup>-6</sup>	high	128°	0656	5/17/69
Seward et al [1973]	Kauai	1 16	300	E > 5 5	100		low			5/26/71
Seward et al [1973]	Kauai	1 16	325	E > 3 5	500		high			10/21/72
Seward et al [1973]	Kauai	1 16	300	E > 5 5	27		low			10/23/71
Seward et al [1973]	Kauai	1 16	300	E > 5 5	9		very high			5/12/70
Hayakawa et al [1973a]	Kagoshima	1 17-1 25	800	E > 5	150			165°		9/3/71
Kohno [1973]	Kagoshima	1 18	300	6 5 < E < 23	27		high		0500	9/2/72
Turiel and MacGregor [1970]	27°N, 125°W	1 4*	225	E > 20	10		very high			11/3/68
Seward et al [1973]	27°N, 125°W	1 4	280	E > 5	800		moderate			4/25/73
Seward et al [1973]	27°N, 125°W	1 4	225	E > 19	15		high			11/3/68
Tuohy and Harries [1973]	Woomera	1 7*	200	E > 25				169°	0030	7/10/70
Morse and Rice [1976]	White Sands	1 8	120	04 < E < 5 5		7×10 <sup>-7</sup>	moderate	122°		1/9/75
Antonova et al [1969]		2 0*	160	E > 1		10 <sup>-2</sup>	low	113°		7/5/68
Tulinov et al [1974]	Volgograd	2 0*	180	E > 1		4×10 <sup>-4</sup>	low			9/25/71
Antonova et al [1972]		2 0*	160	E > 0 5		10 <sup>-3</sup>	low			7/31/68
Antonova et al [1972]		2 0*				10 <sup>-2</sup>	very low			4/19/63
Antonova et al [1972]		2 0*				4×10 <sup>-3</sup>	low			10/21/70
O'Brien et al [1965]	Wallops Island	2 6	167	E > 50	7	2×10 <sup>-2</sup>	low	167°	0413	7/9/64
Smith et al [1974]	Wallops Island	2 6	200	E > 70	550	10 <sup>-2</sup>	very high	130°	0503	11/1/72
Smith et al [1976]	Wallops Island	2 6	200	E > 12	4000	2×10 <sup>-3</sup>	high		0430	11/1/72
Voss and Smith <sup>T</sup>	Wallops Island	2 6	200	E > 13	370	10 <sup>-4</sup>	low		0220	6/30/74
Gough and Collin [1973]	South Uist	3 5	100	E > 40	4		low	125°	2008	11/16/70
Gough and Collin [1973]	South Uist	3 5	100	E > 40	3×10 <sup>-5</sup>		very high	130°	2041	4/21/70
Bryant and Courtier [1973]	South Uist	3 5	100	E > 40	80		low	140°	2118	2/29/68
Bryant and Courtier [1973]	South Uist	3 5	100	E > 40	400		moderate	160°	2240	9/30/69
Bryant and Courtier [1973]	South Uist	3 5	100	E > 40	400		moderate	160°	0120	10/1/69
Bryant and Courtier [1973]	South Uist	3 5	100	E > 40	1258		low	117°	0419	10/1/69
Gough and Courtier [1973]	South Uist	3 5	100	E > 40	13		low	120°	2000	2/25/68
Gough and Courtier [1973]	South Uist	3 5	100	E > 40	31		very low	135°	2100	7/14/71
Gough and Courtier [1973]	South Uist	3 5	100		6		very low	150°	2200	7/14/71

- See Sections 4 1 and 4 2

\* Approximate

# The first two entries are protons, the remainder electrons

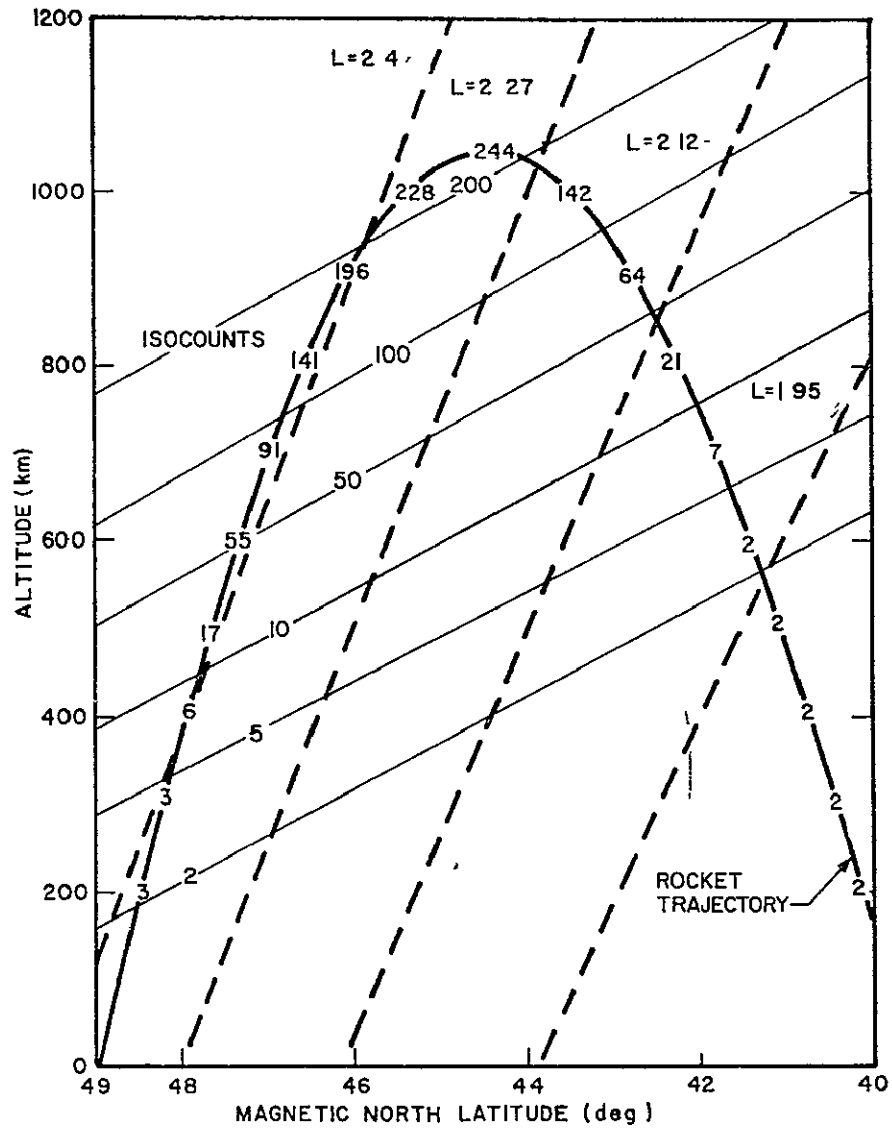


Figure 4.18 Particle data by *Cladis et al.* [1961] was obtained for electron with  $E > 50$  keV from a Javelin sounding rocket launched from Wallops Island which covered  $L$  shells between 2.5 and 1.9. Also illustrated are the iso-count rates indicated by these data. The flux at a given altitude decreases with decreasing latitude.

several magnetic field lines and contours of constant particle flux. The lines of constant count rate remain parallel for differing latitude increments and, therefore, a linear variation with latitude is justified to the first order. The particle flux at any height,  $H$ , over Wallops Island is, therefore, approximately the same flux as that over White Sands but at the greater altitude of  $H + 450$  km for  $H$  up to 400 km, at least. Also the flux over White Sands at any altitude is approximately a factor of 30 less than that over Wallops Island at the same altitude in agreement with the satellite data of Figure 4.17. The pitch-angle distribution is centered about  $90^\circ$  and was derived separately from the altitude profile and the detector look angle. The importance of mirroring particles over Wallops Island is evident from this altitude profile since the flux increases strongly with altitude. The total omnidirectional electron ( $E > 50$  keV) intensity at apogee is  $4 \times 10^6 \text{ cm}^{-2} \text{ s}^{-1}$  and this value is consistent with the satellite data of O'Brien at this energy ( $3.2 \times 10^5 \text{ cm}^{-2} \text{ s}^{-1} \text{ ster}^{-1}$ ).

O'Brien *et al.*, [1965] made a measurement of energetic particles (and 391.4 nm emission) using a Nike Apache rocket (167 km apogee) launched from Wallops Island (0413 UT, 9 July 1964,  $K_p = 3$ ). A 6213 Geiger counter was pointed at  $70^\circ$  to the rocket spin axis and had an opening angle of  $\pm 9.5^\circ$  (geometrical factor  $1.9 \times 10^{-2} \text{ cm}^2 \text{ ster}$ ). The flux measured was  $7 \pm 2$  particles  $\text{cm}^{-2} \text{ s}^{-1} \text{ ster}^{-1}$  for electron energies greater than 40 keV. An 8001 Geiger tube was aligned with the rocket spin axis and had an opening angle of  $\pm 33^\circ$  (geometrical factor  $6.7 \text{ cm}^2 \text{ ster}$ ). The measured flux was  $2.7$  particles  $\text{cm}^{-2} \text{ s}^{-1} \text{ ster}^{-1}$  for electron energies greater than 100 keV. The flux was found to be altitude dependent above the absorption region of 100 km as expected at this energy. The fact that July 1964 was at a solar

minimum may have also contributed to these low fluxes.

*Hill et al.* [1970], *Seward* [1973] and *Hayakawa et al.* [1973 a,b] have all recorded anomalously high background count rates with rocket-borne X-ray equipment which are attributed to energetic electrons. The count rates have been found to be either centered about  $90^\circ$  pitch angle or isotropic downward or some combination of the two. These measurements have been taken in the inner radiation belt for  $L$  values less than 1.4.

Some of the first important rocket-borne investigations of midlatitude particle precipitation and have been conducted by *Tulinov et al.* [1967], *Antonova and Ivanov-Kholodny* [1961] and *Ivanov-Kholodny* [1965]. However, incomplete information is known about launch conditions, launch locations and altitude profiles to make comparisons with other related experiments. Briefly, it is found in their analyses that particle fluxes are very large ( $10^{-1}$  ergs  $\text{cm}^2 \text{s}^{-1} \text{ster}^{-1}$ ) in the daytime and near sunrise and sunset but are of the order of  $10^{-3}$  to  $10^{-4}$  ergs  $\text{cm}^{-2} \text{s}^{-1} \text{ster}^{-1}$  during the night in agreement with other nighttime rocket data.

#### 4.5 Summary of Observations

In this final section of the chapter an attempt is made to summarize the observations of energetic electrons at midlatitudes. First the geographic variations are considered with particular reference to the location of Wallops Island, Arecibo and other observing stations in relation to the precipitation zones. Then the variation of count rate is considered and finally the relation between magnetic activity and particle precipitation

4.5.1 *Geographic variations and precipitation zones.* The latitudinal variation of particle precipitation may be represented in a  $B$ - $L$  space diagram, Figure 4.19, with *Seward's* [1973] satellite flux contours. Also shown are the various locations of rocket launch sites and the Arecibo observatory at

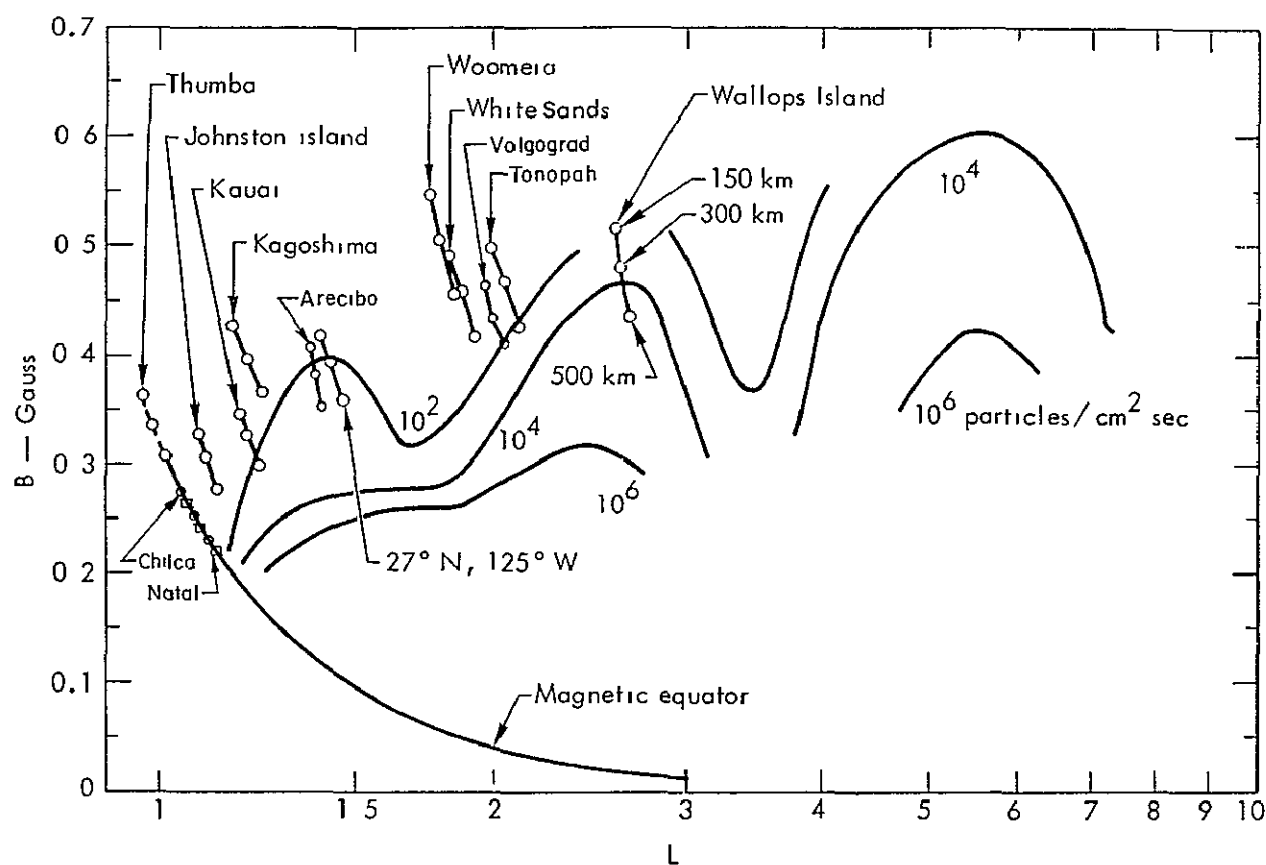


Figure 4.19 This figure, adapted from *Seward* [1973], shows the omnidirectional flux of energetic electrons for  $E > 100$  keV. Added to his figure are the B-L coordinates of Chilca, Natal, Arecibo and Volgograd for altitudes 150, 300, and 500 km. The Arecibo and Wallops Island precipitation zones are clearly evident.



designated altitudes. In this diagram (which represents predominantly the trapped flux) the longitudinal variations of particle precipitation is clearly seen. The main feature shown here is the identification of two midlatitude precipitation zones. One of these may be labeled the Wallops Island precipitation band ( $L = 2.6$ ) and the other the Arecibo precipitation zone ( $L = 1.4$ ). These precipitation zones are found to be associated with the resonant interaction of ELF waves (hiss) propagating in the plasmasphere (Chapter 6)

Further verification of the existence of these zones may be seen in the satellite data of *O'Brien* [1962] (Figure 4.17), *Larsen et al.* [1976] (Figure 4.16) and *Seward* [1972] (Figure 4.15) as a pronounced minimum at  $L = 2.0$  and a small flux enhancement at  $L = 1.4$ . Rocket data from Wallops Island, White Sands (between loss zones) and the Arecibo zone (Seward, Hill and Hayakawa data) is similarly in agreement with this concept. Furthermore, *Shen et al.* [1976] have established the necessity for a particle source above Arecibo in the region above 120 km.

4.5.2 *Variation of count rate with altitude.* The existence of the precipitation zones suggested in the previous section provides a basis for considering all available data concerning electron fluxes below 500 km. In this section we examine the variation of count rate (i.e., flux) with altitude in relation to the location with respect to the precipitation bands.

Figure 4.20 is a plot of count rate against altitude on a linear scale for trapped particles in the Arecibo zone (from data of *Seward et al.*, 1973). The conclusion is drawn that the trapped flux is a linear variation up to at least 500 km. The altitude intercept is in the range 100 to 140 km.

Altitude profiles in the outer zone are observed similarly to have this

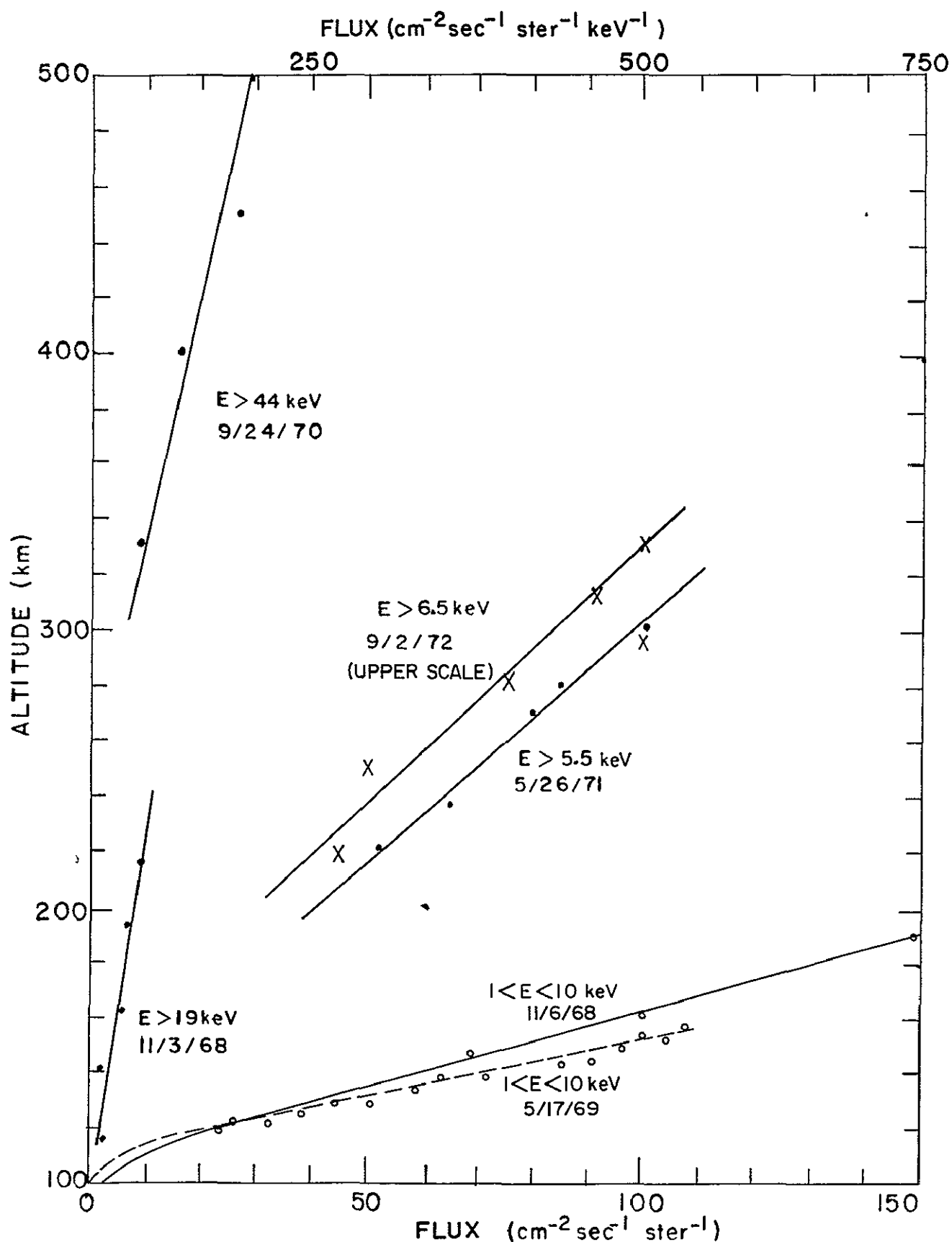


Figure 4.20 Count-rate profiles for quasi-trapped electrons observed by rockets launched in the Arecibo precipitation zone. Identification is given in Table 4.1 according to the launch date.

linear increase of count rate with altitude (Figures 4.5 and 4.6), however, the trapped fluxes are much larger. For the Wallops Island precipitation band the trapped flux extends down to 100 to 140 km and consequently does interact significantly with the ionosphere. The Wallops Island and Arecibo precipitation zones are caused by resonances in the outer and inner radiation zones by wave-particle interactions with the trapped flux. On the other hand the isotropic flux is not so simply explained and is complicated by the source mechanism (see Chapter 6). As shown in Figures 4.15 and 4.17 this isotropic flux decreases monotonically with decreasing latitude from the outer zone.

The altitude profile of the trapped flux is believed to be due to the interaction of energetic electrons with the atmosphere (scattering and ionization) as described in Section 6.4. The explanation for the high altitude intercepts in the equatorial experiments (Figures 4.12 and 4.13) is interpreted as an indication that the equatorial particles are protons.

4.5.3 *Magnetic activity and particle precipitation.* The particle flux observed below 400 km altitude is found to vary strongly with magnetic activity. For precipitation from the inner zone the flux (both quasi-trapped and direct) is found to be correlated not only with magnetic activity but also with the time of the last sudden commencement [Seward *et al.*, 1973]. Seward *et al.* [1973] find that the decay rate after a sudden commencement may be approximated by a power-law variation. These data may be represented by the relation

$$F_{200} = 3.6 \times 10^3 D^{-1.87} \quad (4.3)$$

where  $F_{200}$  is the measured parallel flux ( $\text{cm}^{-2} \text{ s}^{-1} \text{ ster}^{-1}$ ) at 200 km and  $D$  is the number of days since the last sudden commencement. The dependence of the parallel

flux on the five day sum of the magnetic Ap index is similarly given by

$$F_{200} = 0.126 A_p^{1.6} \quad (4.4)$$

For the perpendicular flux the five day sum of the Ap index is found to be

$$F_{300} = 3.2 A_p^{1.1} \quad (4.5)$$

where  $F_{300}$  is the perpendicular flux at 300 km. From this analysis it seems that the parallel flux (exponent 1.6) may be slightly more dependent on magnetic activity than the perpendicular flux (exponent 1.1).

From the new results at the equator (see Section 4.2) (Figures 4.12 and 4.13) the flux variation using differing indices of magnetic activity is given by Table 4.2 assuming a power-law variation at 200 km of the form

$$F_{200} = KI^x \quad (4.6)$$

where  $K$  is a constant and  $I$  is the magnetic index which is represented as.

1) the 5 day sum of Ap, 2) the average Kp over the previous 24 hours, and 3) as the Kp during the flight only. Also shown in Table 4.2 is the ratio of the magnetic index observed on these two occasions.

As found in the table the ratio between these two flights of the magnetic index is the largest for the Kp index (2.14) and therefore seems to indicate that the flux at the equator can build up rapidly. Satellite data from *Moritz* [1973] for protons at low altitudes seem to confirm this. Furthermore, it is found that pitch-angle scattering at the equator by wave-particle interactions is extremely small. Hence, the strong dependence of the equatorial flux on the Kp index is an indication of a rapid injection mechanism. Since the equatorial ring current follows Kp directly, the conclusion is strengthened that the equatorial flux measured is a result of

Table 4 2

Magnetic Index Comparisons for Equatorial Rocket Launches

	5 day $\Sigma Ap$	24 hour average of Kp	Kp at launch time	Count rate at 200 km ( $\text{sec}^{-1}$ )
30 May 1975	50	2.5	2+	1.3
2 June 1975	77	3.9	5	7
Spectral index	3.9	3 8	2.1	--
Ratio	1.54	1 56	2 14	5.3

the double charge exchange process of ring current protons (see *Mizera and Blake*, 1973). Thus particle precipitation at the equator is a quite different process than for  $L$  values greater than 1.1

The precipitation characteristics versus magnetic activity for the midlatitude Wallops Island precipitation band is not so simply understood. Figure 4.21 presents the particle flux variation versus  $K_p$  for differing energies of 13, 16, 32, 40, 57 and 70 keV electrons. Three rocket flights are illustrated: 14.439 for which  $K_p = 8$ , 14.520,  $K_p = 5+$ ; and 14.521,  $K_p = 3+$ . Rockets 14.520 and 14.521 were each instrumented with an EES and rocket 14.439 with a Geiger counter. Also shown in this figure is the ionization rate curve calculated from the integrated electron-density profile (Figure 2.9) and satellite data (Injun III) of precipitating particles with energy greater than 40 keV by *O'Brien* [1964]. The rocket data are measurements of the quasi-trapped flux at 155 km.

Some of the significant conclusions which may be inferred from this graph are: 1) the ionization rate in the upper  $E$  region changes proportionally with the particle flux for energies less than 30 keV, 2) the aggregate precipitating flux for  $E > 40$  keV measured by *O'Brien* [1964] at 100 km changes in the same way as the  $E < 30$  keV trapped flux, 3) the trapped flux variation with magnetic activity at low altitudes (155 km) shows a marked dependence on  $K_p$ , 4) the flux with  $E > 50$  keV does not vary appreciably for  $K_p$  values between 2 and 6; and 5) the flux  $E > 70$  keV is observed to increase by an order of magnitude or more for high values of  $K_p$  at Wallops Island (plasmopause crossing). The strong correlation of particle flux ( $E < 30$  keV) with ionization rate lends good support for the corpuscular hypothesis.

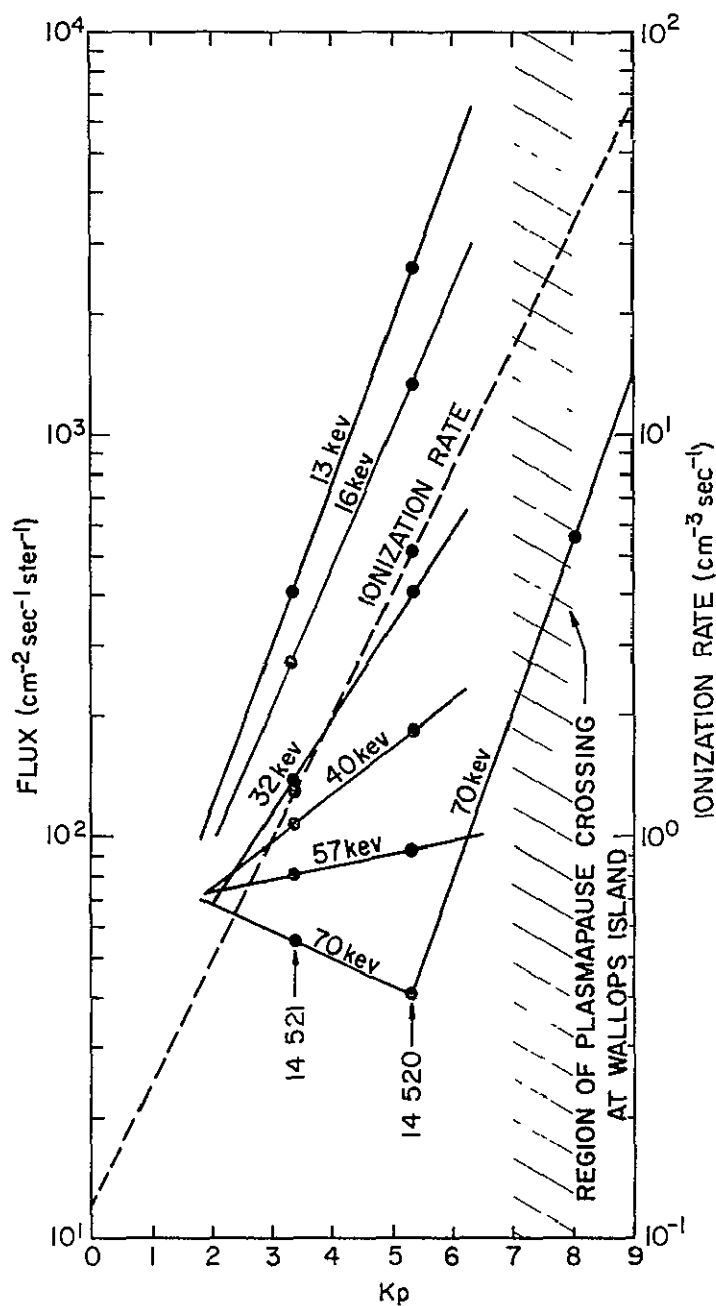


Figure 4.21 The particle flux at 150 km is shown versus magnetic activity index  $K_p$  for different energies at Wallops Island. Before the plasmasphere crossing (cross hatched area) and for  $E > 50$  keV the flux does not change much with  $K_p$ . For lower energies the electron flux depends strongly on  $K_p$ . Also shown is the ionization rate (from Figure 2.8).

## 5 INDIRECT EVIDENCE OF ENERGETIC ELECTRON PRECIPITATION

A number of indirect techniques may be employed to further understand the morphological characteristics of particle precipitation. The kinds of indirect measurements which will be investigated in this section include 391.4 nm emission, ionization-rate measurements, VLF Doppler shifts, critical-frequency variations, electron-temperature variations and Bremsstrahlung X-ray emission.

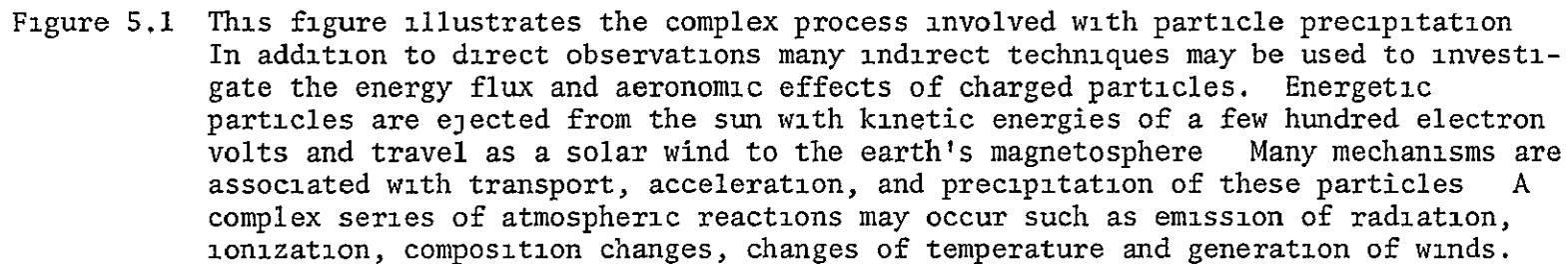
Ideally, a model capable of predicting global particle effects from proper interpretation of various ground-based experiments is desired. For example, from analysis of solar activity, magnetic field deviations and extremely-low-frequency hiss one could possibly predict with good certainty the electron-density increases, temperature changes, ion-density variations and general EM-wave propagation.

Even more fundamental is the prediction of particle effects a few days in advance by proper interpretation of solar activity and measurement of interplanetary particle data from satellites in conjunction with a realistic magnetosphere model. Figure 5.1 illustrates the complexity of the interactions involved for such a precipitation model. A discussion of the magnetosphere and radiation belt physics will be given in Chapter 6. Ionization and scattering processes will be discussed in Chapter 7. The present section concerns the indirect observations of particle ionization.

### 5.1 *Midlatitude 391.4 nm Emission*

Historically, various attempts have been made to link many of the visible midlatitude airglows (particularly 557.7 nm) to particle precipitation. Analysis by *O'Brien et al* [1965] has shown that most midlatitude airglows are not the result of excitation by energetic particles. However, the emission of 391.4 nm radiation of molecular nitrogen ions is clearly related to the precipitation of energetic electrons.





The excitation energy for the first negative band system of the molecular nitrogen ion is so high (18.8 eV) that no mechanism other than energetic particles seems to be a viable explanation of the 391.4 nm band. The emission intensities of 391.4 nm band are found to be directly proportional to the total energy of the incoming particles [Stanford, 1968, Stair and Gauvin, 1967] Stair and Gauvin [1967] have found the absolute production cross sections for the first negative band of  $N_2^+$  by the interaction



The second reaction here requires only 3.2 eV for excitation of an  $N_2^+$  ion and therefore seems susceptible to other ionization sources. However, no two-body mechanism (other than particle precipitation) is known to bring  $N_2^+(X^2\Sigma_g^+)$  to  $N_2^+(B^2\Sigma_u^+)$  and since the concentration of  $N_2^+$  is extremely small there is similarly no explanation for the observed fluxes of  $10^6$  photons  $\text{cm}^{-2} \text{sec}^{-1}$  of 391.4 nm emission. From Rees [1963], for isotropic angular distributions and monoenergetic beams, the flux needed to produce one rayleigh ( $10^6$  photons  $\text{cm}^{-2} \text{s}^{-1}$ ) is  $10^6$  and  $8 \times 10^4 \text{ cm}^{-2} \text{s}^{-1}$  for 5.6 and 40 keV electrons respectively (corresponding to an energy flux of about  $10^{-2} \text{ ergs cm}^{-2} \text{s}^{-1}$ ).

The latitudinal variations for various 391.4 nm measurements in the Northern Hemisphere are shown in Figure 5.2. Although statistics are not good, the results seem to correlate well with the interpretation of two zones of precipitation. Hirao *et al.* [1965] (point 1) have measured approximately one to three rayleighs for moderate values of  $K_p$  at Niigata ( $L = 1.3$ ). This measurement is indicative of the Arecibo band of precipitation

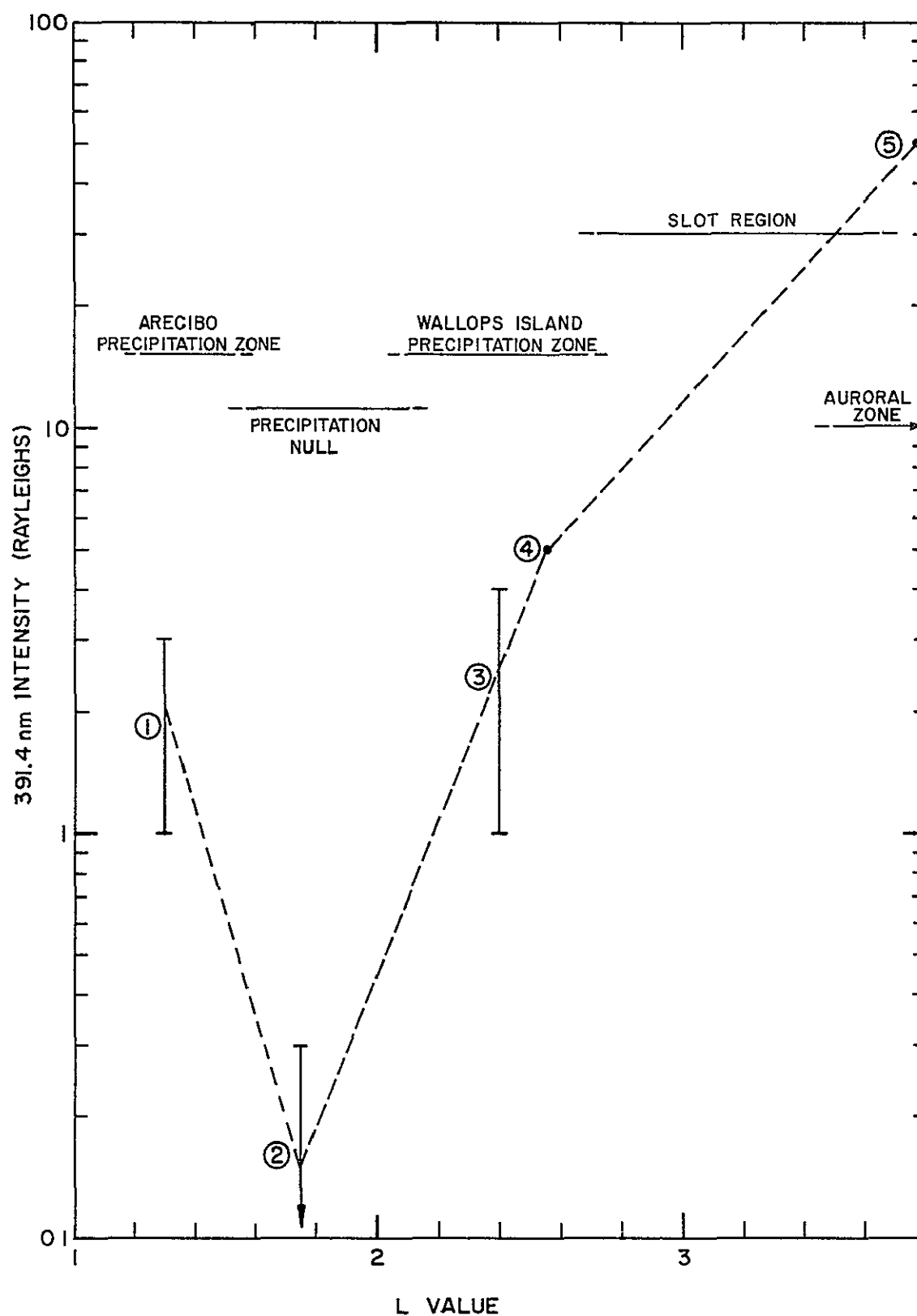


Figure 5.2 Various measurements of midlatitude 391.4 nm radiation are consistent with the concept of an Arecibo zone and a Wallops Island zone of particle precipitation. Identification of the measurements is given in the text

mentioned previously in Section 4.5.1. This intensity is also found to correlate strongly with magnetic activity and hence suggests particle precipitation. In Section 6.3 this is discussed in terms of the plasmaspheric hiss maximum at  $L = 1.4$  which produces particle scattering resulting in ionization and 391.4 nm emission.

Point 2 in the figure is taken between the precipitation zones and consequently the intensity is expected to be and is observed to be small (0.2 rayleighs). The data were obtained by Hunten and Broadfoot at Kitt Peak, Tucson, Arizona (see *Potemra and Zmuda*, 1972). On the basis of this observation *Broadfoot and Hunten* [1966] have concluded that  $N_2^+$  emission might not even exist in the nightglow at midlatitudes. However it is now apparent that the  $N_2^+$  emission is vanishingly small only between the precipitation zones.

Point 3 is derived from a 427.8 nm measurement by R. Hickerson (see *Potemra and Zmuda*, 1972) at Silver Springs, Maryland, which is located in the Wallops Island precipitation band. The range of intensity is 1 to 4 rayleighs. Also *O'Brien et al.* [1965] find an intensity, at Wallops Island, of approximately 4 rayleighs. At Saskatoon, Saskatchewan ( $L = 3.8$ ) an intensity of 391.4 nm emission of 50 rayleighs has been measured by *Maartense and Hunten* [1963]. This is in accord with higher precipitation values expected as one moves toward the auroral region from Wallops Island and corresponds with the steadily increasing loss cone flux with latitude (see Figure 4.17).

The agreement between the 391.4 nm emission maximum at  $L = 1.4$ , minimum at  $L = 1.8$  and maximum for  $L > 2.5$  with the similar variation in particle flux measurements supports the conclusion that ionizing particles are a permanent feature of the nocturnal ionosphere.

## 5.2 Ionization Rate Variations with Kp

*Smith et al.* [1974] have shown a strong correlation with Kp of the ionization rate deduced from seven electron-density profiles in the region 120 to 180 km at Wallops Island (see Section 2.3). These results are shown in Figure 2.8 and a least squares fit to the data may be represented by

$$q = 0.12 \exp(0.7 Kp) \quad (5.2)$$

where  $q$  is the ionization rate measured in ion-pairs  $\text{cm}^{-3} \text{s}^{-1}$ . The correlation coefficient is 0.92.

*Shen et al.* [1976] have found evidence (see Section 2.3) that the ionization observed above Arecibo (in the altitude range of 120 to 180 km) is only explainable in terms of particle precipitation. These measurements are indicative of the  $L = 1.4$  precipitation zone.

*Wakar* [1967] has made a detailed study at Boulder, Colorado of nocturnal electron densities in the region 100 to 300 km. These results show conclusively that the ionization is significantly enhanced during magnetic disturbances. Boulder is expected to register particle effects since it is located within the Wallops Island precipitation band.

## 5.3 VLF Doppler Shifts and Field Intensity Variations

From analysis of LF (30–300 kHz) and VLF (3–30 kHz) phase and amplitude variations at midlatitudes *Belrose and Thomas* [1968], *Reder and Westerlund* [1970] and *Doherty* [1971] have determined a correlation with particle precipitation. *Potemra and Rosenberg* [1973] and *Potemra and Zmuda* [1970] have reviewed the subject and have extended these results with additional measurements and calculations.

Low frequency pulse transmissions reflect in the ionospheric D region at a height of approximately 90 km during the night and 70 km during the day. Observations made on various LF propagation paths show that the phase and

amplitude of the received signals can vary indicating that there is a change in the ionospheric conditions at the reflection point. These reflection height changes (phase changes) in the earth-ionosphere waveguide are correlated with balloon Bremsstrahlung X-rays and magnetograms. These reflection height changes [Potemra and Rosenberg, 1973] are attributed to ionization enhancements produced by electron fluxes ( $E > 40$  keV) of  $10$  to  $100 \text{ cm}^{-2} \text{ s}^{-1} \text{ ster}^{-1}$ . These small fluxes are well below the limit of most ground-based detection schemes (including Bremsstrahlung X-rays and riometer absorption) and therefore VLF propagation can serve as a useful tool for the detection of low-intensity electron precipitation.

The *D*-region ionization is principally caused by the incident loss-cone flux and to a lesser extent by the scattered quasi-trapped flux. Satellite data from Larsen *et al.* [1976 a,b] show that this direct (or loss-cone) precipitation decreases with latitude. Although VLF transmissions are sensitive to loss-cone precipitation of particles in the *D* region they give us information on the energy spectrum and pitch-angle distribution of the incident flux. Further problems associated with the interpretation of phase shifts are proper inclusion of density gradients, diurnal variations of the ionosphere lower boundary and transport of ionization at the reflection region. Nevertheless this technique is quite useful in recording the effects of particle ionization in the low *D* region.

#### 5.4 The Critical Frequency, $f_{XEN}$ , of the Nighttime Intermediate Layer

Hirao *et al.* [1965] have found that the critical frequency (obtained from ionograms) of the nighttime intermediate layer varies proportionately with the three-hourly K index for midlatitude measurements made at Wakkanai, Akita, Kokubunji and Yamugawa. This positive correlation of the critical frequency with magnetic activity they believe to be representative of electron

density increases due to increased ionization by energetic particles at midlatitudes. *Wakai* [1967] has also found this positive correlation at Denver, Colorado.

*Smith et al.* [1974] have verified that the intermediate layer is sensitive to energetic particle precipitation and have found that both the integrated electron density of the intermediate layer and the layer maximum increases strongly with magnetic activity. Figure 5.3 shows the variation of the peak electron density of the intermediate layer with magnetic index  $K_p$  for the seven nighttime electron-density profiles previously shown in Figures 2.1 and 2.7 where the correlation coefficient is 0.9. The layer peak ( $\text{cm}^{-3}$ ) is given approximately by

$$N_p = 1110 \exp (0.39 K_p)$$

The peak density of the intermediate layer is also a function of the wind velocity as shown previously in Figure 2.12. The sensitivity to wind velocity is small compared with the sensitivity to ionization rate; a change from 20 to 50  $\text{m s}^{-1}$  in the vertical ion drift velocity produces a change in the maximum electron density from  $7.8 \times 10^4$  to  $9 \times 10^4 \text{ cm}^{-3}$ , i.e., a 15% increase.

Further characteristics of the intermediate layer have been discussed in Chapter 2 for the temporal evolution at night. *Hirao et al.* [1965] have also found that the absorption of 5 and 10 MHz radio waves is correlated with magnetic activity and is the result of an increase of nondeviative absorption in the nighttime intermediate layer. This occurs because of increased electron density and temperature and increased collision frequency.

### 5.5 $K_p$ Variations and Electron Temperature

*Smith et al.* [1974], using data from *Evans* [1973], have found that the electron temperature ( $T_e$ ) above 120 km at Millstone Hill varies with geomagnetic activity during nighttime (2100-0300 EST) and may be represented at

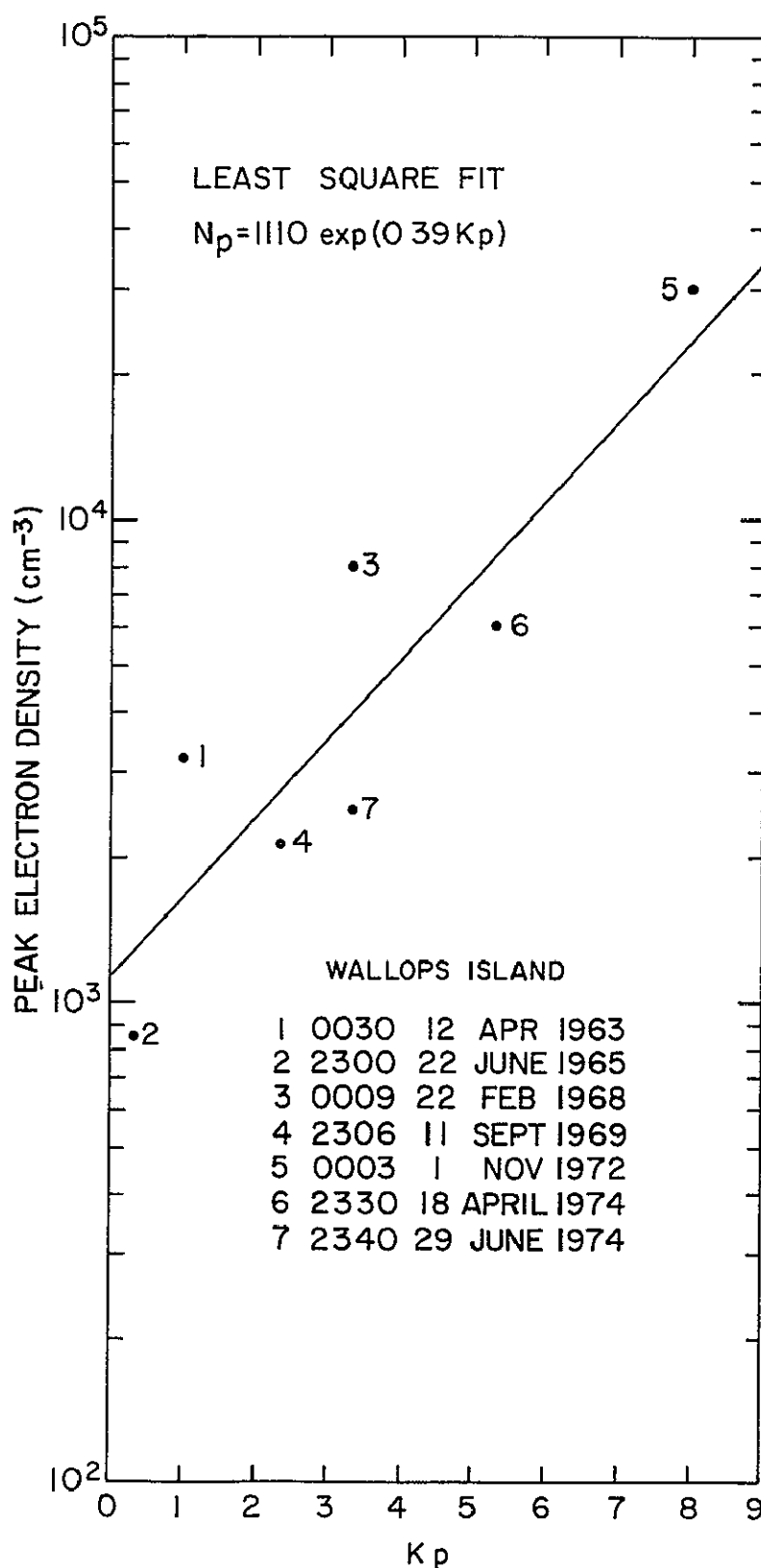


Figure 5 3 Variation of the peak electron density of the intermediate layer with magnetic activity. These measurements were taken from the electron-density profiles of Figures 2 1 and 2 7. Times are EST.



200 km as

$$T_e = (112 K_p + 588)^\circ K \quad (5.3)$$

These observations were made on eight occasions in 1966 and 1967 with a range of values of  $K_p$  from 1 to 5 and a correlation coefficient of 0.90. Following Evans the electron temperature at 120 km is assumed to be  $T_e = 355^\circ K$ . A linear interpolation for altitude between 120 and 200 km gives

$$T_e(z) = (z-120)(1.4 K_p + 2.9) + 355^\circ K \quad (5.4)$$

Millstone Hill is located in the Wallops Island precipitation zone and is therefore expected to be strongly influenced by particle precipitation

*Hirao et al.* [1965] have found a strong correlation of magnetic activity with electron temperature and a latitude effect which indicates strong precipitation in the Wallops Island precipitation band. A qualitative explanation for this temperature increase is believed to be the result of collisions between the energetic and ambient electrons and subsequent recombination with ion species. Section 7.1 shows the cross section formula for electron-electron collisions. This energy loss mechanism can transfer approximately 10% of the total decay energy to heat the ambient electrons.

#### 5.6 *Bremsstrahlung X-rays as a Global Precipitation Snapshot*

All the previous measurements of energetic electrons have been limited in scope to small regions of space or short durations in time. The sporadic nature of these measurements makes the task of interpretation and correlation difficult and expensive. What is needed is a global "snapshot" of the precipitating electrons and Bremsstrahlung X-rays televised on a satellite afford such an opportunity.

When a charged energetic particle collides with matter, there is a deceleration and hence an emission of electromagnetic radiation [*Jackson*, 1962].

This radiation emitted during an atomic deceleration is termed Bremsstrahlung (or braking radiation). Utilizing a properly designed X-ray detector, this Bremsstrahlung radiation can be measured and the particle energy spectrum can be determined from the X-ray spectrum. With proper design and implementation on a satellite this "X-ray camera" could give an instantaneous map of the midlatitude precipitation belt with intensity and geographic variations.

*Imhof et al.* [1974] have reported for the first time on the effectiveness of this method. Utilizing a 50 cm<sup>2</sup> Ge-Li gamma-ray spectrometer aboard the spin-stabilized satellite 1972-076B at 750 km altitude the Bremsstrahlung intensity and energy spectra above 50 keV was measured. Their results indicate the occurrence of nearly simultaneous precipitation over a wide range of local times. Further research is necessary for developing a rapid scanning X-ray detector with high resolving capabilities and energy spectrum information. This is a most promising field of endeavor for unraveling the dynamic nature of particle precipitation.

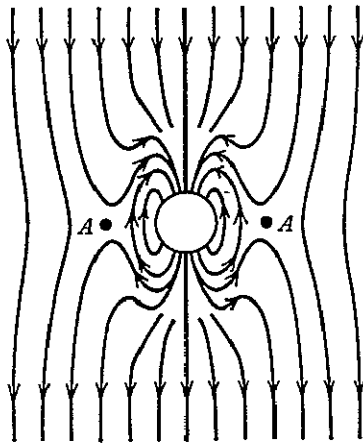
## 6 PARTICLE INJECTION AND DIFFUSION

To facilitate an understanding of the global characteristics of particle precipitation, it is necessary to explain the particle phenomena in terms of a working model of the magnetosphere. Basic questions of fundamental importance include 1) what is the source and mechanism for mirror height lowering or pitch angle scattering? 2) how do particles enter and become accelerated within the radiation belt? 3) why are there two midlatitude precipitation zones? and 4) what causes the longitudinal variations of particle precipitation? Figure 5.1 illustrated the numerous interactions involved within the magnetosphere for transferring solar wind particles to accelerated energies within the midlatitude ionosphere.

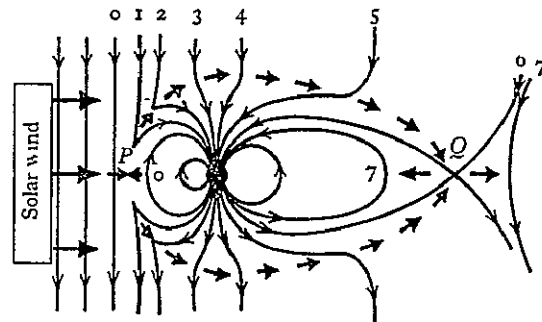
This section will begin with a discussion of how particles are transferred from the solar wind and migrate, via radial diffusion, into the radiation belts. Next, an explanation is given for the existence of the two zones of precipitation at midlatitudes. This invokes pitch angle scattering mechanisms. Finally, a discussion is given of the longitudinal variations of trapped particles.

### 6.1 *The Magnetosphere*

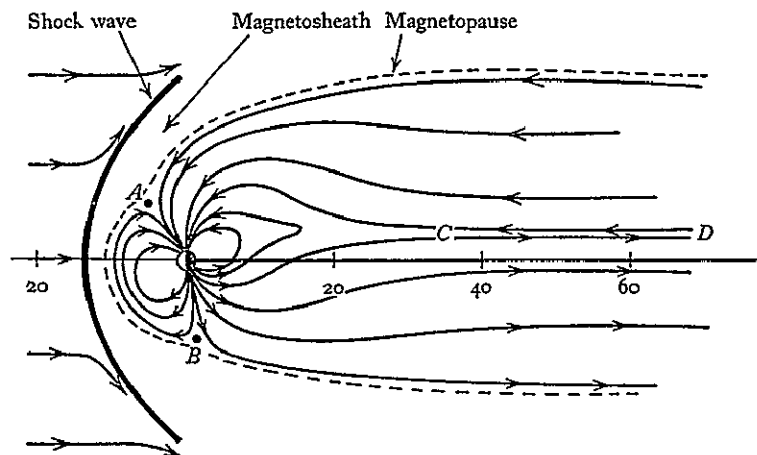
This section will briefly discuss the relevant mechanics of how low-energy plasma of the solar wind intercepts the earth's magnetic field and becomes accelerated and ultimately trapped within the radiation belts. Figure 6.1 outlines the complex nature of the earth's magnetosphere [Ratcliffe, 1970]. The earth's magnetic field exhibits tremendous modification from the expected simple dipole because of the interaction of the solar corpuscular wind. The source of the solar wind is the supersonic expansion of the solar corona with typical radial velocities of 300 to 400 km s<sup>-1</sup> (1 e, electron energy of  $\approx 0.25$  eV and proton energy of  $\approx 0.5$  keV), a flux (at one astronomical



(a)



(b)



(c)

Figure 6.1 Representation of the earth's dipole field interconnecting with the interplanetary magnetic field and being modified by the solar wind. Figures are from *Ratcliffe* [1972]

unit) of  $1.5 \times 10^8 \text{ cm}^{-2} \text{ s}^{-1}$ , a density of  $5 \text{ cm}^{-3}$ , and an energy density of  $4 \times 10^{-16} \text{ J cm}^{-3}$ . The approximate sun-earth transit time is four days.

The interplanetary magnetic field connects with the earth's magnetic field and provides a path for solar plasma to enter the earth's radiation belt. The interplanetary magnetic field is generated by the sun and is broken into four or six sectors having alternate inward and outward directed field lines. Furthermore, the interplanetary field lines are "frozen in" and carried with the solar plasma since the magnetic diffusion time is on the order of  $10^8$  years [see *Jackson*, 1962].

The solar magnetic field is found to rotate with a 27-day period and the radial ejected plasma "freezes in" the solar field lines. Consequently the conservation of angular momentum requires that the interplanetary magnetic field be distributed in an Archimedean spiral. At the earth's orbit the interplanetary field is about  $45^\circ$  from radial and is found to reverse direction every 3 to 6 days. A review of this material is given by *Williams* [1976].

Two waves can propagate within the solar wind. The acoustic wave has a velocity of about  $50 \text{ km s}^{-1}$  and the Alfvén (hydromagnetic) wave has a velocity of about  $10 \text{ km s}^{-1}$ . Since the wind velocity is greater than the wave velocity, a supersonic standing shock wave exists (Figure 6 1c) at about  $10 R_e$  on the solar side at which the flow lines abruptly change their direction. The solar wind pressure at this boundary just balances the magnetic pressure of the compressed earth's dipole magnetic field. Increases in solar flux result in further dipole compression at the boundary, measurable magnetic flux changes at the earth, possible radial diffusion of particles into the radiation belts and generation of plasmaspheric hiss.

The interplanetary magnetic field (assuming no solar wind, i.e., freezing-in of field lines) when directed from north to south across the earth is simply superimposed on the earth's dipole field to give a symmetrical configuration with a neutral ring about the equatorial plane (Figure 6.1(a)). If the interplanetary magnetic field is directed from south to north, the symmetrical configuration has two neutral points over the poles.

For the more complex situation of a solar wind with "captured" magnetic field lines in the north-to-south direction the phenomenon which takes place is a compression and field interconnection on the sun-side of the earth. There is a sweeping action which carries the interconnected field lines to the antisolar side and stretches them into the magnetotail over many earth radii. Finally, the earth and interplanetary lines separate and rejoin as shown in Figure 6.1(b).

The final configuration that results is shown in Figure 6.1(c) and is due to further remodification by plasma build up and generation of electric and magnetic fields within the magnetosphere itself. For example, plasma builds up in the neutral sheet region (low field region, also called plasma sheet) and becomes highly conductive. An effective dynamo generator producing 40-50 kilovolts across the magnetosphere exists due to the  $\vec{V} \times \vec{B}$  force exerted by the solar wind moving across the magnetic field lines. Two solenoidal currents, in the northern and southern halves, are formed across the plasma sheet and magnetopause. Magnetopause currents thus generated can reach  $\approx 5 \times 10^7$  amp which can appreciably alter the magnetosphere and cause the magnetotail to look like a cylinder which is swept out to about 1000 earth radii. Some of this current ( $\approx 10^6$  amp) is also conducted to the earth's ionosphere through auroral field lines and ionosphere currents. This auroral current moves plasma which collides with and excites the ionospheric consti-

tments and produces the auroral oval.

Some of the particles from the outer magnetosphere diffuse radially inward due to substorm generation of electric and magnetic fields and thus violate the third adiabatic invariant ( $L$ -shell conservation) of trapped particles. The diffusion coefficients which are required to transport the outer zone particles to the inner regions are consistent with magnetospheric and plasmaspheric electric fields of  $0.28 \text{ mV m}^{-1}$  and characteristic periods of 1600 seconds [Tomassion *et al* , 1972]. Also, Walt [1971] has reviewed the radial diffusion characteristics of trapped particles.

Another important feature of the magnetosphere is the existence of the plasmasphere, a region ( $L < 4$ ) populated by photoelectrons with typical energies of 0.1 eV. The sharp cutoff of electron density at  $L = 4$  (e.g., a reduction from  $10^3 \text{ cm}^{-3}$  to  $10 \text{ cm}^{-3}$ ) is known as the midlatitude trough or plasmopause and is the result of a closed electric field produced by the earth's rotation [Williams, 1976]. Ionospheric plasma is able to remain in diffusive equilibrium within the plasmasphere because of the containment by the closed electric field lines. For  $L > 4$  the ionospheric plasma is not in equilibrium and is able to diffuse into either the plasmasheet or the interplanetary medium (polar wind). The plasmasphere and plasmopause are crucial to the understanding of particle precipitation since VLF electromagnetic waves can propagate in this region and cause pitch angle scattering of energetic particles by wave-particle interactions.

## 6.2 Radiation Belts

Historically, the Van Allen radiation belts were found to be divided into the outer and inner zones. It is now known that the spatial distribution of particles within the radiation belt is a function of particle type and

energy [see *Hess*, 1968]. For electrons with energy greater than 40 keV there is essentially one large belt extending between  $L = 1.6$  and  $L = 8$  ( $J_o = 10^7 \text{ cm}^{-2} \text{ s}^{-1}$ ). For much higher energies ( $E > 1.6 \text{ MeV}$ ) the belt narrows to the region between  $L = 3$  and  $L = 4$  ( $J_o \approx 10^4 \text{ cm}^{-2} \text{ s}^{-1}$ ). For protons there are two belts, one ( $E > 30 \text{ MeV}$ ) located between  $L = 1.4$  and  $L = 1.5$  ( $J_o \approx 10^4 \text{ cm}^{-2} \text{ s}^{-1}$ ) and the other ( $1 < E < 5 \text{ MeV}$ ) between  $L = 2.5$  and  $L = 6$  ( $J_o = 10^8 \text{ cm}^{-2} \text{ s}^{-1}$ ). Due to the nature of trapped particles in a dipole field the third adiabatic invariant causes the electrons to drift eastward around the earth as they spiral and bounce between conjugate points and causes protons to drift westward yielding a westward ring current.

The mechanism responsible for accelerating low energy solar plasma to keV and MeV energies is unknown. *Akasofu* [1967] suggests that plasma instabilities accelerate the particles, *Axford* [1967] and *Hoffman and Evans* [1968] suggest that acceleration occurs much closer to the earth, *Papadopoulos and Coffey* [1974], *Evans* [1974] and *Papadopoulos* [1977] suggest that an anomalous resistivity produces a potential drop along the field lines and *Hasegawa* [1976] suggests a kinetic Alfvén wave mechanism. More experimental and theoretical studies are necessary to understand which of these (if any) or combination thereof are the primary accelerators.

### 6.3 Particle Precipitation Excited by Wave-particle Interactions

It is now known that LF (30-300 MHz) electromagnetic waves propagating within the radiation belts are the primary mechanism for scattering trapped electrons [*Paulikas*, 1975, *Gendrin*, 1975]. These waves may be excited by lightning discharges [*Dungey*, 1963, *Reeve and Rycroft*, 1976], by magnetospheric storms and turbulence [*Hasegawa*, 1969], by plasmapause instabilities [*Cornwall*, 1971] and by man-made VLF transmissions (e.g., Morse-code trans-



missions and powerline radiation) [Hellwell et al., 1975]. When detected, these waves have sounds referred to as whistles, chorus, hooks, hiss, etc due to the dispersive and erratic nature of the plasmaspheric medium.

For electromagnetic waves propagating within a plasma with a magnetic field, use can be made of the Appleton-Hartree formula giving the refractive index as

$$n^2 = 1 - X / \left[ 1 - \frac{Y^2 \sin^2 \theta}{2(1-X)} \pm \left( \frac{Y^2 \sin^4 \theta}{4(1-X)^2} + Y^2 \cos^2 \theta \right)^{1/2} \right] \quad (6.1)$$

where  $X \equiv \omega_p^2 / \omega^2$ ,  $\omega_p$  is the plasma frequency,  $Y \equiv \omega_B / \omega$ ,  $\omega_B$  is the gyro-frequency and  $\theta$  is the angle between  $\vec{B}$  and the wave propagation direction. The two signs indicate the two characteristic modes. The electric field vector  $\vec{E}$  may be expressed as

$$\vec{E} = E_0 (R_x \hat{x} + \hat{y} + Q R_x \hat{z}) \exp [j\omega(t - nz/c)] \quad (6.2)$$

where  $\vec{B}_0$  is in the  $y$ - $z$  plane,  $\vec{k}$  is along the  $z$  axis and  $R_x$  and  $Q$  are given by

$$R_x = \frac{j}{\cos \theta} \left[ \frac{Y \sin^2 \theta}{2(1-X)} \pm \left( \frac{Y^2 \sin^4 \theta}{4(1-X)^2} + \cos^2 \theta \right)^{1/2} \right] \quad (6.3)$$

and

$$Q = j Y \sin \theta \frac{(1-n^2)}{1-X} \quad (6.4)$$

For the special case when  $\theta = 0^\circ$  and the wave propagation is in the direction of the static magnetic field (whistler mode), equation (6.1) reduces to

$$n = \left( 1 - \frac{x}{1+y} \right)^{1/2} \quad (6.5)$$

with  $R_x = \frac{1}{1+y}$  and  $Q = 0$ .

These whistler waves are circularly polarized and purely transverse. Since  $n$ , the refractive index, is a function of frequency, the transmission

is dispersive and thus differing frequencies travel at varying speeds and give the sound effect of a whistle.

Furthermore, whistler waves are detected for propagation paths only within the plasmasphere since wave propagation is dependent on the refractive index and thus the plasma frequency and electron density. The sharp cutoff of the plasmasphere at the plasmopause marks the sharp decrease in whistler detection.

Figure 6.2 from *Lyons et al.* [1972] illustrates a 500 Hz whistler mode wave which is generated at the plasmopause and propagates within the plasmasphere. *Dungey* [1963, 1967] and *Lyons et al.* [1972] show that the maximum wave-particle interaction occurs for a wave number  $k_{11}$  given by

$$\omega - k_{11} v_{11} = N\omega_B \quad (6.6)$$

where  $\omega$  is the wave frequency,  $\omega_B$  is the gyrofrequency,  $v_{11}$  is the particle parallel velocity and  $N$  is an integer descriptive of the resonance mode. For  $N = 0$  Landau resonances occur at the mirror points, for  $N = 1$  the whistler mode resonances occur and for  $N > 1$  various higher order cyclotron resonances are possible (chorus, hooks, hiss, etc.) Plasmaspheric hiss is observed within the plasmasphere and has a maximum intensity (at a frequency of about a few hundred hertz) of  $10^{-7}$  to  $10^{-5} \gamma^2/\text{Hz}$  which yields amplitudes of 5 to 50 mV for usual bandwidths of a few hundred hertz.

*Lyons et al.* [1972] and *Lyons and Thorne* [1973] have computed electron lifetimes and pitch-angle distributions using generalized cyclotron ( $N > 1$ ) and Landau resonances. These calculations are in good agreement with experimental observations by *Imhof et al.* [1975], *Tsurutani et al.* [1975], and *Lyons and Williams* [1975a and 1975b]. Additional theoretical and experimental studies have been made by *Thorne et al.* [1973], *Imhof et al.* [1974], *Schulz and Lanzerotti* [1974], *Murphy et al.* [1975] and *Anderson*

ORIGINAL PAGE IS  
OF POOR QUALITY

### SLOT-REGION ELECTRON LOSSES

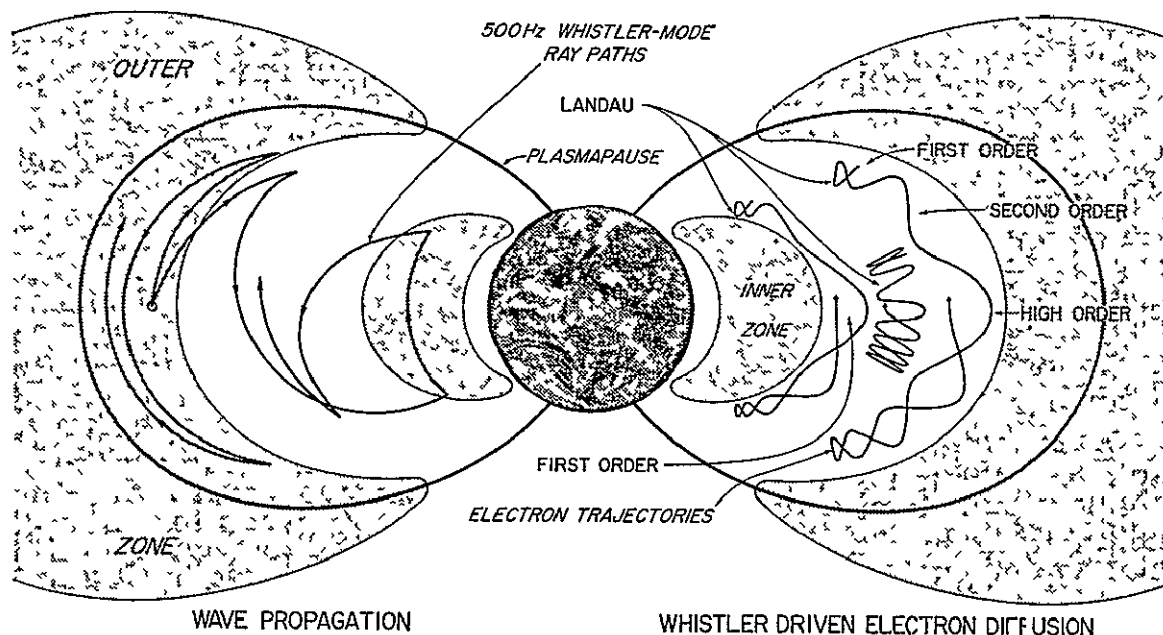


Figure 6.2 Illustration of 500 Hz whistler-mode propagation and the electron pitch-angle diffusion [Lyons *et al.*, 1972]. Waves are thought to be generated near the plasmapause as shown on the left-hand side. The right-hand side shows the resonant interactions that occur between the low frequency waves and the radiation belt electrons. Landau resonances occur near the mirror points with higher order resonances occurring towards higher latitudes.

and Maeda [1977]. Further successes of the theory of wave-particle interaction include the explanation of the Wallops Island precipitation zone ( $2 < L < 3$ ), the slot region of the radiation belt ( $3 < L < 4$ ), the energy spectrum maxima and flux variations with magnetic  $L$  value.

In order for particle precipitation to occur, it is necessary that there be an injection of particles into the appropriate  $L$  shell by radial diffusion and simultaneously a pitch angle scattering mechanism with a time constant of a few days. The radial diffusion of trapped particles to lower  $L$  values is seen in satellite data of Lyons and Williams [1975a] and is shown in Figure 6.3. The evolution of the equatorial trapped flux ( $35 < E < 50$  keV) is observed to behave like a flux pulse starting at  $L = 5$  (excited by a magnetic storm) and traveling inward toward  $L = 2$  in about one day with the result that the slot region is completely filled. In the subsequent 10 days the injected flux is observed to decay to its quiet-time level (dotted lines) by wave-particle scattering. Also, the flux build-up abruptly stops in the vicinity of  $L = 2$  and is in keeping with the observation of the Wallops Island precipitation band and the null at White Sands ( $L = 1.8$ ). The radial diffusive force must therefore also dissipate rapidly at  $L = 2$ . Particle precipitation, to the first order, can be thought of as the loss rate of the injected flux to the equilibrium value.

#### 6.4 *Plasmaspheric Hiss Exciting the Wallops Island and Arecibo Precipitation Zones*

Observations of electromagnetic hiss for  $L < 2$  have only recently been made [Tsurutani *et al.*, 1975]. The 200 to 1000 Hz emissions are found to correlate well with magnetic activity. At the start of a storm the intensities are  $> 10^{-6} \gamma^2/\text{Hz}$  during substorms they are between  $10^{-7}$  to  $10^{-6} \gamma^2/\text{Hz}$ ,

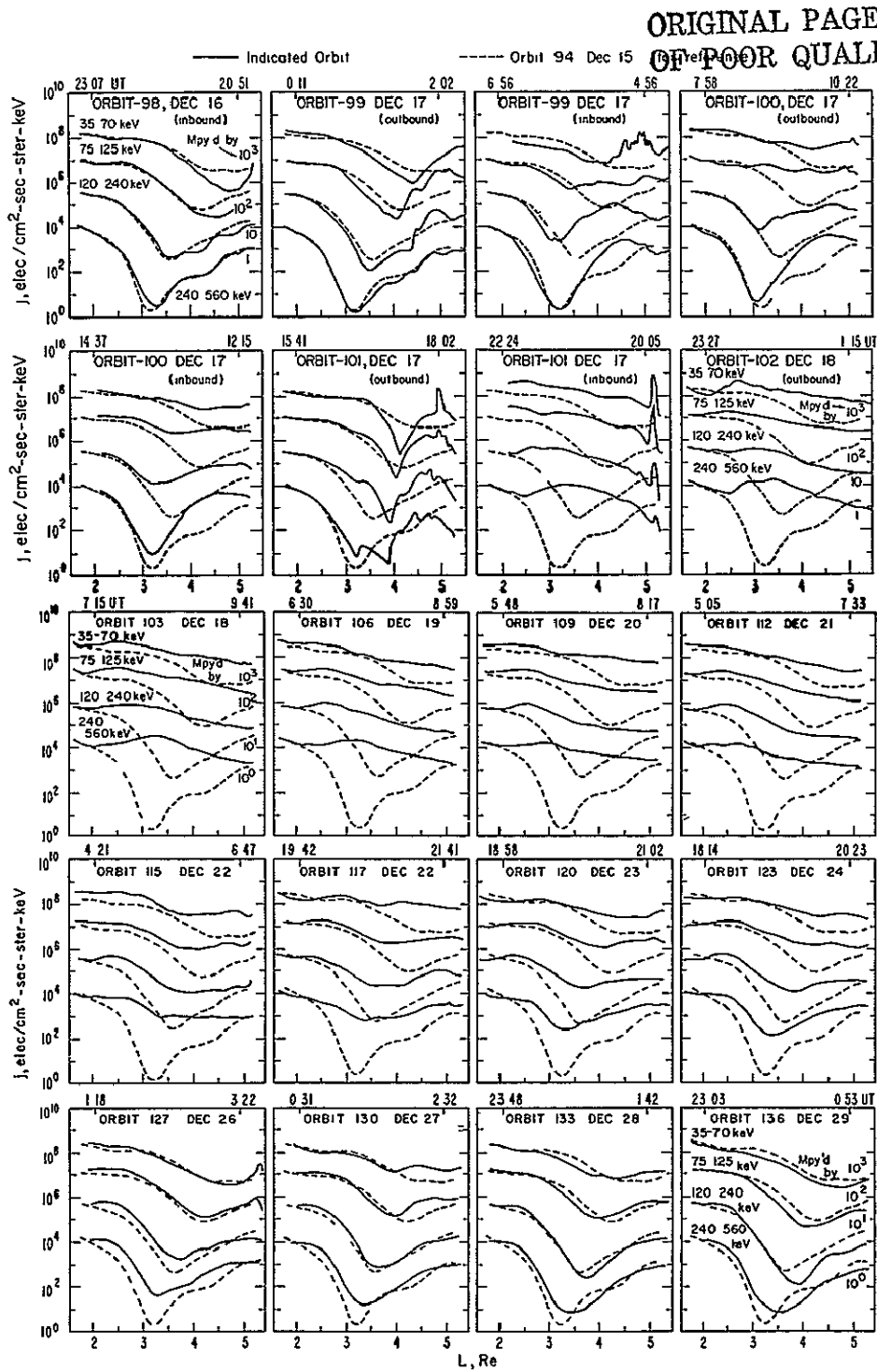


Figure 6.3 The radial diffusion of trapped particles of lower  $L$  values following the magnetic storm of 17 December 1971 is shown in satellite data analyzed by *Lyons and Williams* [1975b].

and  $< 10^{-7} \gamma^2/\text{Hz}$  during quiet periods. The hiss is found to be maximum during the daytime (12 to 18 hr local time) with a sharp minimum below  $L = 1.1$ .

*Kenel and Petschek* [1966] have shown that the amount of time,  $T$ , necessary to resonantly scatter an electron one radian in pitch angle (its effective lifetime) is given by

$$\frac{1}{T} = \bar{D} = \eta \omega_B \frac{b^2}{B_o^2} \quad (6.7)$$

where  $b^2$  is the mean-square wide-band wave amplitude,  $\eta$  is the fraction of time in one bounce period when in resonance with a wave,  $B_o$  is the magnetic field and  $\bar{D}$  is the average pitch angle diffusion coefficient. For a wave with a bandwidth of 300 Hz and an amplitude of  $4 \times 10^{-7} \gamma^2/\text{Hz}$  the wide-band amplitude is  $b = 10 \text{ mV}$  and letting  $\eta = 1/5$  yields realistic inner zone lifetimes between 10 and 60 days [*Tsurutani et al.*, 1975]. Since the diffusion time is proportional to the square of the wide-band wave amplitude, the magnitudes are most important.

A possible explanation for the Arecibo precipitation zone ( $L = 1.4$ ) is that on average there is a maximum in the low frequency (3 to 3000 Hz) wave amplitude in this zone as shown in Figure 6.4. Further measurements are necessary to verify that this is indeed the driving mechanism for the Arecibo precipitation zone and to find how this maxima changes with  $K_p$  and time. The wave amplitude at 550 Hz and  $L = 1.4$  is approximately twice that at  $L = 2$  or  $L = 1.1$  and since the diffusion rate is proportional to the square of the amplitude a considerable change in precipitation is expected at  $L = 1.4$ . Observations appear to support this.

The sharp cutoff of the hiss at  $L = 2$  with the minimum at  $L = 1.8$  is in keeping with the White Sands ( $L = 1.8$ ) precipitation null. Likewise, the sharp cutoff of the hiss near the equator ( $L < 1.1$ ) lends support to the

ORIGINAL PAGE IS  
OF POOR QUALITY

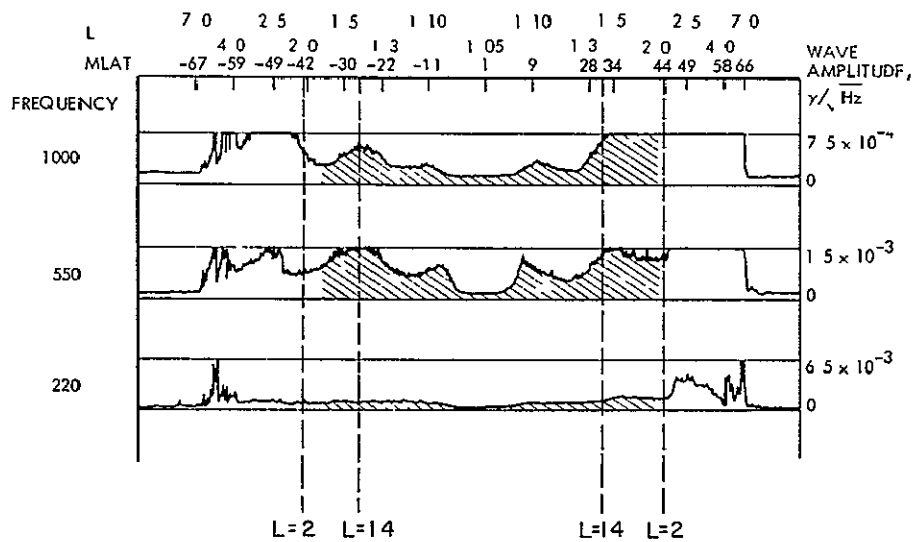


Figure 6.4 A possible explanation for the Arecibo precipitation zone ( $L = 1.4$ ) is the marked increase of low frequency hiss at  $L = 1.4$  as shown in these data from *Tsurutani et al.* [1975]. The rapid cutoff of low frequency hiss at  $L = 2$  and minimum at  $L = 1.8$  are in keeping with the precipitation null at White Sands.

double charge exchange mechanism for supplying ring current protons to the low altitude region since no wave-particle scattering occurs. The strong plasmaspheric hiss in the Wallops Island band ( $L = 2.6$ ) contributes to considerable precipitation in conjunction with the increased radial diffusion. Greater precipitation is observed in the Southern Hemisphere due to both the increased plasmaspheric hiss and the lower  $B$  fields.

*Tsurutani et al.* [1975] have suggested that inner zone hiss originates at the plasmopause and propagates inward. Although this explanation may be valid, the added peaking of the amplitude at  $L = 1.4$  might be caused by interaction with the proton belt peak which is also at  $L = 1.4$ . Some explanation why  $L = 1.4$  is a preferred region for hiss build up and subsequent particle precipitation needs further investigation. The excitations of hiss due to the rapid increase of the energetic proton belt at  $L = 1.4$  is a possibility.

#### 6.5 *Longitude Variations of Particle Precipitation and the Cause of the South Atlantic Magnetic Anomaly Precipitation*

An energetic particle gyrating and bouncing between conjugate points of a field line will also execute an eastward drift for electrons, westward for protons, along a constant  $L$  shell due to the curvature of the dipole field. However, the earth's magnetic field is not symmetrical to the earth's surface but is tilted (about  $11^\circ$ ) and displaced (about 400 km) from the central spin axis of the earth resulting in a nonuniform mirror height altitude variation with longitude and conjugate point. This longitudinal variation of the  $B$  field at 100 km for  $L = 2.5$  and  $L = 1.4$  illustrated in Figure 6.5.

For a particle which mirrors at 400 km above Wallops Island the conjugate mirror height in the Southern Hemisphere is approximately 300 km lower due to the smaller  $B$  field. Particles located with mirror points between these



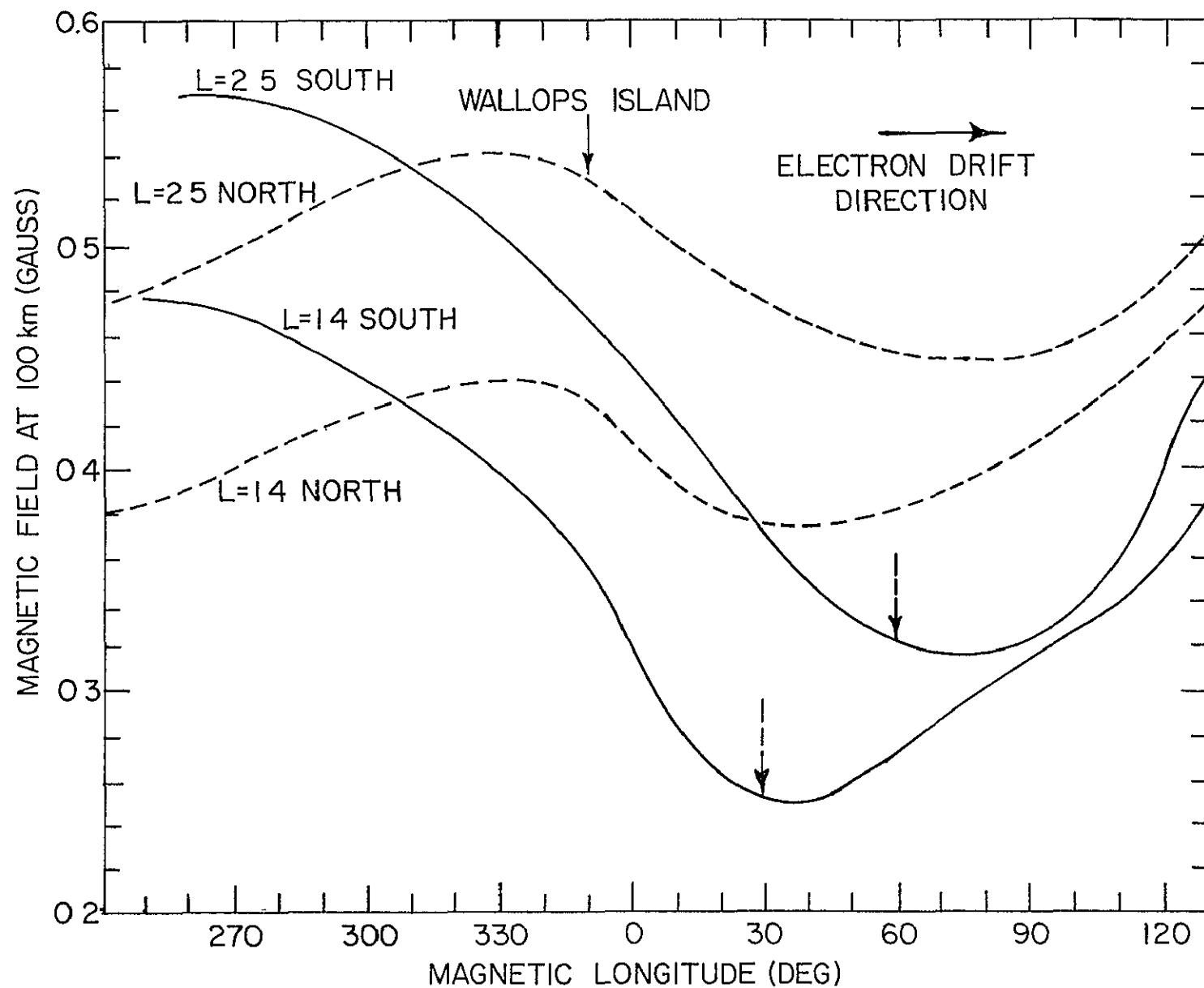


Figure 6.5 The longitudinal variation of the  $B$  field at 100 km for  $L = 2.5$  and  $L = 1.4$  in the northern and southern hemispheres. At Wallops Island the mirror height is about 300 km lower in the southern hemisphere than in the northern hemisphere. The dashed arrows indicate the longitude of maximum precipitation.

two regions are called quasi-trapped particles. It is therefore expected that the particles migrating down from the trapped radiation belt would be predominantly precipitated in the Southern Hemisphere and backscattered into the Northern Hemisphere. This simple picture, however, is not correct but is complicated by the pitch-angle scattering, inhomogeneous electric and magnetic fields and nonuniform particle injection.

*Roederer et al.* [1967] have performed an analysis on how mirror height lowering with longitude produces precipitation. *Torr et al.* [1975] present a model for computing the rates, locations, and aeronomical effects of particle precipitation as a function of longitude for electrons with energies greater than 40 keV. To convert to absolute precipitating fluxes experimental data of *Armstrong* [1965] comprising one averaged  $B$ - $L$  point for each  $L$  shell is used to normalize their calculations. The longitudinal results presented by *Torr et al.* [1975] are shown in Figure 6.6 and dramatically illustrate the effect of the South Atlantic anomaly. Also shown are the predicted precipitation flux, energy flux and 391.4 airglow intensity.

The precipitation maximum at  $L = 2$  deduced by *Torr et al.* [1975] is in direct conflict with low altitude satellite measurements of *Seward* [1973], Figure 4.15, and a conclusion of this thesis that there is a precipitation null between  $L = 1.6$  and  $L = 2.2$ . The  $L$  value particle magnitudes used by *Torr et al.* [1975] are based on Injun 3 measurements made by *Armstrong* [1965] for  $B$  values of approximately 0.25 gauss or equivalent altitudes of 1500 km.

Figure 6.7 shows scatter plots by *Armstrong* [1965] for  $L = 2.2$  and  $L = 2.6$  with inclusion of lines through median points every 0.2 gauss. The particular detectors used by *Armstrong* to measure the precipitated flux and trapped flux have a conical collimator full angle of  $86^\circ$  and  $26^\circ$  and geometrical factors of  $5.5 \times 10^{-2}$  and  $0.65 \times 10^{-2} \text{ cm}^2 \text{ ster}$ , respectively. One finds that

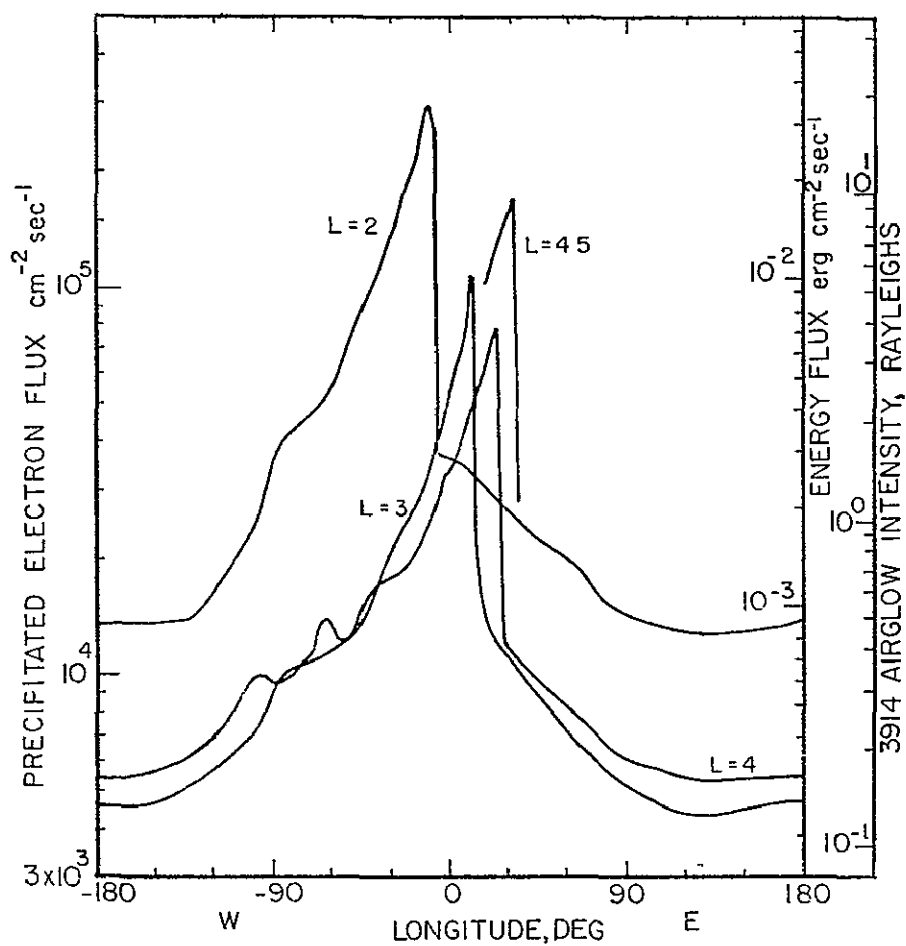


Figure 6.6 Longitudinal variation of precipitated electron flux deduced by *Torr et al.* [1975]. The relative magnitudes for the different  $L$  shells are inconsistent with data from rockets and satellites.

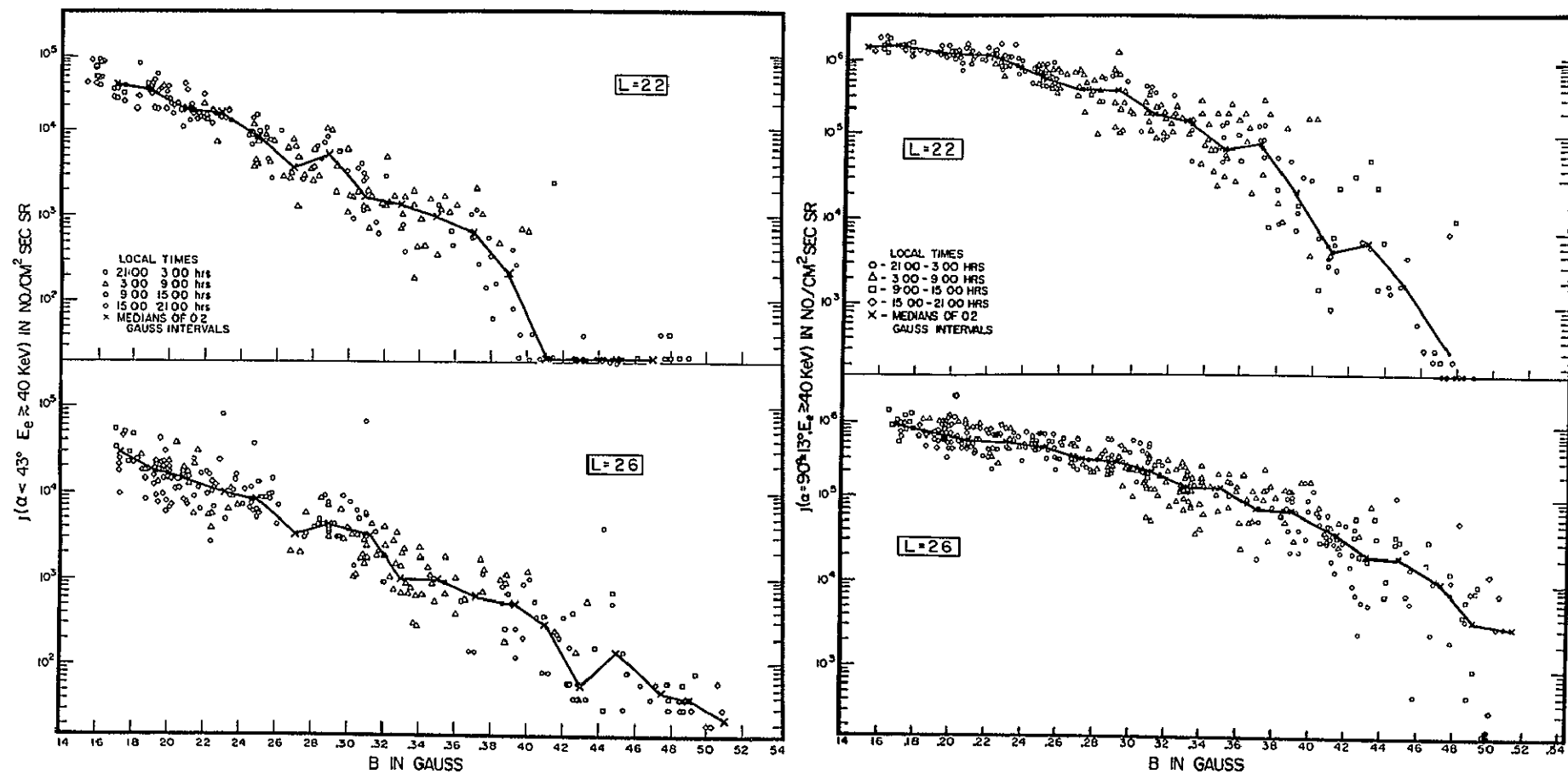


Figure 6 7 Scatter plots for trapped and precipitated particles are shown for  $L = 2.2$  and  $L = 2.6$  from *Armstrong* [1965]. Lines are drawn through the median points every 0.2 gauss

indeed at  $B = 0.25$  gauss the "precipitated" flux at  $L = 2.2$  is greater than at  $L = 2.6$ . This conclusion neglects the precipitation cut-off observed at  $B = 0.39$  gauss. Taking the precipitating fluxes measured by Armstrong at an altitude of 300 km shows that the flux increases with  $L$  value for  $2 < L < 5$ , as is observed in data from many satellites discussed in Chapter 4.

The precipitation cut-off may be explained in terms of the pitch-angle distribution. A discussion of the technique by which the pitch-angle distribution may be derived from a profile of count rate is given in Section 7.1.

A significant feature of the precipitation maximum located in the South Atlantic anomaly region can be explained in terms of the Arecibo ( $L = 1.4$ ) and Wallops Island ( $L = 2.6$ ) precipitation zones. Realizing that most precipitation occurs when the magnetic field reaches a minimum on a particular  $L$  shell, and that maxima occur in the two precipitation bands at midlatitudes the prediction is made that two primary maxima will occur in the region of the South Atlantic magnetic anomaly. *Ginzburg et al.* [1962], *Vernov et al.* [1967] and *Gledhill and Daves* [1976] using satellite measurements support this conclusion.

From Figure 6.5, the minimum  $B$  field for different  $L$  shells occurs at different longitudes, with increasing values of  $L$  having field minima further eastward. Maximum precipitation is expected to occur near the lowest  $B$  field when the rate of change of  $B$  with longitude ( $dB/d\phi$ ) starts to rapidly approach zero. The two vertical arrows in Figure 6.5 designate this longitude for  $dB/d\phi = 8 \times 10^{-4}$  G deg $^{-1}$  ( $30^\circ$  and  $60^\circ$  geomagnetic or  $-35^\circ$  and  $-5^\circ$  geographic) for  $L = 1.4$  and  $L = 2.5$  respectively. Figure 6.8 gives a comparison of the precipitation regions predicted by the two zone model ( $L = 1.4$  and  $L = 2.6$ ) and those regions of maximum precipitation experimentally determined

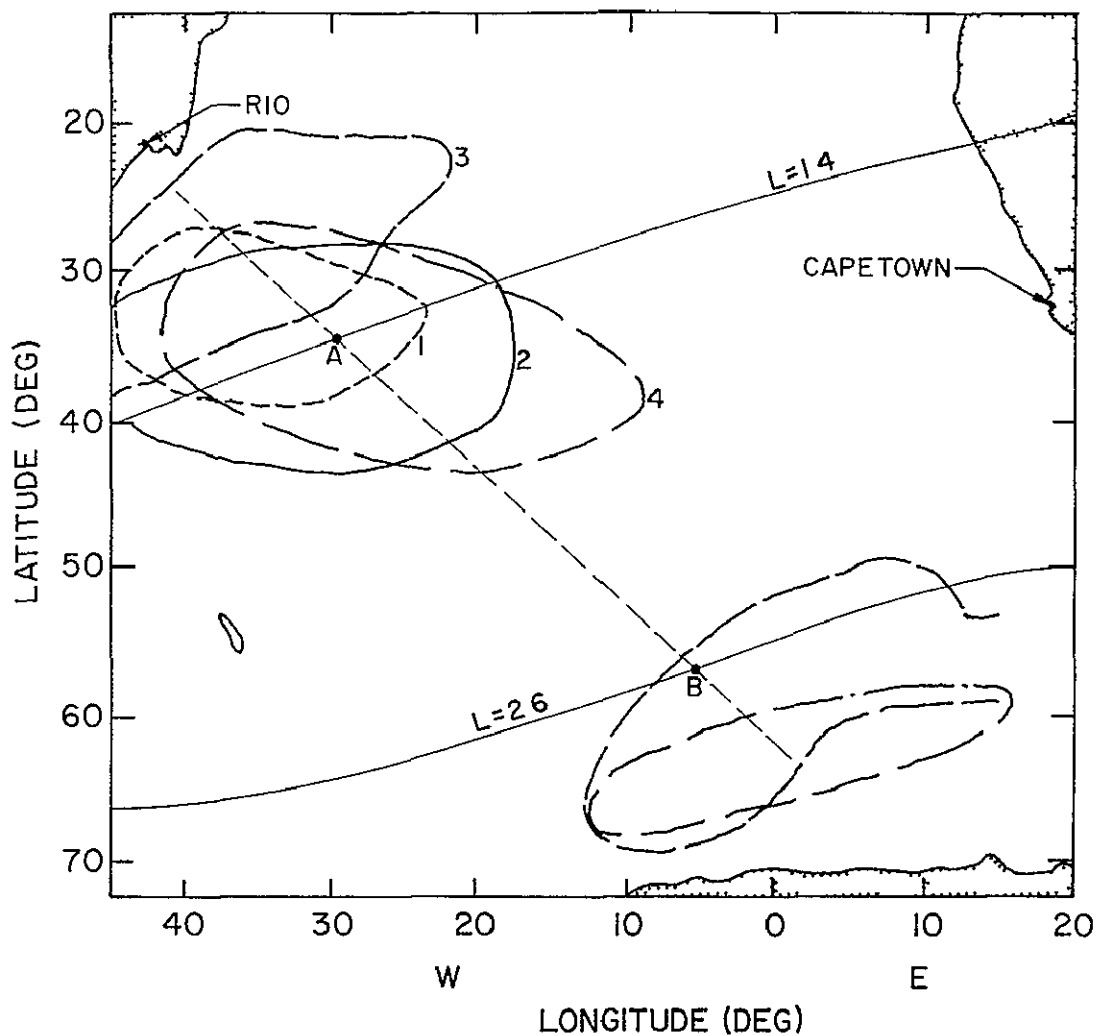


Figure 6.8 Satellite observations of the South Atlantic anomaly are consistent with the maximum precipitation in the Arecibo zone ( $L = 1.4$ ). Contours 1, 2, 3, and 4 are given by *Ginzburg et al.* [1962], *Vernov et al.* [1967], *Seward* [1973], and *Gledhill and Daves* [1976], respectively. The points A and B correspond to the dashed arrows of Figure 6.5.

by *Ginzburg et al.* [1962], *Vernov et al.* [1967], *Seward* [1973] and *Gledhill and Daves* [1976]. The agreement with the  $L = 1.4$  and  $L = 2.6$  precipitation model is quite good and gives a qualitative understanding of the South Atlantic particle anomalies. Further studies are needed to understand quantitatively the mechanism for exciting precipitation in these  $L$  shells and inhibiting precipitation at the equator and the region  $1.8 < L < 2$ . During disturbed and moderately disturbed conditions the slot region ( $L = 3.5$ ) fills up with particles and yields greater precipitation at  $L$  values greater than the Wallops Island precipitation zone.

Additional studies of particle precipitation in the South Atlantic magnetic anomaly have been made by *Zmuda* [1966], *Gough* [1975] and *Imhof* [1968].

It is shown in this section that the radiation belts are in dynamic motion with the solar plasma continuously supplying charged particles to the magnetosphere. During magnetic storms radial diffusion forces move flux into the midlatitude radiation belts. Wave-particle interactions are then able to scatter the trapped flux into precipitating trajectories within the atmosphere culminating in excitation and ionization reactions. The scattering mechanism appears to preferentially scatter particles into two zones corresponding to  $L$  values of 2.6 and 1.4. The maximums of energetic particle precipitation at  $L \approx 1.4$  and  $L \approx 2.4$  in the south magnetic anomaly are manifestations of the low  $B$  field in this region and the scattering force.

## 7 MODELING THE SOURCE FUNCTION

This chapter gathers together the many observations and conclusions developed in the preceding three chapters. From this material a global picture of particle precipitation at midlatitudes is developed. Topics of discussion include 1) the explanation of the linear count rate increase with altitude, 2) the characteristics of the midlatitude energy spectrum and pitch angle distribution, 3) a computer model simulation of the count rate versus altitude profile, 4) comparisons between nearly simultaneous rocket and satellite data, 5) equatorial proton precipitation, and 6) a global precipitation map

### 7.1 *The Variation of Count Rate with Altitude*

The new observations made at Wallops Island and presented in Section 4.1 show clearly the linear increase with altitude of particle flux in the region 120 to 200 km. Various other measurements of count rate reviewed in Section 4.5 similarly show this monotonic increase with altitude.

Some excellent documentation of midlatitude particle flux variation with magnetic field intensity (or altitude) and  $L$  shell is given by *Armstrong* [1965] from Injun 3 data. Scatter plots for  $L = 2.2$  and  $L = 2.6$  were shown in Figure 6.7 for the precipitated flux and trapped flux at various  $B$  values. The Injun 3 orbit had a perigee of 237 km, an apogee of 2785 km and covered  $L$  shells between 2.0 and 4.0. The precipitated flux was measured by a Geiger counter with an included half angle of  $43^\circ$  and geometrical factor  $5.5 \times 10^{-2} \text{ cm}^2 \text{ ster}$  and the trapped flux was measured by a Geiger counter with an included half angle of  $13^\circ$  and a geometrical factor of  $0.65 \times 10^{-2} \text{ cm}^2 \text{ ster}$ .

This most intensive midlatitude particle study clearly shows that at altitudes where  $B < 0.37$  gauss (i.e.,  $>700$  km over North America), the particle flux is nearly the same at all  $L$  values. At lower altitudes there



is an abrupt decrease for  $L < 2.2$  as compared with higher  $L$  values. This sharp cutoff at low  $L$  values is in good agreement with the precipitation null observed at  $L = 2$ . The explanation of this cutoff phenomenon needs further investigation, it may be linked to a cutoff in the pitch angle distribution caused by resonant wave-particle interactions

Further examination of the scatter plots of Figure 6.7 shows that the trapped flux is approximately two orders of magnitude greater than the precipitated flux. The monotonic decrease of trapped flux with altitude and ratio of precipitated to trapped flux are in good agreement with the new rocket measurements presented in Section 4.1.

Since magnetic mirroring is the primary factor governing the count rate profile for the trapped flux above 140 km at energies  $>20$  keV, it is possible to derive the pitch-angle distribution from the count-rate profile.

An analytic solution is possible for the experimentally observed case of a count rate increasing linearly with altitude. For this case it was shown in Section 3.3 that the count rate profile,  $C(\alpha)$ , is related to an incident flux,  $F = I_0 E^{-\alpha} f(z_m)$ , at the top of the atmosphere by

$$C(\alpha) = \frac{2A_d I_0}{1-\alpha} \left( E_H^{1-\alpha} - E_L^{1-\alpha} \right) \int_{z_0}^{\alpha} \frac{f(z_m)}{k(z_m, \alpha)} dz_m \quad (7.1)$$

where

$$k(z_m, \alpha) \approx 2\pi \sqrt{3(\alpha - z_m)/R_0} \quad (7.2)$$

and  $A_d$  is the area of the detector,  $I_0$  is the flux constant,  $\alpha$  is the power law spectrum exponent,  $E_H$  and  $E_L$  are the high and low energy thresholds of the detector,  $f(z_m)$  is the mirror-height distribution of the incident flux.

( $\text{km}^{-1}$ ),  $z_o$  is the lowest altitude where mirroring particles are observed and  $R_o$  is the earth radius

From this equation it is desired to find  $f(z_m)$ , the incident flux mirror-height distribution, assuming that  $C(\alpha)$  varies in a linear fashion with altitude as is experimentally observed. This integral equation may be solved when  $f(z_m)$  is represented by

$$f(z_m) = \sqrt{z_m - z_o} \quad (7.3)$$

where  $z_o$  is the lowest altitude where mirroring particles are observed and  $R_o$  is the radius of the earth. This pitch angle distribution is plotted in Figure 7.1 at 200 km altitude for  $z_o = 120$  km. For this case the pitch-angle distribution required to give a linear count-rate profile with altitude is peaked near  $90^\circ$ . Furthermore, the effects of scattering have been taken into account, to the first order, since the count rate variation with altitude was used to derive the distribution. The effects of scattering when applied to this effective pitch-angle distribution would tend to narrow the distribution width somewhat. A detailed analysis of scattering is given in Chapter 8.

The count rate may be solved for by substituting equation (7.2) into the integral equation (7.1). In order to solve the integral, substitution in the integrand of  $u = z_m - z_o$  is required and rearranging so that the radical in the denominator becomes  $[1 - u/(a - z_o)]^{1/2}$ . Making the further substitution that  $u/(a - z_o) = \sin^2 \theta$ , the integral may be evaluated using the appropriate trigonometric identities. The count-rate profile is then given by, for  $x > 1$

$$C = \frac{A_d}{2(x-1)} \sqrt{\frac{R_o}{3}} I_o(a - z_o) \left( \frac{1}{E_H^{x-1}} - \frac{1}{E_L^{x-1}} \right) \quad (7.4)$$

and, for  $x = 1$

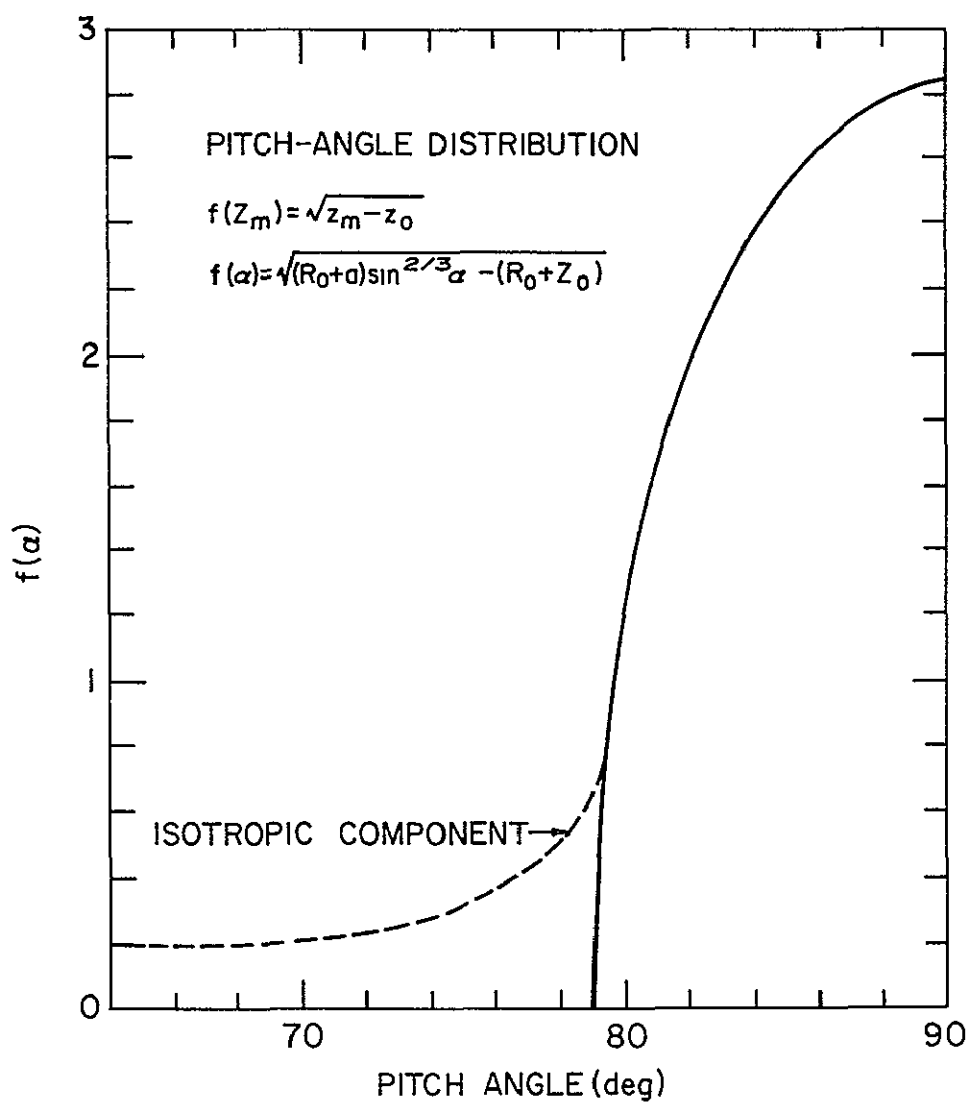


Figure 7.1 Shown is the effective pitch-angle distribution at 200 km (solid line) for a count-rate profile which increases linearly with altitude. The dashed line indicates the isotropic component of the flux.

$$C = \frac{A_d}{2} \sqrt{\frac{R_o}{3}} I_o (\alpha - z_o) \ln \frac{E_H}{E_L} \quad (7.4)$$

and shows the linear variation of count rate with altitude. These equations will be used to calculate the ionization rates in Chapter 9.

The explanation of the count rate monotonically increasing with altitude is intimately connected with the pitch-angle distribution and thus the wave-particle scattering mechanism. It is now known that for the outer radiation belt wave-particle interactions are the primary driving force for bringing trapped particles into quasi-trapped and precipitated orbits. The count-rate profile is a balance between the wave-particle injection source and the atmospheric loss processes. First, a brief discussion will be given of the loss process mechanism which will then be followed by a study of the production or injection of particles by lowering of mirror heights.

*Maeda* [1965] has explained the increasing count rate with altitude in terms of atmospheric loss processes only. In this analysis Maeda assumed that the particle lifetime is inversely proportional to the average collision frequency experienced by a spiraling particle near its mirroring altitude. The collision frequency at the mirroring altitude is given by

$$\nu_m = n_m \sigma v = 1.87 \times 10^9 n_m \sigma E \quad (7.6)$$

where  $n_m$  is the neutral particle density ( $\text{cm}^{-3}$ ) at the mirroring altitude,  $\sigma$  is the cross-section ( $\text{cm}^2$ ) for ionization and excitation of atomic oxygen (see *Tohmatsu and Nagata*, 1960],  $v$  is the energetic particle velocity ( $\text{cm s}^{-1}$ ) and  $E$  is the energy (in keV) for a non-relativistic particle. The lifetime,  $\Delta t$ , of an energetic particle may then be represented by

$$\Delta t = \frac{E}{I} \frac{1}{v} \approx \frac{E}{I} \frac{1}{\nu_m} = \frac{E}{I} \frac{1}{n_m \sigma v} = \frac{E}{1.87 \times 10^9 I n_m \sigma} \quad (7.7)$$

where  $I$  is the average ionization potential (in keV) The lifetime is consequently inversely proportional to the neutral density and proportional to the square root of the energy

A more accurate analysis of the average collision frequency is given by *Maeda* [1965] as

$$\bar{v} = \frac{1}{T} \int v dt = \frac{R_o}{2V} v_m e^{gx_m} \int_{x_m}^1 \frac{e^{-gx} \sqrt{(4-3x)/(1-x)}}{\sqrt{1 - [(x_m/x)^3 \sqrt{(4-3x)/(4-3x_m)}]}} dx \quad (7.8)$$

where  $x = R/R_o$ ,  $R_o$  is the radius of the earth,  $x_m = R_m/R_o$ ,  $R_m$  is the distance from the center of the earth to the mirror altitude,  $v_m$  is the collision frequency at the mirror altitude,  $V$  is the particle velocity and  $g$  is the acceleration due to gravity.

Since the atmosphere is approximately exponential over the range of interest, the loss rate and lifetime must decrease in an exponential manner with increasing altitude. However, since the count-rate altitude profile shows a linearly increasing rate, it follows that pitch-angle diffusion must increase as the mirror altitude is lowered

The observed count-rate profile requires a production rate which changes with altitude in a manner which compensates for the exponential loss term. The source function must therefore preferentially scatter more particles into the lower mirror-height regions where absorption is greater. Assuming a typical pitch-angle profile, as derived in Figure 7 1, it can be seen that maximum diffusion will indeed occur at the lowest mirror heights since the gradient of the pitch-angle distribution  $df(\alpha)/d\alpha$  is steepest there.

Another characteristic of the altitude profile as mentioned in Section 4.1 is that the low altitude intercept of the count-rate profile moves towards

higher altitudes during disturbed conditions e.g , from 105 km to 135 km as  $K_p$  increases from 3+ to 5+ A qualitative explanation of this phenomenon which is supported by experimental evidence is that during periods of significant particle precipitation the atmospheric density changes at a particular altitude due to atmospheric heating.

*Allen* [1974] has determined global density changes in the region near 150 km from satellite drag measurements during the magnetic storm of 25 May 1967. These results are shown for two satellite passes in Figure 7 2 and clearly illustrate the density increase at Wallops Island of a factor of approximately 1.3 above the average density The density measurements are in agreement with work done by *DeVries* [1972a,b] The density increase, although related to magnetic activity, is not simply explained by particle precipitation

An alternative explanation of the properties of the count-rate profile over North America is based on backscattering at the conjugate point in the Southern Hemisphere, where the mirror heights are about 300 km lower (Section 6.4) Such an explanation is believed to be of only secondary importance since backscattering would not yield a pitch-angle distribution with a maximum at about  $90^\circ$ , as is observed, but would be more nearly isotropic. Monte Carlo simulations of electron backscattering at Wallops Island [*McEntire et al.*, 1974] show this spreading effect due to conjugate backscattering. Many other relevant Monte Carlo results are reported on by *McEntire et al.* [1974] and *Winckler* [1973]. They also discuss a sounding rocket experiment launched from Wallops Island which injected electron beams into the geomagnetic field and subsequently measured their return echoes and dispersion characteristics The experimental results indicate that the flux backscattered was an order of magnitude less than their Monte Carlo calculations predicted These results



suggest that conjugate backscattering contributes only about 5 to 10% at most to the observed quasi-trapped flux

## 7.2 *The Pitch-Angle Distribution*

A most important consideration in the formulation of a model of particle precipitation and subsequent calculation of ionization rate for the ionosphere is the precise description of the pitch-angle distribution. Additionally, since a slight disturbance of the pitch angle may cause a large change in the mirroring altitude, the pitch-angle distribution is very important in the source function.

7.2.1 *Observations of pitch-angle distributions* A few measurements of the pitch-angle distribution have been made by rocket and satellite experiments at midlatitudes. The distributions are, however, difficult to compare because of the different launch times, magnetic conditions, altitudes, instrumentation and launch locations. One feature common to all the midlatitude observations above 120 km is that the flux is maximized at a pitch angle of about  $90^\circ$ , i.e., with the majority of particles near their mirroring altitudes. Various examples of these pitch-angle distributions are given by *Cladis et al.* [1961, 1976], *Tuohy and Harries* [1973], *Seward et al.* [1973], *Hayakawa et al.* [1973 a,b], *Kohno* [1973], *Aikin et al.* [1976], and *Imhof et al.* [1976].

A comparison of the inferred pitch-angle distribution determined from the count-rate profile of Figure 7.1 with some normalized theoretical and experimental distributions is shown in Figure 7.3.

Curve 1 in Figure 7.3 is from *Tuohy and Harries* [1973] for a rocket measurement of 25 keV electrons at approximately 185 km (and  $L = 1.75$ ) during a magnetic storm ( $K_p = 7-$ ). Curve 2 is from *Cladis et al.* [1961] for a rocket measurement of 40 keV electrons at 750 km at Wallops Island ( $L = 2.6$ ). Curve 3 is a theoretical profile deduced by *Spjeldvik* [1976].



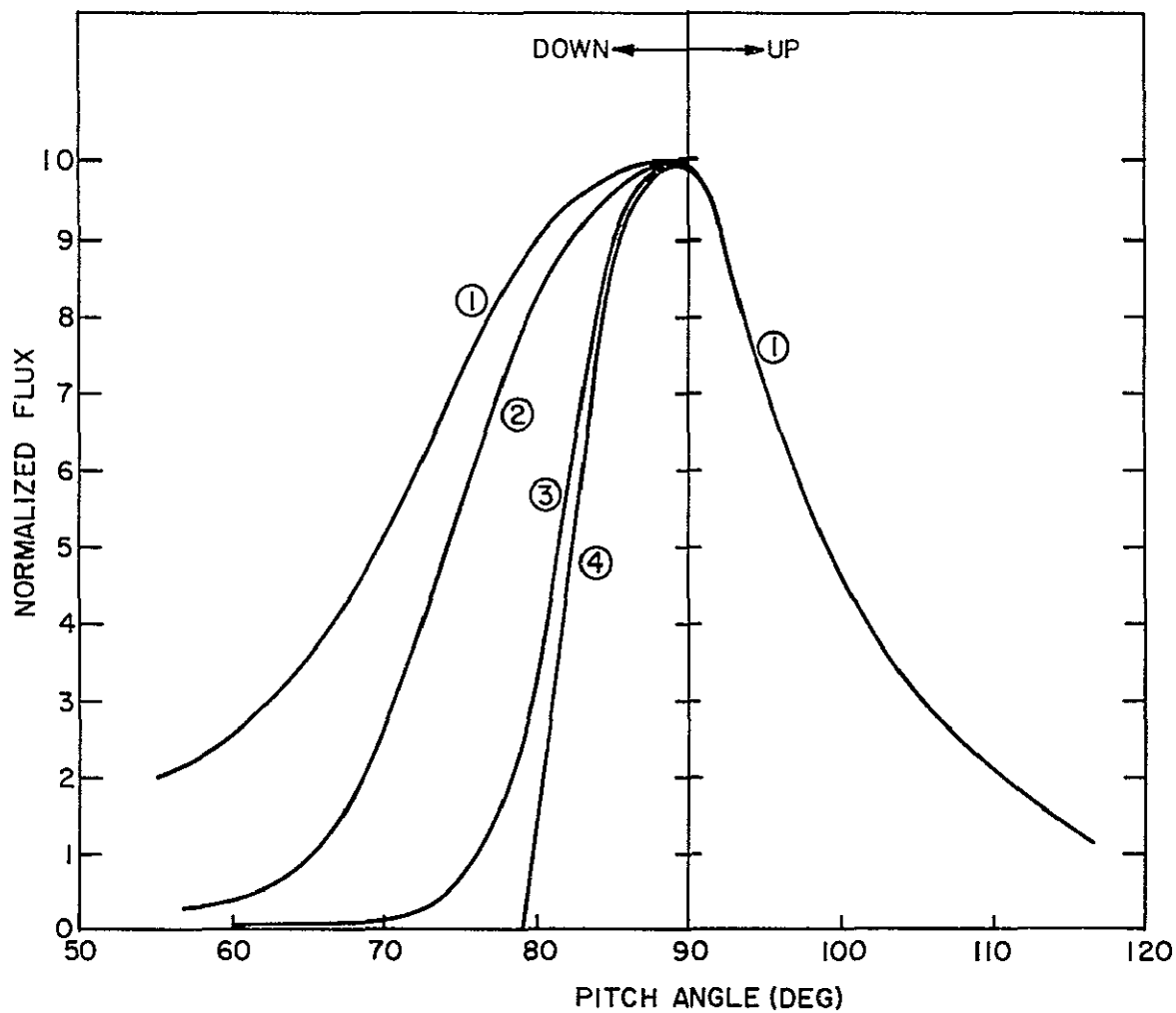


Figure 7.3 The pitch-angle distribution at midlatitudes peaks near  $90^\circ$ . Curve 1 is from *Tuohy and Harries* [1973], curve 2 from *Cladis et al.* [1961], curve 3 is a theoretical profile by *Spjeldvik* [1976]. Curve 4 from Figure 7.1 is the pitch-angle distribution deduced from the linear count-rate profile.

from wave-particle scattering effects. This profile is for 20 keV electrons at a height of 300 km (and  $L=4$ ) and a scattering amplitude of  $10m\gamma$ . Curve 4 is the inferred distribution at 200 km for a linear count-rate profile as observed at Wallops Island (i.e., Figure 7 1).

Although these curves represent different altitudes the similarity of the maximum near  $90^\circ$  is a characteristic feature of midlatitude precipitation. The upward flux in curve 1 shows an asymmetry with respect to the downward flux because of particle absorption and scattering. This asymmetry in the pitch-angle distribution explains the count-rate modulation observed by the rocket-borne particle measurements reported on in Section 4.1 and Figure 4 7. Furthermore, analysis of this asymmetry gives the energy deposition into the atmosphere, as will be shown later. *Davidson and Walt* [1977] have developed a technique for determining this asymmetry for different wave-particle interactions utilizing finite-difference techniques to solve the diffusion equation.

The temporal variations of the pitch-angle distribution depend strongly on the wave-particle interaction. Using a finite-difference computer algorithm to solve the particle diffusion equation with variable wave-particle scattering amplitudes *Cladis et al.* [1976] have obtained various pitch-angle distributions. They use a simple dipole to represent the earth's magnetic field. Some of their results for 20 and 50 keV electrons with wave-particle scattering amplitudes of 10, 30, 100 and  $300m\gamma$  (corresponding roughly to Kp values between 1 and 8) are shown in Figure 7 4. The dashed lines indicate the symmetrical distribution that results in the absence of atmospheric scattering and absorption.

The solid lines show the asymmetry produced when atmospheric scattering and absorption are introduced. These results are in general agreement with experimental observations of Figure 7 3. The difference between the solid

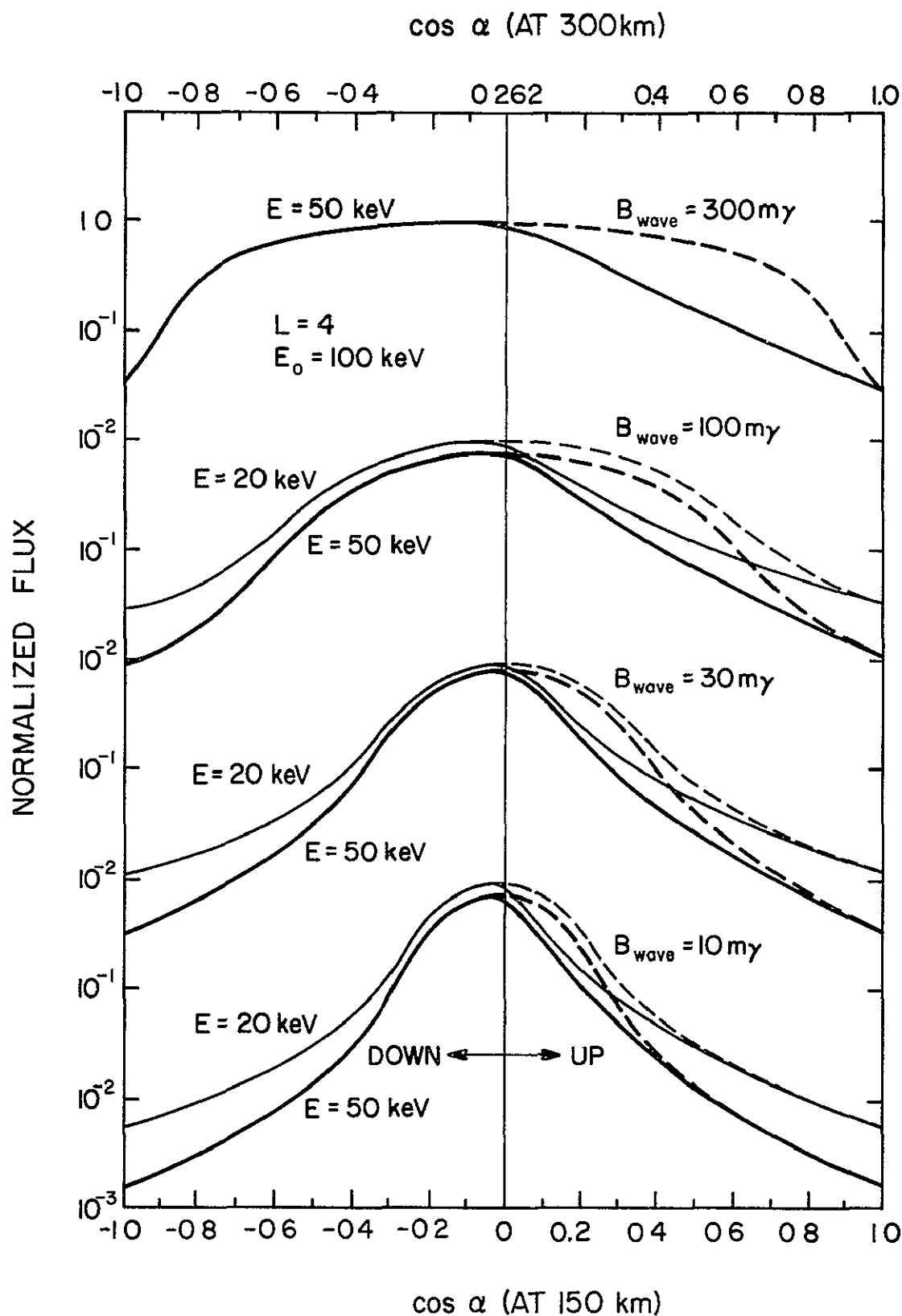


Figure 7.4 Calculations by *Cladis et al.* [1976] show how a quasi-trapped distribution of electrons is scattered for different wave-particle amplitudes. The ascending particles show the effect of energy loss and scattering.

and dashed curves is a measure of the flux which is absorbed.

Some relevant experimental observations of broadening of the pitch-angle distribution with increasing magnetic activity may be seen in Figure 7.5. These are data at 800 km from satellite 1972-076B reported on by *Imhof et al.* [1976]. These data were taken at nearly the same time and location as the launch of rocket 14.439 reported on in Section 4.1.1. The pitch-angle distributions labelled 1 through 4 are for sequential 20-second intervals and illustrate the large temporal variations possible when  $K_p$  is very high ( $K_p = 8$  in this case). During quiet times the pitch-angle distributions are more closely represented by curve 1. The erratic pitch-angle distribution may be compared with the nearly simultaneous rocket count-rate profile shown in Figures 4.1 and 4.2.

7.2.2 *Change of pitch angle with altitude for a dipole field* In order to understand the manner in which the pitch-angle distribution changes with altitude it is necessary to develop an appropriate transformation. In the following analysis only the influence of the magnetic field intensity will be considered and atmospheric scattering will be neglected. This assumption is valid for the energies greater than 20 keV at altitudes above 135 km.

The pitch angle distributions,  $f_1(\alpha)$  and  $f_2(\alpha)$  at altitudes  $z_1$  and  $z_2$  (Figure 7.6) are given in terms of the flux of electrons per unit solid angle. To find the relationship between  $f_1(\alpha)$  and  $f_2(\alpha)$  in a dipole magnetic field, use is made of the first adiabatic invariant

$$\frac{\sin^2 \alpha(z_1)}{\sin^2 \alpha(z_2)} = \frac{B(z_1)}{B(z_2)} = \left( \frac{r_2}{r_1} \right)^3 \quad (7.9)$$

where  $r_1 = R_o + z_1$  and  $r_2 = R_o + z_2$ , and the conservation of flux in a particular flux tube gives

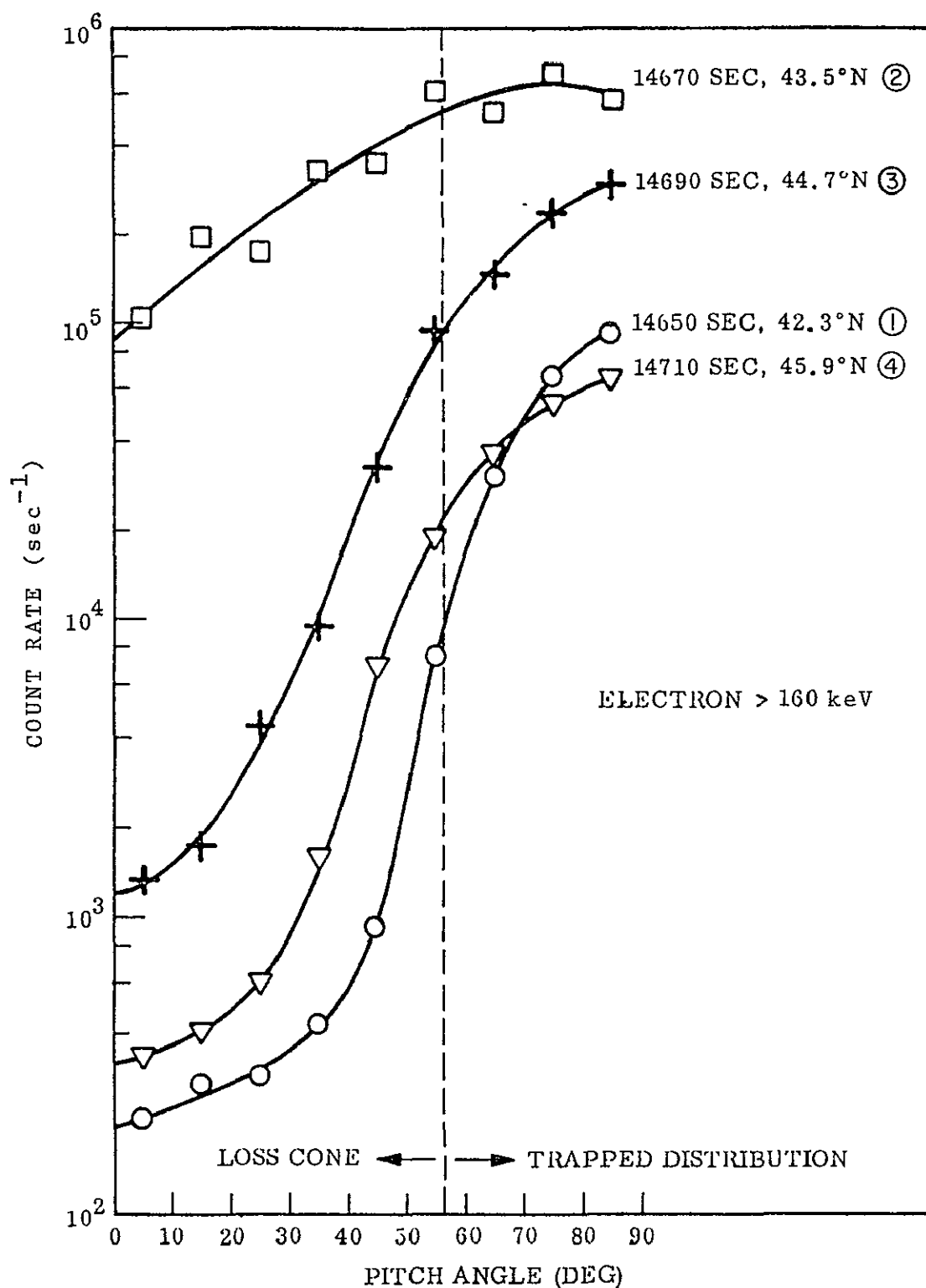


Figure 7.5 During times of high magnetic activity the isotropic component of the flux is very variable and can increase substantially as shown in these satellite data from *Imhof et al.* [1976] Nike Apache 14.439 was launched at nearly the same time that these distributions were observed.

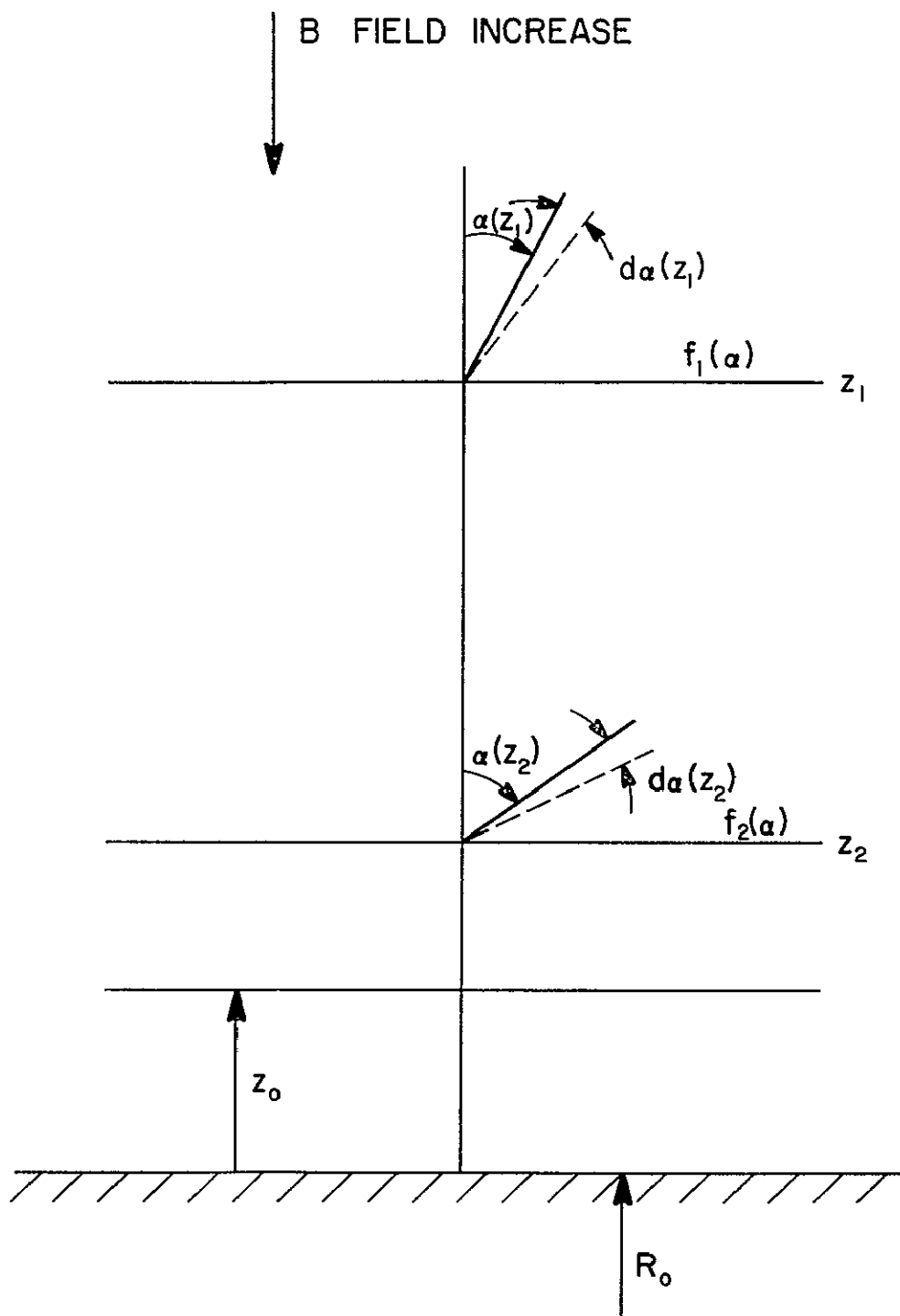


Figure 7 6 Geometry used to convert a pitch-angle distribution from one altitude to another.

$$\text{Flux} = f_1(\alpha_1, B_1) = f_2(\alpha_2, B_2) = \text{constant} \quad (7.10)$$

where  $f_1$  and  $f_2$  are the flux per unit solid angle. If a particle detector of area  $dA$  and solid angle  $d\Omega (=2\pi \sin\alpha \, d\alpha)$  is placed at  $z_1$ , Figure 7.6, and directed along  $\alpha(z_1)$  then the same flux will be measured at  $z_2$  when the detector is pointed in the direction  $\alpha(z_2)$  governed by equation (7.9)

Given  $f_1(\alpha_1, B_1)$  one can make the necessary transformation by simply substituting equation (7.9) for  $\alpha(z_1)$  in terms of  $\alpha(z_2)$ . In this way, given the pitch-angle distribution at any altitude the complete distribution may be obtained at a lower altitude and a partial distribution at any greater altitude. An example for translating the distribution derived in equation (7.3) to lower altitudes is plotted in Figure 7.7 and is represented by

$$\text{Flux} = r_1 [\sin\alpha(z_1)]^{2/3} - (R_o + z_o) = r_2 [\sin\alpha(z_2)]^{2/3} - (R_o + z_o) \quad (7.11)$$

### 7.3 Computer Simulation of the Count-Rate Profile

For an electron ( $E > 20$  keV) which mirrors above 135 km the collision probability with atmospheric neutrals is enhanced approximately 50 times with respect to a vertically incident particle (Section 9.2). Below 135 km scattering plays a dominant role, as will be discussed in Chapter 8.

The significance of the ionization loss mechanism on the quasi-trapped count-rate profile has been investigated by computer simulation. The program is described in Chapter 9. The program calculates and stores the energy loss and ionization rate of the incident energetic electron as a function of altitude for any given pitch-angle distribution and energy spectrum. The essentials of the energy loss calculation are given in

*1-3*

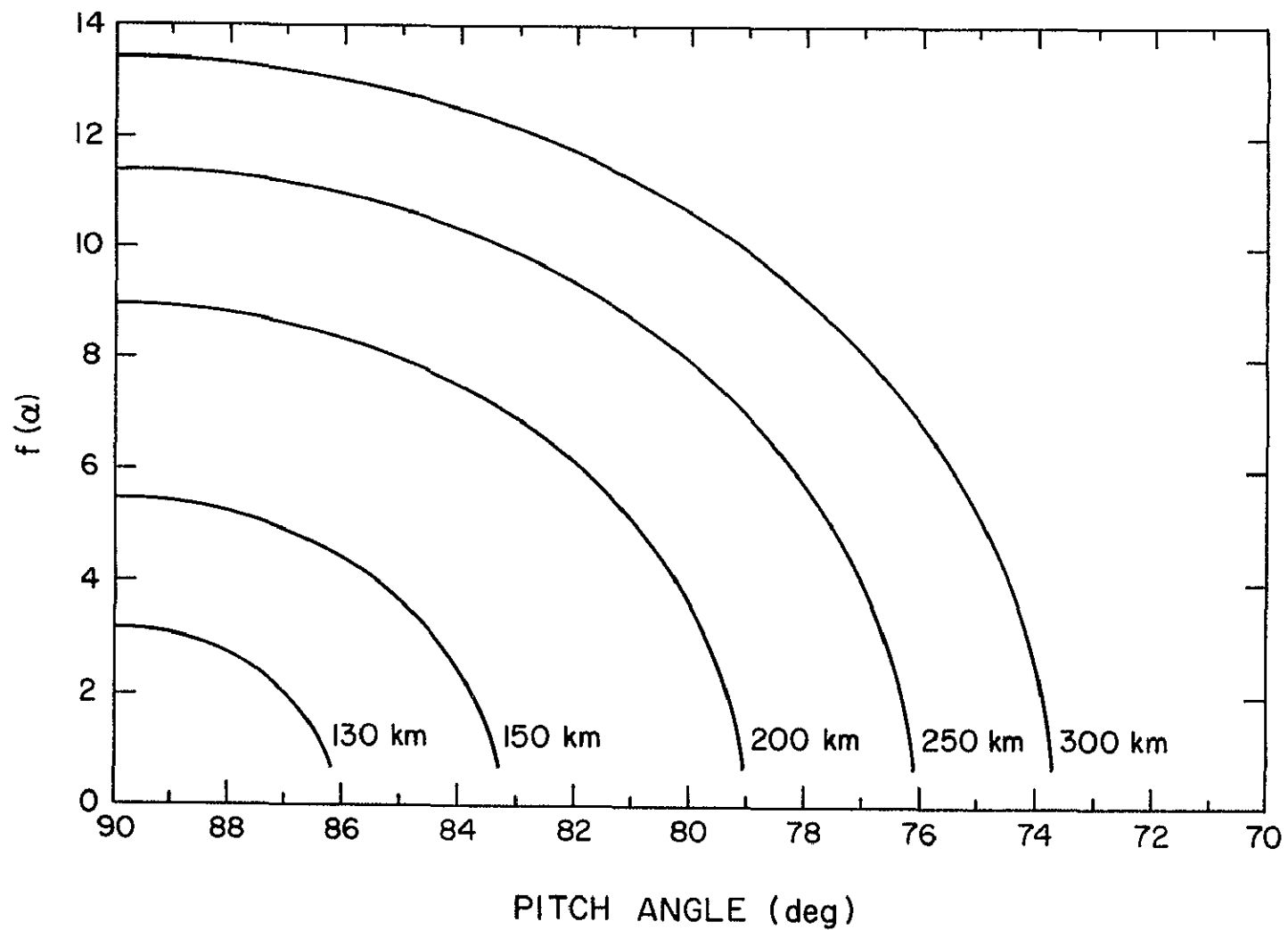


Figure 7.7 The pitch-angle distribution derived from equation (7.3) for different altitudes.



Chapter 8 using the empirical analysis of *Grün* [1957]. The program separately computes the count-rate profiles for electrons moving downward towards their mirror altitude and upward after reflection. Also calculated is the sum of both upward and downgoing electrons. Calculations were made for energies of 1, 3, 5, 7, 9, 11, 15, 20, 25, 30, 40, 50, 60, 80 and 100 keV

Typical computer results of the mirror-height distribution of equation (7.4) for 3 keV and 11 keV monoenergetic electrons are shown respectively in Figures 7.8 and 7.9. Figure 7.8(a) shows the count rate versus altitude profile calculated for particles which are moving downward in their helical trajectory for energy intervals  $2 < E < 3$  keV and  $1 < E < 2$  keV and for  $E < 1$  keV. Figure 7.9(a) is the corresponding data for  $10 < E < 11$  keV,  $7 < E < 10$  keV and  $5 < E < 7$  keV. The various count-rate peaks observed at the lower altitudes are the result of the energy degradation of the incident particles. Figures 7.8(b) and 7.9(b) show those particles which have mirrored (although partially absorbed) and are in an upward helical trajectory. Figures 7.8(c) and 7.9(c) show the superposition of the upward and downward flux and indicate what a particle spectrometer would be expected to measure for monoenergetic electrons having the assumed pitch-angle distribution.

A significant conclusion from this study of energy loss is that the final count-rate versus altitude profile remains linear. It does so because of the low altitude cut-off in the downward flux which is just balanced by the increase in the upward flux at greater altitudes. Therefore the energy loss process does not change the final form of the count-rate versus altitude profile appreciably from the analytic solution of equations (7.4) and (7.5) but does alter the altitude intercept point and slope of the line, the lower the energy the higher the altitude intercept of the count-rate profile

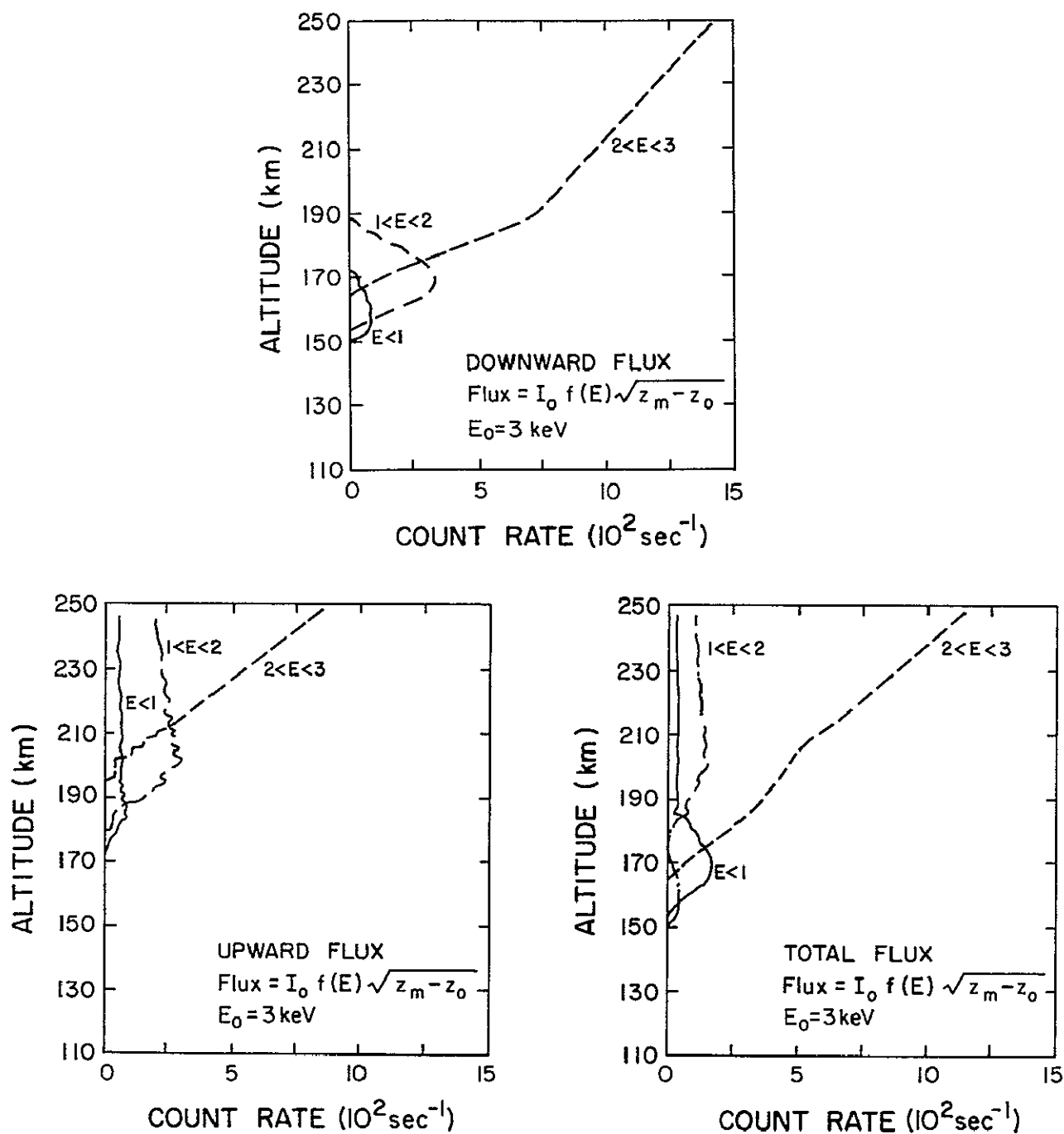


Figure 7 8 Computer simulation of the count-rate profiles for a quasi-trapped distribution of particles in the atmosphere with initial energy of 3 keV. The upper figure shows the downward flux, the lower left figure shows the upward flux and the lower right figure shows the combined upward and downward flux

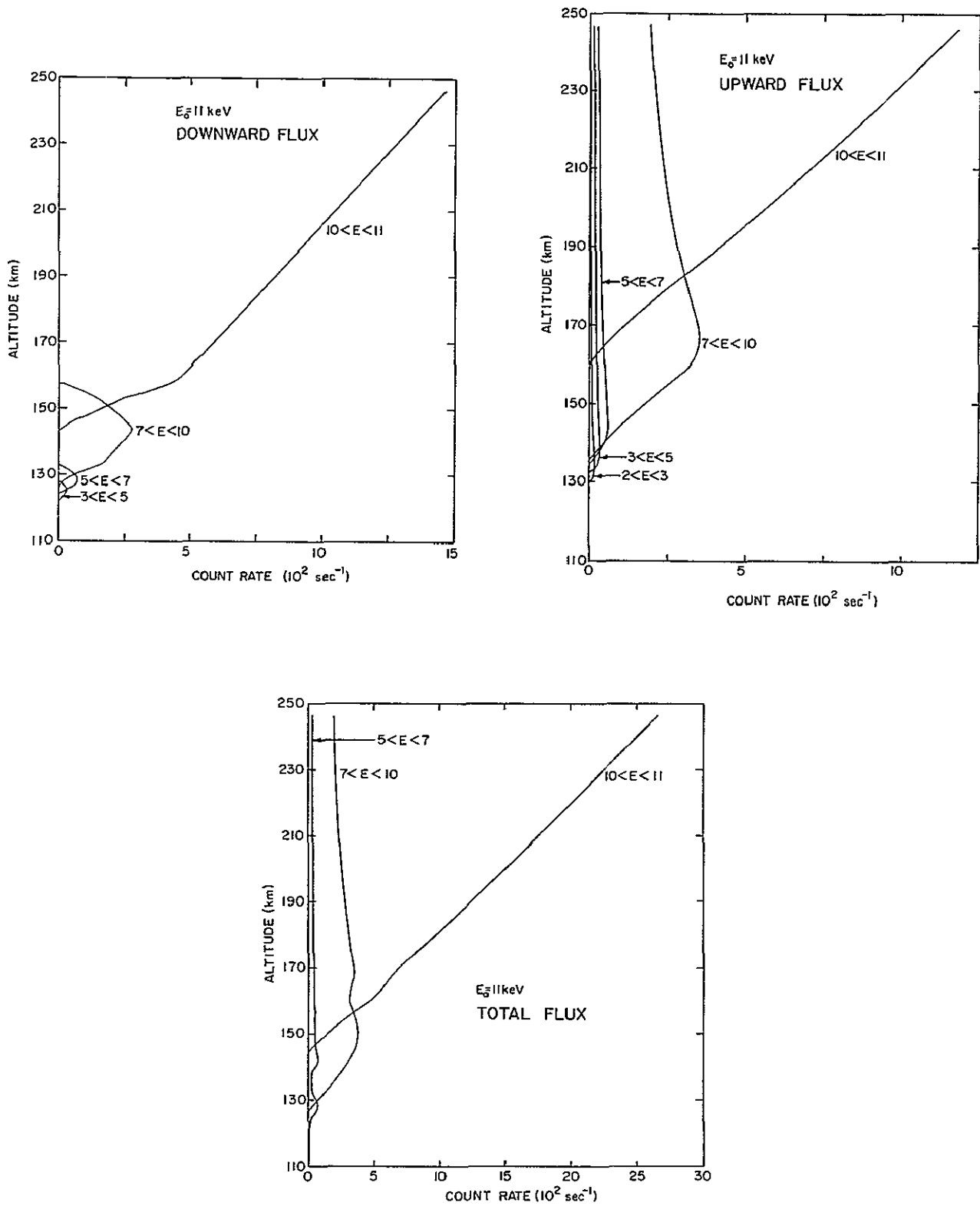


Figure 7 9 Same as Figure 7 8 but for an initial energy of 11 keV.

The small-scale fluctuations of the count-rate curves are due to the limited statistics. Much energy is released in a short altitude range when a particle is near total absorption and consequently the counting rate is abruptly reduced. Discussion of the energy loss process, model atmosphere and further computer calculations are given in Chapters 8 and 9

Also calculated from this program is the count-rate profile expected from a superposition of all the degraded energetic particles for the four typical energy spectra to be shown in Figure 9.9. Spectra 1, 2, and 3 are for power-law energy spectrums with exponent of 1, 2, and 3 and spectrum 4 is experimentally determined. The results of these calculations for  $5 < E < 20$  keV are shown in Figure 7.10 and clearly show a linearly increasing count rate with altitude for the superposition of all degraded energetic particles with a pitch-angle distribution given by equation (7.3). The square-root mirror-height distribution seems to be representative of the typical midlatitude pitch-angle distribution and linear count-rate versus altitude variation.

#### 7.4 Equatorial Proton Precipitation

Analysis of rockets 14.424 and 14.425 launched at Chilca, Peru, as reported on in Section 4.2 indicates that there is a flux of energetic particles at the magnetic equator which 1) begins to increase in intensity above 170 km, 2) has a narrow pitch-angle distribution centered about  $90^\circ$ ; and 3) shows rapid and positive correlation with geomagnetic activity. Various additional measurements of equatorial precipitation have been reported by Heikkila [1971], Hovestadt *et al.* [1972], Moritz [1972], Mizera and Blake [1973], Goldberg [1974], Butenko *et al.* [1975] and Kelley *et al.* [1977].

It is likely that the identification of these particles at relatively

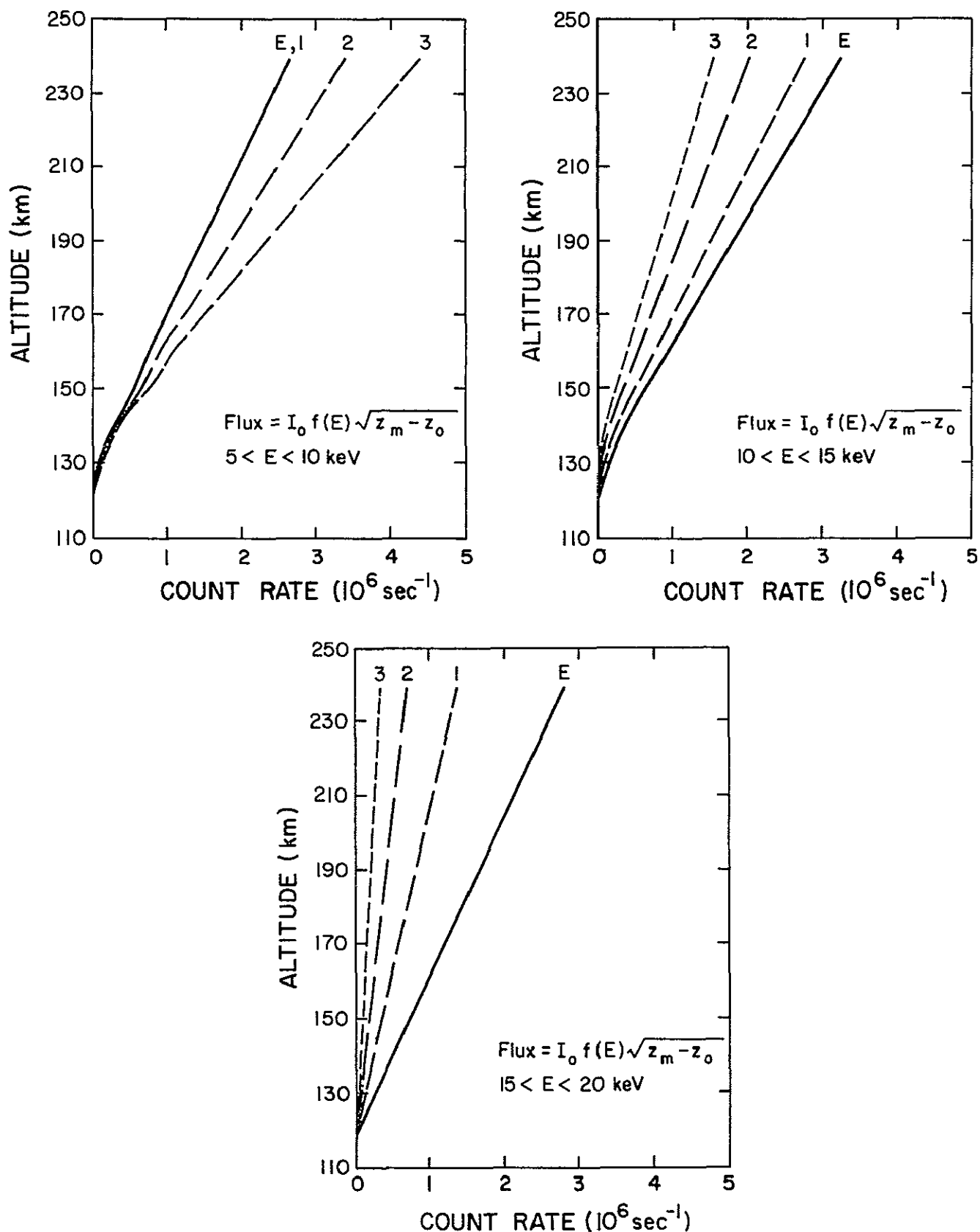


Figure 7 10 The total composite count-rate profile for several energy spectrums (see Figure 9.9) The nearly linear increase of the count rate with altitude in this model is similar to the experimental observations discussed in Section 4.1

low altitudes at the equator as electrons is incorrect because the transport process perpendicular to the magnetic field lines by ELF wave scattering is at a minimum (Figure 6 4) and radial diffusion coefficients are on the order of years.

A more reasonable explanation exists if the particles are identified as protons. *Moritz* [1973] proposes that the mechanism is a double charge exchange process of protons originating in the ring current ( $2 < L < 4$  at the equator). The protons, by charge exchange in the ring current, become high velocity neutral hydrogen atoms which travel to the equatorial atmosphere where they again become protons by an ionization collision.

Further support for this double charge exchange mechanism includes 1) only nighttime build up of protons since the plasmasphere boundary extends further out during the night [*Butenko et al.*, 1975]; 2) a count-rate versus altitude profile which is independent of altitude above 300 km since the second charge-exchange source is proportional to atmospheric density [*Moritz*, 1973]; 3) the shape of the energy spectrum is similar to the ring current spectrum [*Mizera and Blake*, 1973], 4) a localization of fluxes about the magnetic equator, 5) a flux which is independent of geomagnetic and geographic longitude [*Meier and Weller*, 1975], and 6) a dependence on  $K_p$ , since the ring current population is well correlated with magnetic activity. In addition to this source of protons there is some evidence that there may be a local proton and electron acceleration mechanism operable at a few hundred km altitude in the region of the South Atlantic anomaly [*Butenko et al.*, 1975, *Kelley et al.*, 1977]

The rocket data of 14 524 and 14 525 (Section 4.2) are interpreted as measurements of protons created by the double charge exchange process. The count-rate profiles of Figures 4 12 and 4 13 are believed to be the low altitude cut-off of the otherwise height-independent flux. The

following reasons are given for this conclusion 1) the solid-state detector is sensitive to protons with energies greater than 40 keV, 2) the pitch-angle distribution is highly peaked at  $90^\circ$ ; 3) the energy spectrum is identical with that measured by *Mizera and Blake* [1973] with a power law exponent of 2, 4) the recorded flux varies directly with  $K_p$  as expected for ring current injection, and 5) the altitude cut-off of the count rate at approximately 170 km is consistent with equation (7 8) in that the lifetimes are much smaller for protons than for electrons at these altitudes.

Geiger counter measurements of *Goldberg et al.* [1976] at Chilca, Peru show few counts below 300 km. Since these detectors were only sensitive to keV electrons (and X-rays) and insensitive to keV protons, it is concluded, assuming similar precipitation patterns, that the solid-state detectors on Nike Apaches 14 424 and 14 425 measured protons.

The electron flux at the equator during the daytime is an order of magnitude greater than at night whereas the proton flux diminishes considerably, as shown by Kosmos-484 satellite data taken at 200 km [*Butenko et al.*, 1975]. The data of *Kelley et al.* [1977] are consistent with this conclusion since their rocket measurements were made within the South Atlantic anomaly region at twilight and consequently record a larger electron flux, implying a local acceleration, and other anomalous effects.

The measurements of *Goldberg* [1974] recorded an anomalously high background particle flux on a mass spectrometer launched at the equator during a magnetic storm. The data were interpreted to be energetic particles. However the more recent analysis suggests that the particles were in fact protons [*Voss et al.*, 1977].

Rocket studies at altitudes exceeding 200 km are necessary at the

equator in order to properly model the aeronomic effects of proton precipitation. A more complete analysis of the low altitude cut-off region observed between 170 and 200 km and the narrow pitch-angle distribution about 90° need to be extended in both altitude and resolution. Figure 7.11 illustrates the various equatorial particle measurements of protons. Curve 1 is for 50 keV protons measured by rocket 14.525, curve 2 is for 50 keV protons measured by Kosmos-484 [Butenko *et al.*, 1975], curve 3 is the inferred 40 keV proton flux measured by an Azur satellite [Moritz, 1973], and curve 4 is the 40 keV flux measured by the satellite 1969-025A [Mizera and Blake, 1973].

It should be noted in this context that Kp variations can alter the flux by a factor of about 12 at 40 keV [Mizera and Blake, 1973]. Further investigation of a local acceleration mechanism and electric field measurements are necessary in the vicinity of the South Atlantic Anomaly.

#### 7.5 Comparison Between Nearly Simultaneous Rocket and Satellite Particle Measurements

One of the primary problems associated with measuring midlatitude particles by satellites is the small geometrical factors of the on board keV energy particle detectors. Therefore, satellite data are quite insensitive to the fluxes typical of midlatitudes. This, for example, was the case with the AE-C satellite particle experiments when a particle coordination attempt was made in the ALADDIN Program with rockets 14 521 and 14.522.

Some nearly simultaneous data from satellites is available for comparison with data from sounding rockets 14 439 and 14.520, reported on in Section 4.1. Also during the Nike Apache 14.520 flight simultaneous measurements of the electron density were made with the Arecibo radar [Shen *et al.*, 1976].



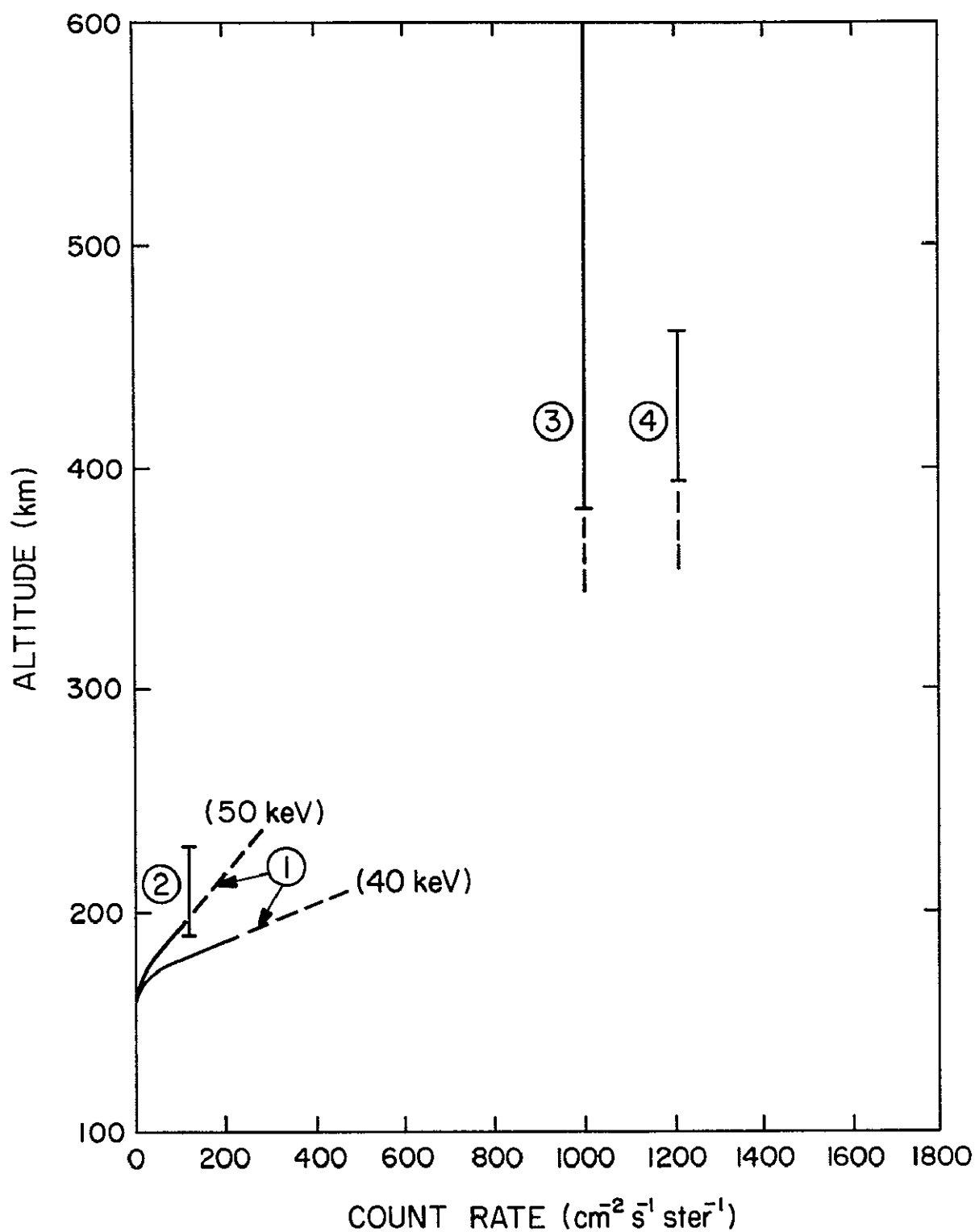


Figure 7.11 Rocket and satellite measurements of protons at the equator. 1 is the rocket data from Nike Apache 14 525, 2 is from *Butenko et al.* [1975], 3 is from *Moritz* [1973], and 4 is from *Mizera and Blake* [1973].

*Imhof et al.* [1976] have reported on satellite particle data between 2300 UT, 31 October to 0545 UT, 1 November 1972, the same night that Nike Apache 14.439 was launched from Wallops Island (0503 UT, 1 November 1972). A detailed analysis of the count rate measured on rocket 14 439 is given in analysis by *Imhof et al.* [1976] Each satellite had a polar orbit and varied in altitude between 750 and 800 km

The map shown in Figure 7.12 gives the times and positions of seven satellite passes made during this night. Also shown is the Kp value ( $5 < Kp < 8$ ) and the measured integral flux ( $E > 160$  keV) of electrons for each satellite pass, the launch location of Nike Apache 14.439 and  $L$  shells (at 100 km) corresponding to 2, 2.5 and 4.

Inspection of the count rates reveals that the flux over Europe is less than it is over North America This may be attributed to geographic variations caused by the South Atlantic Magnetic Anomaly and temporal variations associated with the change in Kp values The two satellites made simultaneous passes at 0405 UT and at 0545 UT over North America They show that there is variation in longitudinal structure but that the average particle flux remains nearly constant.

Count rates from Nike Apache 14.439 (launched at 0503 UT) indicate that at a fixed location the flux of electrons with  $E > 70$  keV can vary significantly in time (Figure 4.1). The large temporal and spatial variations observed on this night should not be regarded as typical since the magnetic conditions are very disturbed and subsequent rocket flights launched during lower values of Kp indicate very stable precipitation patterns

Data from satellite 1972 089A is plotted in Figure 7 13 for electrons with energy intervals of  $0.5 < E < 1$  keV,  $2 < E < 4$  keV and  $20 < E < 32$  keV and with energy  $E > 130$  keV The first three energy intervals were obtained by a ten

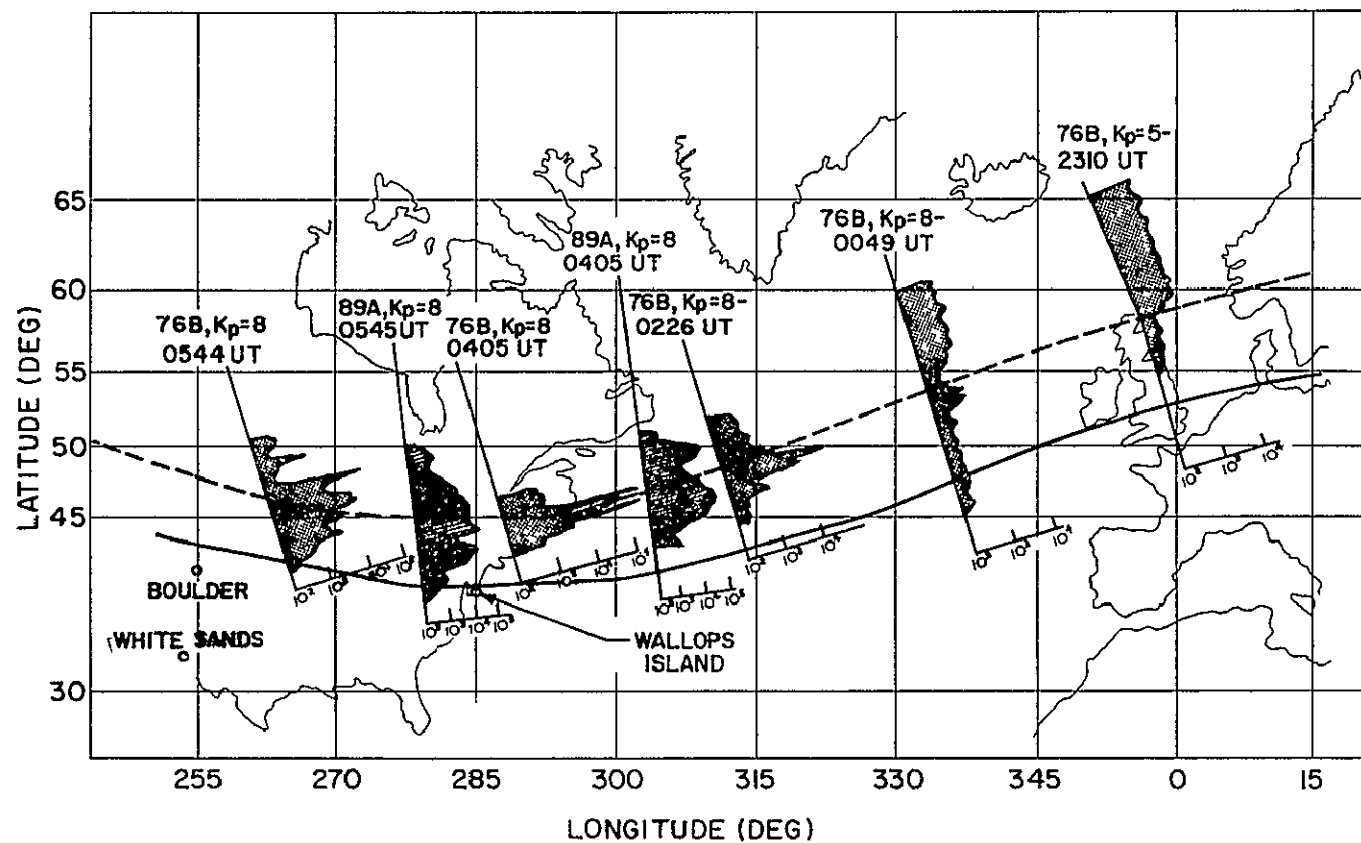


Figure 7.12 Satellite data [Imhof *et al.*, 1976] taken during the same night that Nike Apache 14.439 was launched (0503 UT).

ORIGINAL PAGE IS  
OF POOR QUALITY

## LOCKHEED SATELLITE DATA-1972-089A

- 1 NOV 72
- 01:05 LOCAL TIME
- $K_p = 8$

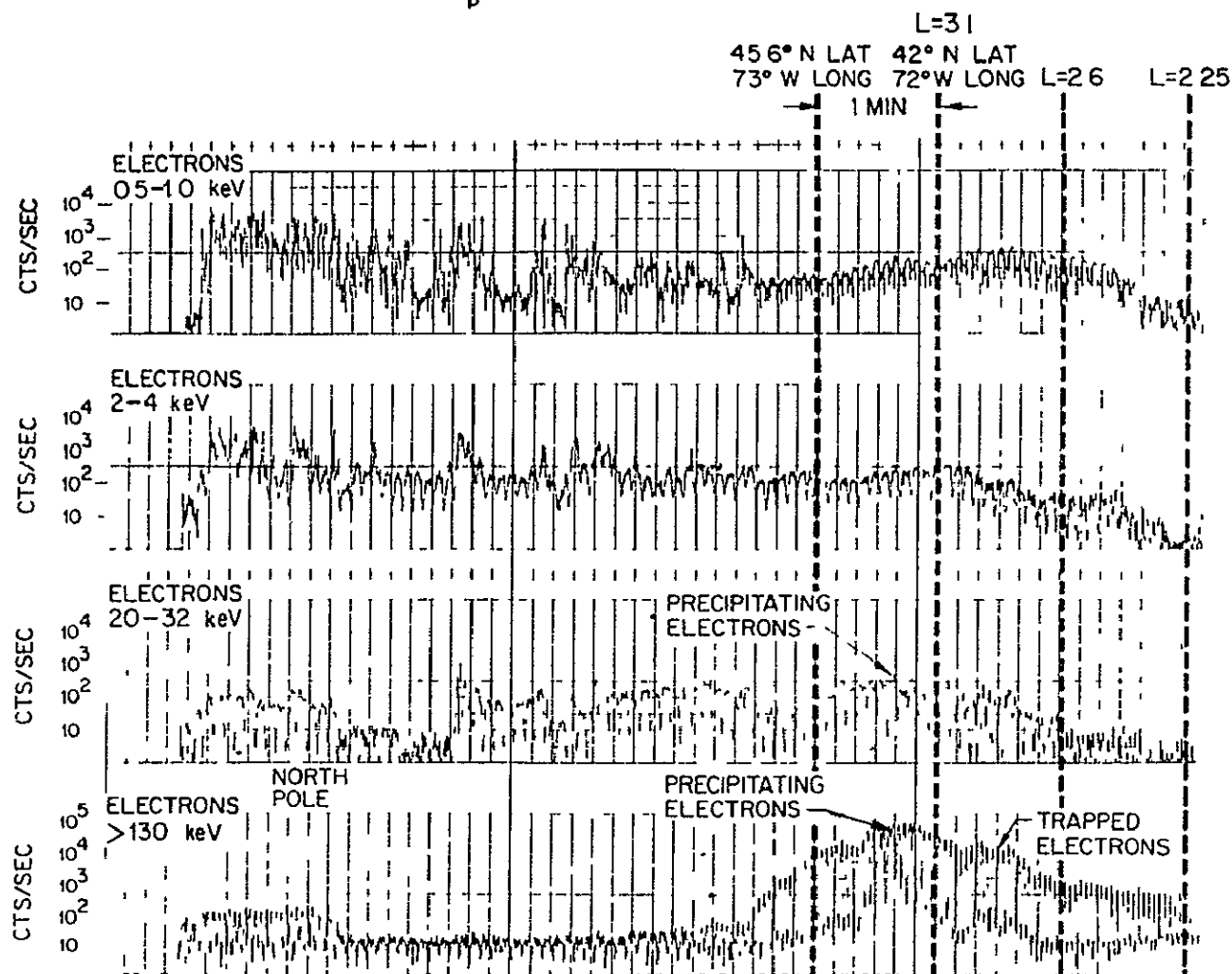


Figure 7.13 Satellite data [Imhof *et al.*, 1976] for different energies taken nearly simultaneously with the launch of Nike Apache 14.439

channel multi-particle analyzer while the latter was obtained by a high energy spectrometer. Also shown is the location of Wallops Island ( $L = 2.6$ ) and examples of the data format for trapped and precipitating particles.

Because the satellite is spinning, the particle detectors move through a pitch angle of  $90^\circ$  twice each revolution as shown in Figure 3.7. For a quasi-trapped flux which is maximized near  $90^\circ$  the count rate varies at twice the spin frequency. For an isotropic downward flux (precipitated) the detectors register counts for pitch angles less than  $90^\circ$  and small fluxes near the nadir direction ( $180^\circ$ ). Consequently the flux varies at the spin frequency.

At these altitudes (750-800 km) and magnetic conditions ( $K_p = 8$ ) the energy flux ( $E < 10$  keV) has a large isotropic component while for higher energies the flux is predominantly quasi-trapped (Figure 7.5). This is consistent with the satellite data of *Larsen et al.* [1976 a,b] shown in Figure 4.17.

The energy spectra measured by the satellite on various passes are shown in Figure 7.14. These spectra are averaged over  $4^\circ$  latitude intervals centered about the region of peak flux. The low energy data points were obtained by a multi-particle analyzer (0.06 keV to 50 keV in 10 channels) and the higher energies (160 to 1000 keV) with a high energy spectrometer. Between 50 and 160 keV a best fit (dashed line) was used to extrapolate between the two instruments. From the figure it can be seen that the power law exponent for energies less than about 50 keV is less than the exponent for greater energies and may vary considerably during disturbed conditions. Also, the flux for energies less than 10 keV does not vary appreciably while the flux in the region 20 to 100 keV may vary by two orders of magnitude. This energy spectrum will be used in Section 9.4 to calculate the ionization rate for this night.

For Nike Apache 14.520 (0430 UT, 19 April 1974) satellite data was obtained from Lockheed satellite S72-1 [*Reagan*, personal communication].

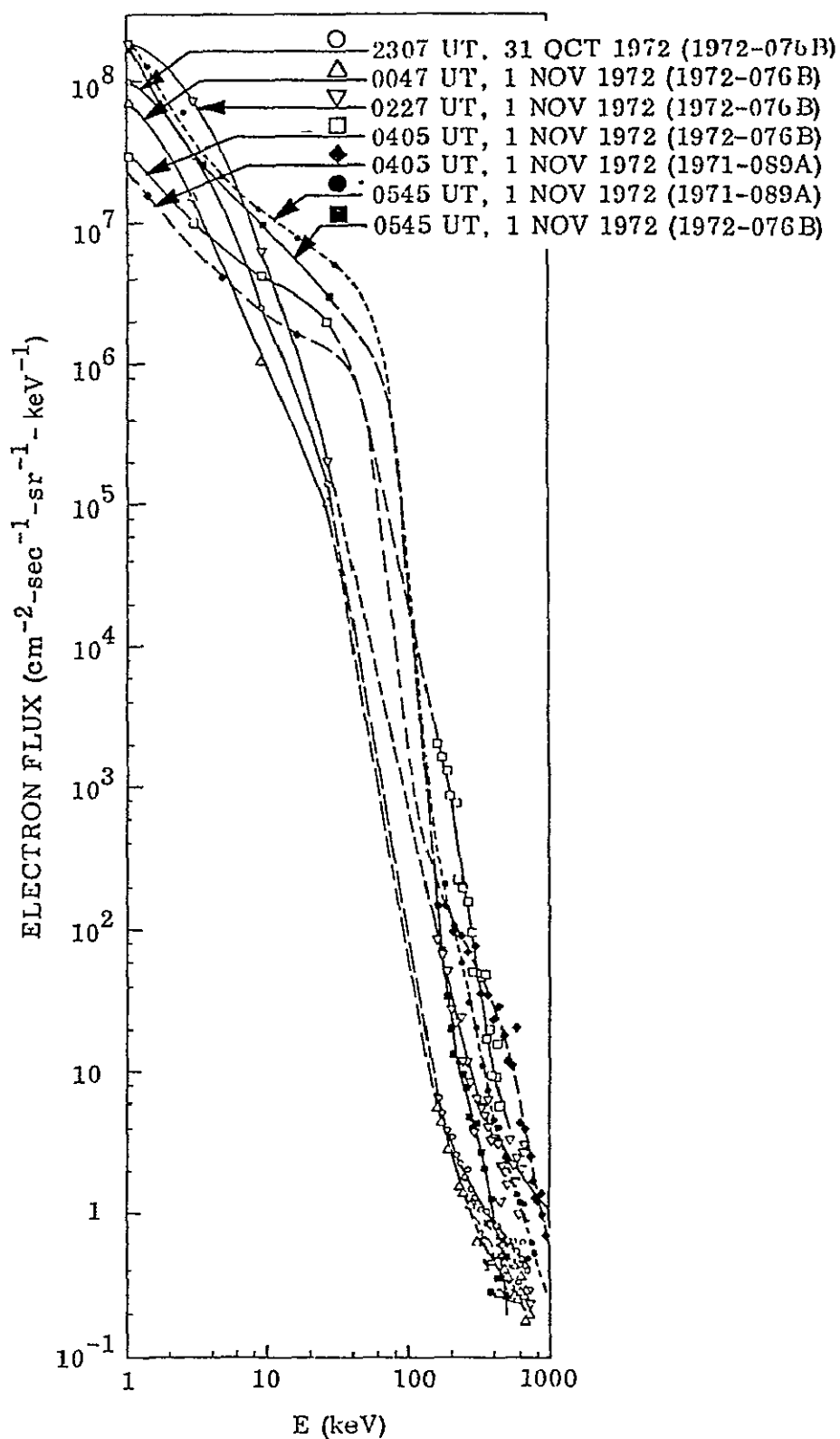


Figure 7 14 Various energy spectrums measured with satellite particle detectors [Imhof *et al* , 1976] during the night of the launch of Nike Apache 14 439.

The position of the satellite at nearest approach to Wallops Island is  $37^{\circ}\text{N}$  and  $59^{\circ}\text{W}$  at 0342 UT. The geomagnetic conditions for this night are moderately disturbed with  $K_p = 5+$ . Data from the satellite is shown in Figure 7.15 for energetic electrons in the  $1.5 < E < 3$  keV channel (geometrical factor  $10^{-5} \text{ cm}^2$ ) and in the 100 to 800 keV channel (geometrical factor  $0.3 \text{ cm}^2$ ). Unfortunately, the low energy detectors have extremely small geometrical factors and are insensitive to the moderate midlatitude fluxes observed by rocket 14.520. The sharp boundary of the precipitated flux in the auroral region at  $L = 3.2$  for this night is quite noticeable and may be compared to the much lower flux cut-off ( $L \approx 2.4$ ) of the quasi-trapped flux in Figure 7.15. This flux boundary is at higher  $L$  values, between 4 and 5, during quite geomagnetic conditions.

#### 7.6 Global Precipitation Patterns at Night

From the observations and conclusions of the previous three chapters a global precipitation model may now be developed. Although such a model is not able to incorporate all the complex mechanisms involved, a general localization of precipitation to certain zones and regional areas is possible. This section will briefly explain a global precipitation map based on the observations and conclusions of the previous chapters. The map is shown in Figure 7.16.

Some of the data used in making this map are primarily from satellite measurements of Seward [1973] for the midlatitude precipitation zones and are supplemented with many rocket, satellite and indirect evidences as discussed in Chapters 4, 5, and 6. The equatorial proton zone is based on data from rockets 14.424 and 14.425 (Section 4.2) and from satellite measurements reviewed in Section 7.4. The South Atlantic anomaly region is based on four satellite measurements discussed in Section 6.5.

Along the geomagnetic equator precipitation of protons occurs at low

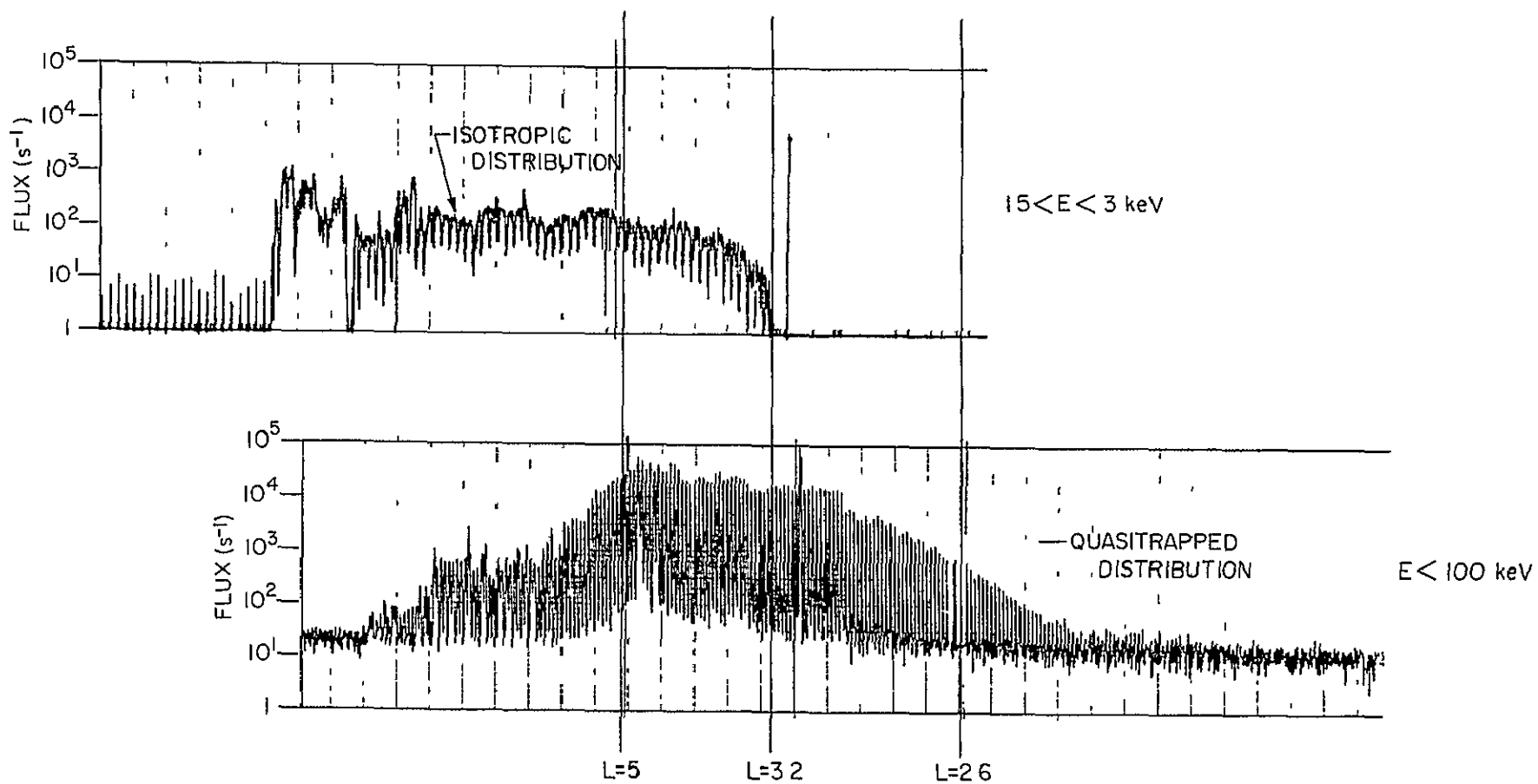
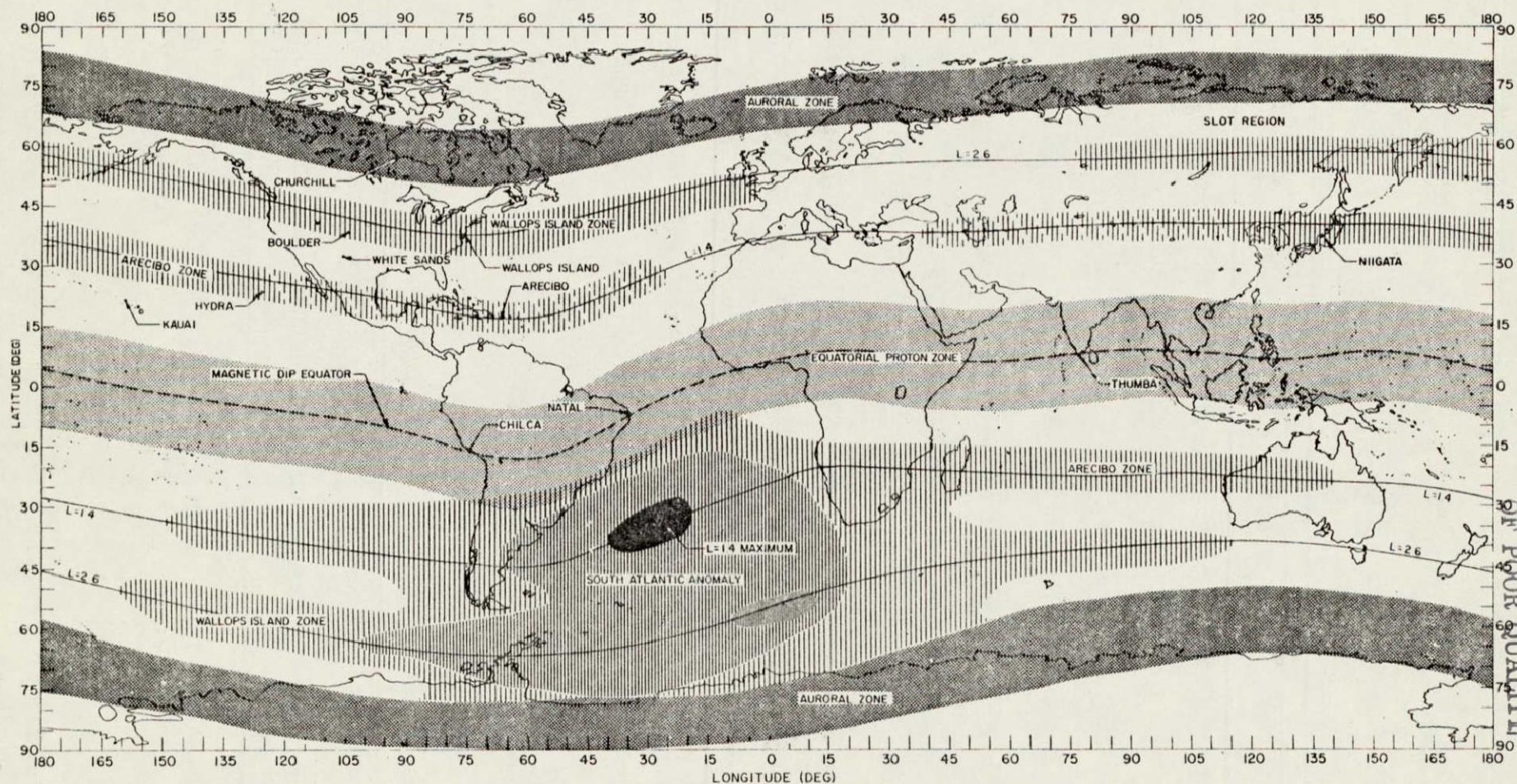


Figure 7.15 Satellite data taken at nearly the same time as the launch of Nike Apache 14 520 [Reagan, personal communication]





ORIGINAL PAGE IS  
OF POOR QUALITY

Figure 7.16 Global precipitation map based on rocket and satellite observations. Shown are the auroral zones, the equatorial proton zone and the midlatitude zones at  $L = 2.6$  and  $L = 1.4$ . The enhancement in the vicinity of the South Atlantic anomaly is also indicated.



altitudes due to the double-charge exchange process of hydrogen with ring current protons (Section 7.4). Nike Apaches 14.524 and 14.525 (Section 4.2) observed these protons down to altitudes of approximately 170 km. Satellites have observed protons in the altitude region above 300 km and have obtained count-rate profiles which are independent of altitude. The low altitude proton flux is sensitive to variation in  $K_p$  since the ring current flux varies in a similar manner. Longitudinal variations are very small along this precipitation zone due to the symmetry of the ring current source.

In the low latitude region, at  $L = 1.4$ , a precipitation zone of quasi-trapped electrons is usually observed during moderate and disturbed magnetic conditions. This conclusion is based on satellite and rocket data (Chapter 4), 391.4 nm measurements (Section 5.1) and enhancements of electromagnetic hiss (Section 6.3). Satellite data by *Seward* [1973] is shown on this map and is supplemented by measurements of electron precipitation over Arecibo and Japan. Further evidence of increased precipitation in this  $L$  shell is the precipitation maximum at  $L = 1.4$  observed in the South Atlantic anomaly (Section 6.5).

Between  $L$  values of 1.6 and 2.2 there is a precipitation null. This precipitation null is evident on rocket and satellite measurements as a sharp cutoff in precipitation at  $L = 2.1$  as discussed in Chapters 4 and 6. An absence of particle-induced 391.4 nm emission in this region is consistent with the interpretation of a null at  $L = 1.8$  (Section 5.1). Wave-particle interactions which are known to scatter particles into precipitating trajectories are found to be minimized in this region (Section 6.3). Particle effects in this zone are therefore negligible except during very disturbed magnetic conditions ( $K_p > 8$ ).

For  $L$  values between 2.2 and 3.5 a precipitation zone of quasi-trapped

energetic electrons is detected. This flux is of sufficient magnitude to cause many aeronomic effects even during moderately quiet geomagnetic conditions ( $K_p = 3$ ). Electron precipitation must therefore be included in a nighttime ionization model in this zone. The quasi-trapped flux is observed to extend down to 120 km altitude. The isotropic component of the flux is quite variable and decreases monotonically from the auroral region. Documentation of the characteristics of this precipitation zone are given in Chapters 4, 5 and 6.

For the slot region between  $L = 3.5$  and  $L = 5$  there is a minimum in the quasi-trapped and isotropic flux during relatively low geomagnetic activity ( $K_p < 3$ ). For increased magnetic activity the isotropic flux rapidly increases to intensities greater than occurs in the  $L = 2.6$  precipitation zone due to inward radial diffusion from the auroral region and increased wave-particle scattering.

The auroral zone is characterized by particle flux intensities which are about three orders of magnitude greater than found in the midlatitude precipitation zones. Particles therefore dominate all other nighttime ionization sources in this region.

The results of this study indicate that the particle flux is localized to certain precipitation zones. A discussion of the properties of the flux distribution is given and primarily differs from previous theories in that the pitch-angle distribution is centered near  $90^\circ$  pitch angle such that most of the particles are in a magnetic reflecting state in the region 120 to 200 km. This causes the count rates in this region to increase linearly with altitude. A global precipitation map is developed which explains and predicts many aeronomic and particle observations.

### 7.7 *The Relative Importance of Energetic Electrons and Protons*

The energetic particles observed at midlatitudes are identified as electrons (Chapters 4 and 6), however, energetic protons may, on occasion, be an important species during the build-up phase of the proton ring current ( $L \approx 3$ ). *Proßss* [1973] suggest that plasma instabilities might produce significant energy deposition of ring current protons into the atmosphere along magnetic field lines at midlatitudes. During the strong magnetic storm of 4-7 July 1974, *Lazarev et al.* (1976) show from satellite data that the proton flux ( $E \approx 20$  keV) increases by two orders of magnitude at night for  $2 < L < 3$ . Energetic proton fluxes could also produce a linear increasing altitude profile in the region 120 to 200 km (Section 4.1) as calculated by *Prag et al.* [1966]. Additional satellite measurements and relevant discussions of proton fluxes are given by *Lindalen and Egeland* [1972], *Kovtyukh et al.* [1976] and *Spjeldvik* [1977]. Further proton versus electron measurements are required to ascertain the relative magnitudes of the particle flux with respect to location and time.

The main evidence for energetic electrons at midlatitudes, in summary, are 1) the satellite and rocket experiments which directly measured both electrons and protons or discriminate by using electric or magnetic analyzers [e.g., *Seward et al.*, 1973; *Butenko et al.*, 1975; *Kubo et al.*, 1976, *Tulinov et al.*, 1976, *Vakulov et al.*, 1976; and those listed in Table 4.1 and Section 4.3], 2) the source mechanism of the radiation belt electrons evident from *Armstrong* [1965] and discussed in Chapter 6, 3) the consistent explanation of the Arecibo and Wallops Island precipitation zones and the explanation of the locations of the intensity maximums in the South Atlantic magnetic anomaly (Section 6.5), and 4) the pitch-angle distribution, although not highly resolved, is consistent with the count rate profile increasing

linearly with altitude.

The identification of the energetic particles as protons is consistent with 1) the linear increase with altitude of the count rate profile [Prag *et al.*, 1966], 2) the rapid variation of the particle flux with  $K_p$  due to the rapid build-up of the ring current source [Prölss, 1973], and 3) the cut-off at  $L \lesssim 2$  of the particle flux due to the lower boundary of the ring current

Energetic protons are also directed towards the equator due to the double charge exchange reaction of neutral hydrogen with the ring current (Section 7.4). Prölss *et al.* [1973] calculates that protons should extend out to approximately  $\pm 30^\circ$  geomagnetic latitude from the equator. However, satellite experiments show that typically the latitude spread is  $\pm 20^\circ$  [Moritz, 1973, Mizera and Blake, 1973; Butenko *et al.*, 1975, Meier and Weller, 1975]

The proton fluxes measured at the equator by rocket 14 525 (Section 4.2) at  $K_p = 5$  are much too small to cause any significant ionization effects below 240 km. At Arecibo the proton flux would be reduced yet further due to the higher latitude and consequently for  $K_p < 5$  the proton flux would be insignificant. However, Shen *et al.* [1976] have found a large ionization rate at night for  $K_p = 5$  in the altitude region above 120 km. At Arecibo energetic electrons are predicted to be the dominant species during moderately disturbed conditions but during very intense magnetic storms ring current protons would be expected to be a significant ionization source at low latitudes [Voss *et al.*, 1977], as well

An excellent review of particle precipitation at middle and low latitudes is given by Paulikas [1975] Additional reference material relevant to the measurement and identification of energetic particles at middle and low

latitudes is given by *Freeman* [1962], *Kazachevskaya and Ivanov-Kholodny* [1965], *Krassovsky et al.* [1965], *Nakagawa et al.* [1965], *Kazachevskaya and Ivanov-Kholodny* [1966], *Frank* [1967], *Kazachevskaya* [1967], *Tulinov* [1967], *Antonova et al.* [1969], *Kazachevskaya and Koryagin* [1969], *Ivanov-Kholodny* [1970], *Ivanov-Kholodny and Krosunova* [1970], *Ivanov-Kholodny and Kazachevskaya* [1971], *Antonova and Ivanov-Kholodny* [1972], *Antonova et al.* [1973], *Korsunova* [1973], *Rycroft* [1973], *Valot and Engelmann* [1973], *Vlasov* [1974], *Scholer et al.* [1975], *Tulinov et al.* [1975], *Blake* [1976], *Hayakawa et al.* [1976], *Kovtyukh* [1976], *Shibaeva et al.* [1976], *Tinsley* [1976], *Tulinov* [1976], *Vakulov et al.* [1976] and *Prange and Crifo* [1977].

## 8. INTERACTION OF ENERGETIC ELECTRONS WITH THE ATMOSPHERE

The interaction of quasi-trapped particles with the atmosphere causes a number of significant aeronomic effects (Figure 5.1) including ionization, chemical change, electron and ion density variations, plasma instabilities, temperature changes, winds, electromagnetic wave excitations, and optical emissions. Fundamental to all these direct and indirect effects associated with particle precipitation is the energy loss rate and scattering processes with the atmospheric constituents.

The first part of this chapter considers the single collision cross sections for energetic electrons with the atmosphere. It is shown that various theoretical and semi-empirical methods for calculating the cross section give, in some cases, different results. The range of applicability and the assumptions made will be compared for these various methods. The second section of this chapter concerns the energy loss process of energetic electrons in air. Comparisons between various models show substantial variations and imply that careful justification must be made for the particular method used. The third section concerns the complex analysis of plural and multiple scattering. Plural scattering involves the beam spreading due to a few collisions (e.g., <50 collisions) where random averaging is not possible. For many collisions (multiple scattering) various statistical approximations can be made which greatly simplify the analysis. The main result of this section is that many of the methods used to compute plural and multiple scattering have been largely in error since the formulas which are applicable at MeV and GeV energies are not applicable at low keV energies. To supplement the theoretical studies of multiple-collisions an experimental apparatus was developed using an electron accelerator to measure multiple and plural scattering typical of atmospheric conditions.

### 8.1 *Electron Scattering Cross Sections*

Energetic electrons interact with atmospheric gases by losing energy and changing their direction of motion. The primary mechanism for transferring energy is inelastic collisions with bound electrons although some energy may be imparted to ionospheric electrons elastically via electron-electron collisions. Elastic collisions with bound electrons are also significant for electrons since scattering can change the pitch angle and thus the altitude for energy deposition. Bremsstrahlung and Cherenkov radiation are of minor importance to the total energy loss.

**8.1.1 *Elastic collisions*** As an energetic electron approaches a charged nucleus beneath the orbital electron screen, the mutual electric fields of the charges act upon each other. Elastic collisions occur when no energy is lost by the incident electron and inelastic collisions occur when the incident electron loses energy with the orbital electrons by excitation or ionization processes.

The differential cross section  $d\sigma$  is defined as the fraction of particles in a beam which are scattered through an angle  $\theta$  into a solid angle  $d\Omega = 2\pi \sin\theta d\theta$ , assuming azimuthal symmetry. The total cross section  $\sigma_T$  is obtained by integrating the differential cross section over all scattering angles.

Assuming only coulomb interaction of point charges the Rutherford formula gives the differential cross section for elastic collisions between an electron and an atom.

$$\frac{d\sigma_{\text{Ruth}}}{d\Omega} = \frac{Z^2}{4} r_o^2 \left( \frac{1-\beta^2}{\beta^4} \right) \frac{1}{\sin^4 \frac{\theta}{2}} \quad (8.1)$$

where  $d\Omega = 2\pi \sin\theta d\theta$ ,  $\theta$  is the scattering angle (with  $\theta = 0$  for no scattering),  $Z$  is the atomic number of the scattering nucleus,  $\beta = v/c$  (the ratio of



the electron velocity to the speed of light), and  $r_o = e^2/(m_o c^2) = 2.82 \times 10^{-13}$  cm (the classical electron radius). This classical treatment is valid for the scattering of non-relativistic electrons by atomic nuclei for angles between about  $10^\circ$  and  $100^\circ$ .

For large scattering angles ( $\theta > 100^\circ$ ) the finite diameter of the nucleus is important. It is then necessary to apply relativistic Dirac theory of the electron to the problem of nuclear scattering [Mott, 1932] McKinley and Feshbach [1948] obtained a correction factor (the Mott factor) for  $d\sigma_{\text{Ruth}}$  given by

$$R \equiv \frac{d\sigma_{\text{Mott}}}{d\sigma_{\text{Ruth}}} = 1 - \beta^2 \sin^2 \frac{\theta}{2} + \pi\beta\alpha(1-\sin\frac{\theta}{2}) \sin\frac{\theta}{2} \quad (8.2)$$

where  $\alpha = Z/137$  is the fine structure constant.

For scattering angles smaller than  $10^\circ$  it is necessary to include the effects of the screening by the electron cloud since the scattering goes to zero for encounters outside the electron shells but  $d\sigma_{\text{Ruth}}$  becomes infinite as  $\theta$  goes to zero. A general method for treating this screening effect is given by Moliere [1947] using a Thomas-Fermi atomic model. These results may be expressed by a correction factor,  $q(\theta)$ , given by

$$q(\theta) = \frac{d\sigma_{\text{Mol}}(\theta)}{d\sigma_{\text{Ruth}}(\theta)} \quad (8.3)$$

A plot of this function is shown in Figure 8.1 for energies of 20 and 50 keV.

For a single elastic collision by an energetic electron with an atom the following formula applies.

$$d\sigma(\theta) = q(\theta) d\sigma_{\text{Mott}} = q(\theta) R d\sigma_{\text{Ruth}}(\theta) \quad (8.4)$$

where  $d\sigma_{\text{Ruth}}$  has been replaced by  $d\sigma_{\text{Mott}}$  in equation (8.3). A simplification of equation (8.4) is possible [Jackson, 1962] at small scattering angles were

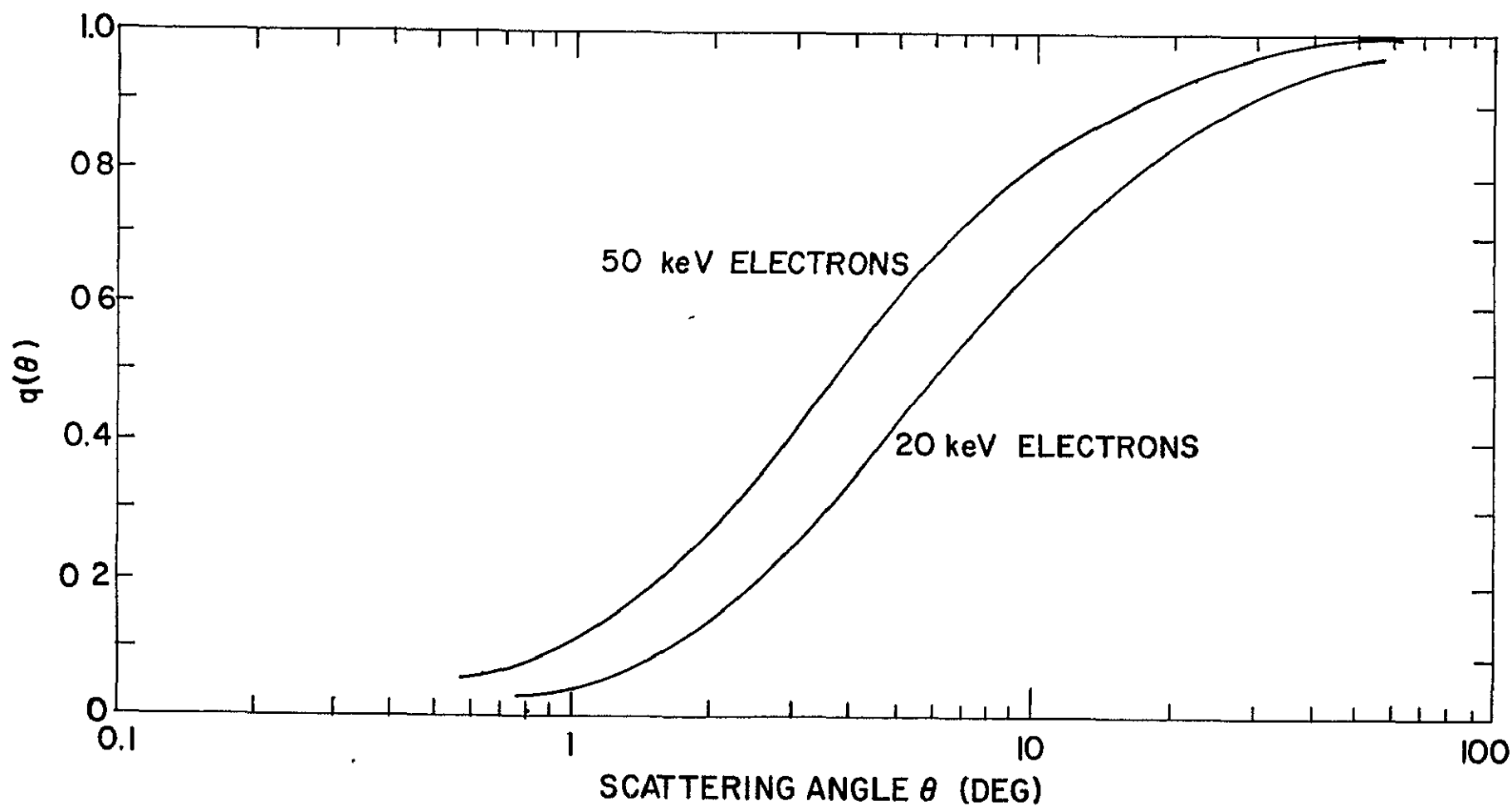


Figure 8.1 Plot of the correction factor,  $q(\theta)$ , to be applied to the Rutherford formula to allow for screening by the electron cloud

$\sin^4 \frac{\theta}{2}$  is approximately  $\left(\frac{\theta}{2}\right)^4$ . Then

$$\frac{d\sigma}{d\Omega} = \frac{N_o}{A} \left( \frac{2Ze^2}{mv^2} \right)^2 \frac{1}{\left( \theta^2 + \theta_{\min}^2 \right)^2} \quad (8.5)$$

where  $A$  is the atomic weight ( $28.8 - 2 = 14.4$  for air),  $N_o$  is Avogadro's number ( $6.02 \times 10^{23} \text{ mol}^{-1}$ ),  $\sigma$  is in units of  $\text{cm}^2 \text{ g}^{-1}$  and  $\theta_{\min}$  is an effective cutoff angle representative of the shielding by the electron cloud. Quantum-mechanically  $\theta_{\min}$  is approximately given by [Maeda, 1962]

$$\theta_{\min} = \frac{mc}{P} \propto Z^{1/3} \quad (8.6)$$

where  $\alpha = e^2/\hbar c \approx 1/137$  is the fine structure constant and  $P$  is the particle momentum. For electrons in air equation (8.6) gives  $\theta_{\min} = 0.08/\beta$  degrees. At 20 keV, for example,  $\theta_{\min} = 2.8^\circ$ .

For electrons in air equation (8.5) may be expressed as

$$\frac{d\sigma}{d\Omega} = \frac{4.5 \times 10^4}{E^2 (\theta^2 + \theta_{\min}^2)^2} \quad (8.7)$$

where  $E$  is the energy in keV and  $\sigma$  is expressed in  $\text{cm}^2 \text{ g}^{-1}$ .

Another useful form of the screened Rutherford formula is given by Berger *et al.* [1970] as

$$\frac{d\sigma}{d\Omega} = Z^2 r_o^2 \frac{1}{\beta^4} \left[ \frac{1}{(1 - \cos\theta + 2\eta)^2} \right] \quad (8.8)$$

where  $\eta$  is a screening parameter which may be expressed as  $\eta = 1.6 \times 10^{-2} E^{-1.03}$  for  $Z = 7$  (representing the atmosphere). The total cross section for this case is obtained by integration of equation (8.8) to obtain

$$\sigma_T = Z^2 r_o^2 \frac{\pi}{\beta^4} \frac{1}{\eta(1+\eta)} \frac{N}{A} \quad (8.9)$$

where  $\sigma_T$  is expressed in  $\text{cm}^2 \text{ g}^{-1}$ . Correspondingly, the total cross section obtained when using the differential cross section form of equation (8.5) is

$$\sigma_T \approx 2\pi \frac{N_o}{A} \frac{r_o^2}{\beta^4} \int_0^\pi \frac{\theta d\theta}{(\theta_{\min}^2 + \theta^2)^2} \approx \pi \frac{r_o^2}{\beta^4} \frac{1}{\theta_{\min}^2} = \frac{1.4 \times 10^5}{E^2 \theta_{\min}^2} \quad (8.10)$$

where  $\sigma_T$  is expressed in  $\text{cm}^2 \text{ g}^{-1}$ ,  $E$  in keV and  $\theta_{\min}$  in degrees.

Equations (8.1), (8.5) and (8.8) are plotted in Figure 8.2 for 10 keV and 50 keV electrons. At scattering angles greater than  $10^\circ$  the results agree with Rutherford scattering. The effects of screening can be seen at small angles.

In addition to a Thomas-Fermi atomic model *Freyer* [1969] has used a Hartree-Fock approximation for both the screened and non-screened case. The cross section for both of these cases differ considerably from (about two order of magnitude) from the Moller or Thomas-Fermi formulation for angles less than ten degrees. This large uncertainty warrants further investigation of the small angle cross section.

Equations (8.5) and (8.8) provide the basis for calculations of the scattering of electrons in the atmosphere. These single scattering formulas will be extended to more realistic multiple and plural scattering events typical of the upper atmosphere.

8.1.2 *Inelastic collisions.* When the energy lost in a collision is much greater than the atomic binding energy, the collision can be treated in the classical manner of two free electrons such that

$$d\sigma_{\text{Ruth}} = r_o^2 \frac{4}{\beta^4} \left( \frac{1}{\sin^4 \theta} + \frac{1}{\cos^4 \theta} \right) \cos \theta \, d\theta \quad (8.11)$$

Using quantam-mechanical methods *Mott* [1932] has obtained a nonrelativistic formulation of the more general case of the impact of an electron with an orbital electron by inclusion of the following additional term within the parentheses of equation (8.11)

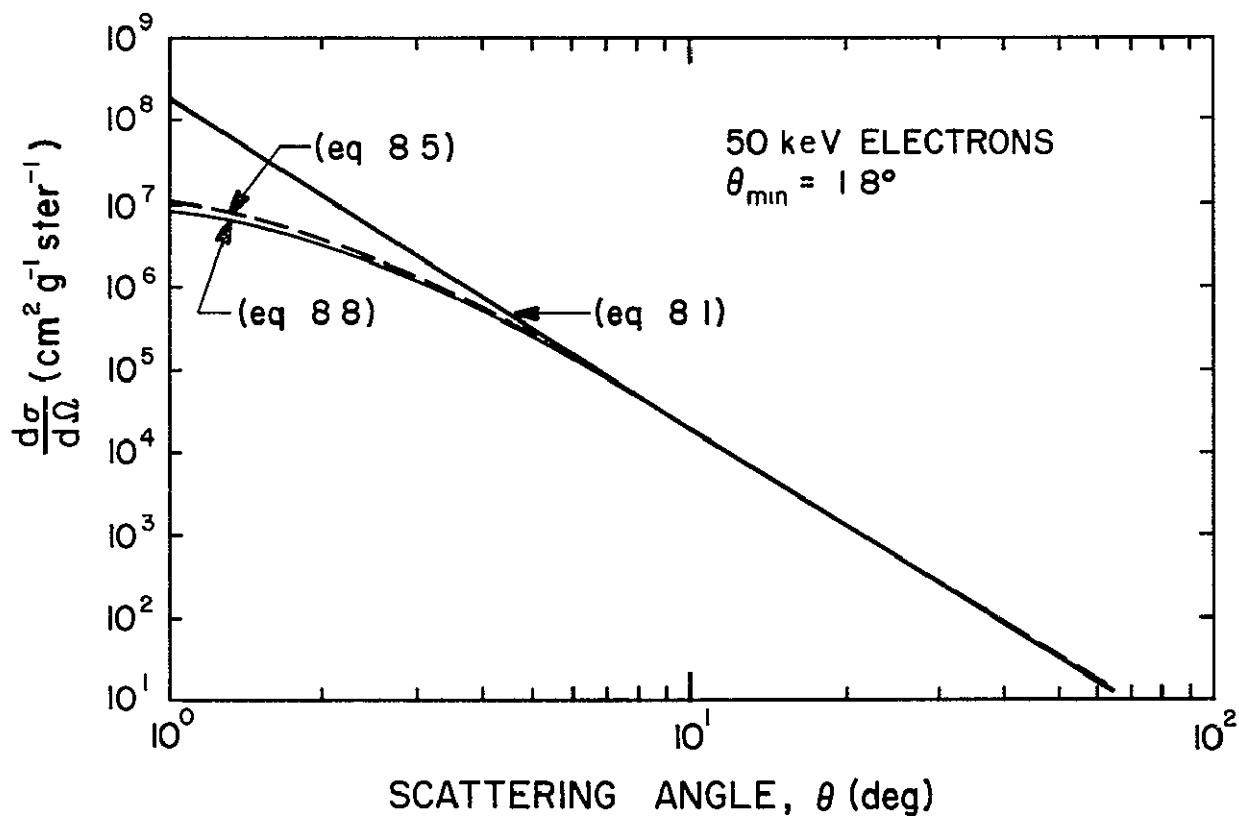
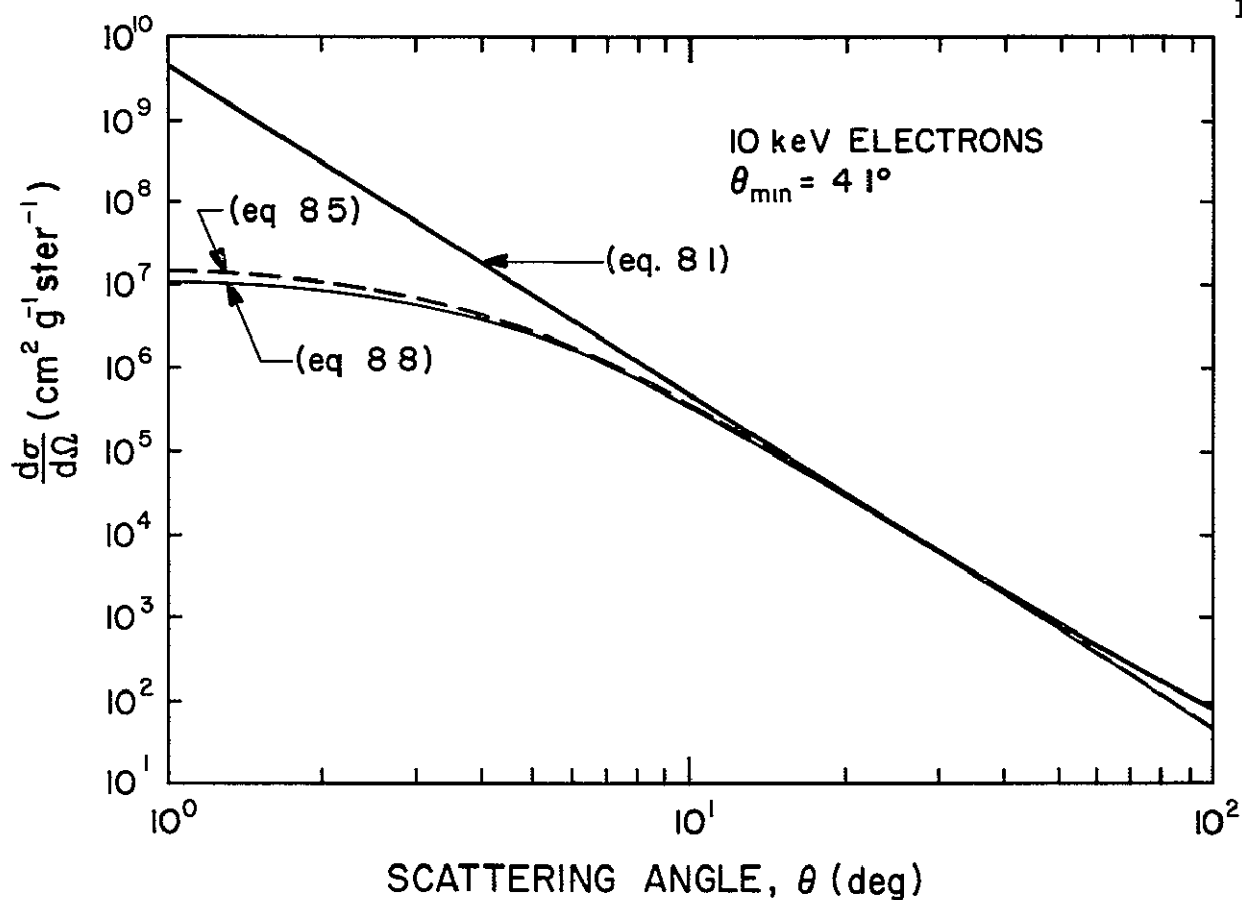


Figure 8.2 Comparison of differential scattering cross-section given by equations (8.1), (8.5) and (8.8), for 10 and 50 keV electrons.

$$- \frac{\cos[(4\pi e^2/hv) \ln \tan \theta]}{\sin^2 \theta \cos^2 \theta}$$

When the energy of the incident beam is much greater than the binding forces ( $4\pi e^2/hv \ll 1$ ), the numerator in this term may be replaced by unity, except at small angles ( $\theta < 10^\circ$ ). With some trigonometrical manipulation equation (8.11) becomes

$$d\sigma_{\text{elec}} = 16\pi r_o^2 \frac{1}{\beta^4} \left[ \frac{4-3\sin^2(2\theta)}{\sin^3(2\theta)} \right] \quad (8.12)$$

For the case of relativistic electron-electron collisions *Moller* [1932] has developed the following expression

$$d\sigma_{\text{Moller}} = 4\pi r_o^2 \frac{1}{\beta^4} \frac{\gamma+1}{\gamma^2} \left[ \frac{4}{(1-x^2)^2} - \frac{3}{1-x^2} + \frac{(\gamma-1)^2}{4\gamma^2} \left( 1 + \frac{4}{1-x^2} \right) dx \right] \quad (8.13)$$

where  $x = [2-(\gamma+3) \sin^2 \theta] / [2+(\gamma-1) \sin^2 \theta]$  and  $\gamma = (1-v^2/c^2)^{-0.5}$ . Equation (8.13) reduces to equation (8.10) as  $\gamma \rightarrow 1$ , i.e., for non-relativistic electrons. The correction is less than 10% for electron energies less than 70 keV.

8.1.3 *Combined elastic and inelastic scattering.* Since there are  $Z$  electrons per atom, the combined elastic and inelastic process may be given as

$$d\sigma(\theta) = [d\sigma_{\text{Ruth}} q(\theta) R(\theta) + Z d\sigma_{\text{elec}}] \frac{N_o}{A} \quad (8.14)$$

where  $d\sigma_{\text{elec}}$  is to be replaced by  $d\sigma_{\text{Moller}}$  for energies greater than 70 keV. The total collision cross section becomes

$$\sigma_T = \int_0^\pi d\sigma(\theta) = \frac{1}{\lambda_p} \quad (8.15)$$

where  $\lambda_p$  is the electron mean free path.

*Maeda* [1962] gives an alternative expression for the total cross section

$$\sigma_T = 4\pi \alpha_o^2 Z(Z+1) \frac{1}{\beta^2} \left( \frac{m}{P \theta_{\min}} \right)^2 + \frac{4\pi \alpha_o^2 Z}{\beta^2} f_1 \left( \frac{P}{mc} \right) \quad (8.16)$$

where

$$f_1\left(\frac{P}{mc}\right) = \left[1 - \left(\frac{mc}{P}\right)^2\right] \frac{1}{\theta_{\min}^2} - \frac{Z}{4} \left(\frac{P}{mc}\right)^2 + \ln \theta_{\min} - 1 \quad (8.17)$$

Assuming  $\alpha_0 = 2.8 \times 10^{-11}$  cm,  $Z = 7.4$  and  $1/\theta_{\min} = 50.4 P/mc$ , equations (8.16) and (8.17) become

$$\sigma_T = \frac{1.6 \times 10^{-19}}{\beta^2} + \frac{7.4 \times 10^{-24}}{\beta^2} f_1\left(\frac{P}{mc}\right)$$

with

$$f_1\left(\frac{P}{mc}\right) = 2550 \left[ \left(\frac{P}{mc}\right)^2 - 1 \right] - \ln\left(\frac{P}{mc}\right)$$

Further detailed analysis of collision cross sections may be found by Wu [1960], Maehlum [1973], Maeda [1962] and Wedde [1970].

## 8.2 Energy Loss by Particle Precipitation: Ionization, Excitation and Heating

This section will study the theoretical and experimental methods used to determine energy loss in the atmosphere by ionization, excitation and heating. Electromagnetic energy loss mechanisms (i.e., Bremsstrahlung, Cherenkov, and optical radiations) contribute only slightly to the total energy loss process and therefore will not be considered.

8.2.1 *Introduction.* As an energetic electron interacts with the atmospheric constituents, a number of possible energy loss processes are possible. On the average, however, the most important ionization reaction is



where  $e'$  represents the energetic electron and  $e$  a photoelectron.

For nitrogen the first ionization energy is 14.5 eV. However, Valentine and Curran [1958] have found that, on the average, 35 eV is expended per ion

pair formed by a beam of fast electrons and thus nearly half of the initial energy goes into ion excitations and thermal velocity increases. Approximately 10 to 20% ( $\approx 5$  eV) is directly transferred into thermal energy [Omholt, 1973]. The rest of the energy is stored in excited ionic states. For example 2%, 0.7% and 0.2% are stored in the 0-0, 0-1 and 0-2 bands, respectively, of the first negative system of molecular nitrogen.

As the initial particle energy is reduced to about 7 eV, the predominant energy loss mechanism is vibrational excitation of molecular nitrogen. The last few electron volts, on the average, are lost to ambient electrons by elastic collisions and hence increase  $T_e$  (producing the effects described in Section 5.5)

Other loss mechanisms contribute to heating of the electron gas.

Dalgarno *et al.* [1963] state that the rate of loss of energy,  $E$  in eV, given to the ambient thermal electron gas is

$$\frac{dE}{dx} = - \frac{2 \times 10^{-12}}{E} n_e \text{ eV cm}^{-1} \quad (8.19)$$

where  $x$  is distance in cm and  $n_e$  is the ambient electron number density in  $\text{cm}^{-3}$ . The energy loss rate in exciting atomic O(1S) is given by

$$\frac{dE}{dx} = -2 \times 10^{-17} n(O) \text{ eV cm}^{-1} \quad (8.20)$$

where  $n(O)$  is the oxygen number density.

Ultimately, all the energy deposited in the atmosphere becomes thermalized. Most of this energy is lost through collisional transfer with atmospheric atoms and molecules and some is lost by dissociative recombination or is radiated away as electromagnetic radiation.

8.2.2 *Electron energy loss rate in air.* Various theoretical studies have been made of the energy loss rate of electrons in air. Assuming the kinetic energy of an electron is sufficiently high, ( $> 1$  keV), Heitler [1954]



has found the energy loss rate to be given by

$$\frac{dE}{dx} = - \frac{N}{\cos \alpha} Z Q_o \frac{3\mu^2}{4E} \left( \ln \frac{E}{IZ\sqrt{2}} + \frac{1}{2} \right) \quad (8.21)$$

where  $E$  is the kinetic energy (ergs),  $Z$  is the average atomic number of air ( $\approx 7.2$ ),  $Q_o$  is the Thomson scattering cross section ( $6.65 \times 10^{-25} \text{ cm}^2$ ),  $\mu$  is the rest mass of an electron ( $9.11 \times 10^{-31} \text{ kg}$ ),  $I$  is the average ionization energy of air,  $\alpha$  is the pitch angle and  $N$  is the number density of air molecules.

Heitler's formula has been used extensively by *Kamiyama* [1966] and is used in some of the calculations presented in Section 9.1. Integration of this equation from  $x_j$  to  $x_{j+1}$  gives

$$E_{j+1}^2 = E_j^2 - \frac{3}{2} Z Q_o \mu^2 \left( \ln \frac{E_j}{IZ\sqrt{2}} + \frac{1}{2} \right) \frac{1}{\cos \alpha} \int_{x_j}^{x_{j+1}} N(x) dx \quad (8.22)$$

where  $x$  is measured along the field line and the assumption is made that the expression in parentheses changes very little for energies of interest.

*Bethe* [1930] has developed a more general formula for the relativistic case of electron energy loss in air. He finds

$$\frac{dE}{dx} = - \frac{2\pi e^4 Z}{m_o v^2} \frac{N_o}{A} \left[ \ln \left[ \frac{m_o v^2 E}{2I^2(1-\beta^2)} \right] - (2\sqrt{1-\beta^2} - 1 + \beta^2) \ln 2 + \frac{1}{8}(1-\sqrt{1-\beta^2})^2 \right]$$

This energy loss relation is used by *Wedde* [1970] and *Stadsnes and Maehlum* [1965].

A totally different approach to calculating energy loss rate uses experimental data on energy loss by electrons in air. The experimental relation provides a very simple mathematical formulation and is

consequently amenable to subsequent analytic use. The experimental energy loss rate takes into account the scattering effects. As determined by *Grun* [1957] the energy loss rate is

$$\frac{dE}{dR} = -AE^{-m} \quad (E \text{ in keV}) \quad (8.24)$$

where  $A = 1.25 \times 10^4$  and  $m = 0.75$  for electrons over the energy range 4 keV to 100 keV and  $R$  is given in units of  $\text{cm}^2 \text{g}^{-1}$ . *Rees* [1963] has used this relation to compute energy loss and ionization profiles with altitude. This relation is also used for some of the ionization calculations in Chapter 9.

Equations (8.21), (8.23) and (8.24) are compared in Figure 8.3. These energy loss calculations show considerable difference, in part due to the inclusion of scattering effects in the experimental data of *Grun* [1957]. The use of various theoretical models requires careful justification of the basic assumptions made. Further refinements in the energy loss calculations are necessary.

An important consideration for understanding the energy loss of a gyrating particle in the earth's upper atmosphere is the effect of atmospheric scattering. For the case of few sequential scattering events (i.e., plural scattering) the analysis is very complicated. As the number of scattering events increases a diffusion (i.e., multiple scattering) formulation is possible and the mathematics can be greatly simplified. For a particle which has over a hundred scattering encounters the angular distribution is no longer characterized by a simple Gaussian but has the form of  $\cos^2 \theta$  with a mean scattering angle of  $33^\circ$  for all subsequent collisions [*Wu*, 1960]. This section looks at the multiple scattering case to gain an understanding of the processes involved.

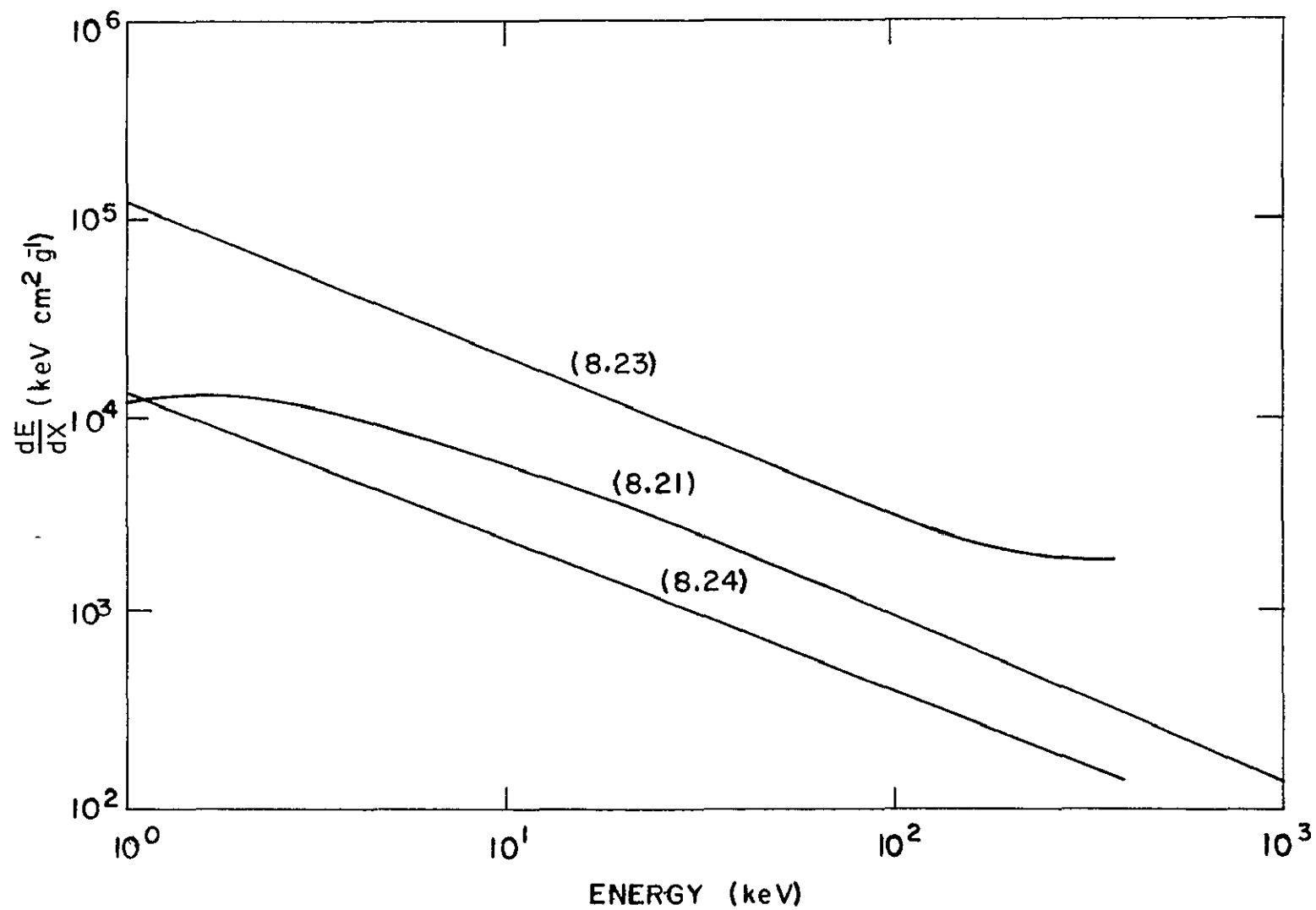


Figure 8.3 The energy loss rate for electrons in air computed by three methods corresponding to equations (8.21), (8.23), and (8.24)

### 8.3 Basic Multiple Scattering Formulas.

The multiple scattering of energetic electrons with the atmosphere has been treated in detail by *Mott* [1929], *Williams* [1939], *Fermi* [1958] and *Wu* [1960]. The essentials as outlined by *Jackson* [1962] are given below

Since the collision cross sections are largest for small angles (Figure 8.2) multiple scattering is most significant for small angle deflections. The angle,  $\theta$ , which results after a large number of small-angle deflections symmetrically distributed about the incident direction can be related to the mean square angle of an individual collision where

$$\theta_{\text{rms}} = \sqrt{\langle \theta^2 \rangle} = \frac{\int \theta^2 \frac{d\sigma}{d\Omega} d\Omega}{\int \frac{d\sigma}{d\Omega} d\Omega} \quad (8.25)$$

and the collision cross section  $d\sigma/d\Omega$  is given by equation (8.14), which is plotted in Figure 8.2.

For an approximate analysis the simplified cross section of equation (8.5) may be applied. For this case the limits of integration are values of the impact parameter  $b_{\text{min}}$  and  $b_{\text{max}}$ , where  $b$  is the distance between the interacting particles at closest approach if no deflection occurred. For the angular representation of equation (8.5) the limits would be  $\theta_{\text{min}}$  and  $\theta_{\text{max}}$  yielding the integrated solution of equation (8.25) as

$$\theta_{\text{rms}} = \sqrt{\langle \theta^2 \rangle} = 2\theta_{\text{min}}^2 \ln \left( \frac{\theta_{\text{max}}}{\theta_{\text{min}}} \right) \quad (8.26)$$

where  $\theta_{\text{min}}$  is the effective small angle cut-off due to electron cloud shielding (equation 8.6) and  $\theta_{\text{max}}$  is the effective large angle cutoff due to the finite size of the scattering nucleus. The assumption of sharp cut-offs at  $\theta_{\text{min}}$  and  $\theta_{\text{max}}$  corresponding to  $(b_{\text{min}}$  and  $b_{\text{max}})$  is not quite correct

However the logarithmic term considerably reduces the effect of this inaccuracy.

The angle  $\theta_{\max}$  has the numerical value [Jackson, 1962]

$$\theta_{\max} = \frac{274}{A^{1/3}} \left( \frac{mc}{P} \right) \quad (8.27)$$

where  $A$  is the total number of nucleons in the nucleus. For air  $A = 29$  and  $\theta_{\max} = 90/\beta$  and consequently  $\theta_{\max}$  is nearly  $180^\circ$ .

The root-mean-square angle for a single scattering event is  $6.2^\circ$  from equation (8.26), using  $\theta_{\min} = 2.1^\circ$  (equation 8.6) and  $\theta_{\max} = 180^\circ$ . Since each collision is an independent event, the central-limit theorem of statistics shows that for a large number of collisions,  $p$ , the final distribution is approximately Gaussian about the forward direction with a mean square angle,  $\langle \theta^2 \rangle$ , given by

$$\langle \theta^2 \rangle = p \langle \theta^2 \rangle = 2p \theta_{\min}^2 \left[ \ln \frac{\theta_{\max}}{\theta_{\min}} \right] \quad (8.28)$$

where  $p$  is the total number of collisions. For  $\theta_{\text{rms}} = 6.2^\circ$  and  $p = 20$  collisions the angle  $\theta_{\text{rms}}$  is  $28^\circ$ . Increasing  $p$  to 50 collisions increases  $\theta_{\text{rms}}$  to  $44^\circ$ . A good approximation is  $\theta_{\text{rms}} = 3\theta_{\min} \sqrt{p}$  for multiple scattering.

The root-mean-square angular spread may be transformed into other useful units such as  $\sigma$  (the standard deviation), FWHM (the full width at half maximum) and HWHM (the half width at half maximum) using

$$\theta_{\text{rms}} = 2\sigma = 0.602 \text{ FWHM} = 1.2 \text{ HWHM} \quad (8.29)$$

The total number of collisions  $p$  which occur when an energetic electron travels a distance  $x$  in a medium may be obtained from equations (8.28), (8.26), (8.9), (8.6) and is

$$p = N\sigma_T x = 8\pi N x Z^2 r_o^2 \frac{1}{\beta^4} \ln \left[ \frac{\alpha_o \beta^2}{2Z^{4/3} r_o} \right] \quad (8.30)$$

where  $N$  is the number of atoms per unit volume,  $r_o = 2.82 \times 10^{-13}$  cm,  $Z$  is the average atomic number of air (7.2),  $\alpha_o = 0.53 \times 10^{-8}$  cm (the Bohr radius) and  $\beta = v/c$  (the ratio of velocity to the speed of light). Solving equation (8.30) numerically and using equation (8.26), the angle  $\theta_{\text{rms}}$  for a large number of scatterings is found to be

$$\theta_{\text{rms}} = \sqrt{p} \quad \theta_{\text{rms}} = \frac{2000}{E} \sqrt{Px} \quad (8.31)$$

where  $E$  is the energy (keV),  $P$  is the pressure (atmospheres),  $x$  is the distance traveled (cm) and  $\theta_{\text{rms}}$  is measured in degrees. This equation shows, for example, that a 50 keV electron will be deflected  $40^\circ$  (on average) in passing through 1 cm of air at STP.

For multiple scattering the resulting angular distribution  $P_n$  may be expressed as a Gaussian

$$P_n(\theta') = \frac{1}{\sqrt{\pi}\theta^2} \exp \left( -\frac{\theta'^2}{\theta^2} \right) d\theta' \quad (8.32)$$

where  $\theta'$  is the projected angle of a scattering event on the  $x$ - $y$  plane for an incident particle along the  $z$  direction.  $\theta'$  can be shown to be equal to  $(\frac{1}{2}\langle\theta^2\rangle)^{1/2}$  for small angles [Jackson, 1962].

The rms angle for scattering (equations 8.26 and 8.28) is proportional to  $Z$  and  $x$  and inversely proportional to the kinetic energy of the incident particle. Low  $Z$  gases such as hydrogen and helium (which dominate the exosphere) contribute proportionately less to scattering than do oxygen and nitrogen atoms. An additional observation is that an electron and a proton with the same energy will be scattered by the same amount, however, because

the energy loss rate is much greater for a proton than for an electron scattering is less important for protons in the atmosphere.

When the number of collisions per electron is about 100 (i.e.,  $x \gg 1/\sigma_T N$ ), saturation is established and the electron beam is completely diffused. The electron beam is no longer Gaussian but assumes the form of  $\cos^2 \theta$  with the maximum mean angle of scattering maintained at about  $33^\circ$  for all further increases in thickness [Wu, 1960].

The analysis of electron scattering is very complex and use must be made of several models to properly analyze the upper atmosphere (plural scattering, multiple scattering and complete diffusion). Williams [1939] notes for electron ( $\ll 1$  MeV) inconsistencies between multiple scattering experiments and theoretical treatments, the experiments indicate that scattering of electrons ( $\ll 1$  MeV) is much less than that predicted by theory. The many approximations and differing models warrant more study both theoretically and experimentally. Various quantitative studies for lower energy electrons have been developed using Monte Carlo simulation [Wedde, 1970; Maeda, 1965; Berger et al., 1970] and diffusion techniques [Walt et al., 1968, Strickland et al., 1976; Banks et al., 1970]. These will be discussed in Section 9.1. A new experimental study is reported on in the next section.

#### 8.4 *Experimental Study of Electron Scattering in Air*

The analysis of scattering by air of electrons with energies of a few keV is very complicated. The regions of plural scattering, multiple scattering and complete diffusion are all encountered for quasi-trapped particles in the upper atmosphere. The analysis of Section 8.3 is primarily useful for energies  $\gg 100$  keV and for an understanding of the functional dependence of the variables.

Some of the approximations are, however, not strictly justified at low

pressures and energies [Williams, 1939]. The basic equations of scattering are consequently often misinterpreted and misused when applied to lower energies as in studies of auroras. For example, the form of the scattering distribution may vary considerably from Gaussian and change shape dramatically with atmospheric depth. The simplified analysis also leads to extremely large multiple scattering angles which are not in agreement with the small angular spread observed in auroras. To eliminate many of these approximations and to understand firsthand the electron interaction an experimental study was pursued.

This section will report on an experimental apparatus using a linear accelerator to study electron scattering in air. The results will be used to develop a more accurate picture of the transitional regions of plural and multiple scattering in the calculation of ionization rates in the atmosphere

8.4.1 *Experimental arrangement.* A diagram of the experiment is shown in Figure 8.4. Energetic electrons (10 to 100 keV) from an electric field accelerator are focused into a narrow beam and directed through three vacuum chambers separated by two small diaphragms. Each chamber has a vacuum pump attached such that there is a sufficient pressure drop from 10 torr to  $10^{-4}$  torr between the final test chamber and the accelerating electrodes (to prevent breakdown at the accelerator). The two diaphragms have diameters of 0.4 and 0.6 mm respectively. Two steering magnets are used to guide the beam through the diaphragms and into the test chamber for analysis. A solid state detector is mounted on a platform which can be rotated to give scattering data and energy degradation as the pressure in the test chamber is varied. The principal detector is located 21.5 cm behind the diaphragm. Two photographs of the equipment are shown in Figure 8.5.

The pressure is measured with a mercury manometer and two electronic



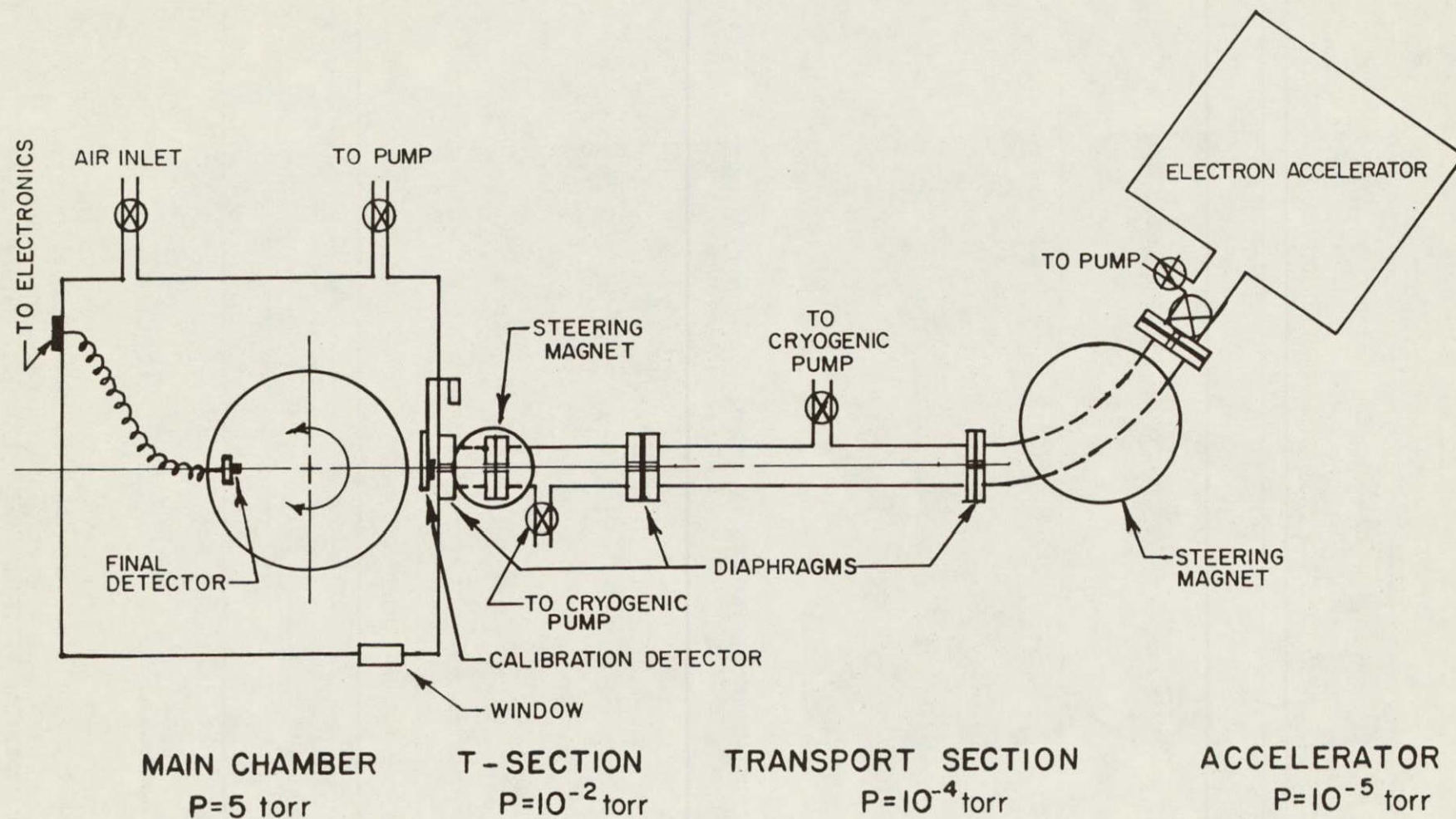


Figure 8.4 Block diagram of the experimental apparatus used to measure the scattering of electrons in air.

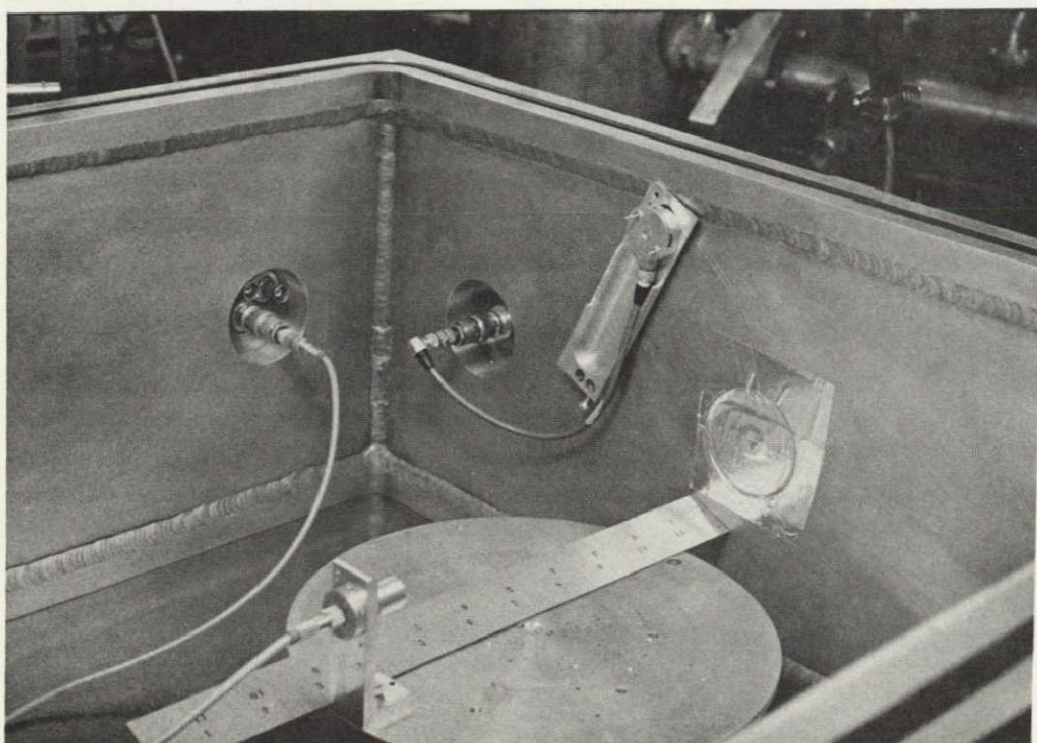
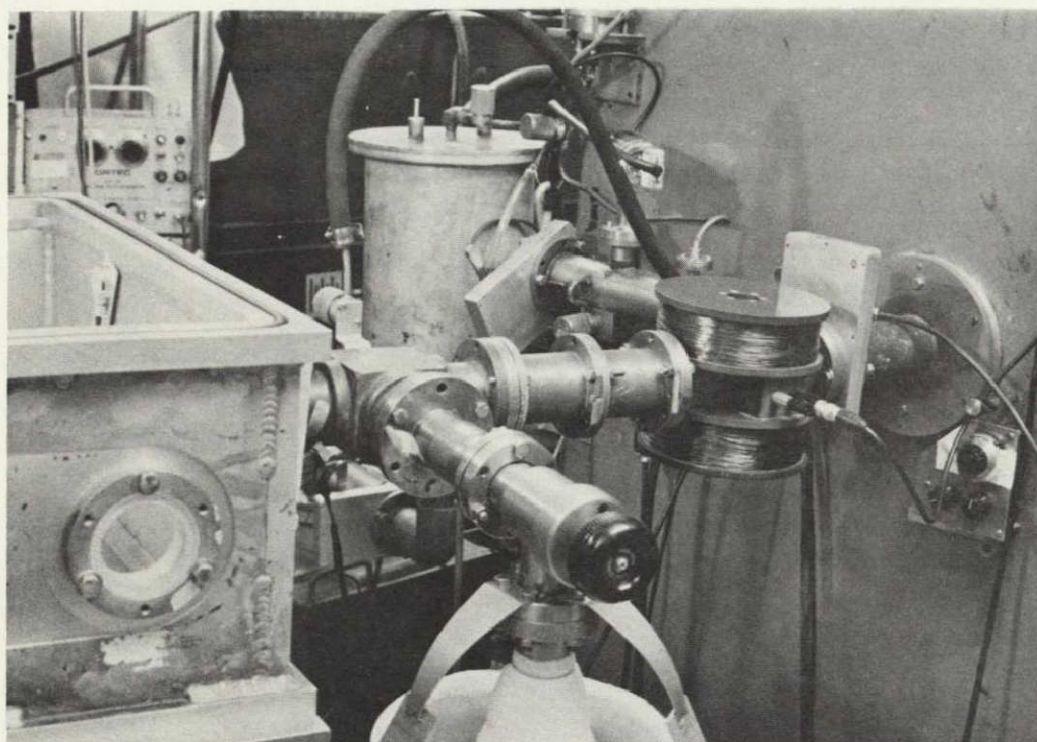


Figure 8.5 The beam transport section with the T mount and steering magnet is shown in the upper photograph and the vacuum chamber, rotating platform, and solid-state detectors are shown in the lower photograph.

ORIGINAL PAGE IS  
OF POOR QUALITY



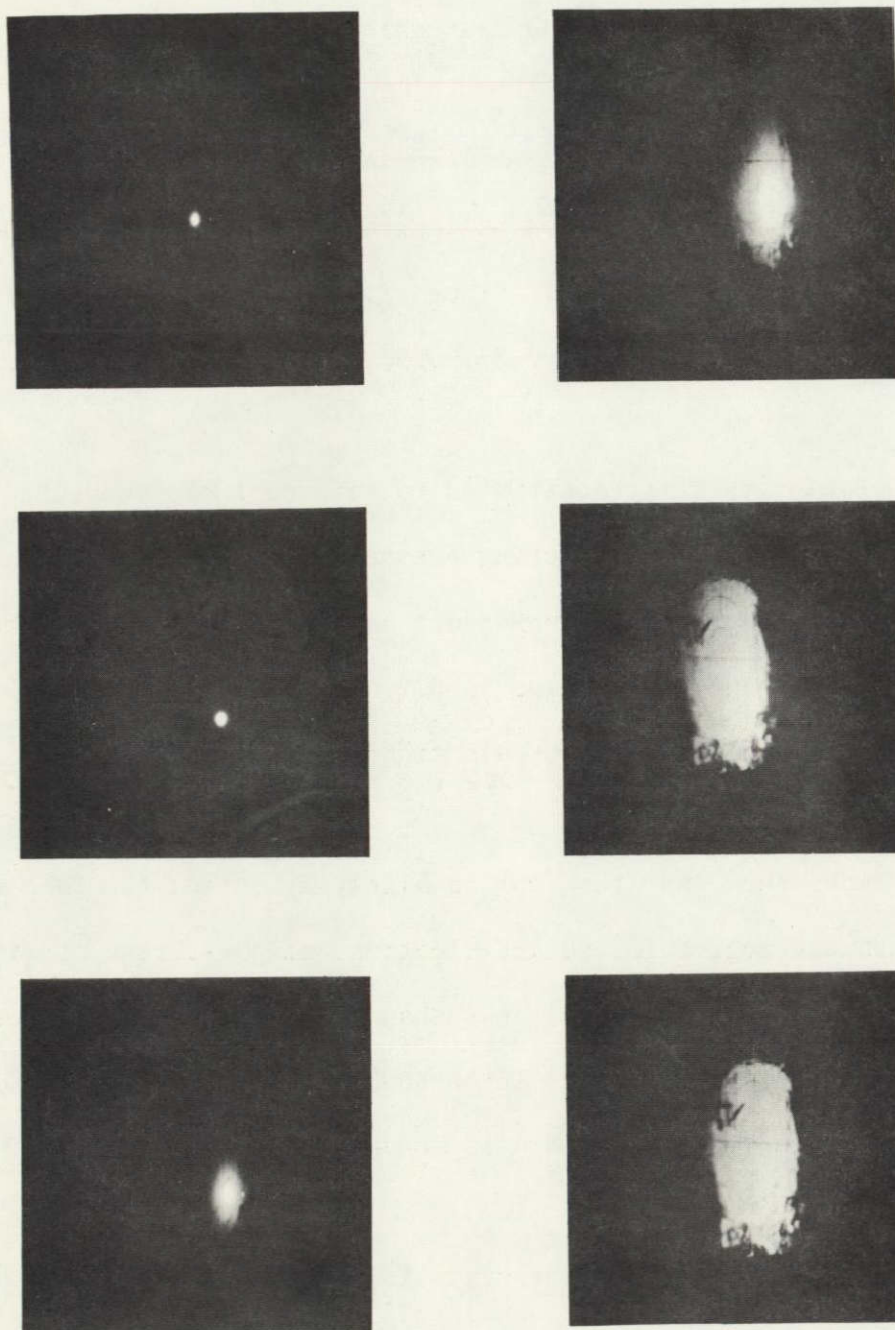
pressure gauges. Under vacuum conditions the angular diameter of the beam is less than  $0.3^\circ$  with a typical flux of  $10^3 \text{ s}^{-1}$ . A calibration detector on a moveable arm is located in front of the test chamber diaphragm and is used to monitor the incident flux.

8.4.2 *Experimental results of electron scattering.* The angular dispersion of the beam may be visually recorded by looking through the side window of the test chamber at a phosphor plate. Figure 8.6 shows photographs of the phosphor plate with pressures of 0, 0.37, 0.7, 1, 2 and 5 torr in the chambers.

The particle detector is first positioned to intercept the complete pencil beam at zero pressure. For differing pressures the platform on which the detector is mounted is rotated in increments of  $0.1^\circ$  near the peak and at larger intervals away from the peak. Figures 8.7 and 8.8 show two representative distributions for 30 and 50 keV electrons at chamber pressures of 0.005, 0.5, 1, 2, 4 and 7 torr.

These distributions show that the flux is highly directed; the FWHM of the beam is less than one degree for 50 keV electrons at pressures less than about 2 torr and for 30 keV at pressures less than 1 torr. At higher pressures the central peak rapidly decreases into the broader distributions of the skirts. For 30 keV the initial beam width is somewhat larger than the 50 keV case due to space charge spreading.

The beam width (HWHM) in these experiments is plotted in Figure 8.9 versus the product atm-cm. For a 50 keV electron beam which travels through 0.2 cm of air at 1 atmosphere the angular spread (HWHM) is about 4 degrees. Also plotted on this figure are theoretical curves (equation 8.31) for electron scattering [Hess, 1968; Tuohy and Harries, 1973; Fermi, 1958; Wu, 1960]. The theoretical results differ strikingly from the experimental results and



ORIGINAL PAGE IS  
OF POOR QUALITY

Figure 8.6 The angular spreading of the electron beam may be seen by looking through the side window of the test chamber at a phosphor plate. Chamber pressures are 0, 0.37, 0.7, 1, 2, and 5 mm of mercury for the increasing diameters in the photographs shown. The ellipsoidal shape is due to the off-axis viewing angle.

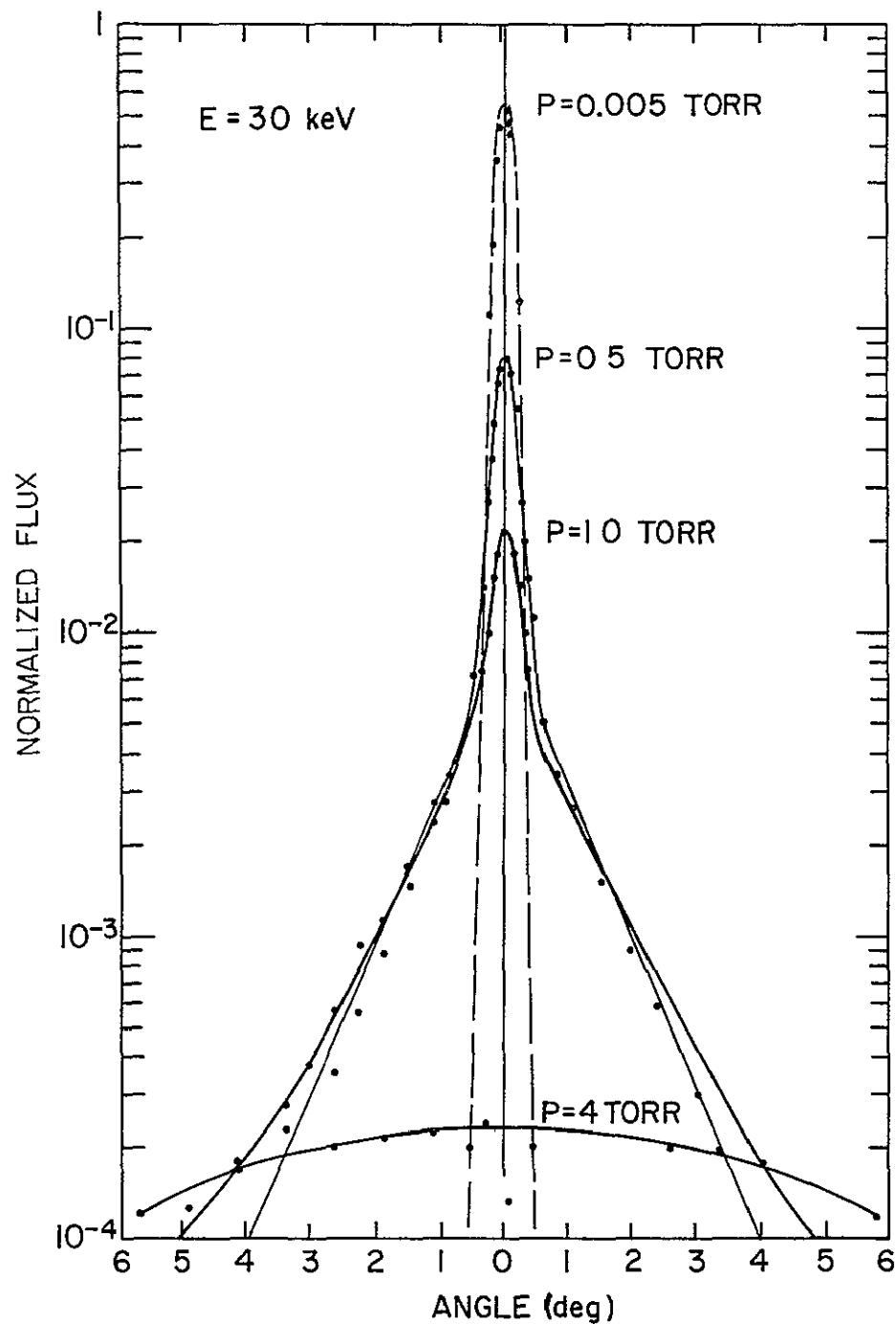


Figure 8.7 Experimental results for 30 keV electrons scattering in air at different pressures

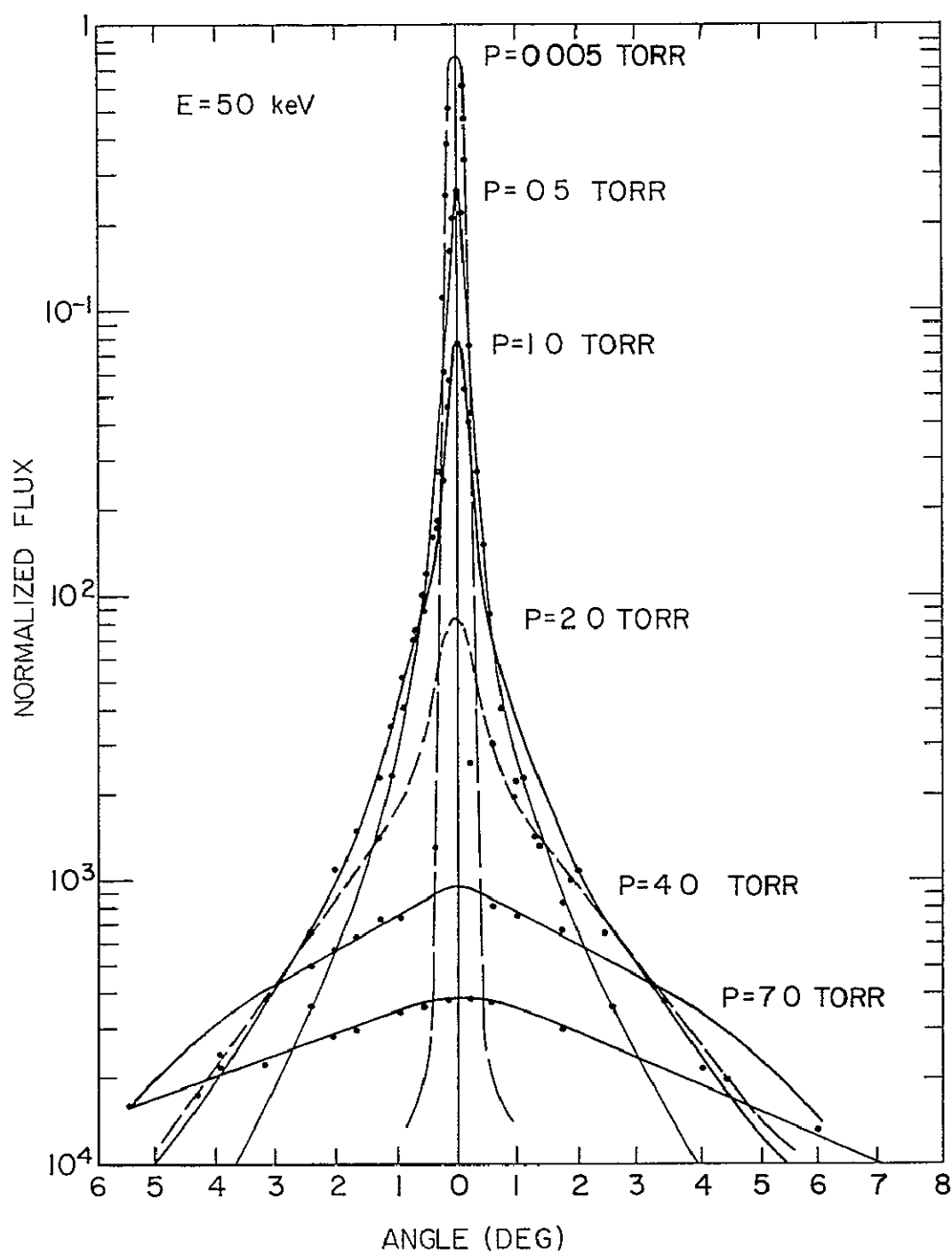


Figure 8.8 Experimental results for 50 keV electrons scattering in air at different pressures

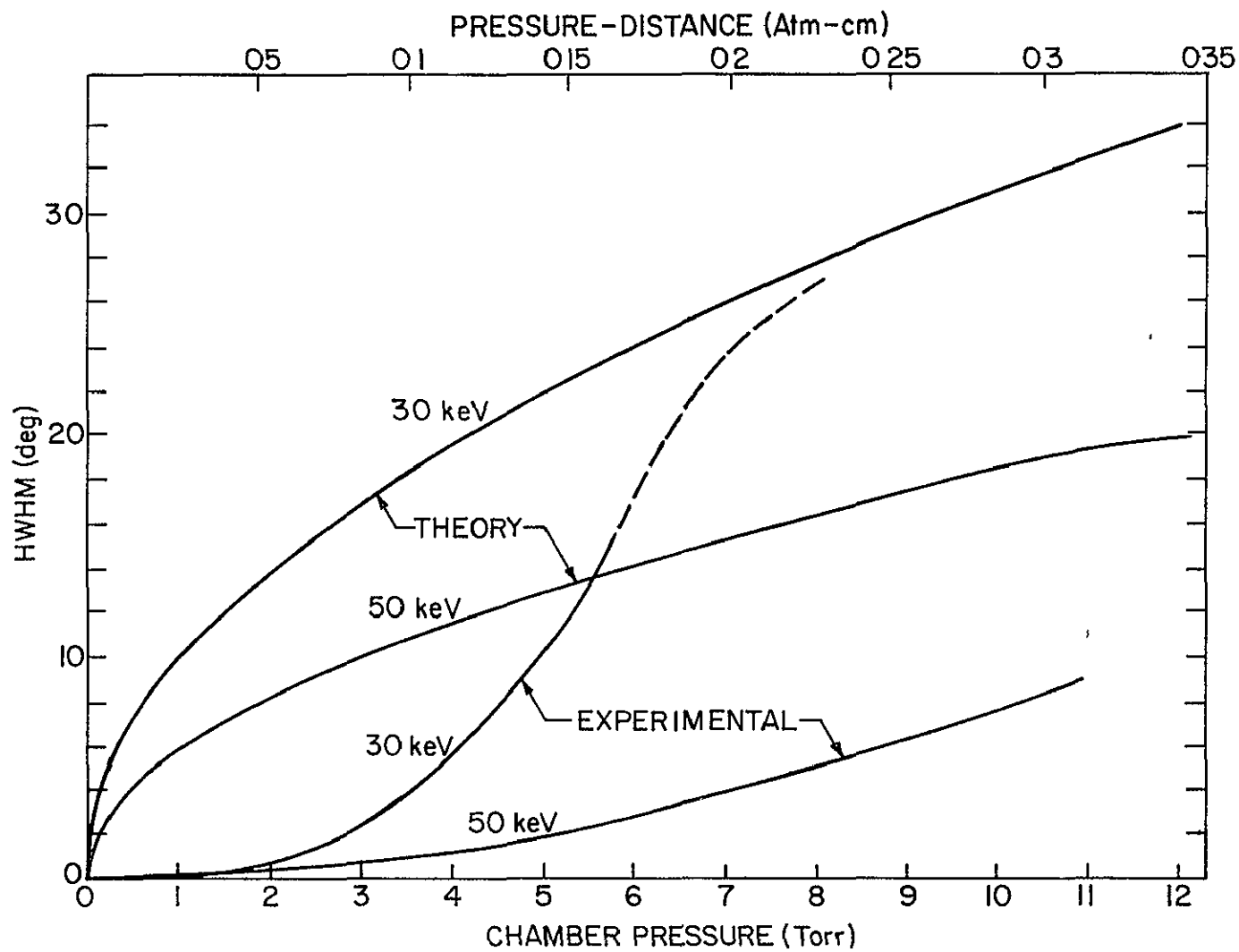


Figure 8 9 Comparison between calculated and experimental spreading of an electron beam in air. The method commonly used for approximation can be seen to differ significantly from the experimental results.

clearly show the disagreement with the scattering equation (8.31) at low values of pressure-distance. This range of values of pressure-distance in the figure is the primary region of interest for upper atmospheric studies and hence use will be made of the experimental curves in subsequent discussions. Further theoretical studies are required to explain the scattering of electrons of these energies at low pressures.

8.4.3 *Observations of electron energy loss in air.* The energy loss is also monitored as a function of chamber pressure and for various energies and pulse-height energy spectrums were made. Typical results are shown in Figure 8.10 for 50 keV electrons. The upper photograph is for zero chamber pressure and shows a Gaussian distribution centered about the dotted line. The Gaussian distribution is due to preamplifier noise. The lower photograph is for a pressure of 6 torr (0.17 atm-cm) and the energy loss is evident in the displacement of the Gaussian to lower energies. According to the energy loss equation (8.25), this behavior is expected. The average energy lost by 50 keV electrons in traversing 0.17 atm-cm is 1 keV. This is approximately the displacement which is observed.

### 8.5 *Scattering Influence on the Pitch-Angle Distribution*

As gyrating energetic electrons intercept the atmosphere, they are scattered randomly and lose energy. The path traced out by a beam of particles in a converging magnetic field is strongly dependent on the initial energy and initial pitch angle of the beam. For the case of mirroring an energetic particle will make many more collisions than for a particle with a small pitch angle over the same height range. For a mirroring particle most of the collisions occur when the pitch angle is near  $90^\circ$ .

In this section it is shown that the change in pitch angle due to collisions is smallest for a charged particle near its mirroring altitude.



ORIGINAL PAGE IS  
OF POOR QUALITY

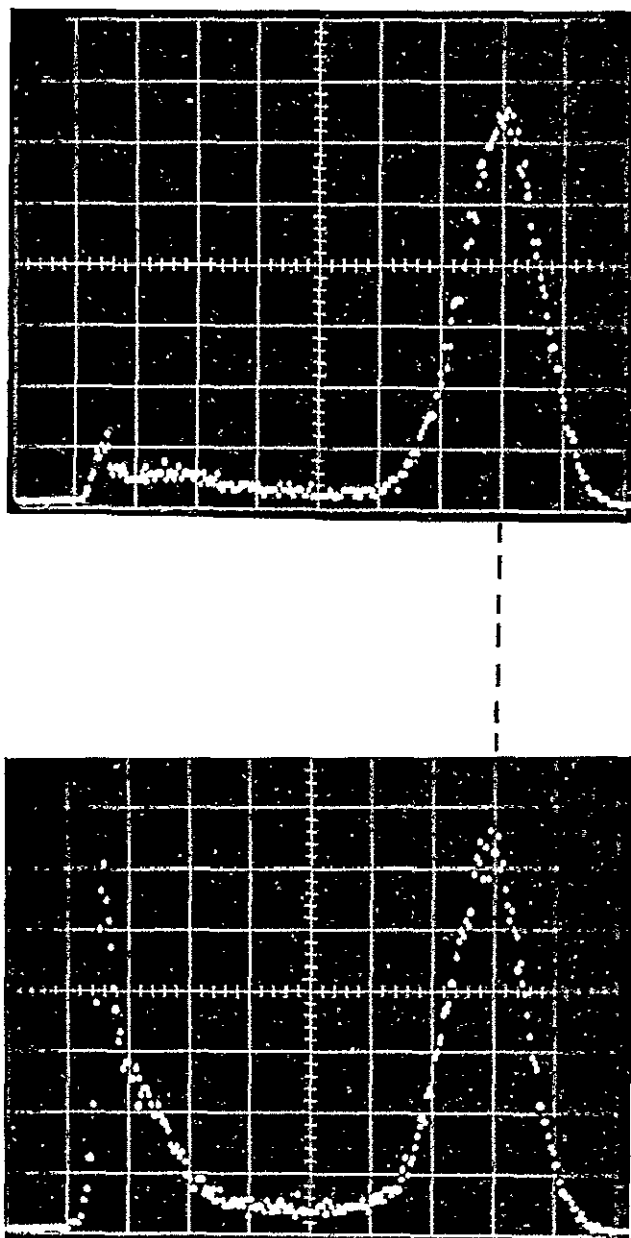


Figure 8.10 The upper figure is the pulse-height distribution for 50 keV electrons at essentially zero chamber pressure. The lower figure shows the slight displacement ( $\approx 1$  keV) of the profile to the left when the pressure is increased to 6 torr. The full width at half maximum for the distribution.

For a particle which mirrors at an altitude  $\alpha = z_m$ , the number of collisions,  $p$ , in each height interval above the mirror point may be found by using equation (3.21) and by assuming an exponential atmosphere approximation,  $N(z)$ , near the mirror height such that

$$p(\alpha) = \sigma_T N(z) \Delta s = \frac{\sigma_T N_m}{\sqrt{\alpha - z_m}} e^{-\alpha/H_m} \quad (8.33)$$

where  $H_m$  is the scale height at  $z_m$ ,  $N_m$  is the number density at  $z_m$  and  $\Delta s$  is the distance traveled by the mirroring particle as given by equation (3.18). Equation (8.33) is plotted in Figure 8.11 and shows that the greatest number of collisions occur near the mirroring altitude where the pitch angle is  $90^\circ$ .

The increase in the total number of collisions for a particle which mirrors as compared with a vertically incident particle may be obtained by integration of equation (3.18). The assumptions are made that the number of collisions is proportional to the atmospheric density and that the atmosphere is exponential with a scale height,  $H_m$ , measured at the mirroring altitude. Hence

$$P_H \propto N_H = N_m e^{-z'/H_m} \sqrt{\frac{R_o}{3z'}} dz \quad (8.34)$$

where  $P$  is the number of collisions,  $N_H$  is the helical or effective number density seen by a spiraling particle.  $N_m$  is the mirror height number density and  $z'$  is the altitude above the mirror height. The number of collisions for a vertically incident particle,  $p_V$ , is simply proportional to  $N_m H_m$  and therefore the ratio of  $p_H$  to  $p_V$  upon integration of equation (8.34) is

$$\frac{p_H}{p_V} = \frac{N_H}{N_V} = \frac{\pi R_o}{3 H_m} = 16 \quad (8.35)$$

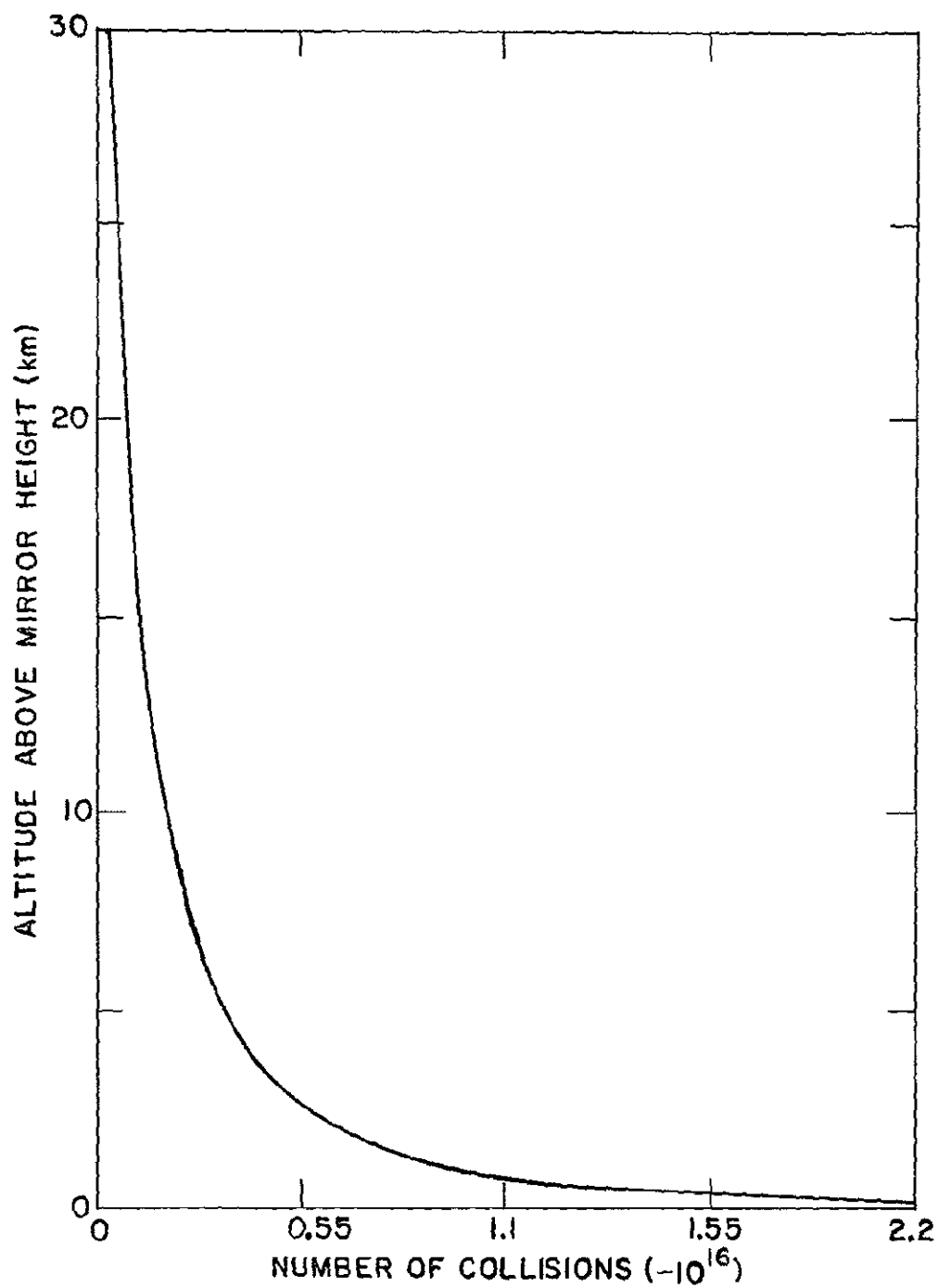


Figure 8.11 Plot of equation (8.34) which illustrates that most of the collision of an energetic particle with the atmospheric constituents occurs near the mirroring altitude. The effect of scattering is not included.

For an altitude of 140 km  $H_m$  is 27 km and the total number of collisions experienced by a particle down to its mirroring altitude is 16 times larger than the number of collisions for a vertically incident particle down to the same altitude.

The amount of atmosphere above 140 km is  $H_m N_m / N_o = 4.4 \times 10^{-3}$  atm-cm ( $N_o = 2.55 \times 10^{19} \text{ cm}^{-3}$ ); hence, a vertically incident beam of 50 keV electrons will be deflected less than  $0.1^\circ$ . For the mirroring case the effective atmospheric depth would be  $16 \times 4.4 \times 10^{-3} = 0.07$  atm-cm and from Figure 8.9 the HWHM scattering angle is  $0.5^\circ$ . This corresponds to a HWHM spread in pitch angle at most of  $0.5^\circ$ . For 30 keV electrons the spread is  $15^\circ$ .

This scattering will cause a change in the mirror height according to the first adiabatic invariant. A plot of the reduction in mirror altitude versus change in pitch angle for scattering at the mirror altitude is shown in Figure 8.12. A  $4^\circ$  change in pitch angle will lower the mirror height by 10 km.

When a particle is scattered through an angle  $\theta$  from an initial pitch angle  $\alpha_1$  to a new pitch angle  $\alpha_2$ , the new pitch angle is not simply the addition  $\alpha_1 + \theta$  but is always less than this for pitch angles  $\alpha_1 \neq 0$  with maximum insensitivity at  $\alpha_1$  about  $90^\circ$  (i.e., near mirroring). The collision geometry is shown in Figure 8.13. The first pitch angle is given by

$$\cos \alpha_2 = \cos \alpha_1 \cos \theta + \sin \alpha_1 \sin \theta \cos A_Z \quad (8.36)$$

where  $\theta$  is the scattering angle,  $\alpha_1$  is the initial pitch angle and  $A_Z$  is the azimuthal angle referenced to the plane defined by the magnetic field and the initial velocity vector. Near  $\alpha_1 = 90^\circ$  the change in pitch angle is approximately 0.5 times the change in  $\theta$  and consequently reduces the influence of scattering.

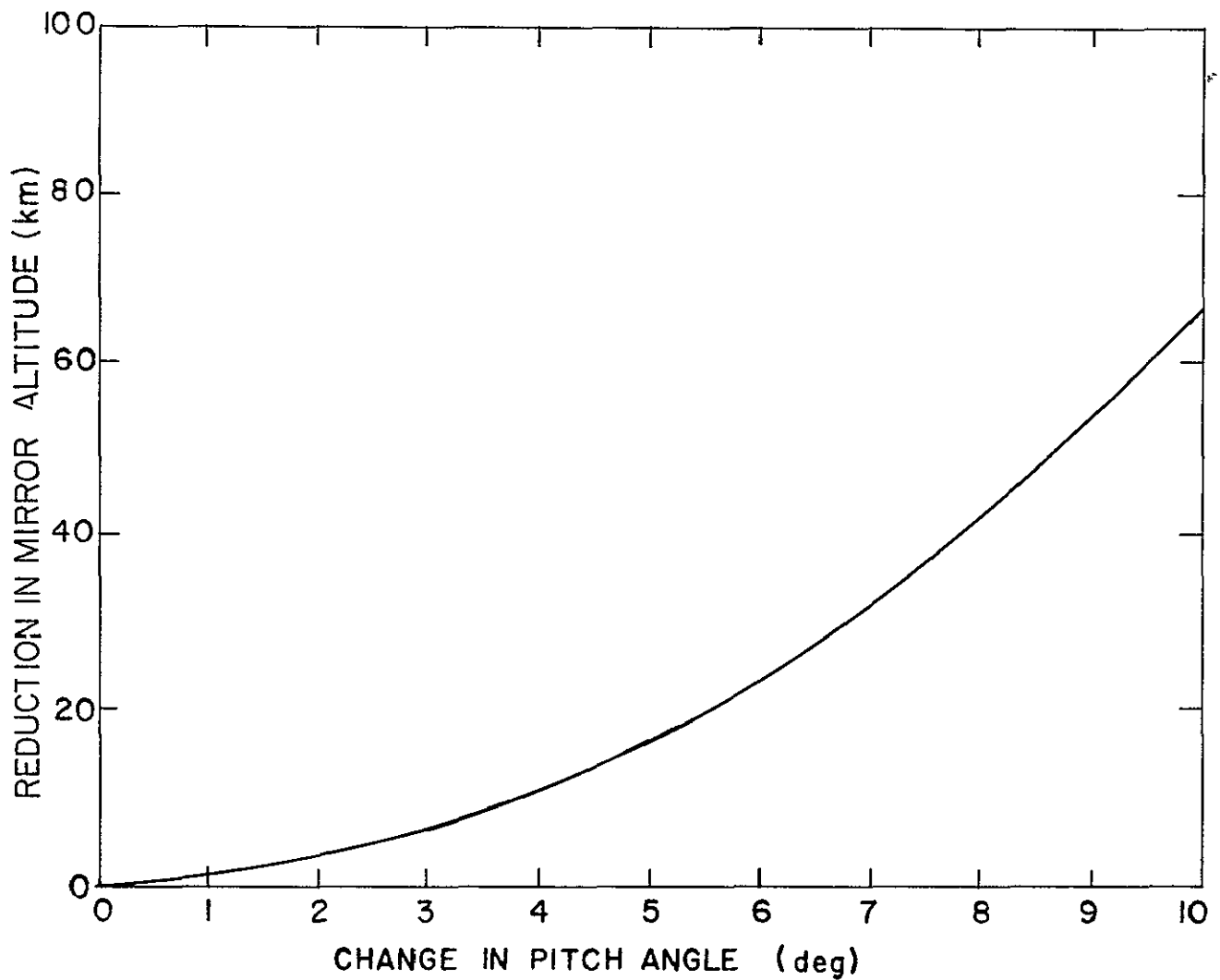


Figure 8 12 The reduction of mirror altitude caused by a change in pitch angle at the mirror altitude The reduction is least sensitive for small changes in pitch angle near the mirroring point

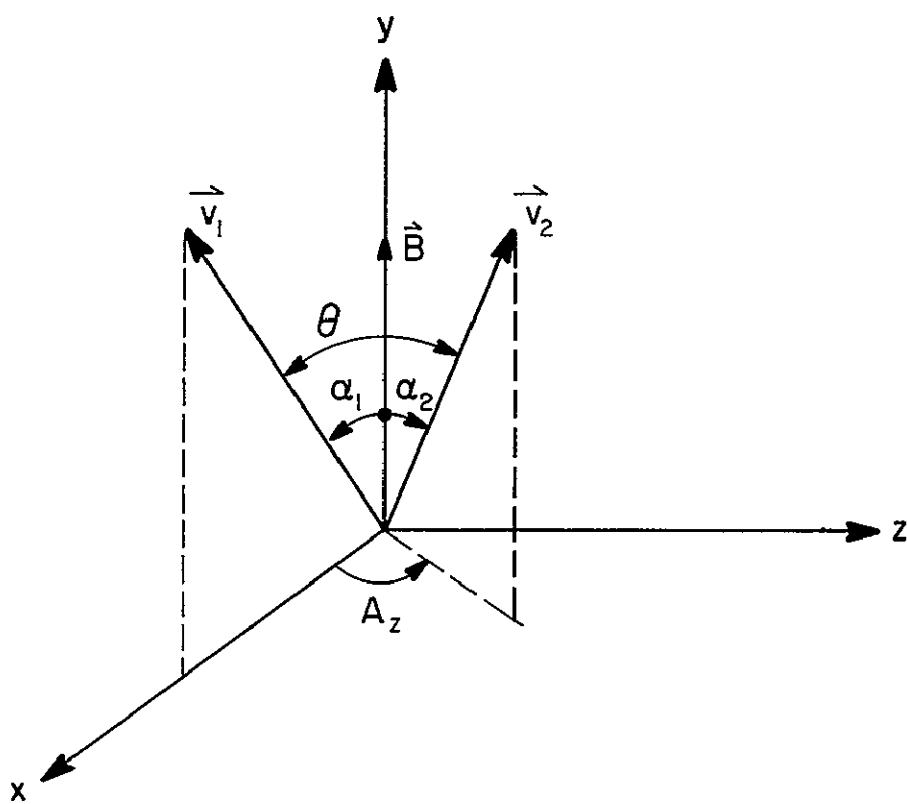


Figure 8 13 The change in pitch angle from  $\alpha_1$  to  $\alpha_2$  associated with a collision process having a scattering angle  $\theta$   $v_1$  and  $v_2$  are the initial and final velocities

The spreading of the mirror-height distribution by atmospheric scattering can be computed using the mirroring equation and assuming a Gaussian scattering distribution such that

$$f(Z_m) = \exp \left[ \frac{\left[ \frac{\pi}{2} - \sin^{-1} \left( \frac{6370+Z_m}{6370+Z_{mo}} \right)^{3/2} \right]^2}{2\sigma^2} \right] \quad (8.37)$$

where  $Z_{mo}$  is the original mirror height (in km). This function is plotted for various mirroring altitudes in Figure 8.14 with appropriate values of  $\sigma$  taken from the experimental scattering data of Figure 8.9.

The scattering plot shows that the transition between the dominance of mirror height reflection and atmospheric scattering occurs at a sharply defined altitude. For the energies under consideration ( $E > 20$  keV) the influence of scattering is small in the region 120 to 200 km, with increasing importance at lower altitude and for lower energy.

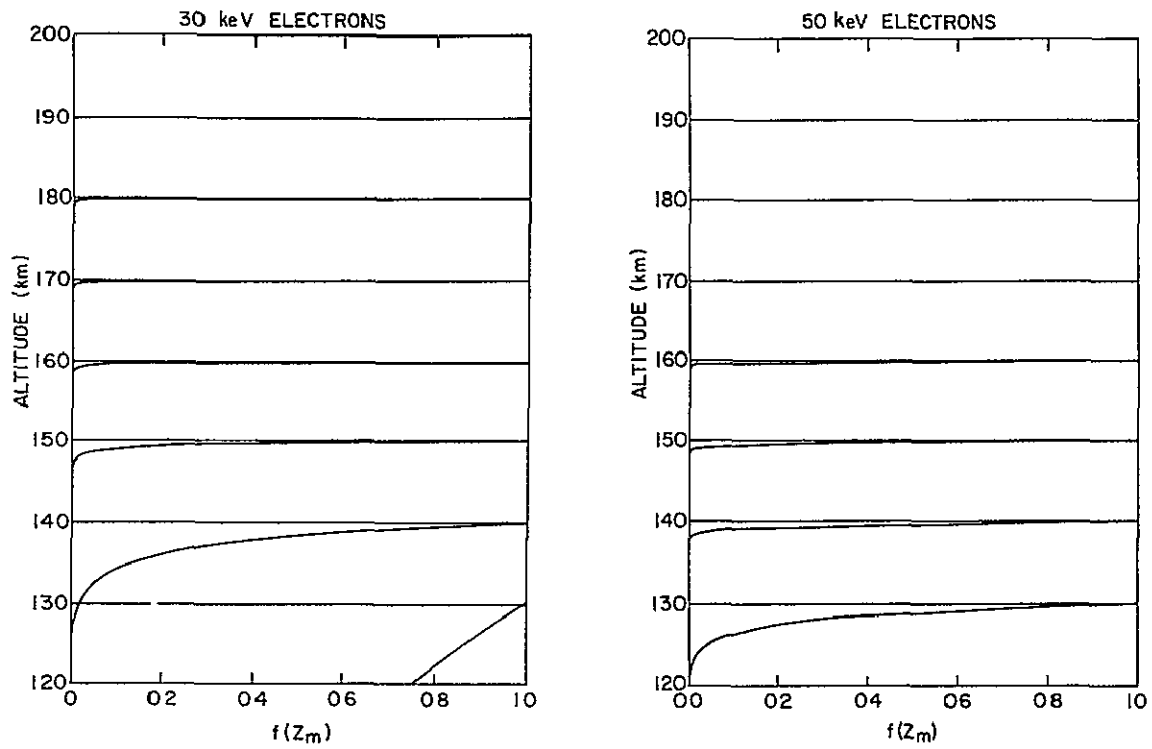


Figure 8.14 The spreading in mirror-height distributions due to atmospheric collisions for 30 and 50 keV electrons which, in the absence of collisions, would mirror at altitudes of 120, 130, . . . , 200 km



## 9. CALCULATION OF IONIZATION RATES FOR ENERGETIC PARTICLES

Various techniques are available to calculate the ionization rate produced by energetic particles interacting with the atmosphere. The choice of technique depends upon the accuracy desired and the properties of the initial flux distribution. Furthermore, the implicit assumptions in each of these techniques are crucial to accurately modeling the behavior of a typical midlatitude distribution of quasi-trapped particles. The magnetic field and pitch-angle distribution must be properly incorporated as must the effects of scattering.

The first part of this chapter will briefly review the various techniques which have been used to calculate the ionization rate, energy spectrum and pitch-angle distribution as a function of altitude. The second part will deal with the actual ionization rates calculated for various energy spectrums and pitch-angle distributions typical for midlatitude precipitation.

### 9.1 *Atmospheric Ionization by Electrons*

The purpose of this section is to consider the various techniques for computing the energy loss of electrons and protons and consequent ionization of the atmosphere. The assumptions, limitations and regions of applicability for each will be outlined as functions of the flux distribution and atmospheric depth. The ionization deposition rate calculations may be classified into empirical, Monte Carlo and Boltzmann equation methods according to the manner in which scattering is treated.

9.1.1 *Empirical methods.* The essence of the empirical methods is the use of the range-energy loss rate equation (8.22 or 8.25) to compute the energy loss in each height increment. The ionization rate is then obtained by dividing the energy loss by the average energy loss per collision (35 eV) to yield the number of ion-pairs produced. Examples of this type of

calculation may be found in *Rees* [1963], *Kamiyama* [1966], *Prasad and Singh* [1972], *Wulff and Gledhill* [1974] and *Smith and Voss* [1976]

The method used by Rees involves integration of the energy loss equation (8.24) over height increments,  $\Delta z_i$ , to give

$$\Delta E_i^{1.75} = 1.25 \times 10^7 \bar{\rho}_i (\cos \alpha) \Delta z_i \quad (9.1)$$

where  $E_i$  is the energy (keV),  $\alpha$  is the pitch angle and  $\bar{\rho}_i$  is the average atmospheric density in the  $i$ th height interval ( $\text{kg m}^{-3}$ ). The calculation is repeated for different energy spectrums and pitch angle distributions. In Rees' calculations the magnetic field is assumed vertical and non-convergent although, as will be discussed, this technique may be easily adapted for a dipole field model.

This method is very useful for quasi-isotropic distributions and quickly gives reasonably accurate ionization rate profile. The accuracy is compared to the more elaborate Monte Carlo analysis of *Wedde* [1970] in Figure 9.1. The agreement between these two calculations is very good for the conditions chosen.

The weakness of the empirical method is that the detailed effect of atmospheric scattering in changing the pitch angle is not taken into account. Thus it is not suitable for pitch-angle distributions which are sharply peaked and, to a lesser extent, peaked energy spectrums. Non-isotropic pitch-angle distributions may, however, be accurately investigated with the empirical technique for higher energies or higher altitudes where scattering is negligible.

9.1.2 *Monte Carlo simulation.* Computer simulation of the path followed by many individual particles according to their energy loss rate and differential scattering are the basis of the Monte Carlo technique. This method can include a number of extremely complex external forces, source

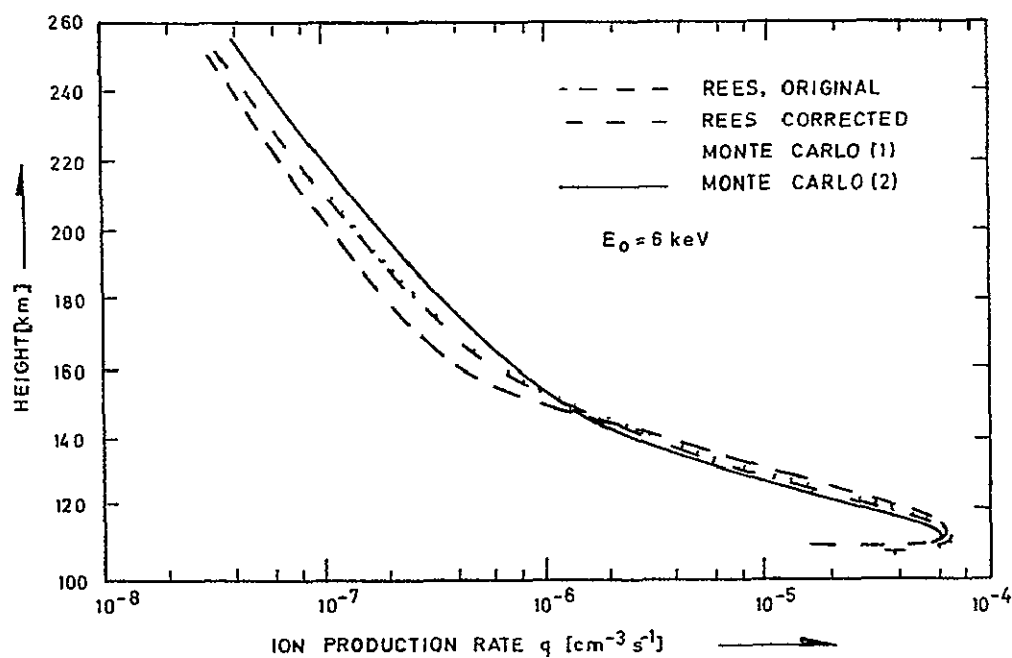


Figure 9.1 Comparison by *Wedde* [1970] of the Monte Carlo method and the empirical method of *Rees* [1963]. For the isotropic distributions chosen these two methods are in good agreement. The Rees Original and the Monte Carlo (1) are for an isotropic distribution between 0 and 80 deg pitch angle and the Rees Corrected and Monte Carlo (2) are for an isotropic distribution between 0 and 90 deg pitch angle.

distributions and perturbations or alterations in spatial or temporal profiles.

The path of a single particle is traced through the atmosphere by generating three random numbers which are related to the mean free path, azimuthal scattering angle and elevation scattering angle. The mean free path is  $l = -[\ln(1-l_R)]/\sigma_T$  where  $l_R$  is a random number between 0 and 1 and  $\sigma_T$  is the total cross section at energy  $E$ .

The azimuthal angle of a collision,  $A_z$ , is equally probable in any direction and hence  $A_z = 360 A_R$  (degrees) where  $A_R$  is a random number between 0 and 1. The elevation angle of a collision,  $\theta_e$ , is related to the differential scattering cross section by

$$\int_0^{\theta_e} E d\sigma = Q_R \sigma_T \quad (9.2)$$

where  $Q_R$  is a random number between 0 and 1 and  $d\sigma$  is the differential cross section. The three quantities  $l$ ,  $A_z$  and  $\theta_e$  specify the particle trajectory to the next collision and the process is then repeated until either the particle is absorbed or escapes the region of interest.

The solution found by the Monte Carlo technique is approximate and the error  $\delta$  is related to the number of trials,  $N$ , by

$$\delta = N^{-1/2} \quad (9.3)$$

Therefore, to increase the accuracy ten-fold, a hundred-fold increase in the number of trials is required.

The method is costly due to the required computer time and is therefore justified only for the most complex cases of source parameters or non-analytical boundary conditions. Monte Carlo studies have been pursued by *Maeda* [1965], *Stadsnes and Maehlum* [1965], *Berger et al.* [1970, 1974], *Cicerone and*

*Bowhill* [1971] and *Wedde* [1970]. These references should be consulted for further details of the method.

9.1.3 *Boltzmann equation methods.* The most sophisticated treatment of the ionization rate calculation is the use of the continuity equation where a diffusion term is used to include the effects of scattering. *MacDonald and Walt* [1961] and *Walt* [1968] developed a distribution function to describe the motion of magnetically confined electrons in a scattering atmosphere. A Fokker-Planck approximation was used and straggling effects of electron-electron collisions were ignored. Atmospheric scattering and magnetic field convergence are taken into account.

Since this method requires the numerical evaluation of derivatives, caution must be used in applying it to narrow pitch-angle distributions or energy spectrums. This method is believed to be accurate for energies down to approximately 3 keV and gives good agreement with other calculations of energy deposition.

*Strickland et al.* [1976] have developed a generalized equation of transfer which is applicable to energies as low as 10 eV and gives a good theoretical base to the multi-angle electron scattering and energy loss in the atmosphere. The basic equation of transfer may be obtained from the Boltzmann equation

$$\frac{\partial f}{\partial t}(\vec{r}, \vec{v}, t) + \vec{v} \cdot \nabla_{\vec{r}} f + \vec{a} \cdot \nabla_{\vec{v}} f = \left. \frac{\partial f}{\partial t} \right|_c \quad (9.4)$$

where  $f$  is the distribution function, in phase space, of  $\vec{r}$ ,  $\vec{v}$  and  $t$  the position, velocity and time coordinates respectively, and  $\partial f / \partial t|_c$  is a collision term. For steady-state conditions  $\partial f / \partial t = 0$ ,  $\vec{a} \cdot \nabla f = 0$  assuming no external force fields and  $\vec{v} \cdot \nabla_{\vec{r}} f = \mu v \partial f / \partial z$  where  $\mu$  is the cosine of the pitch angle

relative to the  $z$  axis

With these restraints the Boltzmann equation is transformed into the generalized equation of transfer using  $\phi = vf$  as the flux ( $\text{cm}^{-2} \text{ s}^{-1} \text{ eV}^{-1} \text{ ster}^{-1}$ ) and the spatial dimensions  $d\tau(E) \equiv n(z)\sigma_T(E)dz$  where  $n(z)$  is the density of scatterers. With these substitutions equation (9.4) becomes

$$\mu \frac{d\phi}{d\tau}(\tau, E, \mu) = -\phi(\tau, E, \mu) + \int \phi(\tau, E', \mu') \sum_z \frac{\sigma_z(\mu', \mu, E', E)}{\sigma_T(E)} dE' d\mu' \quad (9.5)$$

where the  $\sigma_z$  are the cross sections for elastic and inelastic scattering, and for ionization and loss processes. This general equation is solved by *Strickland et al* [1976] using matrix techniques and numerical analysis.

The basic Fokker-Planck equation can be derived from the equation of transfer by expanding equation (9.3) in a Taylor series to second order in  $\mu$  and to first order in  $E$  giving

$$\mu \frac{d\phi}{d\tau} = \frac{Q(E)}{2\sigma(E)} \frac{\partial}{\partial \mu} \left[ (1-\mu^2) \frac{\partial \phi}{\partial \mu} \right] + \frac{1}{\sigma_T(E)} \frac{\partial}{\partial E} [L(E)\phi] \quad (9.6)$$

where  $Q$  and  $L$  are the momentum transfer cross section and loss function, respectively. This is the Fokker-Planck equation solved by *Walt* [1967] who also added a magnetic mirroring term.

Making various additional assumptions in the equation of transfer, *Swartz* [1976] obtained analytical solutions for the upward and downward fluxes of particles. Further references may be made to papers by *Stolarski* [1968], *Banks and Nagy* [1970], *Nagy and Banks* [1970], *Cicerone et al.* [1973], *Walt* [1976] and *Swartz* [1976] for the various approximations and solutions to the Boltzmann equation method.

The theoretical methods provide the best overall solution for solving most cases of electron interaction with the atmosphere. They afford rather

simplified, understandable and accurate solutions to the problem of scattering.

## 9.2 *Ionization Rate for a Quasi-trapped Distribution of Energetic Electrons*

The purpose of this section is to calculate the expected ionization rate for the particle model developed in Chapter 7. The ionization rate depends strongly on the flux, pitch-angle distribution and energy spectrum and therefore previous attempts by others to model the midlatitude particle precipitation phenomena in terms of an isotropic pitch-angle distribution have failed. A more realistic pitch-angle distribution is one that is peaked near  $90^\circ$  resulting in a quasi-trapped flux which is more effective in ionizing the region between 120 and 200 km than is an isotropic distribution. The magnetic mirroring and particle backscattering explain why the count rate is observed to increase with altitude (130 to 200 km) for particles ( $E > 20$  keV) which are not being absorbed in this region (see Sections 4.1 and 6.2).

Some of the basic requirements of an ionization model will first be discussed. A program is then described for computing the ionization rates as a function of altitude for a pitch-angle distribution representative of quasi-trapped particles. In subsequent sections ionization rate calculations at discrete energies and for various energy spectrums will be made. Finally, these concepts and calculations are extended to realistic flux measurements made by rockets to obtain ionization rates over the region of interest.

9.2.1 *Energy considerations.* A straightforward calculation can be made of the average ionization rate in a region of space by simply measuring the energy spectrum and flux of particles entering and leaving the region (Figure 9.2a). For the particular case of a vertical column extending from 120 to 200 km the net energy influx must be equal to the average ion-pair

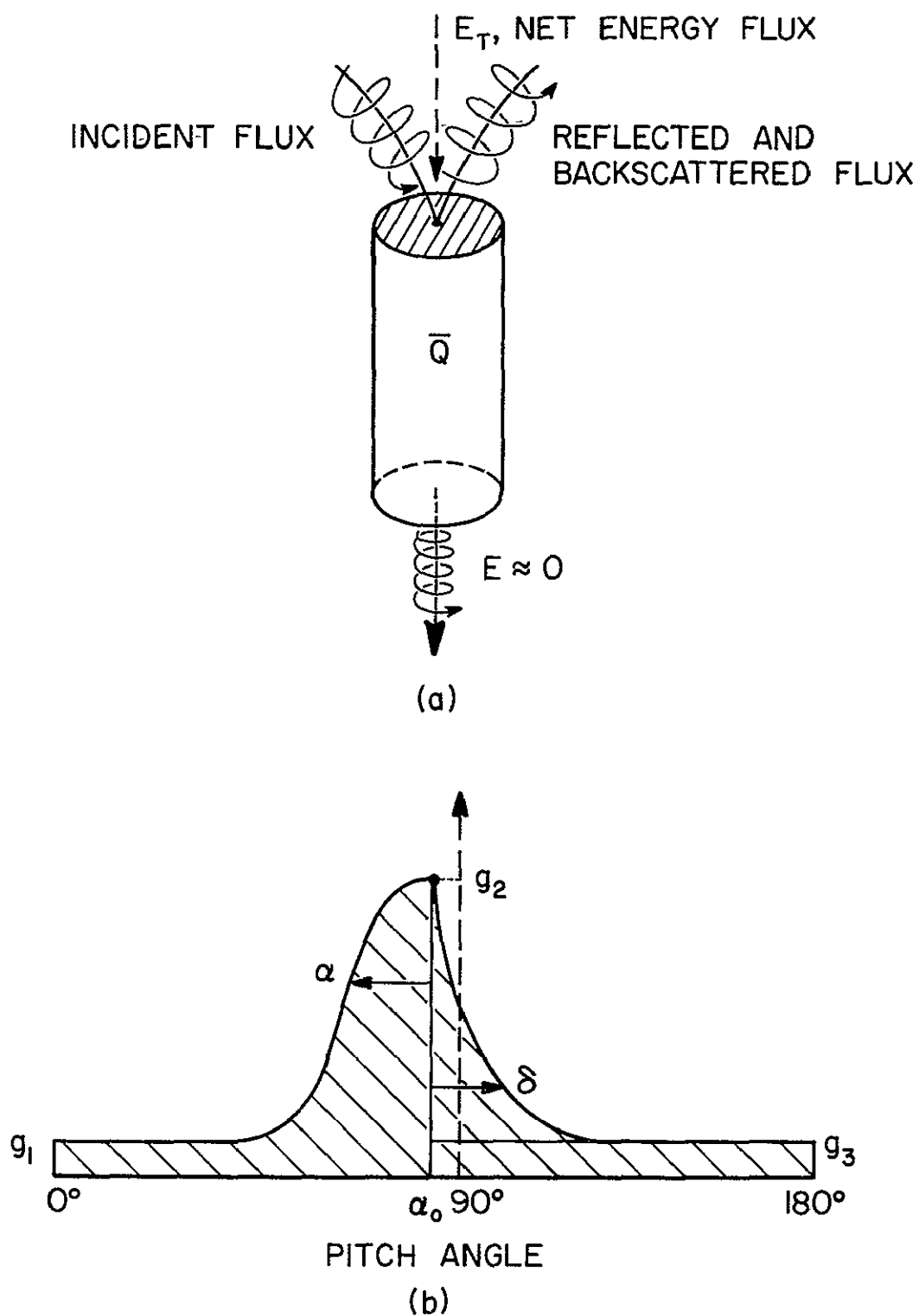


Figure 9 2 The upper figure shows the integral method for determining the average ionization rate from the net incident energy. The lower figure gives a model pitch-angle distribution for the net flux calculations.



production rate multiplied by 35 eV [Dalgarno, 1964] For this case the net energy influx,  $E_T$ , in ergs  $\text{cm}^{-2} \text{s}^{-1}$  is related to the average production rate,  $\bar{q}$ , in ion-pairs  $\text{cm}^{-3} \text{s}^{-1}$  by

$$E_T = 4.48 \times 10^{-4} \bar{q} \quad (9.7)$$

For the typical midlatitude production rates shown in Figure 2.8 the flux varies between  $10^{-4}$  and  $10^{-2}$  ergs  $\text{cm}^{-2} \text{s}^{-1}$

At midlatitudes the energy spectrum may be approximated by a power law. The differential energy spectrum,  $J_D = J_{DO} E^{-x}$ , in particles  $\text{cm}^{-2} \text{s}^{-1} \text{keV}^{-1}$ , is related to the integral energy spectrum,  $J_I(>E) = J_{IO} E^{-y}$ , in particles  $\text{cm}^{-2} \text{s}^{-1}$ , by  $x = y + 1$  and  $J_{DO} = y J_{IO}$ . The total flux (in energy units) associated with a particular energy spectrum for  $x > 2$  may be computed by taking the following integral

$$E_T = \int_{E_1}^{\infty} J_D E dE = \frac{J_{DO}}{x-2} E_1^{2-x} = \frac{y J_{IO}}{y-1} E_1^{1-y} \quad (9.8)$$

Equating equations (9.7) and (9.8), the value of  $J_{IO}$  at the top of the region is

$$J_{IO} = 10^{-3} \frac{\bar{I} D \bar{q}}{y} E_1^{y-1} \quad (9.9)$$

where  $\bar{I}$  is the average ionization energy in eV (35 eV is used),  $D$  is the depth of the atmospheric region in cm ( $8 \times 10^6$  cm for the region considered),  $\bar{q}$  is the average production rate in  $\text{cm}^{-3} \text{s}^{-1}$ ,  $y$  is the integral energy spectrum exponent and  $E_1$  is the lower energy cut-off in keV

Taking a representative spectrum corresponding to  $y = 2$ ,  $E_1 = 1$  keV, and  $\bar{q} = 1 \text{ cm}^{-3} \text{s}^{-1}$  the integral flux is  $1.4 \times 10^5 E^{-2} \text{ cm}^{-2} \text{s}^{-1}$  with  $E$  expressed in keV. For a particle detector sensitive to electrons  $>12$  keV at, say,

200 km, the net downward flux would be  $1.4 \times 10^5 \bar{q} 12^{-2} = 972 \text{ cm}^{-2} \text{ s}^{-1}$  for an average ionization rate  $\bar{q}$  of  $1 \text{ cm}^{-3} \text{ s}^{-1}$ . This rough estimate of the ionization rate is consistent with the flux measurements made by rockets discussed in Section 4.1. When compared to the ionization rates deduced from the electron density profile (Section 2.3), the effects of energetic electron precipitation is most significant.

**9.2.2 Pitch-angle distribution.** The pitch-angle distribution for quasi-trapped particles in the altitude range 120 to 200 km is modeled on the basis of experimental data and theoretical analysis (Section 7.2). Figure 9.2(b) illustrates such a distribution. The downward flux is approximated by a small isotropic component  $g_1$  and by a quasi-trapped part given by a Gaussian where  $\sigma$  is the standard deviation expressed in degrees of pitch angle. The upward flux is characterized by an isotropic part  $g_3$ , usually less than  $g_1$ , and a backscattered and magnetically reflected part given by an exponential with decay constant  $\delta$ . The pitch-angle distribution is thus

$$f_1(\alpha) = (g_2 - g_1) \exp\left(-\frac{(\alpha - \alpha_0)^2}{2\sigma^2}\right) + g_1 \quad 0 < \alpha < \alpha_0$$

$$f_2(\alpha) = (g_2 - g_3) \exp\left(-\frac{\alpha - \alpha_0}{\delta}\right) + g_3 \quad \alpha_0 < \alpha < 180$$
(9.10)

where  $\alpha_0$  is near  $90^\circ$ . All the parameters in this model are functions of energy, altitude, and incident flux and therefore must be matched with experimental data. During magnetically disturbed times the isotropic component of the flux may, on occasion, become very large (Figure 7.7).

The net number of particles which are deposited in the atmosphere is simply the difference between  $f_1$  and  $f_2$ . For  $\alpha_0 = 90^\circ$  at 200 km this gives

$$f_1 - f_2 = \sigma \frac{\pi}{2} (g_2 - g_1) - \delta (g_2 - g_3) + \frac{\pi}{2} (g_1 - g_3) \quad (9.11)$$

For the specific case of  $g_1 = g_3 = 0$ ,  $g_2 = 1$ ,  $\sigma = 8^\circ$  and  $\delta = 4^\circ$  the upward flux is 4 particles  $s^{-1}$ , the downward flux is 10 particles  $s^{-1}$  and the absorbed flux is thus 6 particles  $s^{-1}$ .

These models of pitch-angle distribution will be used in the calculation of ion-pair production rates and are essential for accurate modeling of midlatitude particle precipitation.

### 9 3 *Energy Loss and Ionization by Quasi-trapped Energetic Electrons*

The ionization rates developed in this section follow the empirical techniques discussed in Section 9.1.1. The major addition in these calculations is that the distance traveled by a particle as it mirrors in a geomagnetic dipole field is included.

9 3 1 *Approximate calculation.* It was shown in Section 7.1 that the linear increase of count rate with altitude can be used to obtain the pitch-angle or mirror-height distribution (Figure 7.9). This pitch-angle distribution,  $f(z_m) \propto \sqrt{z_m - z_o}$ , includes the effects of scattering since the actual number of particles in each mirror height interval has been measured directly.

The ionization rate is expected to be proportional to the atmospheric density multiplied by the number of mirroring particles in each height interval. Assuming an exponential atmosphere and a linearly increasing count rate (as observed) the ionization rate has the form

$$q(z) \propto N f(z_m) \Delta z_m \propto \sqrt{z - z_o} \exp[-(z - z_o)/H] \quad (9.12)$$

where  $H$  is the scale height and  $z_o$  is the lowest altitude of the quasi-trapped distribution. Equation (9.12) is plotted in Figure 9 3 for  $H = 20$  km and

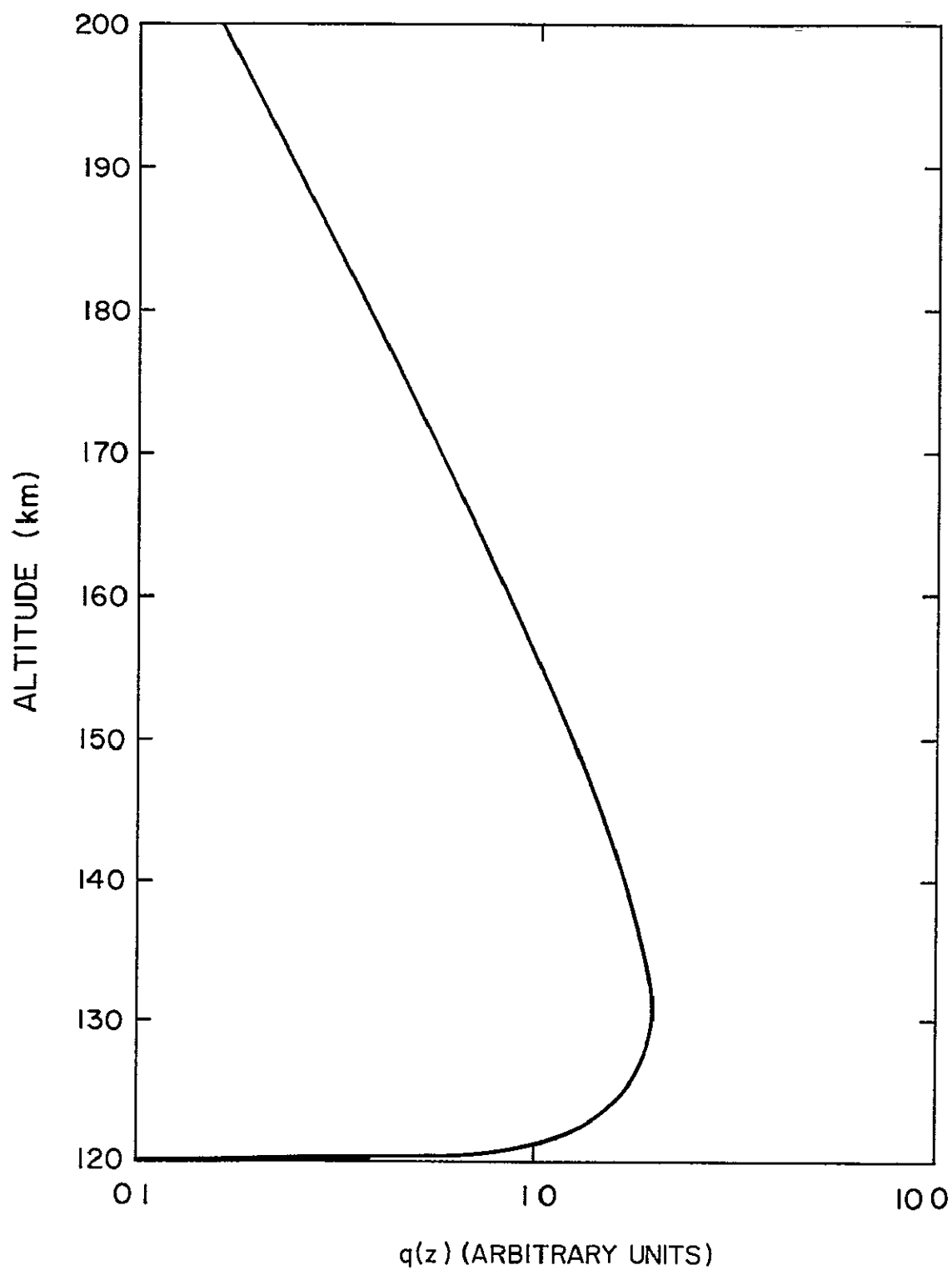


Figure 9 3 An approximate calculation of the variation of ionization rate with altitude for a mirroring distribution of particles. For this case  $H = 20$  km,  $z_0 = 120$  km and an exponential atmosphere is assumed.

$z_o = 120$  km and shows that the ionization rate changes by one order of magnitude over the region 120 to 200 km while the density changes by four orders of magnitude. This is in good agreement with the calculated production rates obtained from the electron-density profile as discussed in Section 2.4.

9.3 2 *Calculation of ionization rates for individual electrons.* For these calculations the CIRA 1972 model atmosphere was adopted with an exospheric temperature of  $1000^\circ\text{K}$  typical for moderate values of magnetic disturbance in the midlatitude nighttime ionosphere (Figure 9.4). The atomic number was also varied according to altitude.

The energy loss curves with altitude for this model atmosphere are shown in Figure 9.5 for different pitch angles,  $\alpha$ , and injection energies,  $E_1$ , at 360 km for a uniform magnetic field with no mirroring. These results are in agreement with the calculations of *Kamiyama* [1966].

For the case of mirroring particles an analytic expression may be obtained by combining the experimental loss rate equation (8.25) and the mirror equation to give

$$\frac{dE}{dz} = 1.25 \times 10^7 \left( \frac{R_o + z_m}{3} \right)^{\frac{1}{2}} \rho(z) (z - z_m)^{\frac{1}{2}} E^{-0.75} \quad (9.13)$$

where  $E$  is the energy (keV),  $\rho$  is the atmospheric density ( $\text{kg/m}^3$ ),  $z$  is the altitude (km),  $z_m$  is the mirror altitude (km) and  $R_o$  is the radius of the earth (km). This equation may be integrated to give the energy loss of a particle at any height  $z$  above the mirror height

$$E(z) = I_o \int_{z_o}^z \left[ E_z^{1.75} + 3 \times 10^7 \left( \frac{R_o + z_m}{3} \right)^{\frac{1}{2}} \rho_o \operatorname{erf} \left( \frac{z - z_m}{H} \right)^{\frac{1}{2}} \right]^{1/1.75} \sqrt{z_m - z_o} dz_m \quad (9.14)$$

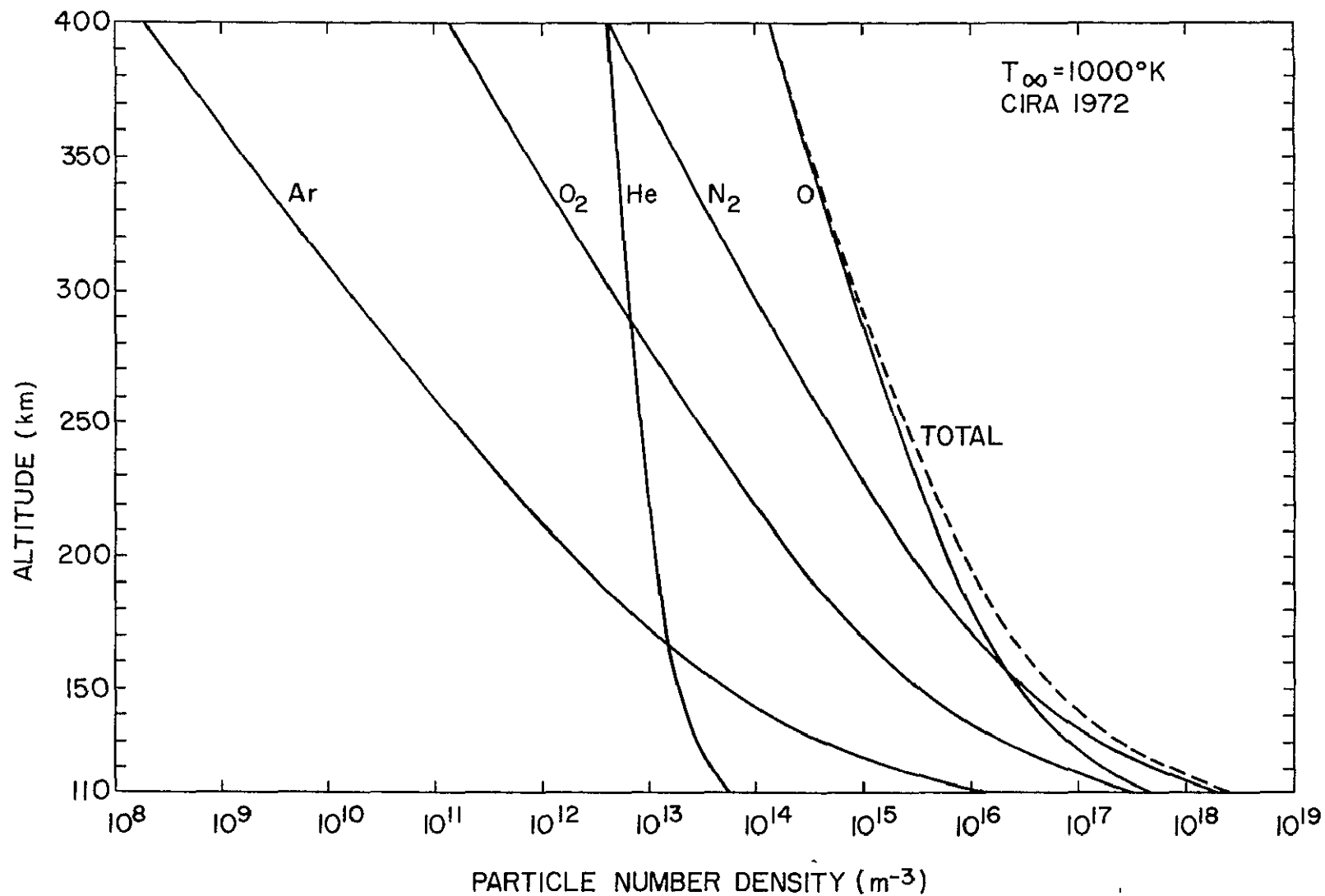


Figure 9 4 The *CIRA* [1972] model used for ionization calculations The assumed value of exospheric temperature is 1000K

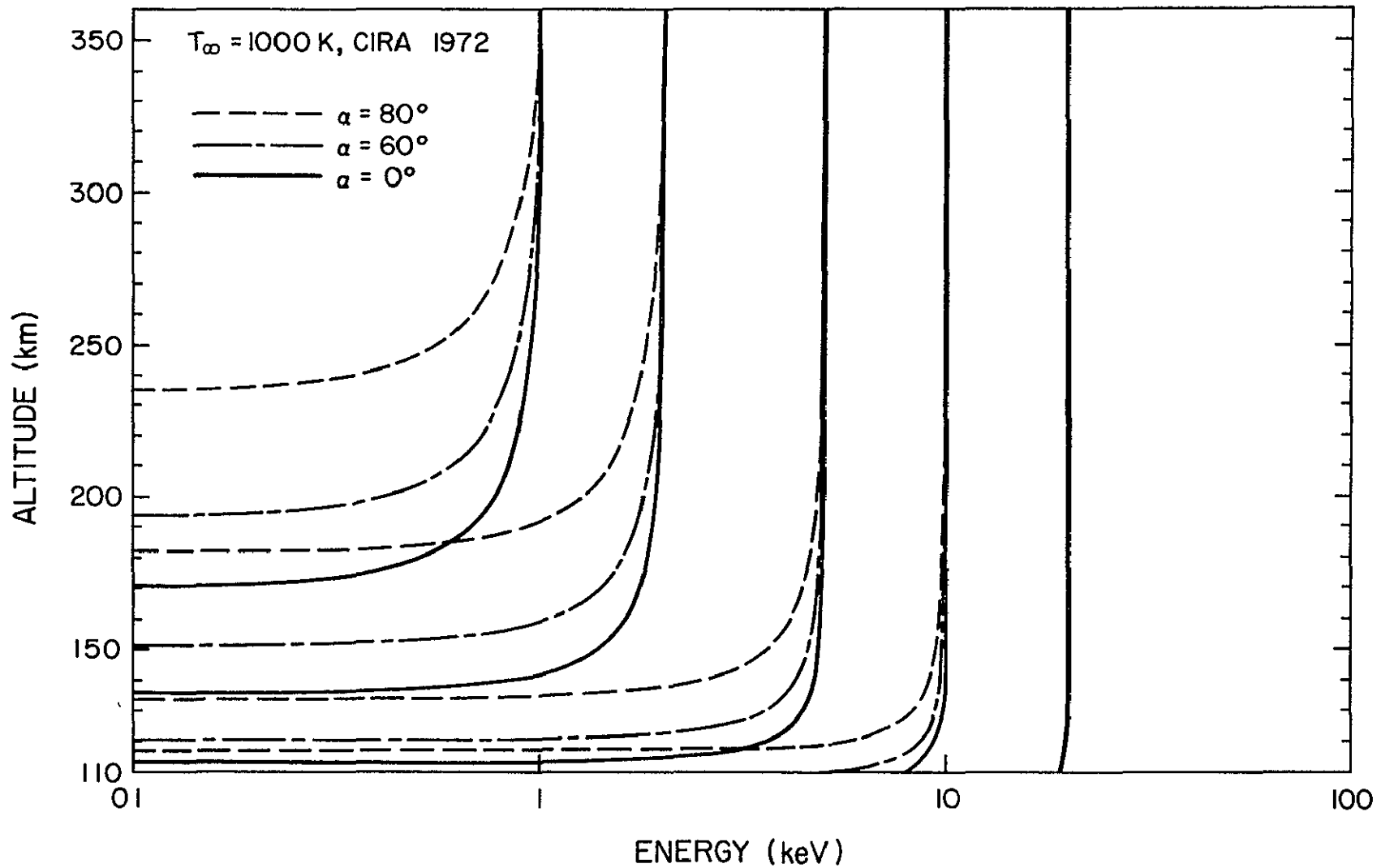


Figure 9.5 Energy loss curves for electrons ( $E_0 = 1, 2, 5, 10, \text{ and } 20 \text{ keV}$ ) in a uniform magnetic field (i.e., no mirroring) for initial pitch angles of  $0, 60, \text{ and } 80$  degrees.

where an exponential atmospheric approximation is made and  $\rho_0$  is a calibration density,  $H$  is the scale height,  $E_z$  is the initial energy of the particle, and erf is the error function.

For cases involving a numerical model of atmospheric density equation (9.13) can be solved over a summation of decrements in altitude from  $z + 1$  to  $z$  such that,

$$E^{1.75}(z) = E^{1.75}(z+1) + 4.4 \times 10^7 \left( \frac{R_0 + z_m}{3} \right)^{\frac{1}{2}} \frac{\rho(z) + \rho(z+1)}{2} \cdot (\sqrt{z - z_m} - \sqrt{1 + z - z_m}) \quad (9.15)$$

This equation has the form

$$E^{1.75}(z) = E^{1.75}(z+1) - f(z, z_m) \quad (9.16)$$

where  $f(z, z_m)$  is independent of energy. The energy loss rate may therefore be simply calculated for the downward and upward trajectory of a mirroring particle for any energy once  $f(z, z_m)$  is calculated

Using equation (9.16) for the energy loss with altitude for a mirroring electron and assuming no scattering the energy loss trajectory is as shown in Figure 9.6. The energies plotted are for 5, 7, 10, 20 and 50 keV electrons mirroring at 170, 160, 150, 140, and 130 km. A noticeable feature of this figure is that most of the energy of an energetic electron is deposited near its mirroring point. For lower energy electrons and lower mirror heights the energy loss is observed to rapidly increase.

At the mirror height of 140 km electrons with energies greater than 7 keV are reflected. At 7 keV the energy is almost all lost and at 5 keV the electron is absorbed at the mirror altitude. At a mirror height of 130 km only electrons with energies of 20 keV and 50 keV are reflected while the 10 keV electron is absorbed after mirroring and the 5 and 7 keV electrons



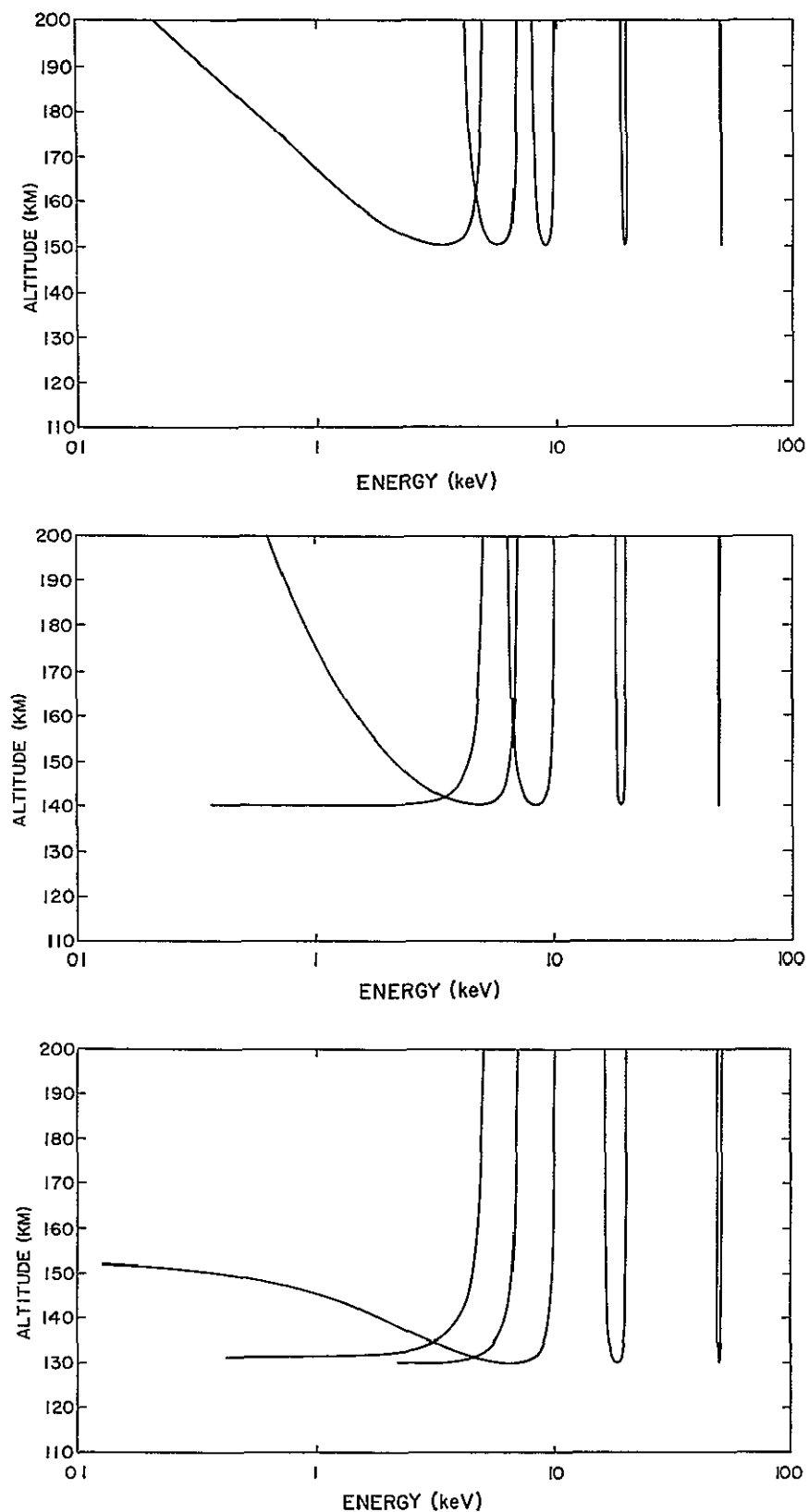


Figure 9 6 Energy loss curves for energetic electrons mirroring at altitudes of 130, 140, 150, 160, and 170 km with initial energies of 5, 7, 10, 20, and 50 keV Atmospheric scattering is not included in these results

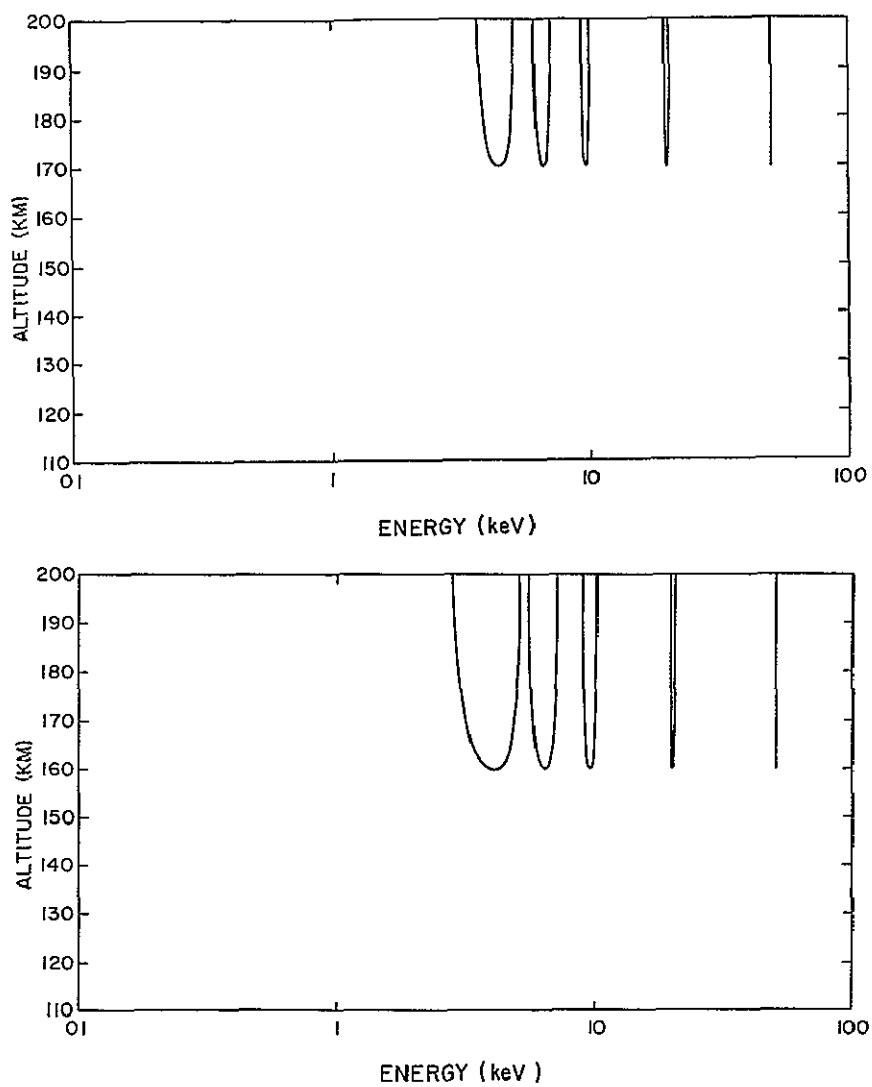


Figure 9.6 (Continued)

are absorbed at the mirror altitude

By dividing the average energy lost per km of altitude by the energy for ion-pair formation (35 eV), an estimate can be made of the ionization rate versus altitude. These results are given in Figure 9.7 for a 10 keV electron and clearly illustrate the increase in ionization near the mirror point compared to a nearly vertically incident electron. The effects of mirroring is to greatly increase the collision rate versus altitude and hence increase ionization.

The next section contains numerical calculations of the ionization rate for the observed pitch-angle distribution and for different energy spectrums.

#### 9.4 *Calculation of Ionization Rate for Models of Quasi-trapped Energetic Electrons*

A detailed analysis of the ionization rate requires consideration of various energy spectrums and the change in the energy spectrum with altitude due to energy loss processes. In the analysis in this section atmospheric scattering has been indirectly accounted for; as in the previous section since the input data are the count rate and energy spectrum versus altitude rather than a pitch-angle distribution at the top of the atmosphere. Consideration of the count-rate profiles indicate that above 130 km the majority of electrons are in a magnetically reflecting state. This conclusion is based on the observations that at altitudes above 130 km the absorption of a vertically incident electron with energy greater than 10 keV is negligible. From the linear count-rate profile that is observed a pitch-angle distribution at the top of the atmosphere (200 km) which accounts for the effects of scattering may be developed according to Sections 7.1 and 7.2. It is this effective pitch-angle distribution in the alternate

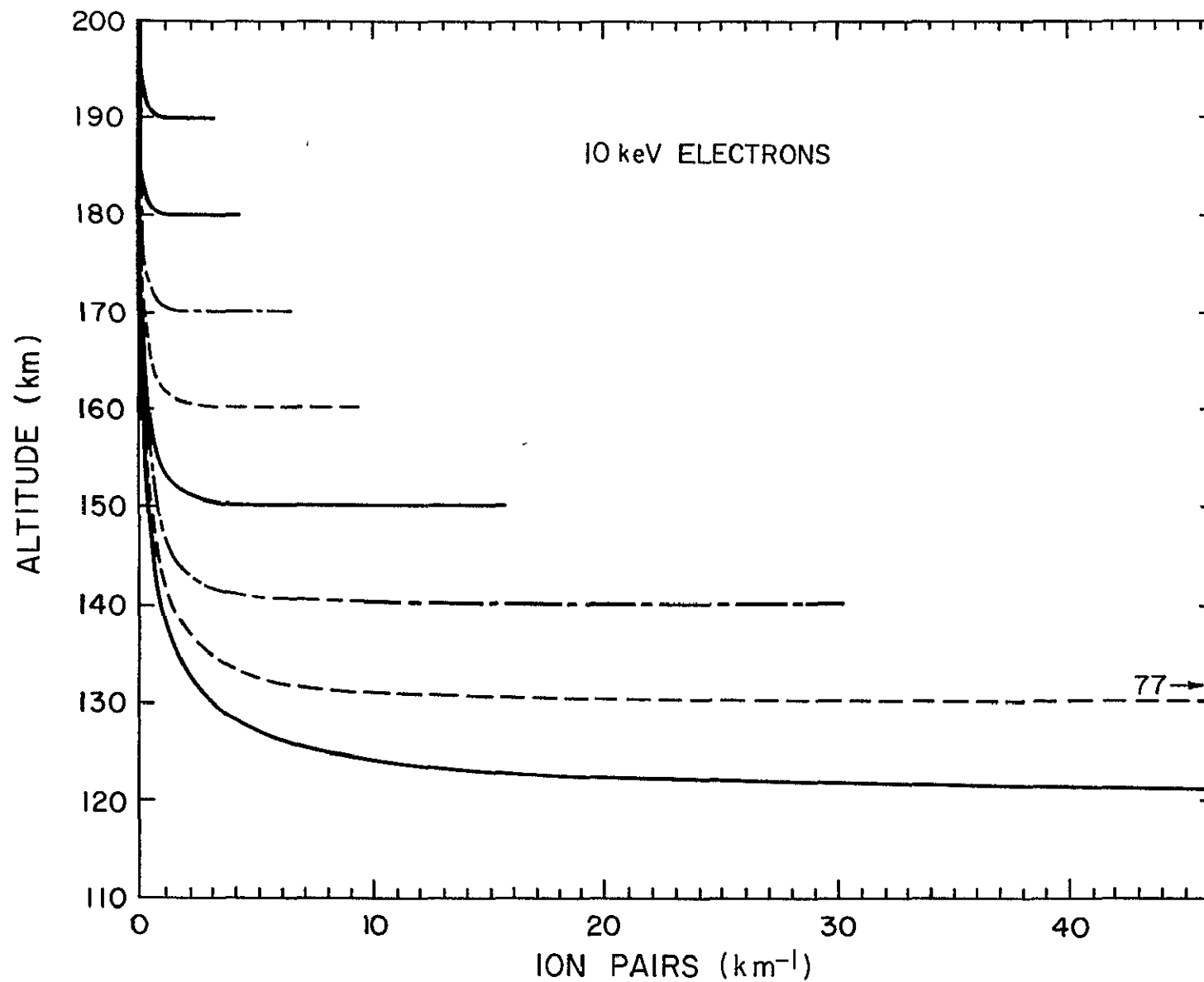


Figure 9.7 Ionization formed in each altitude increment of 1 km by 10 keV electrons with mirror heights at 10-km intervals. Note that all the ionization occurs near the mirroring height. Electrons with a mirror height of 120 km are absorbed, all others escape.

form of a mirror-height distribution which is used in subsequent analysis.

A block diagram of the program used to compute the ionization rate is given in Figure 9.8. The program uses the pitch-angle distribution of Figure 7.2, which is indicative of the observed count-rate profiles, and the energy spectrums shown in Figure 9.9. The spectrum is representative of satellite measurements [Torr *et al.*, 1975]. The flux distribution at the top of the atmosphere is given by

$$F(z_m, E) = I_0 E^{-\alpha} \sqrt{z_m - z_0} \quad (9.17)$$

The atmospheric number density is taken from CIRA [1972] for an exospheric temperature of 1000°K (Figure 9.4). With these input data the program calculates the energy loss and ionization rate for individual electrons sent into the atmosphere along mirroring trajectories. The energy loss and ionization rates are then stored and summed for every km interval in height.

The first part of this program plots out three sets of graphs which cover the energy intervals from 1 to 10 keV, 10 to 25 keV and 25 to 100 keV, respectively. Each set contains three plots of the number of ion-pairs formed per km for initial energy  $E$  with a square-root mirror-height distribution. The first series of profiles are produced using equation (9.17) for the incident flux. The second series of profiles are normalized so that a total of 1 keV of energy is deposited below 250 km for each incident energy. The third series of profiles are normalized so that the energy  $E$  of the initial particle is completely absorbed.

The fourth plot in each set is the ion-pair formation rate for the four energy intervals under consideration. The ionization rate is given as the number of ion pairs  $\text{cm}^{-2} \text{ km}^{-1}$ . When divided by  $10^5$ , this gives the number

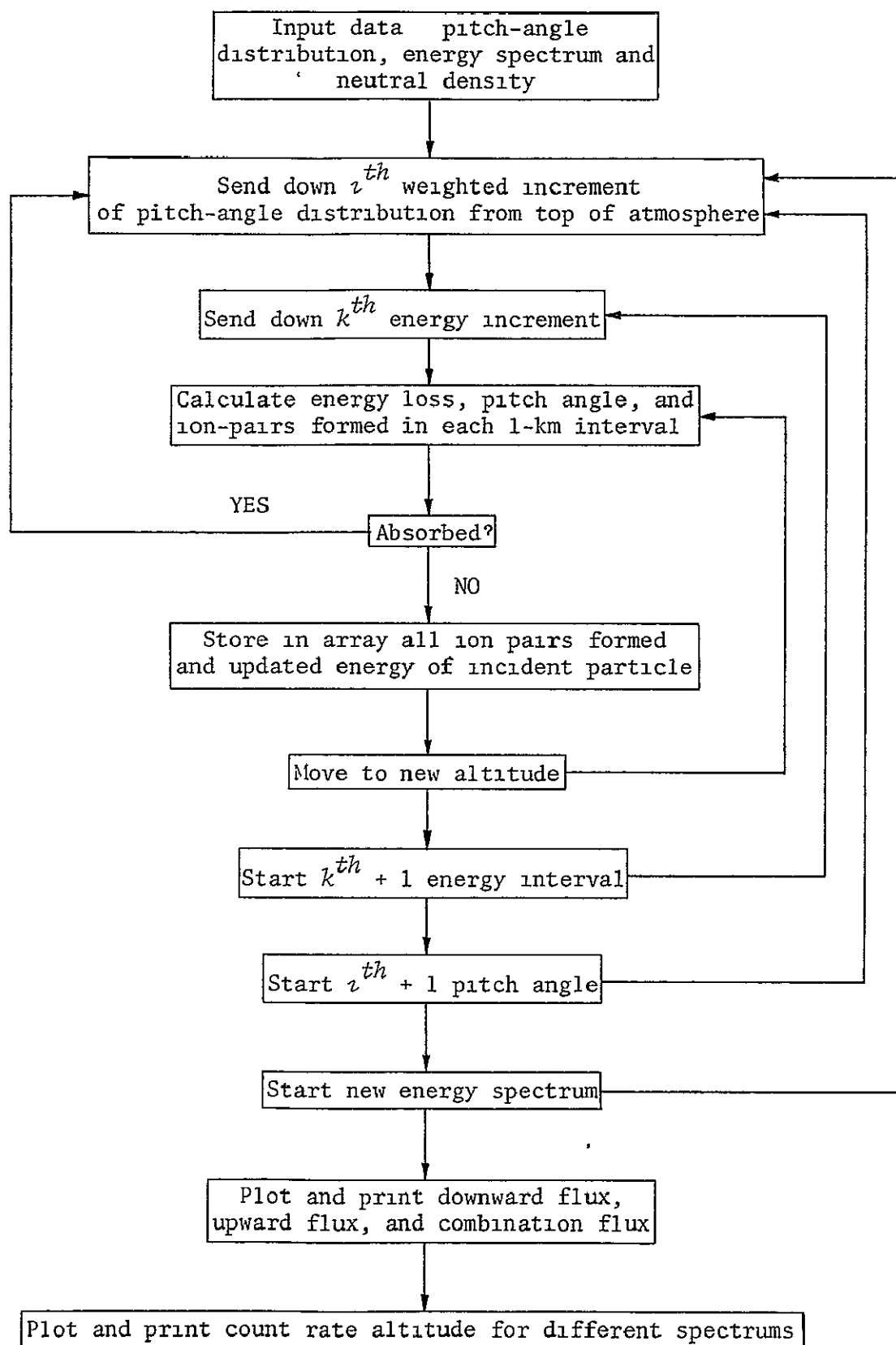


Figure 9.8 Block diagram of the program used to compute the ionization rate and count rates as a function of altitude for a mirroring distribution of electrons with different energy spectrums.

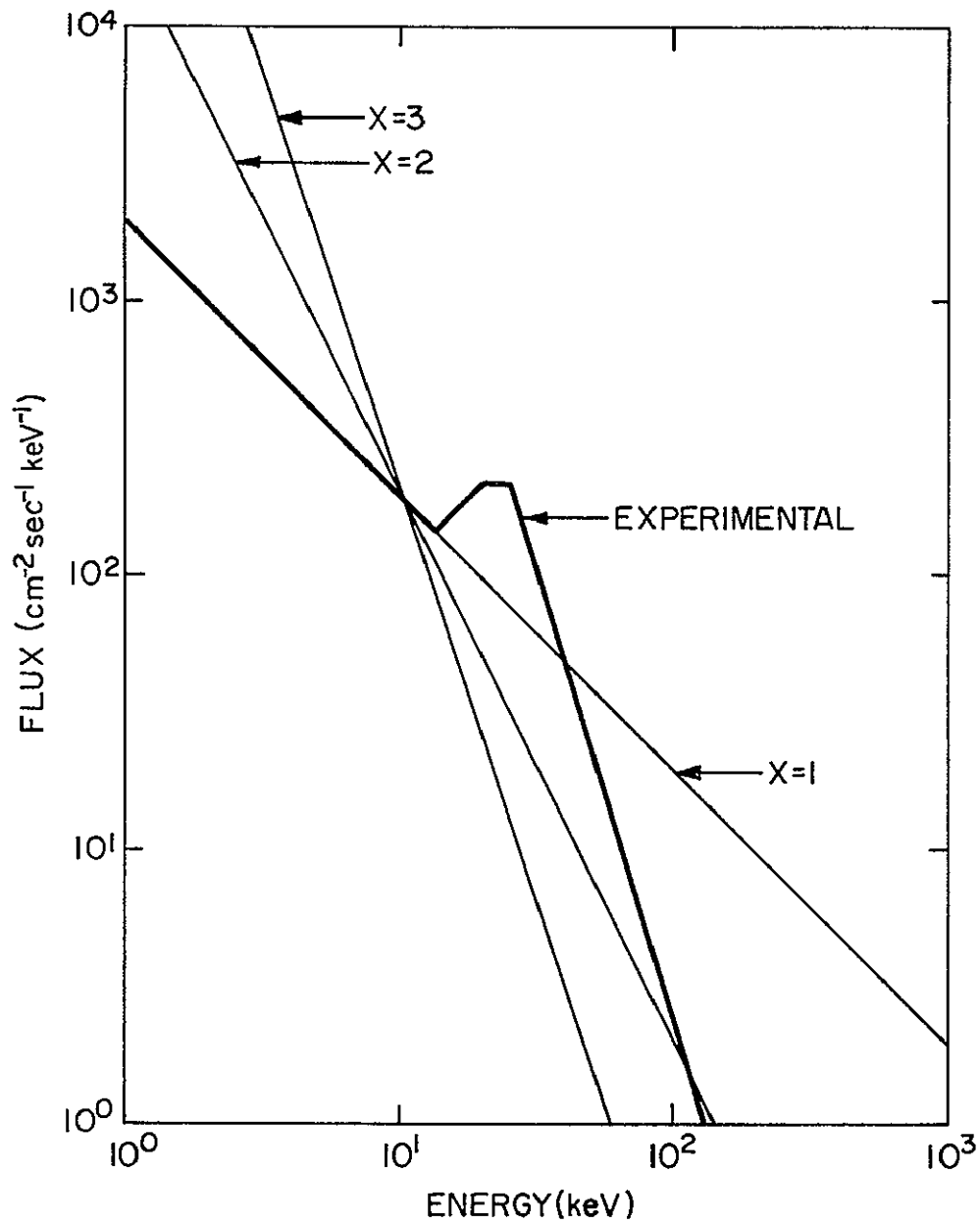


Figure 9.9 Power law energy spectrums for  $x = 1, 2$ , and  $3$  and an experimental spectrum used in the count rate and ionization calculations.

of ion-pairs  $\text{cm}^{-3} \text{ s}^{-1}$  The flux at any altitude is given by equation (9.17).

The results of these computations are shown in Figures 9.10 and 9.11 for  $1 < E < 10$  keV, Figure 9.12 for  $10 < E < 25$  keV and Figure 9.13 for  $25 < E < 100$  keV. Figure 9.14 gives the ion-pair formation for the energy spectrums of  $10 < E < 25$  keV and  $25 < E < 100$  keV. The small dashes are for the lowest energy of the particular data set with increasing dash size associated with increasing energy.

For energies greater than 10 keV the shape of the production-rate curve is independent of energy. This is seen in Figures 9.12(b) and 9.13(b) for the case of equal numbers of total ion-pairs formed. Additionally the curves show that the production rate changes by only an order of magnitude in the altitude region 120 to 250 km. This is significant since the inferred production rates derived from the electron-density profile vary in this same manner (Section 2.3). On the other hand, an isotropic pitch-angle distribution of particles gives a production rate which changes by more than three orders of magnitude in the same altitude region. This is seen when Figure 9.15 is compared with Figure 9.12. The significance of mirroring is clearly demonstrated by this comparison.

The horizontal line at 120 km indicates the region where the quasi-trapped flux becomes insignificant. Below this altitude the isotropic component of the flux dominates as has been reported on in many previous studies in the literature (e.g., Figures 8.14).

The final composite ionization profile for energetic electrons having energies between 1 and 100 keV and having a linearly increasing cut-rate profile and a power-law energy spectrum is shown in Figure 9.16. Above 120 km the nearly constant production rate profiles versus altitude are in good agreement with electron-density measurements presented in Chapter 2.



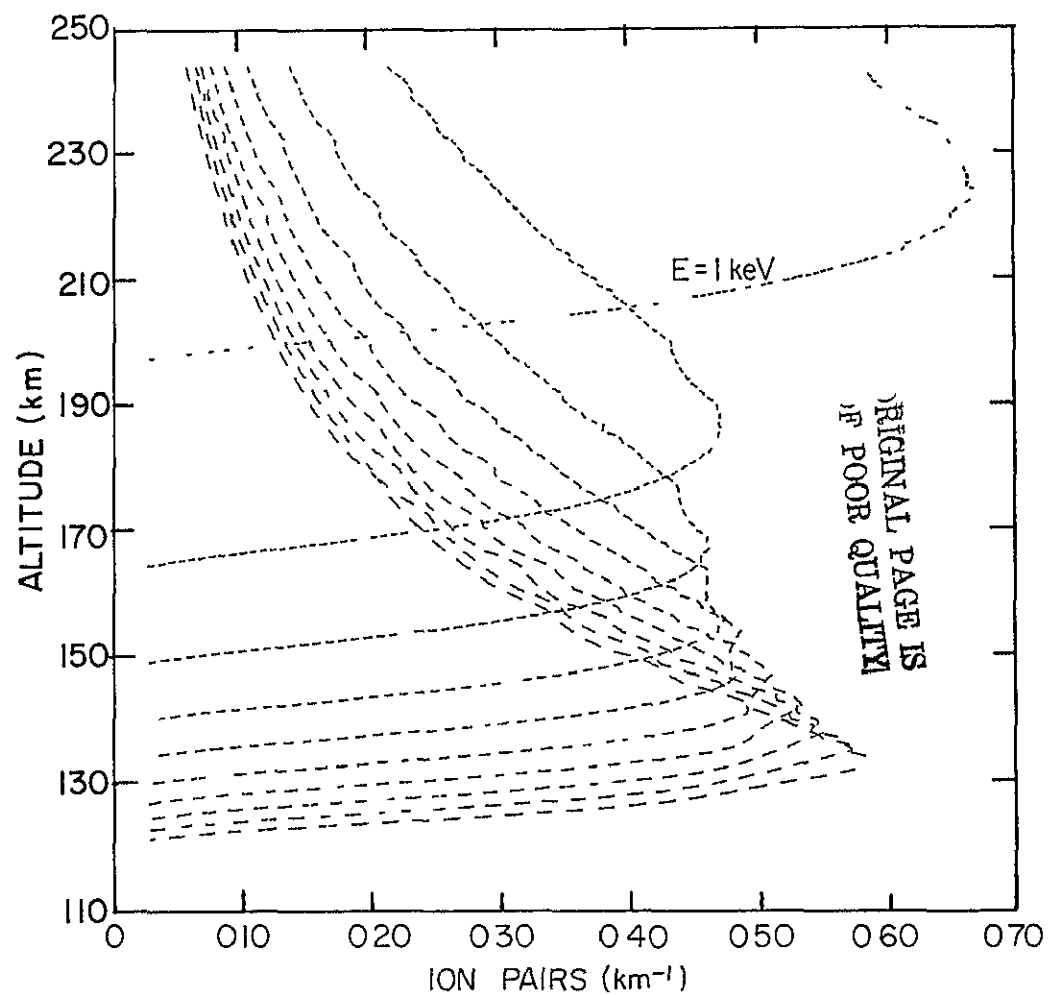
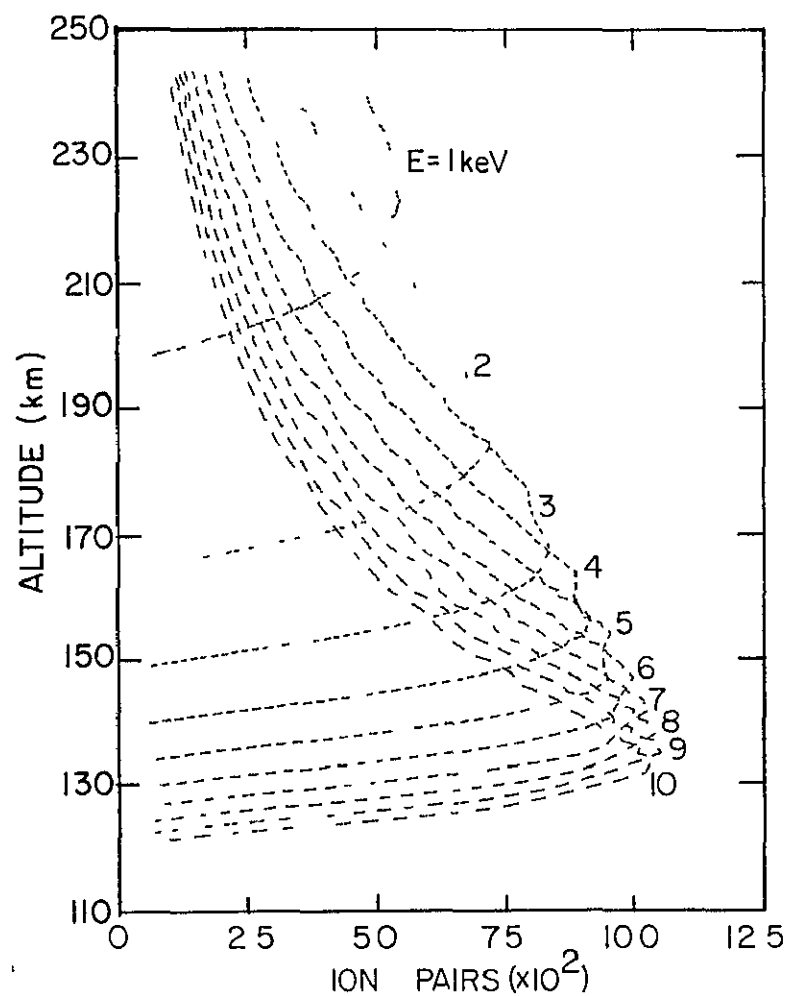


Figure 9 10 The figure on the left shows a series of profiles ( $1 < E < 10 \text{ keV}$ ) of the ionization produced using equation (9 17) for the incident flux. The figure at the right is normalized so that a total of 1 keV of energy is deposited below 250 km for each energy.

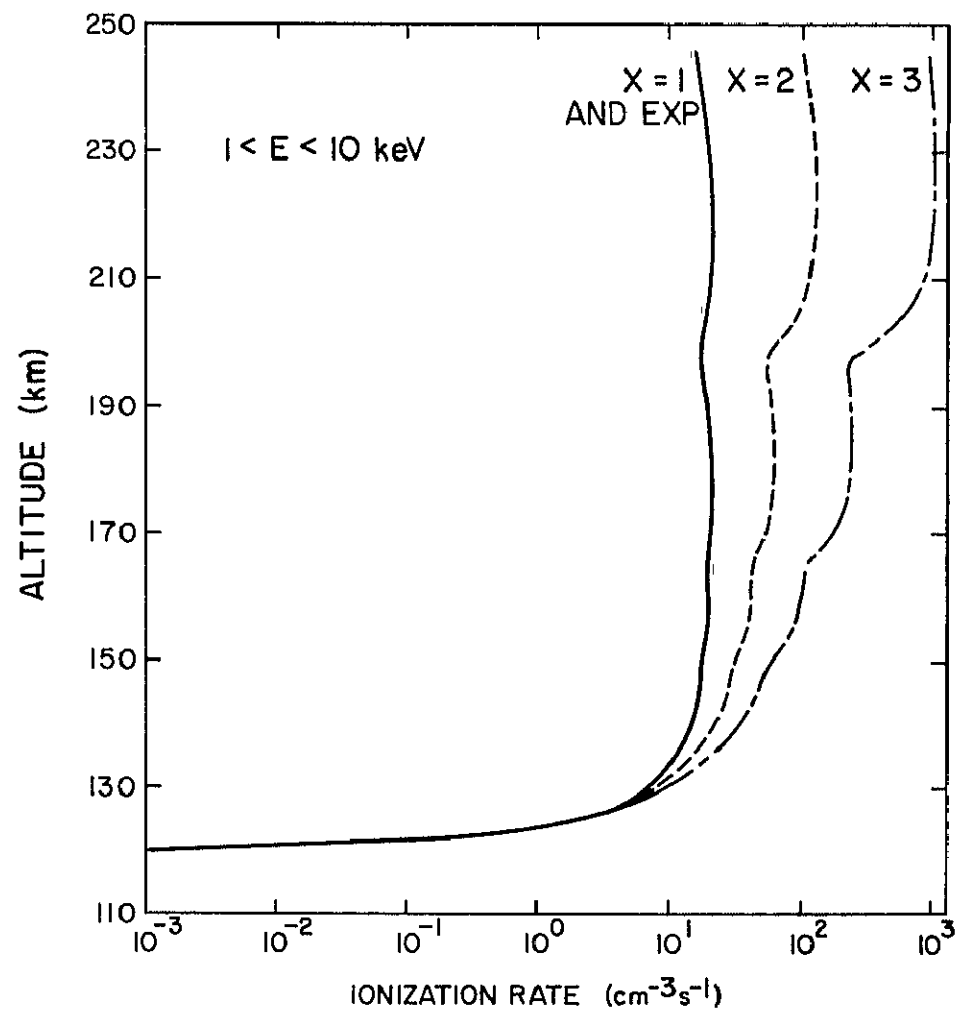
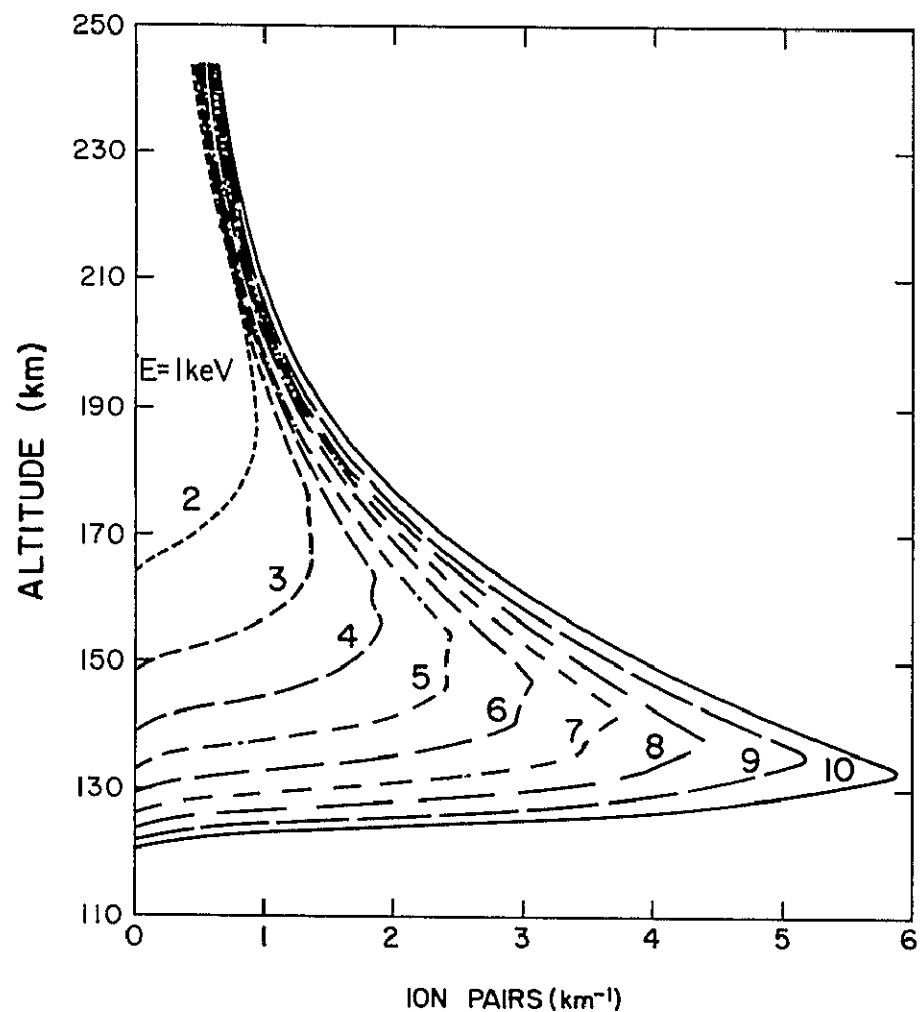


Figure 9.11 The figure at the left shows a series of profiles which are normalized such that the energy absorbed is equal to the incident energy of the particles. The figure on the right is the total ionization for the various spectrums of Figure 9.9 in the energy interval  $1 < E < 10 \text{ keV}$ .

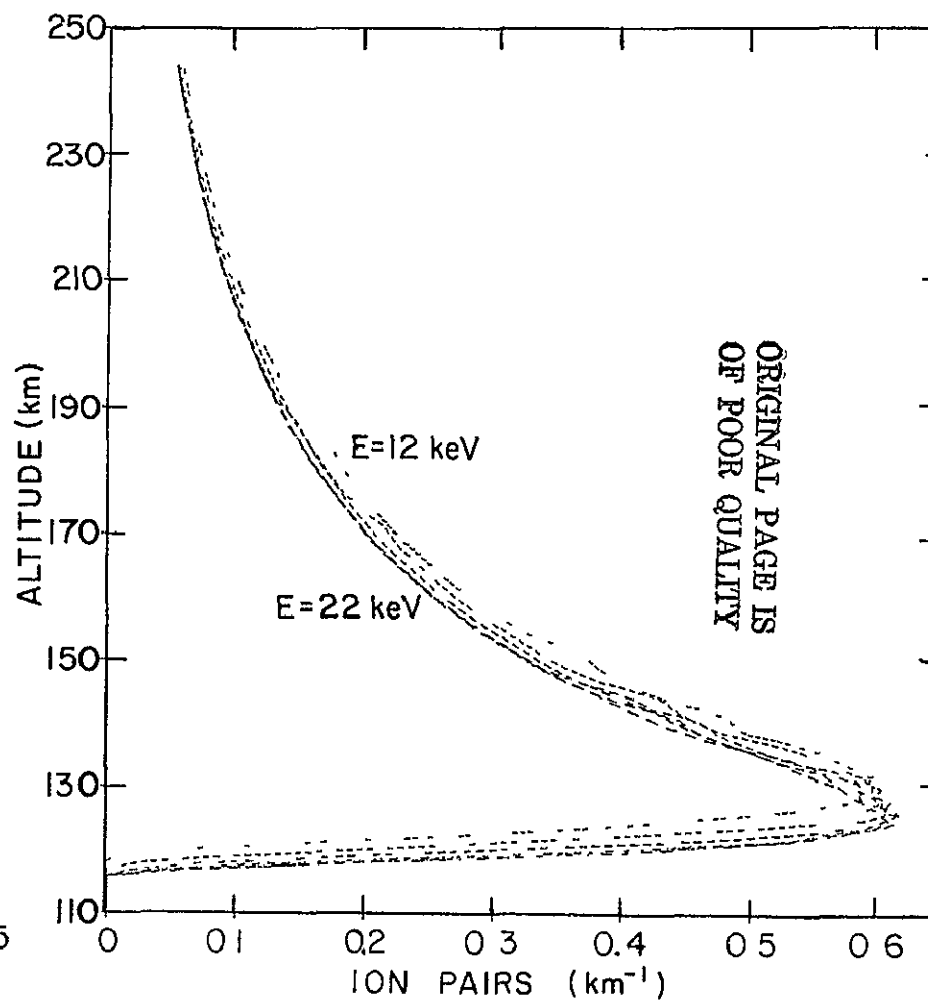
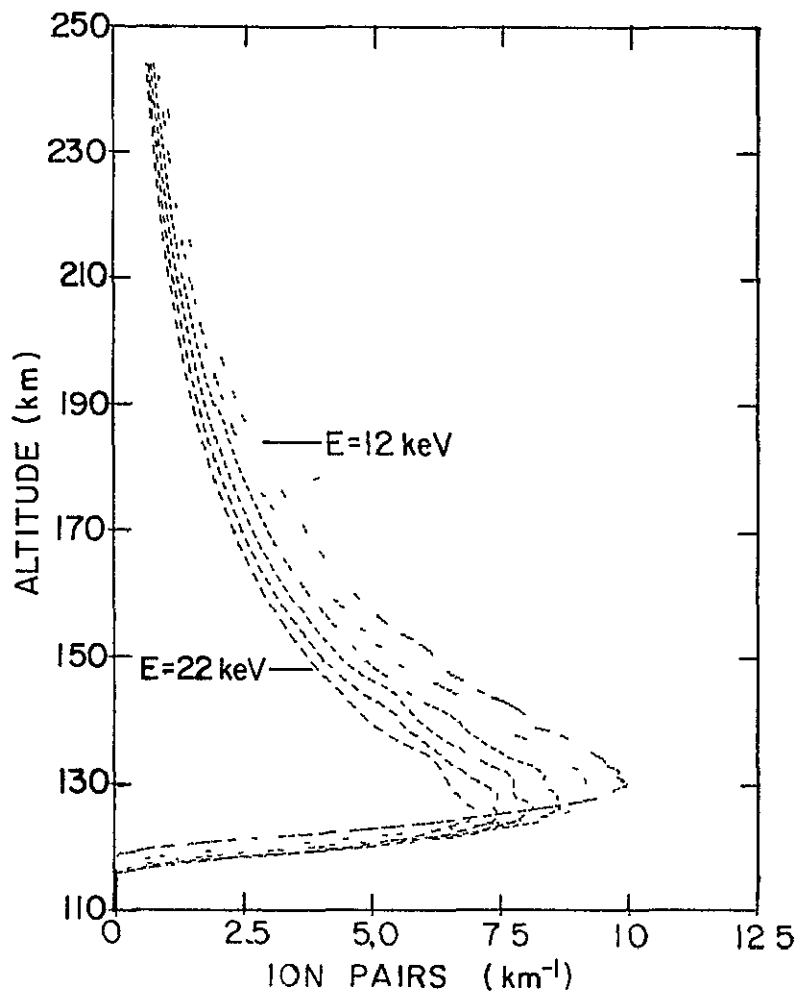


Figure 9.12 These figures are the same as Figure 9.10 but for the energy range  $12 < E < 22$  keV, in intervals of 2 keV

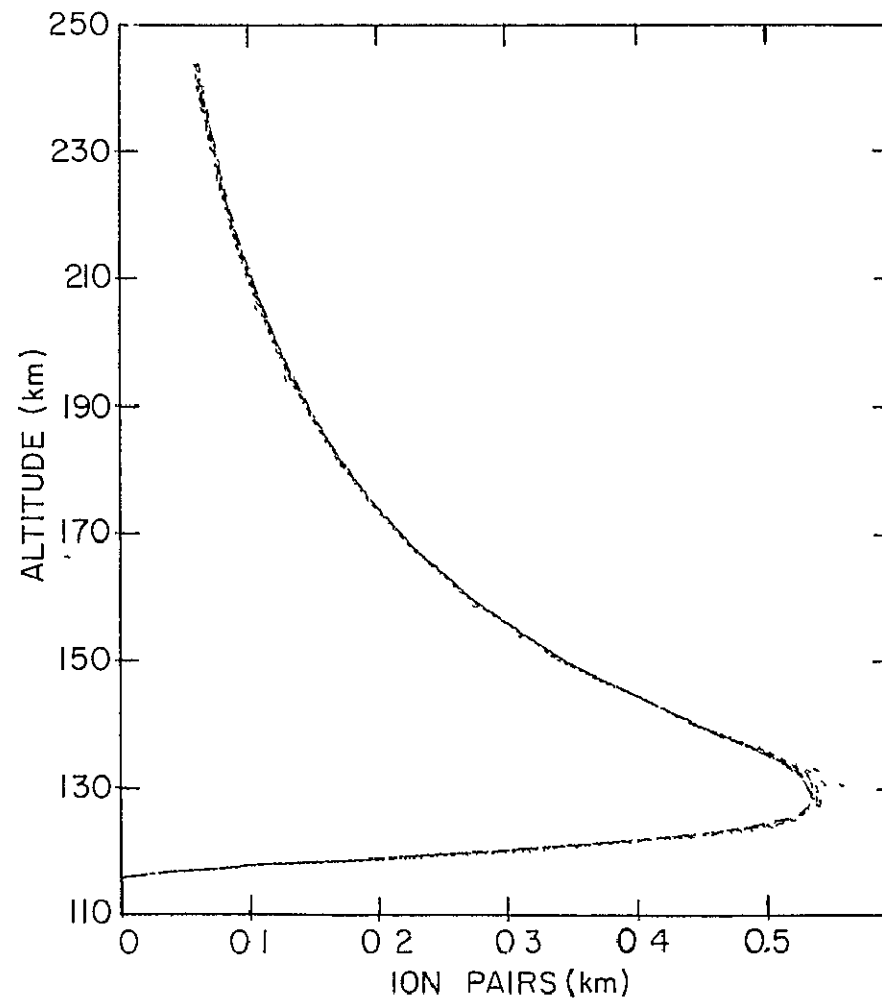
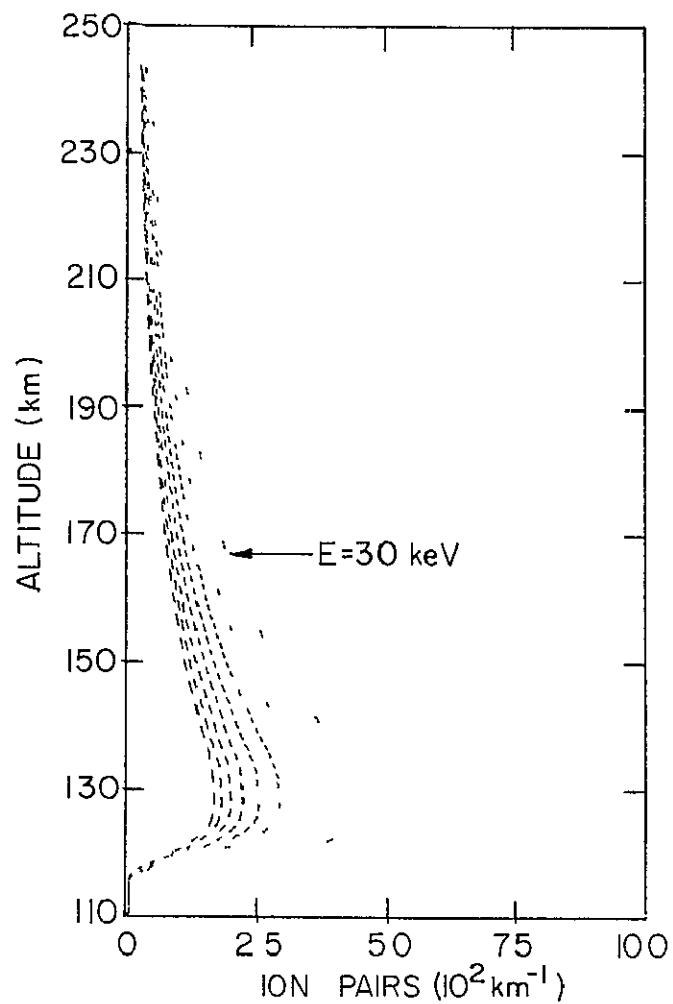


Figure 9 13 These figures are the same as Figure 9 10 but for the energy range  $30 < E < 100 \text{ keV}$  in intervals of 10 keV

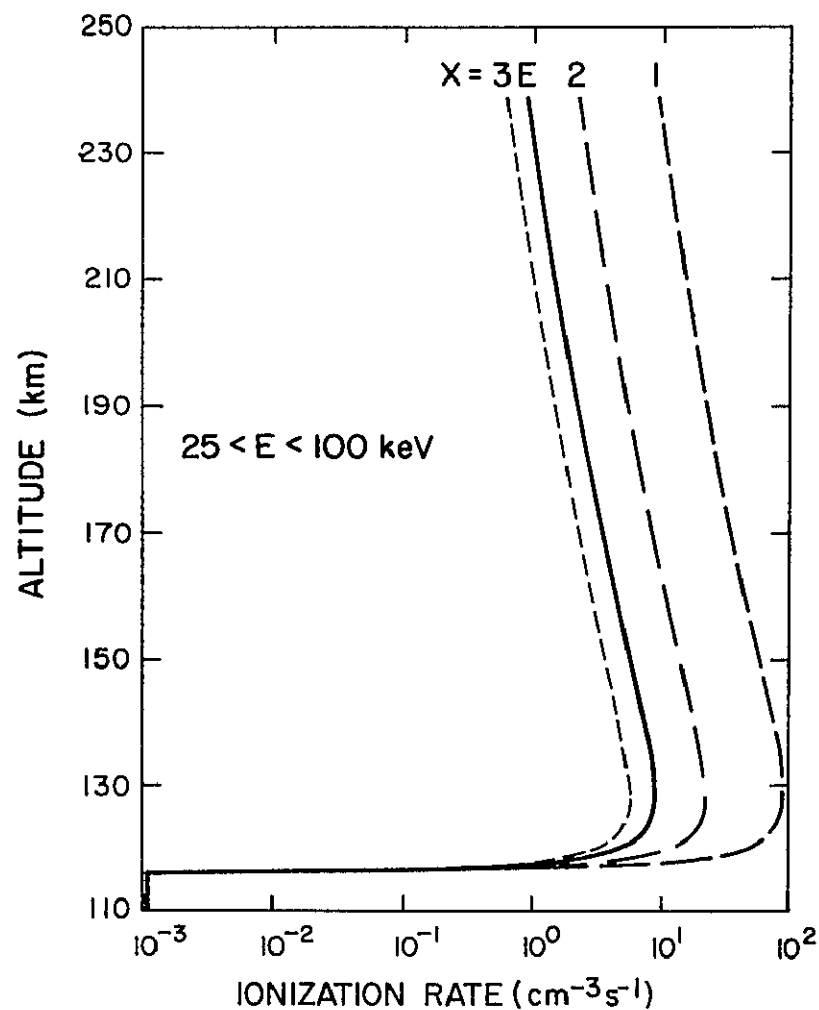
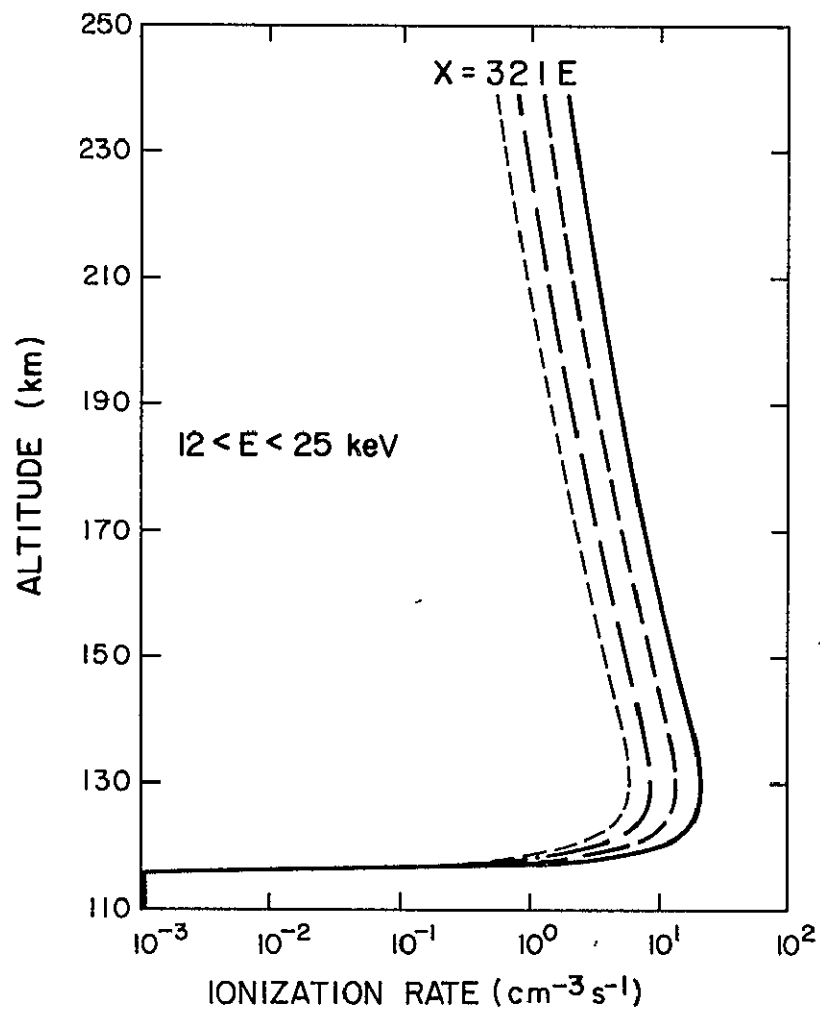


Figure 9.14 These figures show the total ionization rates for the energy intervals of  $12 < E < 25$  keV and  $25 < E < 100$  keV for the various spectrums shown in Figure 9.9 where  $x$  is the exponent of a power law spectrum and  $E$  represents an experimental spectrum

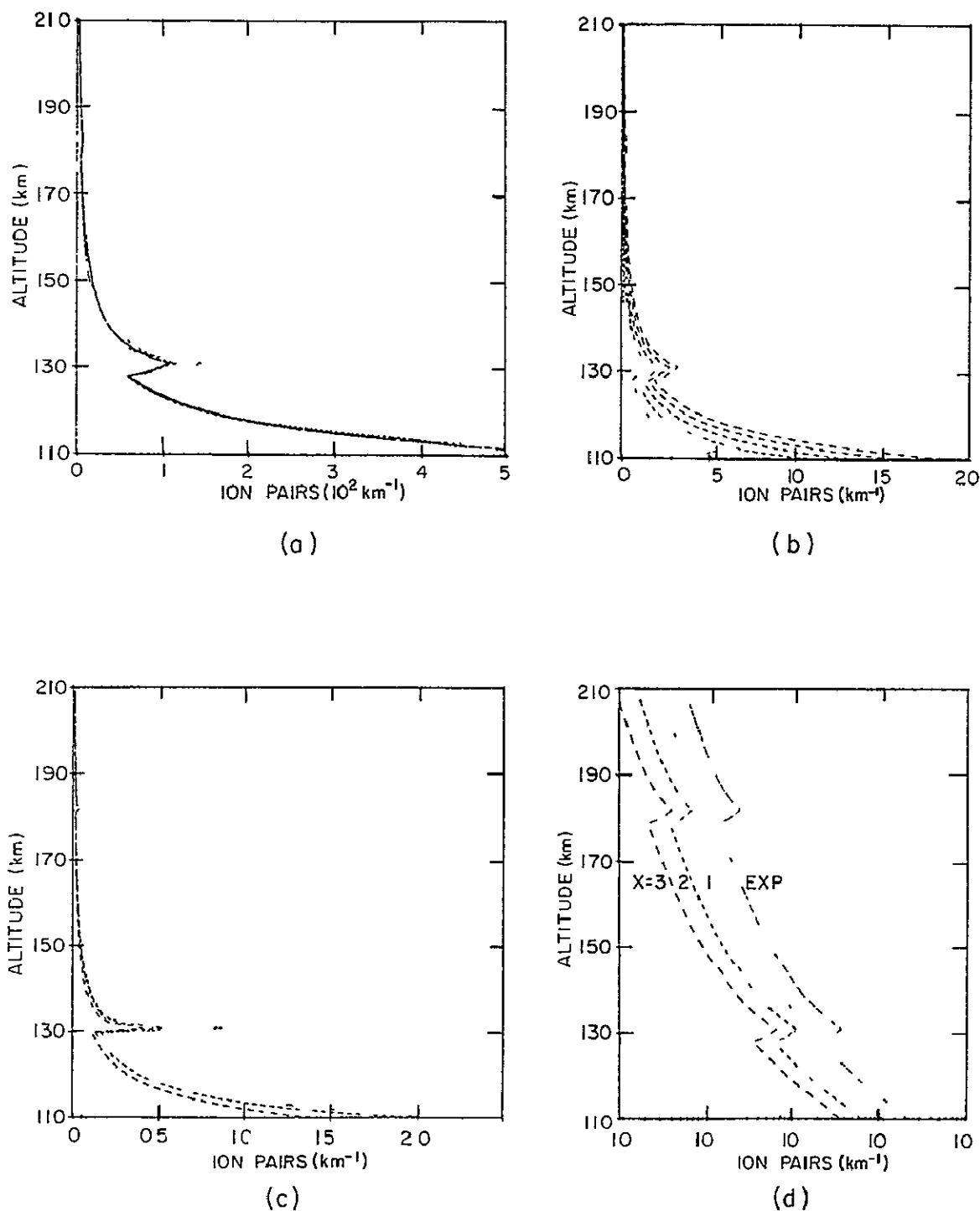


Figure 9.15 Ionization rate calculations for an isotropic distribution of particles. The range of pitch angles is  $0$  to  $89^\circ$ . The upper two figures are similar to Figure 9.10 and the lower two figures to Figure 9.11 except for the energy range  $12 < E < 22 \text{ keV}$

ORIGINAL PAGE IS  
OF POOR QUALITY

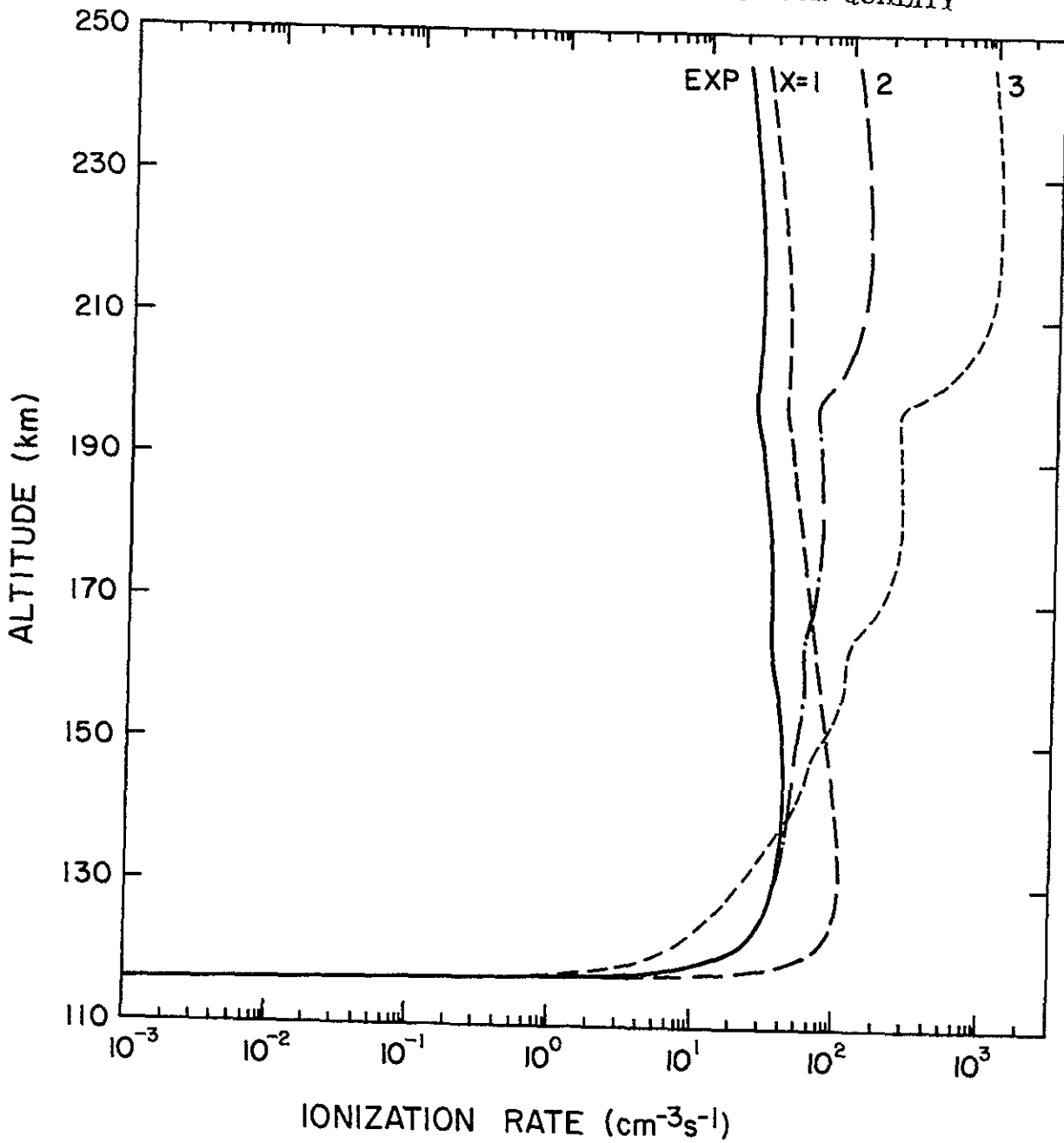


Figure 9.16 The ionization rate profiles are shown for energetic electrons having energies between 1 and 100 keV, having a linearly increasing count-rate profile, and for the energy spectrums of Figure 9.9.

Previous studies have generally considered pitch-angle distributions which are isotropic and thus characterized by a strongly decreasing production rate with altitude profile. Such distributions are inconsistent with our observations.

### 9.5 *Average Ionization Rates Computed from Rocket-borne Particle Measurements*

In this section two methods are used to obtain the ionization rates for the rocket measurements discussed in Section 4.1. The first uses the method of Section 9.2.1 applied to the observed count-rate profile, the energy spectrum and the geometrical factor of the detector to derive the total energy flux and thus the total ion production rate. This method implicitly uses the count-rate profile to show that the energetic particles are distributed over the entire region and are not simply ionizing one localized region

The second method uses the analysis of Chapter 3 to transform the count rate to an incident particle flux at the top of the atmosphere which is then used to compute an ionization rate profile as described in Section 9.4.

9.5.1 *Ionization rates obtained from the incident energy flux.* Nike Apache 14.439, instrumented to obtain the electron-density profile and to measure the flux of energetic electrons, was launched from Wallops Island, Virginia, at 0003 EST (0503 UT) on 1 November 1972, during a magnetic storm. A detailed discussion of the count rate measured on this flight (for which  $K_p = 8$ ) was given in Section 4.1.1 and the electron-density profile (Figure 2.1) was discussed in Sections 2.1 and 2.3. The average count rate above 150 km altitude was determined to be  $550 \text{ cm}^{-2} \text{ s}^{-1} \text{ ster}^{-1}$  for energies greater than 70 keV

Although only the particle flux with energy greater than 70 keV was measured, the energy spectrum and pitch-angle distribution are derived as



follows from nearly simultaneous satellite information (Section 7.5).

The energy spectrum for this night taken from satellite data (Lockheed 1971-089A) at 0545 UT near Wallops Island [*Imhof et al.*, 1976] is shown in Figure 7.14. Various other spectrums taken during the night are also shown. For  $E > 50$  keV the spectrum exponent is about 5. The count rate may therefore be written for  $E > 50$  keV as

$$J_I(>E) = J_{IO} E^{-4} \text{ cm}^{-2} \text{ s}^{-1} \text{ ster}^{-1}$$

where  $J_I(>E)$  is the integral flux measured by the rocket experiment and  $E$  is the energy in keV. For  $J_I = 550 \text{ cm}^{-2} \text{ s}^{-1} \text{ ster}^{-1}$  and  $E = 70$  keV the constant  $J_{IO} = J_{DO}/4 = 1.3 \times 10^{10} \text{ cm}^{-2} \text{ s}^{-1} \text{ keV}^4 \text{ ster}^{-1}$ . The differential flux spectrum is therefore equal to  $5.2 \times 10^{10} E^{-5} \text{ cm}^{-2} \text{ s}^{-1} \text{ ster}^{-1} \text{ keV}^{-1}$  which gives a differential flux at 70 keV of  $31 \text{ cm}^{-2} \text{ s}^{-1} \text{ ster}^{-1} \text{ keV}^{-1}$  and at 50 keV of  $166 \text{ cm}^{-2} \text{ s}^{-1} \text{ ster}^{-1} \text{ keV}^{-1}$ .

The satellite measurements show that for  $E < 50$  keV the differential energy flux is represented by a power law variation with  $\alpha = 1$ . For this case the flux constant  $J_{DO} = 166 \times 50^1 = 8300 \text{ cm}^{-2} \text{ s}^{-1} \text{ ster}^{-1}$ .

The energy associated with this spectrum between the limits of  $E_1$  and  $E_2$  is given by

$$E_T = \int_{E_1}^{E_2} J_{DO} E^{-\alpha} E dE = 1.3 \times 10^{-5} (E_2 - E_1) \quad (9.18)$$

For the energy interval of 1 to 100 keV the energy flux is found to be  $1.3 \times 10^{-3} \text{ ergs cm}^{-2} \text{ s}^{-1} \text{ ster}^{-1}$ .

Assuming 35 eV are required to form an ion-pair and that the flux is averaged over  $\pi$  steradians the ionization rate over the region 130 to 200 km with an input flux of  $10^{-3} \text{ ergs cm}^{-2} \text{ s}^{-1} \text{ ster}^{-1}$  is  $21 \text{ cm}^{-3} \text{ s}^{-1}$ . This

calculated ionization rate from the particle flux is nearly identical to the ionization rate independently calculated from the electron-density profile (Section 2.3). The main conclusion is that the particle fluxes observed at Wallops Island on 1 November 1972 using conservative estimates are adequate to explain the large increase in the ionization rate deduced from the electron-density profile on this very disturbed night

This method probably underestimates the energy flux since the energy spectrum was taken from a satellite at an altitude much higher (800 km) than the rocket flux measurements (200 km). Instead of a differential energy spectrum exponent of 1 for  $E < 50$  keV observed at 800 km the exponent for the same energy range at 200 km was probably between 1.5 and 2.5 based on subsequent rocket flights at lower altitudes (150-200 km). The increase of the spectrum exponent with decreasing altitude is observed in the region 100 to 200 km for the rocket particle data recorded in Section 4.1. Qualitatively it is expected that the energy spectrum would become softer at lower altitudes since the low energy particles are scattered much more easily by the atmosphere and by wave-particle interactions.

Assuming a typical energy spectrum exponent of  $y = 2$  the flux constant  $J_{IO} = 2.7 \times 10^6 \text{ cm}^{-2} \text{ s}^{-1} \text{ ster}^{-1} \text{ keV}^2$  at 200 km and the energy flux would be  $9 \times 10^{-3} \text{ ergs cm}^{-2} \text{ s}^{-1} \text{ ster}^{-1}$  for energies greater than 1 keV, and  $9 \times 10^{-4} \text{ ergs cm}^{-2} \text{ s}^{-1} \text{ ster}^{-1}$  for energies greater than 10 keV. Using this spectrum the total energy is an order of magnitude greater than the energy required to produce the electron-density profile on this night. A later section will show that the incident flux is not simply equal to the count rate of the detector divided by the geometrical factor but is reduced by a factor of approximately 0.16 so that the agreement is maintained.

Energetic electron spectrometers were launched on sounding rockets on

two occasions at Wallops Island near midnight. A detailed discussion of the count rate and energy spectrum measured on these flights has been given in Sections 4.1.2 and 4.1.3 and the electron-density profile (Figure 2.1) was discussed in Sections 2.1 and 2.3. The first rocket, Nike Apache 14.520, was launched at 2330 EST on 18 April 1974 during moderately disturbed conditions ( $K_p = 5+$ ). The integral count rate observed at 200 km altitude is 5000 counts  $s^{-1}$  for  $E > 12$  keV. The power law exponent was  $y = 3$  for  $10 < E < 100$  keV and estimated to be  $y \approx 1.6$  for  $E < 10$  keV. The geometrical factor of the detector is  $0.7 \text{ cm}^2 \text{ ster}$ .

For this case the flux is  $8.6 \times 10^3 \text{ cm}^{-2} \text{ s}^{-1} \text{ ster}^{-1}$  at 12 keV such that the integral flux constant  $J_{IO} = 4.5 \times 10^5 \text{ cm}^{-2} \text{ s}^{-1} \text{ ster}^{-1} \text{ keV}^{1.6}$  for  $y = 1.6$ . Using equation (9.8), the total energy flux is found to be  $1.2 \times 10^6 \text{ keV cm}^{-2} \text{ s}^{-1} \text{ ster}^{-1}$  or  $2 \times 10^{-3} \text{ ergs cm}^{-2} \text{ s}^{-1} \text{ ster}^{-1}$ . The energy flux between 10 and 100 keV ( $J_{IO} = 1.5 \times 10^7 \text{ cm}^{-2} \text{ s}^{-1} \text{ ster}^{-1} \text{ keV}^3$ ) is  $3.6 \times 10^{-4} \text{ ergs cm}^{-2} \text{ s}^{-1} \text{ ster}^{-1}$  for  $y = 3$ . This value can easily explain the ionization rates necessary to maintain the observed electron density.

Nike Apache 14.521 was launched 29 June 1974 during relatively quiet geomagnetic conditions ( $K_p = 3+$ ). The integral count rate observed at 200 km altitude was 600 counts  $s^{-1}$  for  $E > 13$  keV with a power law spectrum exponent  $y = 1.25$ . The geometrical factor of the detector is  $0.6 \text{ cm}^2 \text{ ster}$ .

For this case the flux is 860 counts  $\text{cm}^{-2} \text{ s}^{-1} \text{ ster}^{-1}$  at 13 keV and the integral flux constant,  $J_{IO} = 2.1 \times 10^4 \text{ cm}^{-2} \text{ s}^{-1} \text{ ster}^{-1} \text{ keV}$ . Using equation (9.8), the total energy flux is  $10^{-4} \text{ ergs cm}^{-2} \text{ s}^{-1} \text{ ster}^{-1}$ . The energy flux between 10 and 100 keV is  $4 \times 10^{-5} \text{ ergs}$ .

**9.5.2 Detailed calculations of energy flux.** It is shown in equations (7.3), (7.5) and (7.6) that the incident flux,  $F$ , for a linearly increasing count-rate profile with altitude is given by

$$F = I_0 E^{-x} \sqrt{z_m - z_0} \text{ cm}^{-2} \text{ s}^{-1} \text{ keV}^{-1} \text{ km}^{-1} \quad (9.19)$$

where  $F$  is the number of particles which pass through one square centimeter perpendicular to the magnetic field in one second with an energy  $E$  and with mirroring heights in an increment of altitudes of 1 km between  $z_m(z)$  and  $z_m(z+1)$ . The units of  $I_0$  are  $\text{cm}^{-2} \text{ s}^{-1} \text{ keV}^{x-1} \text{ km}^{-3/2}$  and  $z_0$  is the lowest altitude at which mirroring particles are observed. The flux,  $F$ , in terms of the count-rate profile is given by equations (7.5) and (7.6)

for  $x > 1$

$$C = \frac{mA_d}{2(x-1)} \sqrt{\frac{R_0}{3}} I_0 (a-z_0) \left[ \frac{1}{E_L^{x-1}} - \frac{1}{E_H^{x-1}} \right] \quad (9.20)$$

and for  $x = 1$

$$C = \frac{mA_d}{2} \sqrt{\frac{R_0}{3}} I_0 (a-z_0) \ln \frac{E_H}{E_L} \quad (9.21)$$

where the parameters are defined after equation (7.3)

The count rate measured by a detector looking nearly perpendicular to the magnetic field direction may be related to the total downward flux of quasi-trapped particles,  $F_T$ . This flux is obtained by integrating equation (9.19) over energies from  $E_L$  to  $\infty$ , over mirror heights from  $z_0$  to  $a$ , and over the equivalent area of the detector  $A_d$ . The result is

$$F_T = \frac{2I_0 (a-z_0)^{3/2}}{3(x-1)E_L^{x-1}} A_d \quad (9.22)$$

By eliminating  $I_0$  from equations (9.20) and (9.22) the total flux may be given in terms of the count rate,  $C$ , as

$$F_T = \frac{4C}{3m} \sqrt{\frac{3(\alpha - z_o)}{R_o}} \quad (9.23)$$

For  $z_o = 120$  km,  $\alpha = 200$  km,  $R_o = 6370$  km and  $m = 0.5$  the total flux  $F_T = 0.52$  C. Thus, for particles mirroring in a dipole field the total flux incident in a column with area equal to the detector area is about half the count rate measured by the detector when mounted perpendicular to the rocket axis.

In other words, this result states that for an energetic electron (e.g., 10 keV) the projected area of the detector ( $445 \text{ cm}^2$  for a detector area of  $0.5 \text{ cm}^2$  and  $m = 0.5$  according to equation 3.23) is compensated for by the probability,  $P_1$ , of a particle, within this area colliding with the detector as given by equations (3.21) and (3.22). For the case of a 10 keV particle the probability  $P_1 = 8.16 \times 10^{-3} / \sqrt{\alpha - z_m}$  and for  $\alpha - z_m = 50$  km the value of  $P_1$  is  $1.2 \times 10^{-3}$ . Hence these two effects nearly cancel and give a ratio of 0.6 at 10 keV.

For Nike Apache 14.520 the count rate is  $5000 \text{ sec}^{-1}$ ,  $E_L = 12$  keV,  $y = 2$ ,  $A_d = 0.5 \text{ cm}^2$ ,  $\alpha = 200$  km,  $z_o = 120$  km and  $m = 0.5$ . Solving equation (9.20) for  $I_o$  gives

$$I_o = \frac{2(x-1)E_L^{x-1}C}{mA_d(\alpha - z_o)} \sqrt{\frac{3}{R_o}} \text{ cm}^{-2} \text{ s}^{-1} \text{ keV}^2 \text{ km}^{-3/2} \quad (9.24)$$

which gives  $I_o = 3125 \text{ cm}^{-2} \text{ s}^{-1} \text{ keV}^2 \text{ km}^{-3/2}$ . This is the flux constant to be used in calculating ionization rates.

The total energy of the incident flux may be obtained by taking the integral

$$E_T = \int_{z_0}^{\alpha} \int_{E_1}^{E_2} FE dE dz_m = I_0 \int_{z_0}^{\alpha} \int_{E_1}^{E_2} E^{1-x} \sqrt{z_m - z_0} dz_m dE \quad (9.25)$$

which becomes for  $x \neq 2$

$$E_T = (2/3) \frac{I_0}{x-2} (\alpha - z_0)^{3/2} (E_1^{2-x} - E_2^{2-x}) \quad (9.26)$$

and for  $x = 2$

$$E_T = (2/3) I_0 (\alpha - z_0)^{3/2} \ln \frac{E_2}{E_1} \quad (9.27)$$

For the case under consideration  $x = 3$  and  $I_0 = 3125 \text{ cm}^{-2} \text{ s}^{-1} \text{ keV}^{-2} \text{ km}^{-3/2}$ . This gives a total column energy for  $E_1 > 1 \text{ keV}$ , using equation (9.26), of  $2.4 \times 10^{-3} \text{ ergs cm}^{-2} \text{ s}^{-1}$ . This energy input will produce 5.5 ion pairs  $\text{cm}^{-3}$ , from equation (9.7), over the region 120 to 200 km. This ionization rate agrees with that independently calculated from the electron-density profile for this night.

The various energy fluxes obtained using equation (9.7) for Kp = 3+, 5+ and 8 are shown in Figure 2.8 and clearly indicate the ionization rate deduced from the electron-density profile is proportional to the particle energy flux. The particle energy flux at Wallops Island may therefore be expressed as

$$E_T = 3 \times 10^{-5} \exp(0.7 \text{ Kp}) \text{ ergs cm}^{-2} \text{ s}^{-1} \quad (9.28)$$

9.5.3 *Calculations of ionization rates.* For a quasi-trapped distribution of energetic electrons as represented by equation (9.19) the energy absorbed within the atmosphere is a strong function of the energy spectrum. For electrons with energy of a few keV the atmosphere below 200 km absorbs essentially all of the incident energy as the particles mirror. For higher

energy electrons only a small portion of the original energy is lost and the majority of high energy particles are able to magnetically reflect.

The computer program described in Section 9.2.3 was used to calculate the total energy loss of 477 electrons of the same incident energy having a square-root mirror-height distribution. These results are shown in Figure 9.17 for a range of incident energy of 1 to 100 keV. Also shown is the total incident energy for electrons of energy  $E$  given by

$$E_t = E \int_{z_0}^{\alpha} z_m^{-z_0} dz_m = 477 E$$

for  $\alpha = 200$  km and  $z_0 = 120$  km. For energies less than 6 keV most of the incident energy is absorbed, for energies greater than 6 keV only a fraction is absorbed. In a power law spectrum with the majority of particles below 10 keV over half of the initial energy is absorbed. These calculations are made in the computer program

The ionization rates derived from the calculations of Section 9.4 were shown in Figure 9.16. For  $\alpha = 2$  the incident flux constant for the calculation is  $I_0 = 2 \times 10^4 \text{ cm}^{-2} \text{ s}^{-1} \text{ keV km}^{-3/2}$  and therefore to adjust the ionization rate of Figure 9.16 to the incident flux constant appropriate to the data from Nike Apache 14.520 the values in that figure should be multiplied by  $3125/2 \times 10^4 = 0.16$ . If the ionization rate is desired in units of  $\text{cm}^{-3} \text{ s}^{-1}$  the scale factor of the ionization rate is  $0.16 \times 10^{-5}$ . From Figure 9.16, with  $\alpha = 2$ , the ionization rate changes from  $3 \times 10^6$  ion-pairs per km at 130 km to  $10^7$  ion pairs per km at 200 km. The production rate for the case of Nike Apache 14.520 is thus between 5 and 16 ion pairs  $\text{cm}^{-3} \text{ s}^{-1}$ . This is in close agreement with the ionization rates deduced from the electron-density profile of Figure 2.8, which fall between 4 and 6 ion pairs  $\text{cm}^{-3} \text{ s}^{-1}$ .

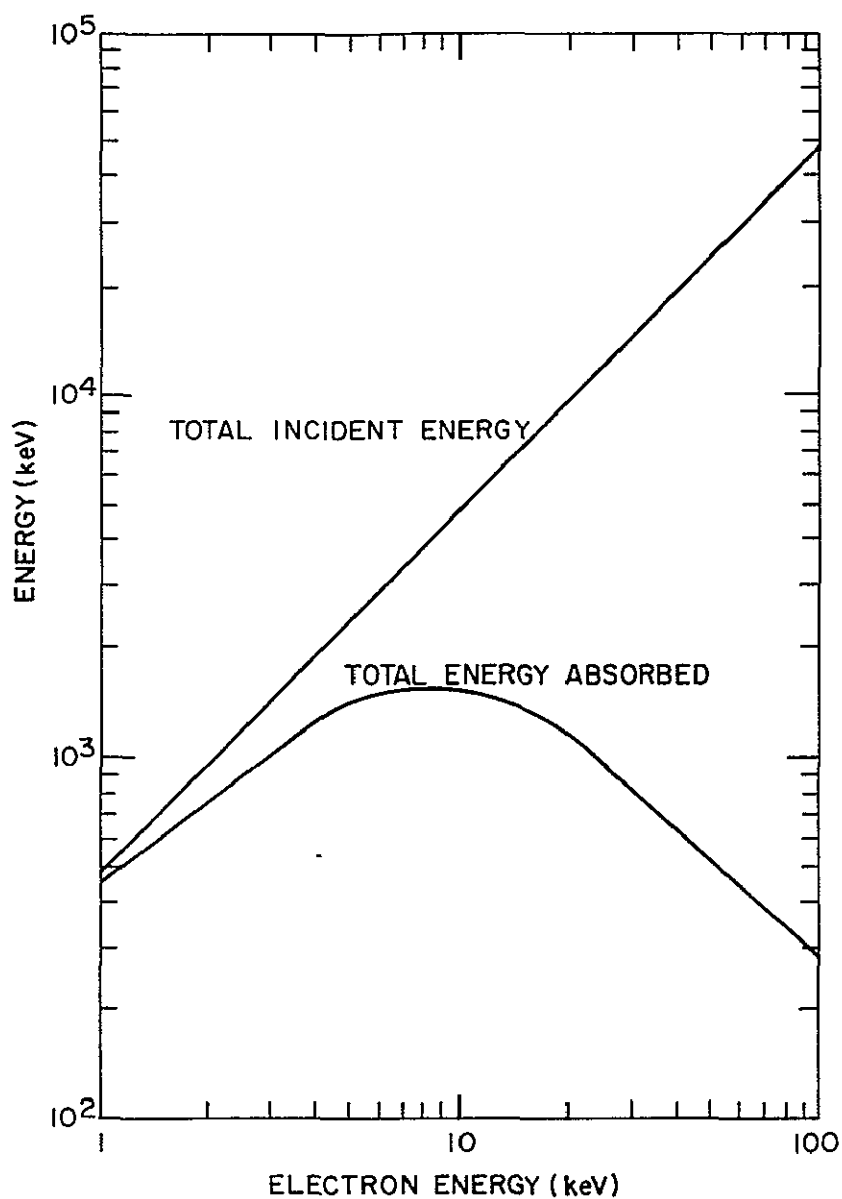


Figure 9.17 For a square-root mirror-height distribution of energetic electrons the energy absorbed versus the incident energy is compared in this figure for different initial energies. The energies are computed for 5000 electrons incident on the atmosphere.

*c-f*



In summary, ionization rates obtained by the electron-density method (Section 2.3), energy method (Section 9.5.1) and flux method (Section 9.5.2) for Nike Apache rockets 14.439, 14.520 and 14.521 are compared in Table 9.1. The close agreement between the energy and flux methods with the electron-density method establishes that energetic particles are the primary ionization source at night in the region 120 to 200 km at Wallops Island for  $K_p \geq 3$ .

9.5.4 *Comparison with ionization rates due to UV.* The altitude variation of the count-rate profile is a function of the energy spectrum and pitch-angle distribution. For the case of quasi-trapped particles the pitch-angle distribution is represented as a square-root mirror-height distribution (equation 9.19). The variation of the ionization rate with altitude is calculated for  $x = 1, 2$  and  $3$  in Figure 9.16. For moderate values of  $K_p$  the energy spectrum exponent is 2 and therefore the ionization rate is approximately constant with altitude as shown in Figure 9.16 over the region 120 to 200 km.

The ion production rates versus altitude are shown in Figure 9.18 for  $K_p = 1, 2, 5$  and  $8$ . Also shown are the ionization rates of Ly- $\alpha$ , Ly- $\beta$ , He I and He II computed by *Ogawa and Tohmatsu* [1966] (dashed line) and the production rates computed by *Strobel et al.* [1974] for  $O_2^+$  and  $NO^+$  ionization caused by terrestrial and extraterrestrial sources of Ly- $\beta$ .

For  $K_p$  values greater than two the ionization rate due to quasi-trapped particle precipitation dominates over nighttime ultraviolet sources at Wallops Island in the region 120 to 200 km. For  $K_p$  equal to 8 the energetic electron ionization is two orders of magnitude greater than the UV sources. During very quiet geomagnetic conditions the UV sources may dominate.

Great care must be taken in translating these ionization rates to different locations due to the geomagnetic dependence of the particle flux. The particle source variation was described in Chapters 4, 5 and 6 and shows

Table 9.1  
Average Ionization Rates (120-200 km)

<div> <div>Rocket</div> <div><math>\text{cm}^{-3} \text{ s}^{-1}</math></div> </div>	14 439 (Kp=8)	14.520 (Kp=5+)	14.521 (Kp=3+)
$\bar{Q}_1$ electron density	35	5	0.6
$\bar{Q}_2$ energy method	21-60	8.8	0.4
$\bar{Q}_3$ flux method	--	5 6	1.1

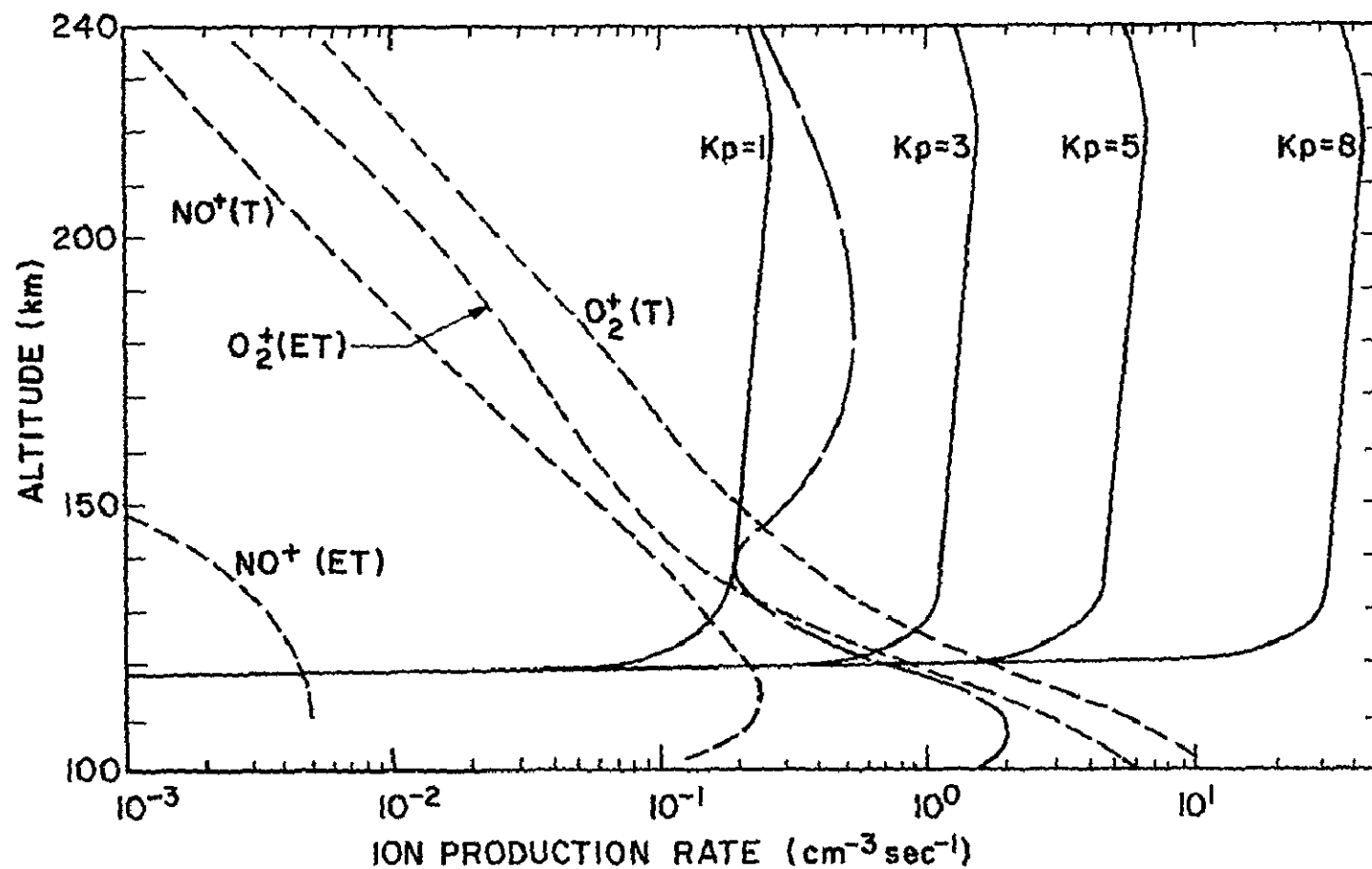


Figure 9.18 The ionization rate computed for energetic electrons for  $K_p = 1, 3, 5,$  and  $8$ . Also shown are the UV ionization rate calculations of *Ogawa and Tohmatsu* [1966] (large dashed line) and *Strobel et al.* [1974] (small dashed lines). For  $K_p \geq 3$  the ionization rate in the region 120 to 200 km at Wallops Island is predominantly due to energetic electrons. T and ET stand for terrestrial and extraterrestrial sources of UV.

various primary zones of ionization at midlatitudes. Wallops Island is in the center of the  $L = 2.6$  precipitation zone.

## 10 SUMMARY AND CONCLUSIONS

### 10.1 *Summary*

The main objectives of this study are to determine the relative importance of various nighttime ionization sources and in particular to investigate the complex phenomena of energetic particles at middle and low latitudes. The first study is concerned predominately with determining the importance of nighttime ultraviolet ionization versus energetic particle ionization at midlatitudes

In the region 90 to 110 km it is found that the nighttime ionization is primarily caused by Ly  $\beta$  radiation from the geocorona and interplanetary hydrogen. The constancy of this radiation between Kp values of 3 to 8 is evidenced in nearly constant electron densities over this region. Simultaneous rocket measurements show that the energetic electron flux is negligibly small below 120 km and is incapable of producing the observed electron densities ( $10^3 \text{ cm}^{-3}$ ). Below 90 km during disturbed conditions energetic electrons can be a significant ionization source.

On the other hand, energetic particles dominate as the ionization source in the region 120 to 200 km in certain midlatitude precipitation zones. Various rocket measurements made with a particle spectrometer indicate that the energetic electron flux increases linearly with altitude to significant intensities. For example, at times when the Kp = 8, the electron ionization is over 100 times greater in the Wallops Island precipitation zone ( $L = 2.6$ ) than is the ultraviolet ionization.

The particle energy flux is strongly dependent on the magnetic index Kp. For  $2 < Kp < 3$  the ionization due to energetic particles is about equal to the ultraviolet ionization rates ( $0.4 \text{ cm}^{-3} \text{ s}^{-1}$ ) at Wallops Island.

The particle flux at midlatitudes is maximized about  $90^\circ$  pitch angle and

consequently the particles are near their mirroring points. Since a mirroring particle travels a much greater distance in a height interval than a vertically incident or isotropic distribution of particles, the probability of collision is enhanced greatly as is the ionization.

The importance of latitude and longitude when referring to particle precipitation is discussed at length. A global precipitation map is developed in Chapter 7 which shows that particle precipitation occurs in zones centered on magnetic  $L$  shells. The Wallops Island precipitation zone is identified at  $L = 2.6$  and the Arecibo precipitation zone at  $L = 1.4$  in addition to an equatorial zone of protons. The cause of the midlatitude precipitation zones are believed to be the result of wave-particle interactions which scatter trapped radiation belt particles into quasi-trapped trajectories.

In the Southern Hemisphere the magnetic field strength is significantly reduced about the South Atlantic magnetic anomaly causing enhanced precipitation. The midlatitude precipitation zones at  $L = 1.4$  and  $L = 2.6$  explain the locations of the two intensity maxima observed in the South Atlantic anomaly region.

In Chapter 3 a method is developed to transform the particle count rate obtained with a rocket-borne particle detector to the actual incident flux. Previous techniques using the concept of a geometrical factor can seriously be in error for measuring particles which are near their mirroring heights.

At keV energies it is shown that the theoretical calculation used for multiple scattering are largely in error. An experimental apparatus was developed to measure the scattering of a beam of electrons in air. These results were then used to obtain profiles of mirror-height spreading as a function of altitude.

The altitude-count-rate profile implicitly includes the effects of

scattering when related to a pitch-angle distribution at the top of the atmosphere (200 km). This pitch-angle distribution is then used in a computer program to calculate the ionization rates due to energetic particles. These ionization rates are found to be in agreement with the ionization rates independently calculated from the electron-density profile.

## 10.2 Conclusions

The following are the main conclusions arrived at through this study

- 1) An ionization source is required to explain the observed nighttime electron-density profiles.
- 2) Ultraviolet radiation by Ly- $\beta$  and Ly- $\alpha$  is the principal ionization source in the region 90 to 110 km at middle and low latitudes even under rather disturbed geomagnetic conditions.
- 3) The ionization rate in the altitude region 120 to 200 km can be enhanced over UV sources by more than a factor of 100 depending on the Kp index. Rocket measurements have confirmed that energetic electrons are the principal ionization source for Kp  $\geq$  3 at Wallops Island.
- 4) The intermediate layer is a result of electron redistribution due to a tidal wind system. For this layer an average ionization rate may be calculated which is independent of diffusion and transport terms. The intermediate layer electron-density profile may also be used to calculate the convergent ion wind velocities.
- 5) A new technique is developed to analyze the count rates from a rocket-borne instrument which is measuring a quasi-trapped distribution of particles. The standard method of analysis using a geometrical factor may give largely inaccurate results.
- 6) The count-rate profile at midlatitudes increases linearly with

altitude in the region 120 to 200 km. The altitude intercept of the count-rate profile is a function of atmospheric density and increases in altitude with an increase in magnetic activity at Wallops Island. The energetic particles have a pitch-angle distribution which is near  $90^\circ$  such that the majority of particles are in a magnetically reflecting state

- 7) The particle energy flux increases exponentially with magnetic index  $K_p$ . At Wallops Island the electron spectrum is well represented by a power law with exponent between 1 and 2.5. For  $K_p$  values between 3 and 6 the particle flux for  $E > 50$  keV remains approximately unchanged. For energies below 20 keV the particle flux depends strongly on  $K_p$ . For plasmopause crossing over a particular location the entire energy spectrum is increased.
- 8) Two precipitation zones have been identified at midlatitudes. The Wallops Island precipitation zone is centered at  $L=2.6$  and the Arecibo precipitation zone is centered at  $L=1.4$ . A precipitation null exists at  $L=1.8$  which is the situation for White Sands.
- 9) At the equator a proton zone exists with count rates beginning near 170 km altitude. The flux is maximized about  $90^\circ$  pitch angle. The flux depends strongly on magnetic activity and is believed to be associated with a double charge exchange mechanism of the ring current.
- 10) In the South Atlantic Magnetic anomaly the locations of maximum precipitation are associated with the precipitation zones at  $L=1.4$  and  $L=2.6$ .
- 11) Many previous theoretical calculations of multiple scattering by the atmosphere of electrons at keV energies are incorrect because of the use of a Gaussian distribution approximation. New experimental measurements were made which give the electron beam spreading as a function of atmospheric depth. These new data were used in subsequent



calculations of mirror-height scattering

- 12) A pitch-angle distribution may be obtained for the top of the atmosphere (i.e., 200 km altitude) from the count-rate profile which implicitly takes into account the effects of atmospheric scattering for a quasi-trapped distribution of particles.

### 10.3 *Suggestions for Future Work*

Global satellite measurements are needed at altitudes of approximately 200 km using particle detectors with fairly large geometrical factors. The satellite should have a polar orbit and be properly spun to obtain necessary pitch-angle information. The global precipitation map shown in Figure 7.17 needs to be verified and refined to include particle precipitation variations for different values of  $K_p$  and altitude. Continued coordination is needed between satellite and rocket measurements to relate vertical count-rate profiles to the horizontal count-rate profiles from satellites.

Rockets instrumented with an energetic-particle spectrometer, electron-density probe and 391.4 nm photometer are needed to study the morphological characteristics of the midlatitude precipitation zones. Specifically, a sounding rocket should be launched near Arecibo, Puerto Rico, to establish the existence of the  $L = 1.4$  zone and to relate these measurements to the observations made simultaneously with the Arecibo radar.

Further rocket measurements are necessary to substantiate the characteristics of the proton zone at the equator. At present no rocket information is available at the equator for energetic particles at altitudes greater than 200 km.

Midlatitude rocket experiments are needed to understand the relative importance of energetic electron and proton precipitation during the main phase and recovery phase of a magnetic storm. During the main phase, for

example, the ring current ( $L \approx 2.5$ ) fills up with energetic protons in the same  $L$ -shell region as the Wallops Island precipitation zone. Various pitch-angle scattering processes could simultaneously cause ring current protons to move along magnetic field lines into quasi-trapped and precipitated trajectories. The low latitude region extending to the Arecibo precipitation zone could be dominated by energetic protons from the double charge exchange reaction of neutral hydrogen with the ring current. The magnitude, energy spectrum, pitch-angle distribution and temporal and spacial variations of the particle flux need to be understood.

The rocket-borne energetic particle measurements made by the USSR experimenters show quite different results from the Wallops Island experiments. In particular the USSR experiments show significant  $D$ -region particle intensities whereas the flux at Wallops Island is only significant in the upper  $E$  region. A coordinated experiment is needed between the USA and USSR probes in both countries to understand the geographical variations on a global scale and the experimental uncertainties.

A more accurate theoretical analysis of the interaction of quasi-trapped particles with the atmosphere is required using the Boltzmann equation techniques and the Monte Carlo simulation method. The effects of mirroring and atmospheric scattering must be rigorously included for an incident pitch-angle distribution which is maximized near  $90^\circ$

## REFERENCES

- Aikin, A. C., R. A. Goldberg, W. Jones, J. A. Kane (1976), Observations of the midlatitude lower ionosphere in winter, Goddard Space Flight Center, X-625-76-70, Technical Information Div , 1-12.
- Akasofu, S. I (1967), The auroral oval and the internal structure of the magnetosphere, in *Aurora and Airglow*, p 267, B. M. McCormac (ed), Reinhold Publ., New York.
- Allan, R R (1974), Response of dayside thermosphere to an intense geomagnetic storm, *Nature*, 247, 23-25
- Anderson, R R and K. Maeda (1977), VLF emissions associated with enhanced magnetospheric electrons, *J. Geophys. Res.*, 82, 135-146
- Antonova, L. A. and G. S. Ivanov-Kholodny (1961), Corpuscular hypothesis for the ionization of the night ionosphere, *Geomagnet Aeron* , 1, 149-156
- Antonova, L A , G S. Ivanov-Kholodny, and V S Medvedev (1969), Electron flux energy spectrum measurements in the middle latitude upper atmosphere, *Cosmic Res.*, 7, 852-854
- Antonova, L. A., and G S. Ivanov-Kholodny (1972), Rocket measurements of electron fluxes in the upper atmosphere at midlatitudes, *Aeron Rep. No. 48*, Aeron Lab., Dep Elec Eng., Univ Ill , Urbana-Champaign, 127-133
- Antonova, L. A., G S Ivanov-Kholodny, and V S Medvedev (1973), Measurements of the energy spectrum of electrons of 0.5 - 24 keV at heights of 80 - 170 km at middle latitudes on October 21, 1970, *Geomagnet Aeron.*, 13, 712-714.
- Armstrong, T. (1965), Morphology of the outer zone electron distribution at low altitudes from January through July and September 1963 from Injun 3, *J. Geophys Res.*, 70, 2077-2102
- Axford, W I (1967), The interaction between the solar wind and the magnetosphere, in *Aurora and Airglow*, p 499, B. M. McCormac (ed), Reinhold

Publ , New York

Banks, P M , and A. F. Nagy (1970), Concerning the influence of elastic scattering upon photoelectron transport and escape, *J. Geophys. Res.*, 75, 1902-1910.

Behnke, R A (1970), Vector measurements of the ion transport velocity with applications to F region dynamics, Ph D thesis, Rice University, Houston, Texas.

Behnke, R., and R M. Harper (1973), Vector measurements of F region ion transport at Arecibo, *J. Geophys. Res.*, 78, 8222-8234

Belrose, J. S., and L. Thomas (1968), Ionization changes in the middle latitude D region associated with geomagnetic storms, *J. Atmos Terr. Phys* , 30, 1397-1413

Berger, M J , S M. Seltzer, and K Maeda (1970), Energy depositon by auroral electrons in the atmosphere, *J Atmos. Terr. Phys* , 32, 1015-1045

Berger, M J , and S. M Seltzer (1974), Some new results on electron transport in the atmosphere, *J. Atmos. Terr. Phys.*, 36, 591-617.

Bethe, H (1930), Zur theorie des durchgangs schneller korpuskularstrahler durch materie, *Ann d Phys.*, 5, 325

Biondi, M A. (1969), Atmospheric electron-ion and ion-ion recombination processes, *Can. J Chem.*, 47, 1711-1722

Blake, J B. (1976), On the ionic identity of the ring current particles, *J Geophys. Res.*, 81, 6189-6192

Broadfoot, A L , and D. M Hunten (1966),  $N_2^+$  emission in the twilight, *Planet. Space Sci* , 14, 1303-1319.

Butenko, V. D , O R. Griguryan, S N Kuznetsov, G S Malkiel', and V G Stolpovskii (1975), Proton currents with  $E_p \gg 0$  keV at low altitudes in the equatorial region, *Cosmic Res* , 13, 457-460

- Carruthers, G. R. , T. Page, and R. R. Meier (1976), Apollo 16 Lyman alpha imagery of the hydrogen geocorona, *J. Geophys. Res.*, **81**, 1664-1672.
- Chastovitin, Yu. K. , and V. P. Nesterov (1976), Some questions of the nighttime ionospheric E region formation in middle latitudes, *Planet. Space Sci.*, **24**, 139-145.
- Cicerone, R. J. , and S. A. Bowhill (1971), Photoelectron fluxes in the ionosphere by a Monte Carlo method, *J. Geophys. Res.*, **76**, 8299-8317.
- Cicerone, R. J. , W. E. Swartz, R. S. Stolarski, A. F. Nagy, and J. S. Nisbet (1973), Thermalization and transport of photoelectrons. A comparison of theoretical approaches, *J. Geophys. Res.*, **78**, 6709-6728.
- CIRA (1972), *COSPAR International Reference Atmosphere*, Akademie-Verlag, Berlin.
- Cladis, J. B. , L. F. Chase, Jr., W. L. Imhof, and D. J. Knecht (1961), Energy spectrum and angular distribution of electrons trapped in the geomagnetic field, *J. Geophys. Res.*, **166**, 2297-2312.
- Cladis, J. B. , G. T. Davidson, W. E. Francis, L. L. Newkirk, and M. Walt (1973), Ionospheric disturbances affecting radio-wave propagation, *Final Rep. DNA 3103F*, Lockheed Palo Alto Research Laboratory, Palo Alto, California, 1-79.
- Cladis, J. B. , W. E. Francis, G. T. Davidson, and M. Walt (1976), Ionospheric effects resulting from precipitating electrons at mid and high latitudes, *Rep. DNA 3884F*, Lockheed Palo Alto Research Laboratory, Palo Alto, California, 1-64.
- Constantinides, E. , and J. F. Bedinger (1971), Observed redistribution of E-region ionization by neutral winds, *J. Atmos. Terr. Phys.*, **33**, 461-472.
- Cornwall, J. M. (1971), Transport and loss processes for magnetospheric Helium, *J. Geophys. Res.*, **76**, 264-267.
- Dalgarno, A. (1964), Corpuscular radiation in the upper atmosphere, *Ann. Geophys.*, **20**, 65-74.

- Dalgarno, A., M. B. McElroy, and R. J. Moffett (1963), Electron temperatures in the ionosphere, *Planet. Space Sci.*, **11**, 463-484.
- Davidson, G. T., and M. Walt (1977), Loss cone distributions of radiation belt electrons, *J. Geophys. Res.*, **82**, 48-54.
- DeVries, L. L. (1972a), Analysis and interpretation of density data from the low-G accelerometer calibration system (LOGACS), *Space Res. XII*, 777-789.
- DeVries, L. L. (1972b), Structure and motion of the thermosphere shown by density data from the low-G accelerometer calibration system (LOGACS), *Space Res. XII*, 867-879.
- Doherty, R. H. (1971), Observations suggesting particle precipitation at latitudes below 40°N, *Radio Sci.*, **6**, 639-646.
- Donahue, T. M. (1966), Ionospheric reaction rates in light of recent measurements in the ionosphere and the laboratory, *Planet. Space Sci.*, **14**, 33-48.
- Dungey, J. W. (1963), Loss of Van Allen electrons due to whistlers, *Planet. Space Sci.*, **11**, 591-595.
- Dungey, J. W. (1967), Magnetohydrodynamics in the magnetosphere, in *Proc. of the Birkeland Symposium on Aurora and Magnetic Storms*, p. 431, A. Egeland and J. Holtet (eds), CNR.
- Evans, D. S. (1974), Precipitating electron fluxes formed by a magnetic field aligned potential difference, *J. Geophys. Res.*, **79**, 2853-2858.
- Evans, J. V. (1973), Millstone Hill Thomson scatter results for 1966 and 1967, *Planet. Space Sci.*, **21**, 763-792.
- Fan, C. Y., P. Meyer, and J. A. Simpson (1961), Dynamics and structure of the outer radiation belt, *J. Geophys. Res.*, **66**, 2607-2640.
- Ferguson, E. E., F. C. Fehsenfeld, P. D. Goldan, and A. L. Schmeltekopf (1965), Positive ion-neutral reactions in the ionosphere, *J. Geophys. Res.*, **70**, 4323-4329.

- Fermi, E (1958), *Nuclear Physics*, A course given by Enrico Fermi, Univ. Chicago Press, 27-43
- Frank, L A (1967), On the extraterrestrial ring current during geomagnetic storms, *J Geophys. Res.*, 72, 3753-3767
- Frank, L. A , J A. Van Allen, and H. K Hills (1964), A study of charged particles in the earth's outer radiation zone with Explorer 14, *J. Geophys Res.*, 60, 2171-2191
- Freeman, J W (1962), Detection of an intense flux of low-energy protons or ions trapped in the inner radiation zone, 1962, *J. Geophys. Res.*, 67, 921-928
- Freyer, G. J (1969), Bremsstrahlung in the lower ionosphere, *Iono. Res Sci Rep.*, 336, Iono. Res. Lab , University Park, Penn
- Fujitaka, K (1974), Modelling of the wind-perturbed middle ionosphere, *J Atmos Terr Phys.*, 36, 1883-1890
- Fujitaka, K , T Ogawa, and T Tohmatsu (1971), A numerical computation of the ionization redistribution effect of the wind in the nighttime ionosphere, *J. Atmos. Terr. Phys.*, 33, 687-700
- Fujitaka, K , and T Tohmatsu (1973), A tidal theory of the ionospheric intermediate layer, *J Atmos. Terr. Phys.*, 35, 425-438
- Geller, M A , L. G. Smith, and H D Voss (1975), Analysis of nighttime E-region winds and ionization production, *Radio Sci.*, 10, 335-345
- Gendrin, R. (1975), Waves and wave-particle interactions in the magnetosphere A review, *Space Sci. Rev.*, 18, 145-200.
- Ginzburg, V L , L V Kurnosova, V I Logachev, A A Razorerov, I A Sirotkin, and M I Fradkin (1962), Investigation of charged particle intensity during the flights of the second and third space ships, *Planet. Space Sci.*, 9, 845-854

- Gledhill, J A , and G. E. Daves (1976), Electron fluxes in the range 1 - 25 keV observed over the South Atlantic anomaly by Injun 5, presented at COSPAR meeting, 1976
- Goldberg, R A (1974), Rocket observations of soft energetic particles at the magnetic equator, *J. Geophys. Res.*, 79, 5299-5303.
- Goldberg, R. A., A C. Aikin, and B. V. Murthy (1974), Ion composition and drift observations in the nighttime equatorial ionosphere, *J. Geophys. Res.*, 79, 2473-2477
- Goldberg, R. A , W H. Jones, P. R Williamson, J. R. Barcus, and L C. Hale (1976), Equatorial X-rays and their effect on the lower mesosphere, Goddard Space Flight Center Preprint X-912-76-166, 1-10
- Gough, M P (1975), Particle precipitation in the South Atlantic anomaly deduced from VLF propagation path measurements, *J. Atmos. Terr. Phys.*, 37, 1379-1383
- Gough, M P , and H. L Collin (1973), Energetic electron precipitation as a source of ionization in the nighttime D-region over the mid-latitude rocket range, South Uist, *J Atmos. Terr. Phys.*, 35, 835-850
- Grün, A E. (1957), Lumineszenz-photometrische messungen der energie absorption in strahlungsfeld von elektronenguellen eindimensionaler fall in Luft, *Zeitschrift fur Naturforschung*, 124, 89-95.
- Harper, R M , R H Wand, and J. D Whitehead (1975), Comparison of Arecibo E-region data and sporadic E theory A measurement of the diffusion coefficient, *Radio Sci.*, 10, 357-361
- Hasegawa, A. (1969), Heating of the magnetospheric plasma by electromagnetic waves generated in the magnetosheath, *J. Geophys. Res.*, 74, 1763-1771.
- Hasegawa, A (1976), Particle acceleration by MHD surface wave and formation of aurora, *J. Geophys* , 81, 5083-5090
- Hayakawa, S , H Iwanami, T. Murakami, F Nagase, Y Tanaka, and K Yamashita



- (1976), *Electron Precipitation Associated with A Magnetic Disturbance at Low L Values*, Akademie-Verlag, Berlin, 491-495.
- Hayakawa, S , T. Kato, T Kohno, T. Murakani, F. Nagase, K. Nishimura, and Y Tanaka (1973a), Suprathermal electrons near the lower edge of the radiation belt, *J. Geomag. Geoelectr.*, 25, 113-129.
- Hayakawa, S , T. Kato, T Kohno, T. Murakani, F. Nagase, K Nishimura, and Y Tanaka (1973b), Existence of geomagnetically trapped electrons at altitudes below the inner radiation belt, *J. Geophys. Res.*, 78, 2341-2343
- Heikkila, W J. (1971), Soft particle fluxes near the equator, *J. Geophys. Res.*, 76, 1076-1078.
- Heitler, W. (1954), *The Quantum Theory of Radiation*, 3rd ed , Clarendon Press, Oxford.
- Helliwell, R. A , J P Katsufrakis, T F Bell, and R Raghuram (1975), VLF line radiation in the earth's magnetosphere and its association with power system radiation, *J. Geophys. Res.*, 80, 4249-4258
- Hess, W N (1968), *The Radiation Belt and Magnetosphere*, Blaisdell Publ Co , Waltham, Massachusetts, 1-548
- Hill, R. W , R. J Grader F. D. Seward, and J. P. Stoering (1970), Soft particle flux above 130 km at midlatitude, *J. Geophys. Res.*, 75, 7267-7271
- Hirao, K , N. Wakai, K Sawada, T Hikosaka, K. Yano, and K. Maeda (1965) Some evidences of the particle effects on the ionosphere at middle latitudes, *Space Res.*, V, 1058-1070.
- Hoffman, R A., J L. Burch, R W Janetzke (1974), AE-LEE measurements at low and midlatitude, in *Proc. of the Workshop of Electron Contamination in X-ray astronomy experiments*, S. S. Hall (ed), Goddard Space Flight Center Rep X-661-74-130.

- Hoffman, R. A , and D. S Evans (1968), Field-aligned electron burst at high latitudes observed by OGO 4, *J. Geophys. Res.*, *73*, 6201-
- Holmes, J., C Y Johnson, and J M Young, (1965), Ionospheric chemistry, *Space Res.*, *V*, 756-766
- Hovestadt, D. B , B Hausler, and M Scholer (1972), Observations of energetic particles at very low altitudes near the geomagnetic equator, *Phys. Rev. Lett.*, *28*, 1340-1344.
- Imhof, W L (1968), Electron precipitation in the radiation belts, *J. Geophys. Res.*, *73*, 4167-4184.
- Imhof, W L , E E. Gaines, and J B Reagan (1974), Evidence for the resonance precipitation of energetic electrons from the slot region of the radiation belts, *J. Geophys. Res.*, *79*, 3141-3146
- Imhof, W L., T. R Larsen, J B Reagan, and E E Gaines (1976), Analysis of satellite data on precipitating particles in corrdination with ELF propagation anomalies, *Ann. Rep. LMSC-D502063*, Lockheed Palo Alto Res Lab., Palo Alto, California, 1-99.
- Imhof, W. L., G H. Nakano, E. E. Gaines, and J. B Reagan (1975), A coordinated two-satellite study of energetic electron precipitation events, *J. Geophys. Res.*, *80*, 3622-3628.
- Imhof, W L , G H. Nakano, R G Johnson, and J B Reagan (1974), Satellite observations of bremsstrahlung from widespread energetic electron precipitation events, *J. Geophys. Res.*, *79*, 565-574
- Ivanov-Kholodny, G S (1965), Maintenance of the night ionosphere and corpuscular fluxes in the upper atmosphere, *Space Res.*, *V*, 19-42
- Ivanov-Kholodny, G. S. (1970), State of research on the aeronomy of the

- ionospheric E- and D-regions (Review), *Geomagnet. Aeron.*, 10, 301-312.
- Ivanov-Kholodny, G. S., and T. V. Kazatchevskaya (1971), Ionization of the E-region by precipitating electrons, *J. Atmos. Terr. Phys.*, 33, 285-287.
- Ivanov-Kholodny, G. S., and L. P. Korsunova (1970), Additional ionization source in the ionospheric E-region. II, *Geomagnet. Aeron.*, 10, 578-580.
- Jackson, J. D. (1962), *Classical Electrodynamics*, John Wiley and Sons, New York.
- Kamiyama, H. (1966), Ionization and excitation by precipitating electrons, *Rep. Ionospheric Space Res. Japan*, 20, 171-187.
- Kazachevskaya, T. V. (1967), Measurements of the total energy of corpuscular radiation at 200 - 500 km height, *Cosmic Res.*, 5, 552-554.
- Kazachevskaya, T. V., and G. S. Ivanov-Kholodny (1965), Rocket data on the behavior of electron concentration in the ionosphere at heights of 100 - 300 km. I, *Geomagnet. Aeron.*, 5, 794-805.
- Kazachevskaya, T. V., and G. S. Ivanov-Kholodny (1966), Rocket data on the behavior of electron concentration in the ionosphere at heights of 100-300 km. II, *Geomagnet. Aeron.*, 6, 19-25.
- Kazachevskaya, T. V., and A. I. Koryagin (1969), Measurement of soft electron energy flux in the nighttime middle-latitude upper atmosphere, *Cosmic Res.*, 7, 950-952.
- Kelley, M. C., W. E. Swartz, Y. Tayan, and R. Torbert (1977), On the relationship between the plasma density profile measured in the equatorial E and F regions and simultaneous energetic particle and spread F observations, *J. Atmos. Terr. Phys.*, to be published.
- Kennel, C. F., and H. E. Petschek (1966), Limit on stably trapped particle fluxes, *J. Geophys. Res.*, 71, 1-28.

- Kohno, T (1973), Rocket observations of suprathermal electrons in the energy range 6.5-23 keV at midlatitude, *J. Geomag. Geoelectr.*, 25, 131-144
- Korsonova, L. P. (1973), Effect of geomagnetic disturbances on the mid-latitude nighttime E region, *Geomagnet Aeron*, 13, 708-711
- Kovtyukh, A. S., M. I. Panasyuk, E. N. Sosnovets, L. V. Tverskaya, and O. V. Khorosheva (1976), Enhancement of proton ring current during magnetic storms and local time asymmetry of low latitude magnetic disturbances, *Space Res.*, XVI, Akademie-Verlag, Berlin, 519-522
- Krassovsky, V. I., I. S. Shklovskii, Yu. I. Gal'perin, E. M. Svetlitskii, Yu. M. Kushnir, and G. A. Bordovskii (1962), The detection of electrons with energies of approximately 10 keV in the upper atmosphere, *Planet. Space Sci.*, 9, 27-40
- Krassovsky, V. I., Yu. L. Truttse, and N. N. Shefov (1965), On the mechanism of maintenance of the nocturnal ionosphere, *Space Res.*, II, Akademie-Verlag, Berlin, 43-48
- Kubo, H., T. Mukai, T. Itoh, and K. Hirao (1976), Rocket observation of low-energy electrons in the mid-latitude night-time ionosphere, *Space Res.*, XVI, Akademie-Verlag, Berlin, 497-501
- Larsen, T. R., J. B. Reagan, W. L. Imhof, L. E. Montribrand, and J. S. Belrose (1976a), A coordinated study of energetic electron precipitation and D region electron concentration over Ottawa during disturbed conditions, *J. Geophys. Res.*, 81, 2200-2212
- Larsen, T. R., W. L. Imhof, and J. B. Reagan (1976b), L-dependent energetic electron precipitation and mid-latitude D region ion pair production profiles, *J. Geophys. Res.*, 81, 3444-3446.
- Lazarev, V. I., B. V. Maryin, L. V. Tverskaya, and M. V. Teltsov (1976), Features of the 2 - 20 keV electron and proton flux distributions in the magnetosphere according to measurements from Molniya, 1, *Space Res*

- XVI, Akademie-Verlag, Berlin, 523-527.
- Lindalen, H. R., and A. Egeland (1972), Observations of trapped and precipitated protons on March 8, 1970, *Ann. Geophys.*, **28**, 129-135.
- Lyons, L. R., and R. M. Thorne (1973), Equilibrium structure of radiation belt electrons, *J. Geophys. Res.*, **78**, 2142-2149.
- Lyons, L. R., R. M. Thorne, and C. F. Kennel (1972), Pitch-angle diffusion of radiation belt electrons within the plasmasphere, *J. Geophys. Res.*, **77**, 3455-3474.
- Lyons, L. R., and D. J. Williams (1975a), The quiet time structure of energetic (35-560 keV) radiation belt electrons, *J. Geophys. Res.*, **80**, 943-950.
- Lyons, L. R., and D. J. Williams (1975b), Storm and poststorm evolution of energetic (35-560 keV) radiation belt electron distributions, *J. Geophys. Res.*, **80**, 3985-3994.
- MacDonald, W. M., and M. Walt (1961), Distribution function of magnetically confined electrons in a scattering atmosphere, *Ann. Phys.*, **15**, 44-62.
- MacLeod, M. A. (1966), Sporadic-E theory. I. Collision-geomagnetic equilibrium, *J. Atmos. Sci.*, **23**, 96-109.
- McKinley, W. A., and H. Feshbach (1948), The Coulomb scattering of relativistic electrons by nuclei, *Phys. Rev.*, **74**, 1759-1763.
- McEntire, R. W., R. A. Hendrickson, and J. R. Winckler (1974), Electron echo experiment 1. Comparison of observed and theoretical motion of artificially injected electrons in the magnetosphere, *J. Geophys. Res.*, **79**, 2343-2354.

- Maartense, I , and D M Hunten (1963), A note on  $N_2^+$  twilight and sunlit aurora, *Can J Phys.*, 41, 1729-1732
- Maeda, K (1962), On the heating of the polar upper atmosphere, *NASA Tech. Rep.*, NASA TR R-141, Washington, D. C., 1-53
- Maeda, K. (1965), Further study on possible effects of the dynamo-electric field on electrons trapped in the magnetosphere, *J. Geomag. Geoelectr.* 17, 1-21.
- Maehlum, B (1973), Particle precipitation: Scattering and absorption, in *Cosmical Geophysics*, A Egeland, Ø Holler, and A Omholt (eds), Universitetsforlaget ISBN 82-60-02256-0, Oslo, Norway, 211-219
- Mechtly, E. A , and L. G Smith (1970), Changes of lower ionosphere electron densities with solar zenith angle, *Radio Sci.*, 5, 1407-1412.
- Meier, R R , and P Mange (1970), Geocoronal hydrogen An analysis of the Lyman-alpha airglow observed from Ogo-4, *Planet Space Sci.*, 18, 803-821.
- Meier, R. R , and P Mange (1973), Spatial and temporal variations of the Lyman-alpha airglow and related atomic hydrogen distributions, *Planet. Space Sci.*, 21, 309-327
- Meier, R R , and C S. Weller (1972), EUV resonance radiation from helium atoms and ions in the geocorona, *J. Geophys. Res* , 77, 1190-1204
- Meier, R. R. and C. S. Weller (1973), Further observations of the 150-1500 Å airglow (abstract), *EOS Trans., AGU*, 54, 401
- Meier, R R , and C S Weller (1975), Observations of equatorial EUV bands Evidence for low-altitude precipitation of ring current helium, *J. Geophys Res* , 80, 2813-2818
- Miller, K L , and L G Smith (1977), Midlatitude sporadic-E layers, *Aeron Rep No. 76*, Aeron Lab , Dep Elec Eng , Univ Ill , Urbana-Champaign
- Mizera, P F , and J B. Blake (1973), Observations of ring current protons at low altitudes, *J. Geophys. Res* , 78, 1058-1062

- Moliere, G (1947), Theory der streuung schneller geladener Teilcher I,  
*Z. Naturforsch 2a*, 133.
- Moller, C. (1932), Zur theorie des durchgangs schneller elektronen durch  
 mateie, *Ann. d Phys.*, 14, 531.
- Moritz, J. (1972), Energetic protons at low equatorial altitudes: A newly  
 discovered radiation belt phenomenon and its explanation, *Z. Geophys.*,  
 38, 701
- Moritz, J (1973), Energetic protons at low L-values of the equatorial  
 magnetosphere, *Space Res. XIII*, Akademik-Verlag, Berlin, 669-674.
- Morse, F. A., and C. J. Rice (1976), Mid-latitude E region; An examination  
 of the existance of a corpuscular source, *J. Geophys. Res.*, 81, 2795-  
 2804.
- Mott, N. F. (1929), The scattering of fast electrons by atomic nuclei, *Proc.*  
*Roy. Soc.*, A124, 425-442.
- Mott, N. F. (1932), A polarisation of electrons by double scattering, *Proc.*  
*Roy. Soc. (London)*, A135, 429-458.
- Murphy, C. H., C. S. Wang, and J. S Kim (1975), Mirror height lowering of  
 trapped electrons by an inductive electric field, *J. Geophys. Res.*, 80,  
 1346-1348.
- Nagy, A. F., and P. M. Banks (1970), Photoelectron fluxes in the ionosphere,  
*J. Geophys. Res.*, 75, 6260-6270.
- Nakagawa, S., M. Tsukuda, A. Sasaki, K. Nagata, and T. Doke (1965), Obser-  
 vation of electron flux by L-3 rockets, *Rep. Ionosphere Space Res.*  
*Japan*, 19, 521-522.
- Narcisi, R. S , and A. D. Bailey (1965), Mass spectrometric measurements  
 of positive ions at altitudes from 64 to 112 kilometers, *J. Geophys.*  
*Res.*, 70, 3687-3700.

- Nesterov, V. P (1974), On the nighttime E-region ionization, *J. Atmos. Terr. Phys.*, 36, 1753-1758.
- Nicolet, M. (1965), Ionospheric processes and nitric oxide, *J. Geophys. Res.*, 70, 691-701.
- O'Brien, B J (1962), Lifetimes of outer-zone electrons and their precipitation into the atmosphere, *J. Geophys. Res.*, 67, 3687-3706.
- O'Brien, B. J. (1963), Review of studies of trapped radiation with satellite-borne apparatus, *Space Sci. Rev.*, 1, 415-484
- O'Brien, B. J (1964), High-latitude geophysical studies with satellite Injun 3. 3. Precipitation of electrons into the atmosphere, *J. Geophys. Res.*, 69, 13-43
- O'Brien, B. J (1965), Precipitation of electrons and protons into the atmosphere, in *Radiation Trapped in the Earth's Magnetic Field*, B M. McCormac (ed), D Reidel Publ , Dordrecht-Holland, 321-336
- O'Brien, B. J , F R Allum, and H. C. Goldwire (1965), Rocket measurements of midlatitude airglow and particle precipitation, *J. Geophys. Res.*, 70, 161-175
- Ogawa, T , and T Tohmatsu (1966), Photoelectronic processes in the upper atmosphere, II The hydrogen and helium ultraviolet glow as an origin of the nighttime ionosphere, *Rep. Ionospheric Space Res. Japan*, 20, 375-417
- Omholt, A (1973), Particle precipitation Ionization and excitation, in *Cosmical Geophysics*, A Egeland, Ø Holter, and A. Omholt (eds), Universitetsforlaget, Oslo, Norway
- Papadopoulos, K (1977), A review of anomalous resistivity for the ionosphere, *Rev. Geophys. Space Phys.*, 15, 113-127
- Papadopoulos, K , and T Coffey (1974), Anomalous resistivity in the auroral plasma, *J. Geophys. Res* , 79, 1558-1561



- Paulikas, G. A (1975), Precipitation of particles at low and middle latitudes, *Rev. Geophys. Space Sci.*, 13, 709-734.
- Paulikas, G. A , J B Blake, and S. C. Freden (1966), Precipitation of energetic electrons at middle latitudes, *J. Geophys. Res.*, 71, 3165-3172
- Pfister, W (1967), Auroral investigations by means of rockets, *Space Sci. Rev.*, 7, 642-688.
- Potemra, T. A., and T. J. Rosenberg (1973), VLF propagation disturbances and electron precipitation at mid-latitudes, *J. Geophys. Res.*, 78, 1572-1580
- Potemra, T A , and A J Zmuda (1970), Precipitating energetic electrons as an ionization source in the midlatitude nighttime D region, *J. Geophys. Res* , 75, 7161-7167.
- Potemra, T. A., and A. J. Zmuda (1972), Nightglow evidence of precipitating energetic electrons in the midlatitude nighttime D region, in *Aeron. Rep. No. 48*, Aeron Lab , Dep. Elec. Eng., Univ. Ill , Urbana-Champaign.
- Prag, A. B., F A Morse, and R J McNeal (1966), Nightglow excitation and maintenance of the nighttime ionosphere by low-energy protons, *J. Geophys. Res.*, 71, 3141-3154
- Prange, R., and J. Crifo (1977), Suprathermal particle observations in the nighttime ionosphere at low latitudes, *Geophys Res. Lett.*, 4, 141-144
- Prasad, R Y., and R N Singh (1972), Impact and bremsstrahlung photo-ionization due to precipitating electrons in the lower ionosphere, *Ann. Geophys.*, 28, 593-605
- Prolss, G W. (1973), Radiation production and energy deposition by ring current protons precipitated into the mid-latitude upper atmosphere, *Planet. Space Sci.*, 21, 1681-1690.
- Prolss, G W , K Najita, and P. C. Yuen (1973), Heating of the low-latitude

upper atmosphere caused by the decaying magnetic storm ring current,

*J Atmos Terr. Phys.*, 35, 1889-1901

Ratcliffe, J. A. (1972), *An Introduction to the Ionosphere and Magnetosphere*,  
Cambridge University Press, 1-256

Reagan, J B , J C Bakke, J R Kilner, J D Matthews, and W L Imhof  
(1973), A high resolution, multiple particle spectrometer for the  
measurement of solar particle events, *IEEE Trans. Nucl. Sci.*, NS-19,  
554-562

Rees, M H (1963), Auroral ionization and excitation by incident energetic  
electrons, *Planet. Space Sci.*, 11, 1209-1218

Reeve, C. D , and M J. Rycroft (1976), Unducted VLF energy from tropical  
lightning as a possible source of mid-latitude VLF emissions and electron  
precipitation, *J Geophys. Res.*, 81, 6201-6202

Reder, F H , and S Westerlund (1970), VLF signal phase instabilities pro-  
duced by propagation medium Experimental results, phase and frequency  
instabilities in electromagnetic wave propagation, *AGARD Conf. Proc.*, 33,  
103-136.

Roederer, J G , J A. Welch, and J V Herod (1967), Longitude dependence  
of geomagnetically trapped electrons, *J Geophys. Res* , 72, 4431-4447

Rycroft, M J. (1973), Enhanced energetic electron intensity associated with  
a whistler propagating through the plasmasphere, *Space Res* , XIII,  
Akademie-Verlag, Berlin, 707-709

Salah, J E , R H Wand, and J V Evans (1975), Tidal effects in the E  
region from incoherent scatter radar observations, *Radio Sci* , 10, 347-  
356

- Scholer, M , D Hovestadt, and G. Morfill (1975), Energetic  $\text{He}^+$  ions from the radiation belt at low altitudes near the geomagnetic equator, *J. Geophys. Res.*, **80**, 80-85.
- Schulz, M , and L. J Lanzerotti (1974), *Particle Diffusion in the Radiation Belts*, Springer-Verlag, New York, 1-215
- Seward, F D , and H N Kornblum, Jr (1963), Near-earth charged-particle backgrounds measured with polar orbiting satellites, University of California, Lawrence Radiation Laboratory, California, *UCRL-6693*.
- Seward, F. D. (1973), The geographical distribution of  $\sim$  keV electrons above the earth's atmosphere, University of California, Lawrence Livermore Laboratory, Livermore, *UCRL-51456*, 1-10.
- Seward, F D., R J Grader, A Toor, G A. Burginyon, and R W. Hill (1973), Electrons at low altitudes A difficult background problem for soft S-ray astronomy, University of California, Lawrence Livermore Laboratory, *UCRL-51470*, 1-29.
- Shen, J S., W E. Swartz, D. T. Farley, and R. M Harper (1976), Ionization layers in the nighttime E-region valley above Arecibo, *J. Geophys. Res.*, **81**, 5517-5526
- Shibaeva, L V , and S. G. Yakovley (1976), Experimental investigation of the anomalous radiation event in the upper atmosphere of the middle latitudes, *Space Res* , **XVI**, Akademie-Verlag, Berlin, 503-507
- Smith, L G (1969), Langmuir probes in the ionosphere, in *Small Rocket Instrumentation Techniques*, North-Holland Publ , Amsterdam, 1-15
- Smith, L G. (1970), A sequence of rocket observations of nighttime sporadic E, *J. Atmos Terr. Phys* , **32**, 1247-1257
- Smith, L. G., M. A. Geller, and H D Voss (1974), Energetic electrons in

- the midlatitude nighttime E region, *J. Atmos. Terr. Phys.*, **36**, 1601-1612
- Smith, L. G., and H. D. Voss (1976), Ionization by energetic electrons in the midlatitude nighttime E region, *Space Res*, **XVII**, 427-432.
- Spjeldvik, W. N. (1976), The equilibrium radiation belt electron pitch angle distribution and its dependence on the radial diffusive source, *J. Geophys. Res.*, **81**, 2931-2934.
- Spjeldvik, W. N. (1977), Equilibrium structure of equatorially mirroring radiation belt protons, *J. Geophys. Res.*, **82**, 2801-2808
- Stadsness, J., and B. Maehlum (1965), Scattering and absorption of fast electrons in the upper atmosphere, *Intern Rapport E-53*, Norwegian Defence Research Establishment.
- Stair, A. T., Jr., and H. P. Gauvin (1967), *Aurora and Airglow*, B. M. McCormac (ed), Reinhold Publ. Co., New York, 365
- Standford, P. B. (1968), Variations of auroral emissions with time, magnetic activity and solar cycle, *J. Atmos. Terr. Phys.*, **30**, 1921-1942.
- Stolarski, R. S. (1968), Calculation of auroral emission rates and heating effects, *Planet. Space Sci.*, **16**, 1265-1276
- Strickland, D. J., D. L. Book, T. P. Coffey, and J. A. Fedder (1976), Transport equation techniques for the deposition of auroral electrons, *J. Geophys. Res.*, **81**, 2755-2764
- Strobel, D. F., T. R. Young, R. R. Meier, T. P. Coffey, and A. W. Ali (1974), The nighttime lower ionosphere, *J. Geophys. Res.*, **79**, 3171-3178
- Swartz, W. E. (1976), Thermalization and transport of photoelectrons: A comparison of theoretical approaches 2. Transport details for isotropic scattering, *J. Geophys. Res.*, **81**, 183-192
- Swider, W. (1972), E-region model parameter, *J. Atmos. Terr. Phys.*, **34**, 1615-1626

- Thomas, G E., and R F. Krassa (1971), Measurement of the Ly- $\alpha$  sky background, *Astrophys. J.*, **11**, 218.
- Thorne, R. M., E J Smith, R. K Boston, and R. E. Holzer (1973), Plasma-spheric hiss, *J. Geophys. Res.*, **78**, 1581-1596.
- Tinsley, B A (1976), Evidence that the recovery phase ring current consists of helium ions, *J. Geophys. Res.*, **81**, 6193-6196.
- Tohmatsu, T , and T. Nagata (1960), Energy and flux of corpuscular streams impinging the earth's atmosphere, *Rep. Ionospheric Space Res. Japan*, **14**, 301.
- Tomassian, A. D., T A. Farley, and A L Vampola (1972), Inner-zone energetic-electron repopulation by radial diffusion, *J. Geophys. Res.*, **77**, 3441-3454.
- Torr, D. G., M. R Torr, R. A. Hoffman, and J. C G Walker (1976), Global characteristics of 0.2 to 26 keV charged particles at F region altitudes, *Geophys. Res. Lett.*, **3**, 305-308.
- Torr, D. G , M R Torr, J C G Walker, and R A. Hoffman (1975), Particle precipitation in the South Atlantic geomagnetic anomaly, *Planet. Space Sci.*, **23**, 15-26
- Tsurutani, B T., E J. Smith, and R M Thorne (1975), Electromagnetic hiss and relativistic electron losses in the inner zone, *J. Geophys. Res.*, **80**, 600-607
- Tulinov, V. F (1967), On the role of corpuscular radiation in the formation of the lower ionosphere (below 100 km), *Space Res.*, **VII**, North-Holland Publ Co., Amsterdam, 386-390
- Tulinov, V. F., V. M. Feigin, V A. Lipovetsky, and Yu. M. Zhuchenko (1974), Sporadic source of ionization in the D- and E-regions of the nocturnal ionosphere at middle latitudes, *Kosmich. Issled.*, **12**, 219.

- Tulinov, V. F., V. M. Feigin, Yu. M. Zhuchenko, V. A. Lipovetsky, V. A. Dyachenko, and L. S. Novikov (1976), Effects of corpuscular radiation on the ionosphere at different geomagnetic latitudes, *Space Res.*, XVI, Akademie-Verlag, Berlin, 509-512.
- Tulinov, V. F., V. M. Feigin, Yu. M. Zhuchenko, V. A. Lipovetsky, and L. S. Novikov (1975), Rocket studies of corpuscular radiation at various geomagnetic latitudes, *Cosmic Res.*, 13, 461-466
- Tuohy, I. R., and J. R. Harries (1973), Observation of electrons at mid-latitude during a magnetic storm, *J. Geophys. Res.*, 78, 8381-8386
- Turiel, I., and A. MacGregor (1970), An observation of mirroring electrons at low altitudes, University of California Lawrence Livermore Laboratory, Rep. UCRL-72615
- Vakulov, P. V., N. L. Grigorov, B. Dobrovolska, Yu. Dubinsky, A. V. Zakharov, K. Kudela, S. N. Kuznetsov, V. A. Kuznetsova, N. F. Pisarenko, L. A. Savenko, S. Fisher, A. Somogyi, and I. A. Yuzefavich (1976), Studies of corpuscular radiation in the earth's environs based on Intercosmos 5 data, *Space Res.*, XVI, Akademie-Verlag, Berlin, 513-517.
- Valentine, J. M., and S. C. Curran (1958), Average energy expenditure per ion pair in gases and gas mixtures, *Rep. Progress Phys.*, 21, 1-29.
- Valot, P., and J. Engelmann (1973), Pitch angle distribution of geomagnetically trapped protons for  $1.2 < L < 2.1$ , *Space Res.*, XIII, Akademie-Verlag, Berlin, 675-681
- Vernov, S. N., E. V. Gorchakov, P. I. Shavrin, and K. V. Sharvina (1967), Radiation belts in the region of the South Atlantic magnetic anomaly, *Space Sci. Rev.*, 7, 490-533.
- Vlasov, M. N. (1974), Secondary electron fluxes by precipitating electrons and the excitation of the atmospheric constituents in the daytime at midlatitude, *J. Atmos. Terr. Phys.*, 36, 1733-1738

- Voss, H. D., and L. G. Smith (1974), Design and calibration of a rocket-borne electron spectrometer for investigation of particle ionization in the nighttime midlatitude E region, *Aeron. Rep. No. 62*, Aeron. Lab., Dep, Elec. Eng., Univ Ill, Urbana-Champaign.
- Voss, H. D., and L. G. Smith (1977), Nighttime ionization by energetic electrons at midlatitudes in the altitude region 120 to 200 km, *EOS, Trans AGU*, 58, 454
- Voss, H. D., L. G. Smith, and R. A. Goldberg (1977), Ionization by energetic protons in the nighttime equatorial F region, for presentation at Fall AGU meeting, San Francisco, CA
- Wakai, N. (1967), Quiet and disturbed structure and variations of the nighttime E region, *J. Geophys. Res.*, 72, 4507-4517
- Walt, M. (1967), Penetration of electrons into the atmosphere, in *Aurora and Airglow*, B. M. McCormac (ed), Reinhold Publ. Co., New York, 287-292
- Walt, M. (1971), Radial diffusion of trapped particles and some of its consequences, *Rev. of Geophysics and Space Physics*, 9, 11-25.
- Walt, M., L. F. Chase, Jr., J. B. Cladis, W. L. Imhof, and D. J. Knecht (1960), Energy spectra and altitude dependence of electrons trapped in the earth's magnetic field, *Space Res.*, Vol. 1, North-Holland Amsterdam, 910-920.
- Walt, M., W. M. MacDonald, and W. E. Francis (1968), Penetration of auroral electrons into the atmosphere, in *Physics of the Magnetosphere*, 10, R. L. Carovillano, J. F. McClay, and H. R. Radoski (eds), 534-555
- Wedde, T. (1970), On the influence of inhomogeneous magnetic fields upon the scattering and absorption of auroral electrons, *Intern. Rapport E-162, N-2007*, Norwegian Defence Research Establishment, Kjeller, Norway, 1-120
- Weller, C. S., and G. R. Carruthers (1972), High altitude observations of

- far and extreme UV radiation at night, *EOS, Trans. AGU*, 53, 1066
- Weller, C S , R R. Meier, and B A Tinsley (1971), Simultaneous measurements of the hydrogen airglow emissions of Lyman alpha, Lyman beta, and Balmer alpha, *J. Geophys Res.*, 76, 7734-7744
- West, H I , and R M Buck (1976), Energetic electrons in the inner belt in 1968, *Planet. Space Sci.*, 24, 643-655
- Williams, D J (1976), *Physics of Solar Planetary Environments*, VI and VII, Proc of the Int Symposium on Solar-Terrestrial Physics, June 7-18, 1976, Boulder, CO, No 76-29443, ISBN8-87590-204-9, 1-510, 511-1038
- Williams, D J., and J. W Kohl (1965), Loss and replenishment of electrons at middle latitudes and high B values, *J. Geophys Res.*, 70, 4139-4150
- Willaims, E. J. (1939), Concerning the scattering of fast electrons and of cosmic-ray particles, *Proc. Roy Soc.*, A169, 531-572
- Winckler, J R (1974), An investigation of wave-particle interactions and particle dynamics using electron beams injected from sounding rockets, *Space Sci. Rev* , 15, 751-780
- Wu, C S. (1960), The interaction of beta particles with matter, in *Nuclear Spectroscopy, Part A*, F. Ajzenbert-Selove (ed), Academic, New York, 15-30.
- Wulff, A , and J A Gledhill (1974), Atmospheric ionization by precipitated electrons, *J. Atmos. Terr Phys.*, 36, 79-91
- Young, J M., C Y Johnson, and J C Holmes (1967), Positive ion composition of a temperate latitude sporadic E layer as observed during a rocket flight, *J Geophys. Res.*, 72, 1473-1479
- Young, J M , C S Weller, C. Y. Johnson, and J C Holmes (1971), Rocket observations of the far UV nightglow at Lyman  $\alpha$  and shorter wavelengths, *J. Geophys. Res.*, 76, 3710-3722
- Zmuda, A J (1966), Ionization enhancement from Van Allen electrons in the South Atlantic magnetic anomaly, *J Geophys. Res* , 71, 1911-1917